Identification of particles and hard processes with the spectrometer PHOS of the ALICE experiment

Gustavo Conesa Balbastre

VNIVERSITAT DE VALÈNCIA

(ESTUDI GENERAL)

DEPARTAMENT DE FÍSICA ATÓMICA, MOLECULAR I NUCLEAR

INSTITUTO DE FÍSICA CORPUSCULAR

Identification of particles and hard processes with the spectrometer PHOS of the ALICE experiment

DOCTORAL THESIS

PRESENTED BY

GUSTAVO CONESA BALBASTRE

TO OBTAIN THE DEGREE OF DOCTOR IN PHYSICAL SCIENCES

2005

VNIVERSITAT DE VALÈNCIA

(ESTUDI GENERAL)

DEPARTAMENT DE FÍSICA ATÓMICA, MOLECULAR I NUCLEAR

INSTITUTO DE FÍSICA CORPUSCULAR

Identificación de partículas y procesos duros con el espectrómetro PHOS del experimento ALICE

TESIS DOCTORAL

PRESENTADA POR

GUSTAVO CONESA BALBASTRE

PARA OPTAR AL GRADO DE DOCTOR EN CIENCIAS FISICAS

2005

UNIVERSITÉ DE NANTES

ÉCOLE DOCTORALE

SCIENCES ET TECHNOLOGIES

DE L'INFORMATION ET DES MATÉRIAUX

Année : 2005 N° B.U. :

Thèse de Doctorat de l'Université de Nantes

Spécialité : Physique Nucléaire

Présentée et soutenue publiquement par

Gustavo CONESA BALBASTRE

le 9 juin 2005

à l'Instituto de Física Corpuscular de Valencia

Identification de particules et de processus durs dans le spectromètre PHOS de l'expérience ALICE

Jury

Président Yves SCHUTZ, *Directeur de Recherche CNRS, CERN Genève*

Rapporteurs Patrick AURENCHE, *Directeur de Recherche CNRS, LAPTH Annecy*

Andreas MORSCH, *Chercheur, CERN Genève*

Examinateurs Nestor ARMESTO PEREZ, *Professeur, Université de Santiago de Compostela*

Hugues DELAGRANGE, *Directeur de Recherche CNRS, SUBATECH Nantes*

José DIAZ MEDINA, *Professeur, IFIC - Université de Valencia*

Pedro LADRON DE GUEVARA, *Chercheur, CIEMAT Madrid*

Directeur de Thèse : Hugues DELAGRANGE
Laboratoire : SUBATECH
Co-encadrant : José DIAZ MEDINA
Laboratoire : IFIC
Composantes de rattachement du directeur de thèse : Faculté des sciences

N° ED 0366-205

D. José Díaz Medina, Profesor Titular de Física Atómica, Molecular y Nuclear y miembro del Instituto de Física Corpuscular de la Universidad de Valencia,

CERTIFICA: Que la presente memoria "Identification of Particles and Hard Processes with the Spectrometer PHOS of the ALICE Experiment" ha sido realizada bajo su dirección en los laboratorios del Instituto de Física Corpuscular y del Departamento de Física Atómica, Molecular y Nuclear por D. Gustavo Conesa Balbastre, y constituye su Tesis para optar al grado de Doctor en Ciencias Físicas.

Y para que así conste, en cumplimiento de la legislación vigente, presenta ante la Facultad de Física de la Universidad de Valencia la referida Tesis, firmando el presente certificado en

Valencia, a 29 de Marzo de 2005

Fdo: José Díaz Medina

Abstract

Heavy-ion collisions are a unique tool to study nuclear matter under extreme conditions of density and temperature as those existing a few moments after the Big Bang, in which is thought that nuclear matter was a plasma of almost free quarks and gluons. The production of the Quark-Gluon Plasma is the main goal of the ALICE experiment at the LHC collider, where Pb-Pb collisions at $5.5A$ TeV will be made. High energy photons are an interesting probe to investigate these collisions because they can give unperturbed information on their creation conditions. The PHOS detector in the ALICE experiment is devoted to their measurement. In this thesis, the PHOS performance is studied and particle and hard processes identification algorithms are developed.

The PHOton Spectrometer PHOS consists of five modules, each composed of 56×64 $PbWO_4$ crystals (Electromagnetic Calorimeter) and associated to a Charged Particle Veto detector. PHOS was designed to measure and identify with high accuracy photons, electrons, and π^0 and η mesons over a broad energy domain, ranging from 0.5 GeV to beyond 100 GeV. PHOS has a small angular acceptance, $\Delta\phi = 100^o$ and $|\eta| < 0.12$, compared to that of the ALICE central tracking system, but this acceptance is sufficient to perform photon physics in the GeV range, as well as to measure rare events at larger energies, in the tens of GeV range. The parameters of the algorithms developed to simulate the response of PHOS and to perform the reconstruction of the signals collected by PHOS have been tuned to reproduce the data measured in test experiments performed with a prototype. PHOS will be able to measure with a high energy resolution, ranging from 5 % at 0.5 GeV to 1 % at 120 GeV in particle free environment, and in heavy-ion environment the energy resolution is worsened by less than 2 %. The material present in ALICE between the interaction point and PHOS, absorbs about 10 % of photons if holes in the TRD and TOF detectors matching the PHOS acceptance are made and about 30 % without holes.

Particle identification with PHOS relies on three identification criteria: time of flight measurement; charged particle matching between the Charged Particle Veto and the Electromagnetic Calorimeter; and shower shape analysis. Combining these criteria we are able to discriminate photons, electrons and hadrons with good accuracy in the energy range from 0.5 to 120 GeV. I find that the contamination of wrongly identified photons in a heavy-ion collision ranges from about 3 % to 1 % depending on the requested level of identification purity and on the particle environment. Neutral pions are identified through an invariant-mass analysis in the energy range between 0 and 40 GeV, and by an event-by-event shower shape analysis for energies from 40 GeV to 120 GeV at which their two decay photons are detected as a single cluster in PHOS. High-energy photons converted in the material in front of PHOS can be recovered with the help of the tracking information collected by the TPC, detector placed before the TRD and TOF, method only useful in the configuration without holes.

Prompt photons are produced in Compton and annihilation processes at the parton level in *pp* and Pb-Pb collisions. The PYTHIA generator was employed to generate *pp* collision events that contain in the final state either a prompt photon and a jet (γ-jet) with energies larger than 20 GeV or two jets (jet-jet) which constitute the main source of background. Pb-Pb collisions were simulated by embedding a *pp* collision in a heavy-ion collision simulated by the HIJING generator. The production rate expected in one ALICE running year was estimated. The predicted background (π^0 photon decay, single and overlapped clusters, and bremsstrahlung) exceeds by a factor two the prompt photon signal. An additional identification method is required to separate prompt and background photons: the Isolation Cut Method. This method is based on the fact that prompt photons are produced isolated whereas the background is mainly produced by π^0 mesons belonging to jets, and therefore accompanied by other particles. I developed isolation criteria based on the particle multiplicity inside a cone of size R around the direction

of prompt photon candidates, and on the momentum of the particles inside this cone. This identification method was applied to the PYTHIA simulations to construct the prompt photon spectrum expected to be measured in one year of data taking. The cross section corrected for the identification efficiencies was calculated and both statistical and systematic errors were estimated.

Prompt photons are associated with recoiling jets. I developed an algorithm to identify γ-jet events based on the identification of the prompt photon in PHOS and the measurement of the recoiling jet particles in the central tracking system and in EMCal (if available). This algorithm has been tested with the signal (γ-jet) and background (jet-jet) events of Pb-Pb and *pp* collisions for jets with energies larger than 20 GeV. Since the cross section of jet-jet production is much larger than the cross section of γ-jet production, there is a huge background due to π^o decay photons but this background can be reduced to a negligible level by the γ-jet identification algorithm together with shower shape and isolation cut analysis. The parton fragmentation function, which is affected by the parton energy loss in the nuclear medium, was calculated for the simulated γ-jet events, for both *pp* and Pb-Pb collisions. From these simulations we found that variations of the nuclear modification factor larger than 5 % in the range $0.1 < z < 0.5$ could be measured.

Resumen

Las colisiones de iones pesados son una herramienta única para estudiar la materia nuclear en condiciones extremas de densidad y temperatura, como las que se dieron poco después del Big Bang, en el cual se cree que la materia nuclear estaba compuesta por un plasma de quarks y gluones casi libres. La producción del Plasma de Gluones y Quarks es el interés central del experimento ALICE del colisionador LHC, donde se realizarán colisiones de Pb-Pb a $5.5A$ TeV. Los fotones de alta energía son sondas muy interesantes para investigar estas colisiones dado que proporcionan información no perturbada de las condiciones de su creación. El detector PHOS del experimento ALICE se encargará de medir estas partículas. En esta tesis se presenta un estudio del rendimiento de PHOS y se desarrollan algoritmos de identificación de partículas y de procesos duros.

El espectrómetro de fotones PHOS consiste en 5 módulos, cada uno compuesto por 56×64 cristales de $PbWO_4$ (Calorímetro Electromagnético) y un detector Veto de Partículas Cargadas. PHOS fue diseñado para medir e identificar con gran precisión fotones, electrones, y mesones π^o y η en un extenso dominio de energía de 0.5 GeV a más allá de 100 GeV. PHOS tiene un tamaño angular pequeño, $\Delta\phi = 100^o$ y $|\eta| < 0.12$, comparado con el del sistema central de muestreo de ALICE, pero este tamaño es suficiente para estudiar física de fotones de baja energía en la zona del GeV, así como medir sucesos raros a energías más elevadas, a decenas de GeV. Los parámetros de los algoritmos desarrollados para simular la respuesta del detector y para realizar la reconstrucción de las señales recogidas por PHOS fueron ajustados para reproducir los datos medidos en pruebas experimentales realizados con un prototipo de PHOS. Estos datos confirman que PHOS es capaz de medir con una alta resolución en energía que va de 5 % para fotones de 0.5 GeV a 1 % para fotones de 120 GeV con un ambiente libre de otras partículas, degradándose menos del 2 % en ambientes de partículas producidos en colisiones de iones pesados. El material de ALICE entre el punto de interacción y PHOS absorbe al menos un 10 % de los fotones si se hacen agujeros en los detectores TRD y TOF en frente de PHOS y un 30 % de los fotones sin estos agujeros.

La identificación de partículas con PHOS se apoya en tres criterios de identificación: la medida del tiempo de vuelo; la identificación de partículas cargadas por medio de la conexión de los impactos de la partícula en el Veto de Partículas cargadas y el Calorímetro Electromagnético de PHOS; y el análisis de la forma de la cascada. Combinando estos criterios somos capaces de separar fotones, electrones y hadrones con una buena precisión en el dominio de energías comprendido entre 0.5 y 120 GeV. Encuentro que la contaminación debida a fotones mal identificadas en una colisión de iones pesados varía entre el 3 % y el 1 % dependiendo del grado de pureza de la identificación y del ambiente de partículas del suceso. Los mesones π^o son identificados o bien mediante análisis de masa invariante en el dominio de energías entre 0 y 40 GeV, o bien suceso a suceso mediante análisis de la forma de la cascada en el dominio de energía entre 40 y 120 GeV, para el cual los dos fotones de la desintegración del mesón son detectados como una sola partícula en PHOS. Los fotones de alta energía convertidos en el material en frente de PHOS pueden ser recuperados con la ayuda de la información proporcionada por el detector TPC, que se encuentra delante de los detectores TRD y TOF, método solo útil en la configuración sin agujeros.

Los fotones *rápidos* se producen en procesos Compton y de aniquilación al nivel de los partones en colisiones *pp* y Pb-Pb. El generador de sucesos PYTHIA fue el empleado para generar sucesos de colisiones *pp* que contienen en el estado final un fotón rápido y un jet (γ-jet) con energías superiores a 20 GeV o dos jets (jet-jet) que constituyen la mayor fuente de fondo de fotones. Las colisiones Pb-Pb fueron simuladas mezclando una colisión *pp* en una colisión de iones pesados simulada por el generador de sucesos HIJING. La tasa de producción esperada de fotones rápidos en un año de funcionamiento de ALICE fue estimada. El fondo que se predice (fotones producidos en la desintegración del π^0 y bremsstrahlung) excederá un

factor dos la señal de fotones prompts. Un método de identificación adicional es necesario para separar los fotones rápidos del fondo, el Método de Corte por Aislamiento. Este método se basa en el hecho que los fotones rápidos son producidos aislados mientras que el fondo es principalmente producido por mesones π^0 pertenecientes al jet y por lo tanto acompañados por otras partículas. He desarrollado un criterio de aislamiento basado en la multiplicidad de partículas dentro de un cono de talla R alrededor de la dirección de la partícula candidata a ser fotón rápido, y en el momento de las partículas dentro del cono. Este método de identificación fue aplicado a las simulaciones PYTHIA para construir el espectro de fotones rápidos que se espera medir en un año de toma de datos. La sección eficaz de producción de los fotones rápidos fue calculada, corregida por la eficiencias de detección, y los errores sistemáticos y estadísticos han sido estimados.

Los fotones rápidos están asociados con un jet en retroceso. He desarrollado un algoritmo de identificación de sucesos γ-jet basado en la identificación del fotón rápido en PHOS y en la medida de las partículas del jet en retroceso por el sistema central de muestreo y, si está disponible, por el detector EMCal. Este algoritmo fue afinado y probado con los sucesos señal (γ-jet) y fondo (jet-jet) de colisiones Pb-Pb y *pp* con jets de energías superiores a 20 GeV. Dado que la sección eficaz de producción de procesos jet-jet es mucho mayor que la sección eficaz de sucesos γ-jet, hay un gran fondo debido a los fotones de desintegración de los mesones π^o. El fondo debido a la identificación de los fotones rápidos puede ser reducido a un nivel despreciable utilizando el algoritmo de identificación de sucesos γ-jet conjuntamente con los análisis de la forma de la cascada y de corte por aislamiento. La función de fragmentación de los partones, la cual es afectada por la pérdida de energía de los partones al atravesar el medio nuclear, fue calculada para los sucesos γ-jet simulados, tanto para colisiones *pp* como Pb-Pb. De estas simulaciones encontramos que variaciones del factor de modificación nuclear superiores al 5 % en el dominio $0.1 < z < 0.5$ podrían ser medidas.

Résumé

Les collisions d'ions lourds sont un outil unique pour étudier la matière nucléaire dans des conditions extrêmes de densité et de température, comme celles présents peu après le Big Bang, où la matière nucléaire aurait été composé d'un plasma de quarks et de gluons quasi-libres. Sa production à l'aide de collisions Pb-Pb à $5.5A$ TeV est le thème central de l'expérience ALICE-LHC. Les photons émis dans ces collisions sont des signatures très intéressantes parce qu'elles apportent des informations non perturbées sur le plasma. Le détecteur PHOS de l'expérience ALICE est dédié à leur détection. Cette thèse présente une étude des performances de PHOS et décrit les algorithmes d'identification de particules et de processus durs.

Le spectromètre de photons, PHOS, est constitué de cinq modules, chacun comportant 56×64 cristaux de $PbWO_4$ (Calorimètre Électromagnétique) et couplé à un détecteur Veto de Particules Chargées. PHOS a été conçu pour mesurer et identifier, avec une grande précision, photons, électrons et mésons π^0 et η, dans un grand domaine en énergie, de 0.5 GeV à au-delà de 100 GeV. PHOS possède une faible couverture angulaire, $\Delta\phi = 100^o$ et $|\eta| < 0.12$, comparée à celle du système central de trajectographie d'ALICE, mais cette couverture est, néanmoins, suffisante pour étudier la physique de photons de basse énergie dans le domaine du GeV et pour mesurer des événements rares, dans le domaine des dizaines de GeV. Les paramètres des algorithmes développés pour simuler le fonctionnement de PHOS et pour reconstruire les signaux collectés par PHOS ont été ajustés afin de reproduire les données mesurées à l'aide d'un prototype de PHOS pendant des test expérimentaux sous faisceau. Ces données confirment que PHOS pourra mesurer avec une grande résolution en énergie qui varie de 5 % pour des énergies de photons de 0.5 GeV à 1 % pour des énergies des photons de 120 GeV dans un environnement libre de particules, et dans un environnement créé par collisions d'ions lourds la résolution en énergie se dégrade moins du 2 %. Les matériaux d'ALICE situés entre le point d'interaction et PHOS absorbent environ 10 % des photons si il y des ouvertures aux détecteurs TRD et TOF vis-à-vis de PHOS, et environ le 30 % des photons quand les détecteurs TOF et TRD restent dans leur intégralité.

L'identification de particules avec PHOS repose sur trois méthodes : la mesure du temps de vol; l'identification des particules chargées grâce au lien entre l'impact au Veto de Particules Chargés et le Calorimètre Électromagnétique de PHOS; l'analyse de la forme de la gerbe électromagnétique. Si nous combinons ces méthodes, les photons, électrons et hadrons sont discriminés avec une bonne précision dans le domaine d'énergie de particules s'étendant de 0.5 à 120 GeV. Je trouve que la contamination due à des photons mal identifiés dans une collision d'ions lourds est faible, et qu'elle varie d'environ 3 % à 1 % en fonction du niveau de pureté et de l'efficacité d'identification et en fonction de l'environnement de particules. Les mésons π^0 peuvent être identifiés soit par l'application de méthodes statistiques avec analyse de la masse invariante pour des énergies de mésons entre 0 et 40 GeV, soit par recours à des analyses, événement par événement, prenant en compte la forme de la gerbe électromagnétique pour des mésons d'énergies entre 40 et 120 GeV, énergies pour lesquelles les deux photons de décroissance sont détectés comme une seule particule par PHOS. Les photons de haute énergie convertis dans les matériaux présents entre le point d'interaction et PHOS peuvent être récupérés en tirant profit d'informations disponibles grâce au détecteur TPC, placé avant le TRD et le TOF, méthode seulement applicable dans le cas de la configuration d'ALICE sans ouvertures supplémentaires.

Les photons prompts sont produits lors de collisions de partons, par, d'une part, processus Compton et, d'autre part, annihilation dans des collisions *pp* et Pb-Pb. Nous avons employé le générateur d'événements PYTHIA pour simuler les événements de collisions *pp* qui contiennent, dans l'état final, soit à un photon associé à un jet émis à l'opposé avec des énergies plus larges que 20 GeV, soit à deux

jets émis à quasiment 180 degrés. Les collisions Pb-Pb ont été simulés en mélangeant les simulations des collisions *pp* avec des collisions d'ions lourds simulées par le générateur d'événements HIJING. J'ai estimé la production de photons prompts attendue pendant une année de fonctionnement de l'expérience ALICE. Le fond prédit (photons de la décroissance du π^0 et radiation de freinage "bremsstrahlung") dépassera d'un facteur deux, le signal dû aux photons prompts. Une méthode d'identification de photons additionnel est nécessaire pour discriminer photons prompts et photons du fond, la Méthode par Coupure d'Isolement. Cette méthode est basée sur le fait que les photons prompts sont produits isolés tandis que le fond est principalement dû à des mésons π^0 qui appartiennent à des jets qui sont, donc accompagnés par d'autres particules. Par conséquent, j'ai développé un critère d'isolement basé sur la considération de la multiplicité de particules dans le cône de taille R autour la direction d'un possible photon prompt, et sur une sélection appliquée à l'impulsion de ces particules présentes dans le cône. J'ai appliqué cette méthode d'identification aux résultats des simulations PYTHIA et j'ai déterminé le spectre attendu de photons prompts, pendant une année de prise de données par l'expérience ALICE. La section efficace a été calculée, en tenant compte des efficacités d'identification, et les erreurs systématiques et statistiques ont, également, été estimées.

Les photons prompts sont couplés à un jet qui recule. J'ai développé une méthode qui permet d'identifier ceux-ci, basée sur l'identification des photons prompts par PHOS et par la mesure des propriétés des particules du jet par le système central de trajectographie et, s'il est installé, par le détecteur EMCal. Cet algorithme a été testé avec des évènements de type "signal" (γ-jet) et de type fond (jet-jet) produits en collisions Pb-Pb et *pp* avec des énergies plus larges que 20 GeV. Étant donnée que la valeur de la section efficace de production des événements jet-jet est plus élevée que celle des événements γ-jet, il existe un fond important dû à la décroissance des mésons π^o. Néanmoins, la contribution du fond peut être réduite à un niveau négligeable par l'algorithme d'identification d'événements γ-jet s'il est utilisé, conjointement, avec les analyses d'isolement et de forme de gerbe. La fonction de fragmentation des partons, laquelle est modifié par la perte d'énergie des partons dans le milieu nucléaire, a été calculé pour les événements γ-jet simulés, pour les collisions *pp* et Pb-Pb. Nos simulations permettent d'apprécier que, des variations du facteur de modification nucléaire supérieures à 5 % dans la région $0.1 < z < 0.5$ pourraient être mesurées.

Agradecimientos / Remerciements / Acknowledgments

En estas breves y claramente insuficientes líneas me gustaría expresar mi agradecimiento a las diferentes personas que sin su apoyo y ayuda no hubiese sido posible este trabajo.

En primer lugar quisiera agradecer a mis directores: a José Díaz por haberme introducido en este campo y haberme proporcionado todos los elementos necesarios para poder realizar este trabajo durante todos estos años así como por todo el trabajo realizado para la corrección de esta tesis; a Hugues Delagrange por haber aceptado mi dirección por parte francesa, haberme facilitado mi trabajo en Nantes y por sus útiles consejos durante la redacción; muy especialmente a Yves Schutz por su dirección científica, trato humano y apoyo durante todo este tiempo.

También quería agradecer a Dmitri Y. Peressounko y especialmente a Yuri V. Kharlov por sus consejos y todo su trabajo sin el cual difícilmente pudiese haber avanzado.

Al personal de SUBATECH y muy especialmente a los estudiantes de doctorado y a Laurent Aphecetche y a Ginés Martínez por haberme acogido durante mis largas estancias en Nantes. Pero sobretodo me gustaría expresar todo mi cariño y gratitud a María Jesús, Raquel y Zaida por todo el apoyo y compañía brindados durante el tiempo que coincidimos en Nantes.

A la ciudad de Nantes y sus creperías, kebabs ...

Gracias a todas las personas que he conocido o compartido el tiempo en Ginebra y muy especialmente a José Enrique, Gabriela, Esteban, Belén, Lluís, Diego y David.

Y por supuesto a toda la gente que me estima y me ha acompañado tanto física como electrónicamente. Gracias a Juande, Ana, Inma y mucha más gente cuyas vidas han cambiado mucho durante este periodo de tiempo y que no se han olvidado de mi.

Finalmente, pero no en estima, agradecer muy especialmente a Jorge y María José todo el apoyo, afecto y cariño que me han brindado y que no he sabido ni sabré devolver aunque digan lo contrario. Y no me olvido de mi familia que me ha sufrido durante todo este tiempo.

A todos vosotros,

GRACIAS.

Par ces lignes, clairement insuffisantes, je voudrais exprimer ma reconnaissance aux différentes personnes dont soutien et aide ont rendu possible ce travail.

D'abord je suis très reconnaissant à mes directeurs de thèse : à José Díaz pour m'avoir introduit dans ce domaine et fournit tous les éléments nécessaires afin de pouvoir réaliser ce travail pendant toutes ces années; à Hugues Delagrange pour avoir accepté ma direction de thèse du coté français, pour avoir facilité mon travail à Nantes et pour ses conseils très utiles pendant la rédaction; très spécialement à Yves Schutz pour sa supervision scientifique, son traitement humain et son soutien pendant tout ce temps.

J'aimerais aussi remercier à Dmitri Y. Peressounko et spécialement à Yuri V. Kharlov pour ses conseils et tout son travail sans lequel difficilement j'aurais pu avancer et obtenir rien.

J'aimerais également remercier tout le personnel de SUBATECH et très particulièrement les thésards et aussi à Laurent Aphecetche et Ginés Martínez pour m'avoir accueilli pendant mes longs séjours à Nantes. Mais surtout je voudrais exprimer toute mon affection et gratitude à María Jesús, Raquel et Zaida pour leur soutien et compagnie pendant le temps que nous avons partagé à Nantes.

J'étends mes remerciements à la ville de Nantes pour ses crêperies, kebabs ...

Merci aux personnes que j'ai connues ou qui m'ont soutenue à Genève et très particulièrement à José Enrique, Gabriela, Esteban, Belén, Lluís, Diego et David.

Et certainement à tout le monde qui m'estiment et qui m'ont accompagné sur place et par courrier électronique, merci à Juande, Ana, Inma et à beaucoup de personnes dont les vies ont changé beaucoup pendant toute cette période et qui ne m'ont pas oublié.

Finalement, j'aimerais remercier très spécialement Jorge et María José pour tout le soutien et affection qui m'ont offerts et que je n'ai su ni serais capable de retourner quoiqu'ils disent le contraire. Et je ne m'oublie pas ma famille qui m'a subi tout ce temps.

À tous d'entre vous,

MERCI.

In the following and clearly insufficient lines I would like to express my gratitude to the different people whose help and support made possible this work.

First of all I would like to thank my supervisors : José Díaz for having introduced me to this field, for having provided me all the necessary elements to do this work all these years and for his work correcting this thesis; Hugues Delagrange for having accepted my supervision for the French part, for having made easy the work performed in Nantes and for his useful advices during the redaction; specially I would like to thank Yves Schutz for his scientific direction, his human touch and his support all this time.

I would like also to thank Dmitri Y. Peressounko and specially Yuri V. Kharlov for their advices and all their work that made possible that I could advance and obtain my results.

To all the SUBATECH staff and very specially to all Ph. D. students and to Laurent Aphecetche and to Ginés Martínez for having welcomed me among them during all my long stays at Nantes. But particularly, I would like to express all my fondness and gratitude to María Jesús, Raquel and Zaida for their support and company offered during the time we shared in Nantes.

To the city of Nantes for its crêperies and kebabs ...

Thanks to all the people that I have known or shared my time with in Geneva and specially to José Enrique, Gabriela, Esteban, Belén, Lluís, Diego and David.

And of course to all those people that appreciates me and who have accompanied me physically and electronically. Thanks to Juande, Ana, Inma and much more people whose lives have changed a lot in this period of our lives and who have not forgotten me.

Finally, last but not least in my thoughts, I would like to thank very specially to Jorge and María José for all the support and fondness that they have offered to me and which I do not know and will not know how to return although they say the contrary. And I am not forgetting my family that have suffered me all along the thesis.

To all of you,

THANK YOU.

Dedicatoria

A mis abuelos

Parece, Sancho,

que no hay refrán que no sea verdadero,

porque todos son sentencias sacadas

de la mesma experiencia,

madre de las ciencias todas.

"El Quijote"

Miguel de Cervantes y Saavedra

Contents

List of Figures

List of Tables

Physique des ions lourds à des énergies ultra-relativistes (LHC)

La physique des hautes énergies est dédiée à l'étude et description des composants élémentaires de la matière et des interactions qui régissent leurs propriétés. En particulier, la physique des ions lourds à des énergies ultra-relativistes concerne les phénomènes collectifs impliquant des particules élémentaires quand elles sont soumises à des conditions extrêmes de pression et température. De telles conditions ont prévalu pendant les premiers instants après le Big Bang. La théorie de l'interaction forte prévoit que la matière nucléaire subit une transition de phase quand de telles conditions sont obtenues. Il y a une évolution d'un système de quarks confinés dans la matière nucléaire normale à celui regroupant des quarks quasi-libres, créant une matière en forte interaction, appelée le Plasma de Quarks et de Gluons (QGP en anglais). De telles conditions extrêmes peuvent être obtenues par l'intermédiaire de collisions entre ions lourds (HIC en anglais) à énergies ultra-relativistes qui sont produites auprès de collisionneurs comme RHIC et dans un futur proche, le LHC. Pouvoir observer qu'une telle transition a eu lieu et décrire quelles sont les propriétés de cette nouvelle matière n'est pas une tâche facile. Il y a plusieurs signatures expérimentales différentes, notamment l'émission de photons de la collision qui est très intéressante étant donnée que ceux peuvent être produits dans de telles conditions de matière dense et chaude et s'échapper sans interagir. Ce processus permet d'obtenir une information directe sur leurs conditions de création.

Dans ce chapitre j'explique brièvement la théorie d'interaction forte et son étude avec des collisions d'ions lourds. Finalement, je détaille la motivation de cette thèse.

Description de la matière, des particules et des interactions

Notre monde, selon le Modèle Standard de Particules, est composé de deux types de particules, d'une part, celles composant la matière, et, d'autre part, celles responsables des interactions. Les composants de la matière sont des *fermions*, particules de spin 1/2. Il y a deux types: les *quarks* q avec *saveurs* u, d, s, c, b, t et ses *anti-saveurs*, tous ayant

une charge fractionnelle $\pm 1/2\, e$ ou $\pm 2/3\, e$; et les *leptons,* $e^{\pm}$, $\mu^{\pm}$, $\tau^{\pm}$, $\nu_{e,\mu,\tau}$ et $\bar{\nu}_{e,\mu,\tau}$. Les particules vecteurs des interactions sont des *bosons*, de spin 0 ou 1. Parmi elles, il y a les photons γ, et les particules $W^{\pm}$ et Z^0, responsables de l'interaction électro-faible, et les *gluons* g, responsables de l'interaction forte.

Les quarks et les gluons sont confinés, dans la matière nucléaire normale, sous forme d'états quantiques appelés *hadrons.* Les hadrons sont classés en baryons, particules composées par la combinaison de 3 quarks de valence[1], et *mésons*, une combinaison de quark et anti-quark de valence. Les protons et les neutrons sont des baryons composés de quarks de valence (uud) et (udd) respectivement, et les pions π^+ et π^- sont des mésons avec quarks de valence $(u\bar{d})$ et $(d\bar{u})$ respectivement. Au sein des hadrons, en plus des quarks de valence, il existe une mer de paires $q\bar{q}$ et de gluons. Le nombre quantique appelé le *nombre baryonique* (B) différencie entre baryons et mésons, égal à $1/3$ pour les quarks et $-1/3$ pour les anti-quarks. Les baryons ont B entier et les mésons ont $B = 0$.

Expérimentalement l'observation directe des gluons et des quarks n'a été pas possible parce qu'ils restent confinés au sein des hadrons. L'existence des quarks a été mise en évidence grâce à des expériences de diffusion inélastique à haute énergie, où des électrons collisionnent avec des nucléons. L'interprétation de leurs résultats est cohérente avec l'hypothèse de la présence de constituants de taille ponctuelle et spin $1/2$ à l'intérieur du nucléon, appelés partons. Cette démarche est similaire en nature à l'expérience de Rutherford où la forme de la distribution angulaire de particules α après l'impact avec les atomes impliquait l'existence du noyau. A encore plus haute énergie, dans les expériences e^+e^-, des jets de particules, assez bien collimatés émergent de la région d'interaction, effet qui s'explique par annihilation en une paire $q\bar{q}$, suivie de la fragmentation de ceux-ci, émis à l'opposé l'un de l'autre. Dans la suite de ce mémoire, ce processus sera appelé simplement *jet.* Egalement, l'existence du gluon est confirmé par l'observation de collisions de particules où 3 jets émergent. Un d'eux doit être le résultat de la radiation d'un gluon de haute énergie par l'un des deux quarks créés et émis lors de la collision initiale.

La description de l'interaction entre quarks et gluons s'inspire de la théorie de *l'Electrodynamique Quantique* (QED en anglais), qui explicite les propriétés de la force existante entre particules chargés électriquement comme les électrons, par l'échange de photons. Dans cette théorie, la force entre 2 charges est décrite par le potentiel

$$V_{QED} = \frac{A}{r}, \tag{1}$$

où A est proportionnel au produit des charges et r est la distance entre elles.

La force fondamentale qui confine les quarks à l'intérieur des hadrons, est l'interaction forte, décrite par la théorie de la *Chromodynamique Quantique* (QCD en anglais). Selon QCD, le nombre quantique de *couleur* agit comme la charge électrique dans l'interaction

[1] Les quarks de valence sont ceux qui donnent à la particule les numéros quantiques (mais seulement une partie de la masse).

électromagnétique, et les gluons sont les responsables du maintien des quarks ensemble dans les hadrons. Il y a 3 couleurs différentes, (*rouge, bleu* et *vert*) et leurs correspondants *anti-couleurs.* A cause de la théorie des groupes il existe 8 gluons colorés. Néanmoins, il n'y a pas d'objets coloré libre dans la nature comme il y existe des charges libres dans QED. Les hadrons ne sont pas colorés et cela est connu comme le *confinement par couleur.* En suivant l'analogie avec QED, l'échange d'un gluon peut être employé pour donner une description précise de l'interaction forte mais seulement à courte distance. A grande distance, la situation est plus complexe. En fait, en plus de leur interaction avec les quarks, les gluons interagissent entre eux, à cause de leur nature colorée. C'est le contraire du cas des photons qui sont électriquement neutres et qui, donc, n'interagissent pas entre eux en processes de premier ordre. Les analyses de QCD sur réseau (Lattice QCD) assument que le potentiel entre une paire $q\bar{q}$ est donné approximativement par :

$$V_{q\bar{q}} = -\frac{A(r)}{r} + Kr. \tag{2}$$

Pour des petites valeurs de r, le premier terme de Eq. (2) domine et équivaut à une interaction de type Coulomb. Des analyses plus détaillées révèlent que $A(r) \propto 1/\ln(r^{-1})$, ce qui implique que l'interaction entre les quarks devient plus faible lors que leur distance de séparation diminue. Quand $r \to 0$, l'interaction entre les quarks disparaît: ce propriété est connu comme la *liberté asymptotique.* Si r augmente, le potentiel s'accroît, et par conséquence l'énergie pour retirer un quark d'un hadron devrais être infinie. Cependant quand une énergie apportée afin de séparer les quarks est comparable au moins au double de la masse au repos du quark, il est possible de désagréger le hadron par création de paires $q\bar{q}$. Ce mécanisme aide à expliquer la production de hadrons issus de la fragmentation de quarks dans des collisions à haute énergie.

Une description assez simple de l'interaction forte, le *modèle du sac*, est basé sur les concepts de confinement par couleur et de liberté asymptotique. Ce modèle assume que des quarks sans masse bougent librement dans un hadron sphérique de rayon R, mais que la pression du vide les empêche de s'échapper. La théorie QCD implique que l'état de plus basse énergie du vide n'est pas 0 mais $\langle\psi\bar{\psi}\rangle \approx -(240\ \mathrm{MeV})^3$, ce qui est responsable de l'effet connu comme la *brisure de la symétrie chirale*. La symétrie chirale prévoit que si les masses des quarks étaient faibles, ils existent en un des deux états possibles d'hélicité $h = \pm 1/2$[2]. Malheureusement, les quarks en mouvement dans le sac ont une *masse nue* et c'est seulement pour les quarks les plus légers, u et d, que la symétrie chirale est une symétrie approchée. Dans la matière nucléaire normale, dû à la pression du vide, ces quarks ne sont qu'une superposition des 2 valeurs, ce qui leur donne une masse additionnelle[3] [Han01, Jac05, MÖ1, Mol03].

[2] $h = \vec{s} \bullet \vec{k} / |k|$, où $\vec{s}$ et $\vec{k}$ sont le spin et l'impulsion de la particule.

[3] Les quarks u et d ont une petite masse nue de ~ 5 MeV, mais à cause de la brisure de la symétrie chirale, leur masse devient $\sim$350 MeV.

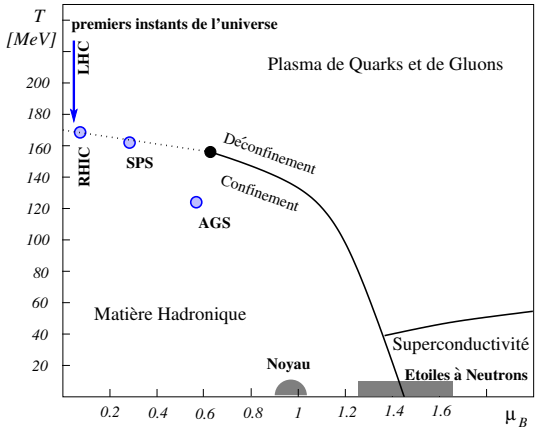

Figure 1: Diagramme de phases prédites par la théorie QCD. La ligne continue indique une transition probable du premier ordre. La ligne en pointillé indique une région avec une possible transition continue mais rapide appelée "crossover". Le cercle plein indique le point final critique d'une ligne de transition du premier ordre où la transition serait de deuxième ordre (qui pourrait être localisée à $\mu_B \sim 700$ MeV). Des phases plus exotiques peuvent exister à haute densité, par exemple à l'intérieur des étoiles de neutrons. Les conditions de gel (freeze-out) chimique atteintes dans des expériences de collisions d'ions lourds à AGS, SPS et RHIC sont aussi montrées. La flèche à haute T et bas μ_B indique le comportement attendu de la matière aux énergies du LHC après le gel (freeze-out), laquelle suit un chemin semblable à celui des premiers instants de l'univers après le Big Bang [Fri04].

Matière chaude et dense: Le Plasma de Quarks et de Gluons

La théorie QCD décrit l'interaction entre des objets colorés mais pour comprendre les propriétés de grands systèmes de particules, comme une matière constituée de quarks et de gluons, il est nécessaire de recourir à la thermodynamique. Les propriétés thermodynamiques d'un système sont normalement présentés dans la forme d'un diagramme de phases. Un diagramme des phases est une illustration graphique en fonction de *paramètres de contrôle*, où les différentes phases de la substance considérée occupent différentes régions. L'exemple le plus connu est le diagramme des phases de l'eau, dont les paramètres de contrôle sont la température T et la pression P. L'eau est généralement décrite en trois phases, liquide, gaz et solide[4]. Il y a des courbes de transition spécifiques $P(T)$ qui décrivent la transition d'une phase à l'autre et aussi dans le cas de l'eau il y a un point critique où les trois phases coexistent.

Dans le cas du diagramme des phases de la matière de quarks et de gluons (Fig. 1), les paramètres de contrôle sont la température et le *potentiel baryon-chimique* μ_B.

Dans les réactions entre particules élémentaires, un baryon qqq est toujours créé ou détruit par un anti-baryon $\bar{q}\bar{q}\bar{q}$ simultanément, et B reste constant. Pour les systèmes

[4]Il y a plusieurs phases solides mais je les regroupe sous le seul vocable solide.

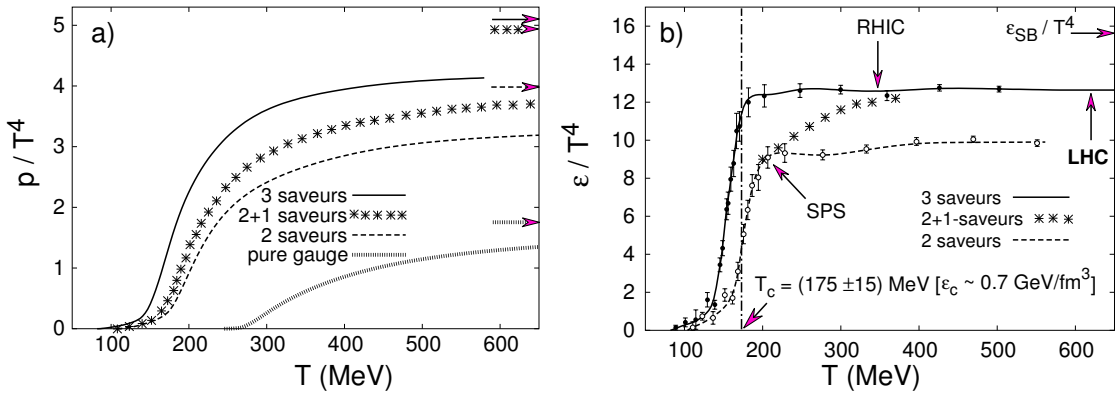

Figure 2: La pression (a) et densité d'énergie (b), prédites par QCD avec 0, 2, et 3 saveurs de quarks de masse légère, et deux quarks légers et un quark plus lourd (étrange). Les flèches sur les ordonnées du côté droit indiquent la valeur de la limite de Stefan-Boltzmann pour un gaz de quarks et de gluons idéal [ALI04].

ouverts où B peut varier, le potentiel le plus approprié à considérer est $\Omega(T, V, \mu_B) = E - T \cdot S - \mu_B \cdot B$. L'équilibre thermodynamique est atteint quand Ω est minimum. Pour un système en équilibre, μ_B peut être interprété comme l'incrément de E par unité de B.

La matière nucléaire pourrait passer par diverses phases quand la température et la densité d'énergie ϵ augmentent. Des températures basses et densités baryoniques $\mu_B \simeq m_{proton} \simeq 940$ MeV caractérisent la matière nucléaire ordinaire. Si la température ou la densité d'énergie du système augmente, une phase de gaz hadronique est atteinte dans laquelle les nucléons interagissent en créant des hadrons, principalement des pions. Si T et ϵ sont augmentés encore plus, il est prédit une transition de phase vers un plasma déconfiné de quarks et de gluons (lignes dans Fig. 1). Cette transition correspond à une situation où les quarks et les gluons passent d'un état confiné (un gaz de hadrons) à un état déconfiné (un gaz de quarks et de gluons en interaction). Quand le QGP est formé, la pression du vide disparaît et la symétrie chirale est partiellement rétablie, en conférant aux quarks leur masse nue.

Les résultats de QCD sur réseau prédisent cette transition à $T_c \approx 175$ MeV $\approx 10^{12}$ Kelvin (Fig. 2) [Han01, Jac05, ALI04, Fri04, Mol03]. Cette transition correspond à une densité d'énergie $\epsilon \approx 1$ GeV/fm^3, valeur presque un ordre de grandeur plus élevée que celle correspondant à la matière nucléaire ordinaire. Le changement significatif du comportement du système s'effectue pendant un faible intervalle de température ($\Delta T \sim 20$ MeV). Les transitions de phase sont caractérisées par un *ordre de la transition*, lequel correspond à l'ordre de la dérivée du grand potentiel Ω, lequel diverges pour une valeur critique du paramètre de contrôle. Les transitions sont caractérises par une discontinuité quand le paramètre de contrôle atteint la valeur critique, indépendamment de l'ordre de la transition. Les transitions du premier ordre sont caractérisées par une région de coexistence entre les deux phases autour de la valeur critique. S'il n'y a pas de discontinuité, alors

il n'y a pas une transition mais un "crossover" [Mol03]. L'ordre de la transition n'est pas connu. S'il n'y avait que des gluons, la transition serait du premier ordre mais s'il y a considération de 2 ou 3 quarks légers ou 2 quarks légers et un quark plus lourd, la transition peut être du deuxième ordre ou correspondre à un crossover rapide[5]. Pour des grandes valeurs de T et pour des petites valeurs de la densité baryonique, les résultats de QCD sur réseau semblent indiquer que la transition est un simple crossover. En plus, il y a peut-être un point critique de deuxième ordre présent dans le diagramme des phases qui relie la région de transition de phase du premier ordre existant à haute densité baryonique, au crossover (Fig. 1).

Aux premiers instants de l'univers, le QGP pourrait avoir existé $10^{-4} - 10^{-5}$ s après le Big Bang, ce qui correspond à une densité baryonique $\mu_B = 0$. Cette valeur peut être atteinte, seulement approximativement avec des collisions d'ions lourds (voir la section suivante). Pour des valeurs petites de T et grandes de μ_B, peut s'observer dans le diagramme des phases illustrée par Fig. 1, une transition de phase conduisant à une phase de matière supraconductrice, dans laquelle les partons forment des *paires de Cooper*. Cette phase pourrait être formée à l'intérieur des étoiles à neutrons.

Création du QGP : Collisions d'ions lourds ultra-relativistes

Des collisions entre ions lourds tels que S, Au ou Pb accélérés à des vitesses ultra-relativistes sont une façon de produire un vaste système dense et chaud dans lequel il est prédit que le QGP pourrait être formé. Durant les vingt dernières années cette transition a été étudié dans des expériences d'ions lourds sur cible fixe auprès des accélérateurs AGS et SPS [BNL, CER], avec des énergies du centre de masse, respectives de $\sqrt{s} = 5$ et 17 GeV par nucléon. Plus récemment, depuis l'année 2000, auprès du collisionneur RHIC à BNL, ont été produites des collisions Au-Au à $\sqrt{s} = 130$ et 200 GeV par nucléon [RHI]. Dans un futur proche, officiellement à la fin de l'année 2007, le collisionneur LHC au CERN, produira des collisions Pb-Pb à $\sqrt{s} = 5500$ GeV par nucléon [LHC]. Grâce aux programmes expérimentaux passés et présents, divers indices de la formation du QGP ont été révélés. Ces découvertes seront discutées en détail au chapitre 2.

Au cours d'une telle collision à ces énergies, où les deux ions sont deux disques aplatis le long de leur direction de déplacement à cause de la contraction de Lorentz ; ces ions ont été accélérés à des vitesses relativistes (voir appendice B.1). L'évolution de la collision s'effectue en plusieurs étapes :

1. *Pré-équilibre*: Les nucléons passent à travers l'un l'autre laissant le champ libre à des interactions parton-parton. Dans cette matière nucléaire à forte densité, les partons

[5]Seuls les quarks les plus légers, u, d et s sont considérés. En fait, les quarks plus lourds ne peuvent pas être produits par le plasma, parce que leur masse est d'un ordre de grandeur plus élevée que T_c.

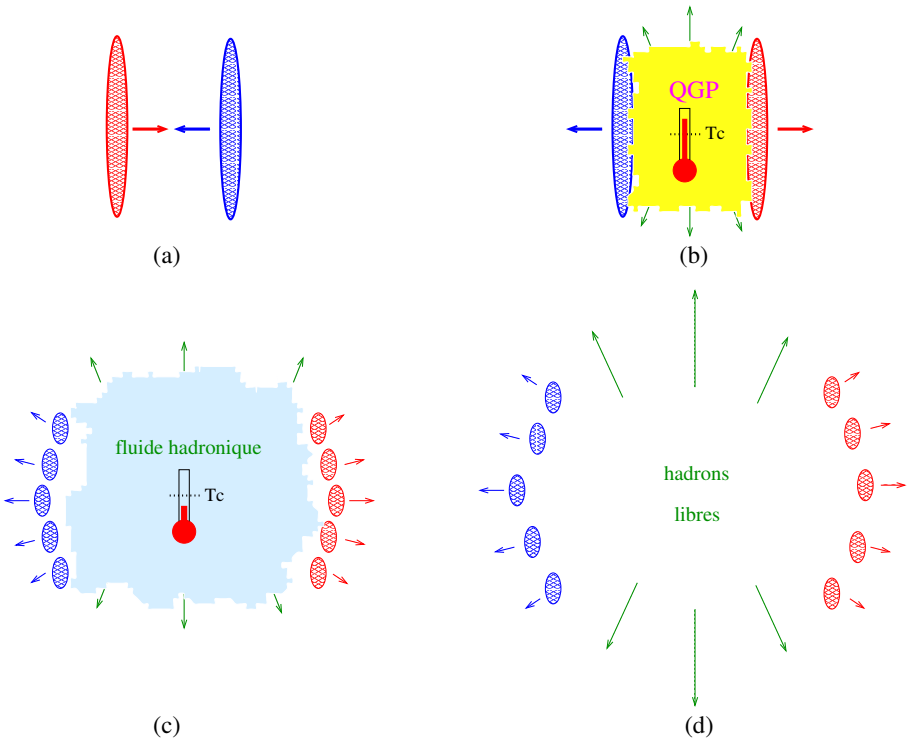

Figure 3: Représentation schématique des diverses étapes de l'évolution d'une collision ultra-relativiste entre ions lourds. Les thermomètres indiquent la température à laquelle l'équilibre thermique pourrait être atteint.

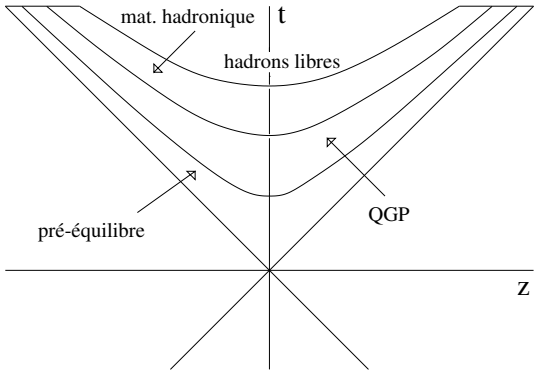

Figure 4: Évolution d'une collision nucléaire haute énergie selon Bjorken [Bjo83].

libérés peuvent souffrir plusieurs diffusions, en perdant une partie de leur énergie initiale dans la région d'interaction. Une "boule de feu" de quarks et de gluons en interaction s'établit à mi-rapidité ($y \simeq 0$), où la densité baryonique s'évanouit. Par contre les régions plus en avant et en arrière ($y > 0$) sont relativement riches en baryons, comme elles correspondent aux restes des noyaux incidents (Fig. 3). A cet instant, les partons de grande impulsion transverse, dits "durs" vont être libérés et conduire à la création de jets et paires $c\bar{c}$, notamment. Ces phénomènes sont très intéressants afin de cerner les propriétés des étapes suivantes de la collision grâce à l'interaction des espèces créées, avec le milieu.

2. *Équilibre chimique et thermique* : La matière nucléaire atteint l'équilibre par la diffusion des partons dans le milieu, à un temps donné τ_0. La densité d'énergie ϵ à laquelle les collisions tant au CERN et qu'à permettent d'aboutir BNL, dépasse la valeur critique : au SPS $\epsilon \sim 1 - 3.5$ GeV/fm^3 [Abr00] et à RHIC $\epsilon \sim 15$ GeV/fm^3 [Adc04]. Donc, si le milieu en interaction est thermalisé un QGP peut être produit. Cette phase évolue en accord avec les prévisions de l'hydrodynamique.

3. *Hadronisation et gel (freeze-out)* : Le plasma en expansion se refroidit et atteint rapidement la température de transition à laquelle il se transforme en un gaz de hadrons[6], processus connu comme le *gel (freeze-out) chimique*. Le gaz de hadrons résultant continue son expansion et refroidissement jusqu'au moment où la fréquence d'interaction entre les hadrons est insuffisante pour maintenir l'équilibre thermique ; ce processus est connu comme le *gel (freeze-out) thermique*. Ensuite, les hadrons n'interagissent plus et, donc, seront détectés avec l'énergie qu'ils avaient au moment du gel.

N'importe quelle information sur le QGP ou le gaz de hadrons en équilibre thermique doit être déduite des propriétés des particules qui restent après le gel thermique. Quelques signatures comme la production de photons, de particules étranges et de J/ψ peuvent révéler les aspects de phénomènes intervenus avant le gel (chapitre 2).

Motivation de la thèse et sommaire détaillé

Cette thèse est dédiée à l'étude des photons dans l'expérience ALICE[7] au LHC[8] avec un soin particulier porté à l'analyse de la performance du détecteur PHOS et au développement d'algorithmes d'identification de particules et de jets.

Les collisions d'ions lourds à des enérgies ultra-relativites produient des sondes différents aux différents étapes décrites à la section précédent et illustrées au diagramme de

[6] Autour de T_c il est prédit une phase mixte QGP et gaz de hadron.
[7] A Large Ion Collider Experiment.
[8] Large Hadron Collider.

la Fig. 4. Cettes sondes donnent des signals très intéressants pour étudier les propriétes de la matière nucléaire pendant la collision. La production de photons est l'une des signatures plus intéressantes pour comprendre les collisions d'ions lourds, grâce à l'information non perturbée qu'ils apportent sur la matière chaude et dense, parce que les photons interagissent seulement électromagnétiquement avec la matière nucléaire (l'interaction forte ne les affecte pas). Les photons sont produits au cours des différentes étapes, décrites dans la section précédente. Au stade du pré-équilibre, ils sont produits par l'interaction entre partons durs suivant les processus $g + q \rightarrow \gamma + q$ (Compton) et $\bar{q} + q \rightarrow \gamma + g$ (annihilation), conduisant à un événement de type γ-jet. Ces photons, dits prompts, apportent des informations sur le parton produit. Egalement ils sont émis par le milieu en équilibre et leurs propriétés dépendent de la température de la matière nucléaire.

Au chapitre 2, seront brièvement décrites les propriétés des différentes signatures étudiées par les expériences passées, présentes et à venir, en se concentrant sur la physique des photons.

L'expérience ALICE est décrite dans le chapitre 3. Le LHC produira des collisions proton-proton (pp) et Pb-Pb, respectivement, à 14 et 5.5 TeV par nucléon. Parmi les expériences auprès du LHC, ALICE a été conçue spécialement pour étudier les collisions Pb-Pb et déterminer les propriétés du QGP. ALICE est composé de sous-détecteurs dont les caractéristiques principales seront également décrites. Les caractéristiques principales du logiciel de cette expérience, AliRoot, essentiel dans l'analyse des données d'une telle expérience seront exposées dans ce chapitre.

Le seul détecteur de photons, approuvé par la collaboration ALICE, à mi-rapidité est PHOS (PHOton Spectrometer). La description des performances de ce détecteur fait l'objet du chapitre 4. PHOS est un spectromètre à haute résolution, composé par un calorimètre de cristaux de $PbWO_4$, couplé un Veto de Particules Chargés (CPV). Les performances de ce détecteur ont été étudiées dans différentes conditions comme par exemple les conditions de faible et grande multiplicité de particules (cette dernière correspond à l'environnement présent dans les collisions d'ions lourds). L'impact d'un éventuel ajout de détecteurs et donc de matériel en face de PHOS est également analysé.

Finalement, les chapitres 6 et 7 traitent de l'identification de processus durs. Dans le chapitre 6, est décrite la génération, avec l'aide du générateur d'événements PYTHIA, de la distribution de photons prompts attendus dans l'expérience ALICE, produits par les processus Compton et annihilation. Egalement il est pertinent de rajouter d'autres sources de photons attendues comme celles dues à la décroissance des mésons neutres et aux radiations de freinage (bremsstrahlung). Pour obtenir une identification précise des photons prompts, nous avons développé une méthode d'identification additionnelle, la Méthode par la Coupure d'Isolement. Grâce à ces outils il a été possible de construire un spectre final de photons, attendu, prenant en compte les erreurs dues aux méthodes d'identification et aussi les erreurs statistiques, pour des événements accumulés pendant

une année de prise de données par l'expérience.

Le chapitre *7* est ciblé sur l'identification des événements γ-jet. En effet, Les photons prompts générés ont, chacun, un parton associé émis à opposé, qui s'hadronise et produit un jet. Une fois qu'un tel photon prompt a été identifié, il faut appliquer un algorithme de corrélation entre le photon et le jet. Ce dernier est détecté dans la Chambre de Projection Temporelle (TPC en anglais) et par le détecteur EMCal (ElectroMagnetique Calorimeter en anglais), bien évidemment si celui-ci est approuvé et financé. Le parton qui génère le jet, a pu subir l'influence du QGP. Celle-ci modifie les propriétés finales du jet et cet effet est connu comme le jet-quenching (chapitre *2.3.1*). Une part importante de ce chapitre est consacrée à l'étude de la sensibilité de la mesure des propriétés du jet, en fonction des différentes conditions d'application de la méthode d'identification des événements photon-jet.

Física de iones pesados ultrarrelativistas en el LHC

La física de altas energías se dedica al estudio y a la descripción de los componentes elementales de la materia y de las interacciones que los gobiernan. En particular, la física de iones pesados ultrarrelativistas se interesa en los fenómenos colectivos de las partículas elementales cuando éstas están bajo condiciones de alta presión y temperatura, como las que se supone que existieron durante los primeros instantes del universo, poco después del Big Bang. Cuando tales condiciones se alcanzan, la teoría de la interacción fuerte predice que la materia nuclear sufre una transición de fase, pasando de la materia nuclear normal en la que los quarks están confinados, a un nuevo estado de la materia, en el que los quarks están casi libres, llamado Plasma de Gluones y Quarks (QGP). Tales condiciones extremas pueden ser alcanzadas en colisiones de iones pesados (HIC) a energías ultrarrelativistas como las que se efectúan en el colisionador RHIC y en un futuro próximo en el LHC. No es una tarea fácil demostrar que esta nueva fase se ha producido y describir sus propiedades. Hay diversas señales experimentales que pueden ayudar a responder esta pregunta, en particular los fotones de alta energía producidos en la colisión, dado que cuando se producen en esta materia caliente y densa, escapan sin interaccionar, proporcionando información directa acerca de las condiciones en la que dichos fotones han sido creados.

En este capítulo expongo brevemente la teoría de la interacción fuerte y su estudio con colisiones de iones pasados. Finalmente expongo la motivación de esta tesis.

Descripción de la materia de las partículas y de las interacciones

Nuestro mundo, según el Modelo Estándar de las Partículas, está compuesto por dos tipos de partículas, las componentes de la materia y las responsables de las interacciones. Las partículas componentes de la materia son *fermiones,* partículas con espín 1/2. Hay dos tipos: *quarks* q con *sabores* u, d, s, c, b, t y sus *anti-sabores*, todos con carga fraccionaria $\pm 1/2\, e$ ó $\pm 2/3\, e$; y *leptones,* $e^{\pm}$, $\mu^{\pm}$, $\tau^{\pm}$, $\nu_{e,\mu,\tau}$ y $\bar{\nu}_{e,\mu,\tau}$. Las partículas portadoras de las

interacciones son *bosones*, con espín entero 0 ó 1: los fotones γ, los responsables de la interacción electromagnética, los bosones $W^{\pm}$ y Z^0, portadores de la interacción electrodébil, y los gluones g, portadores de la interacción fuerte.

Los quarks y los gluones están confinados en la materia nuclear normal en estados cuánticos llamados *hadrones*. Los hadrones se clasifican en *bariones*, partículas compuestas por una combinación de tres quarks de valencia[9], y en mesones, una combinación de un quark y un anti-quark de valencia. Los protones y los neutrones son bariones con quarks de valencia (uud) y (udd) respectivamente, y los piones π^+ y π^- son mesones con quarks de valencia $(u\bar{d})$ y $(d\bar{u})$ respectivamente. En los hadrones, aparte de los quarks de valencia, hay un mar de pares $q\bar{q}$ y gluones. El número cuántico llamado número bariónico B, distingue entre bariones y mesones, siendo $1/3$ para los quarks y $-1/3$ para los anti-quarks. Los bariones tienen B entero y los mesones tienen $B = 0$.

Experimentalmente, no se han observado ni los quarks ni los gluones directamente; siempre están confinados en los hadrones. La existencia de los quarks se demuestra en experimentos de dispersión de electrones sobre nucleones a alta energía. Los resultados observados son consistentes con la presencia de constituyentes puntuales de espín $1/2$ en el nucleón, llamados *partones*. Estos experimentos y sus resultados son comparables al de Rutherford, donde la gran dispersión de partículas α en átomos demostró la existencia del núcleo. A todavía más altas energías, en experimentos de colisión e^+e^-, chorros de partículas bastante colimados emergen del punto de interacción, efecto que se explica como la dispersión de un quark que se hadroniza formando este chorro. De ahora en adelante me referiré a estos procesos como *jet*s. Además, la existencia del gluón se confirma por la observación colisiones donde tres jets emergiendo del punto de interacción. Uno de ellos se interpreta como producido a partir de un gluón de alta energía, el cual es radiado por uno de los quarks dispersados en la colisión.

El fundamento de la teoría de la interacción entre quarks y gluones se basa en la teoría de la Electrodinámica Cuántica (QED), que describe la fuerza entre partículas cargadas eléctricamente como los electrones por mediación del intercambio de fotones. La fuerza entre dos cargas viene descrita por el potencial de Coulomb:

$$V_{QED} = \frac{A}{r}, \tag{3}$$

donde A es proporcional al producto de las cargas y r es la distancia entre ellas.

La Cromodinámica Cuántica (QCD) es la teoría que describe las propiedades de la interacción fuerte, la fuerza fundamental que mantiene a los quarks confinados. Según QCD, el número cuántico de *color* actúa como la carga eléctrica en la interacción electromagnética, con gluones como portadores que mantienen a los quarks confinados en los hadrones. Hay tres colores (*rojo*, *azul* y *verde*) y sus correspondientes *anti-colores*.

[9]Los quarks de valencia son aquellos que dan a las partícula sus números cuánticos (pero sólo una parte de la masa).

Como consecuencia de la estructura *SU(3)* de la teoría, hay ocho gluones coloreados. Sin embargo, no hay objetos coloreados libres en la naturaleza similares a las cargas libres de QED. El hecho de que los hadrones no tienen color se conoce como *confinamiento por color.* Siguiendo la analogía con la QED, el intercambio de un gluón puede usarse para dar una descripción precisa de la interacción pero sólo a pequeñas distancias. A grandes distancias, la situación es más complicada. De hecho, los gluones además de interaccionar con quarks y anti-quarks, también pueden interaccionar con ellos mismos debido a su naturaleza coloreada. Esto contrasta con los fotones, que son neutros eléctricamente y por lo tanto no auto-interactúan en procesos de primer orden. Análisis de QCD en red (Lattice QCD) suponen que el potencial entre un par $q\bar{q}$ viene dado aproximadamente por

$$V_{q\bar{q}} = -\frac{A(r)}{r} + Kr. \tag{4}$$

Para valores de r pequeños, el primer término en Eq. (4) domina y es equivalente a una interacción como la de Coulomb. Análisis detallados revelan que $A(r) \propto 1/\ln(r^{-1})$, lo que implica que la interacción entre quarks es más débil cuanto más pequeña es la separación entre ellos. En el límite $r \to 0$ la interacción entre los quarks se desvanece; esta propiedad se denomina *libertad asintótica.* Cuando r aumenta el potencial es mayor, y consecuentemente la energía para extraer un quark de un hadrón debería ser infinita. Pero una vez que la energía de separación de un quark es comparable al doble de la masa en reposo del quark, es posible romper el hadrón mediante la creación de un par $q\bar{q}$. Este mecanismo proporciona una explicación de la producción de hadrones en colisiones de alta energía.

Una descripción bastante simple de la interacción fuerte, conocida como el *Modelo de la Bolsa*, se ha desarrollado basada en los conceptos de confinamiento por color y libertad asintótica. Este modelo asume que quarks sin masa se mueven libremente dentro de un hadrón esférico de radio R, pero la presión del vacío les impide escapar. QCD predice que el valor esperado de la densidad de energía del vacío no es nulo sino $\langle\psi\bar{\psi}\rangle \approx -(240\,\mathrm{MeV})^3$, lo cual es responsable de la llamada *rotura de la simetría quiral.* Esta simetría implica que si los quarks no tuvieran masa existirían solo en uno de los dos posibles autoestados de helicidad, $h = \pm 1/2$[10]. Sin embargo, los quarks que se mueven dentro de la bolsa tienen una *masa desnuda,* y sólo para los quarks más ligeros, u y d, la simetría quiral es una simetría aproximada. En materia nuclear normal, debido a la presión del vacío, estos quarks son una superposición de los estados correspondientes a los dos autovalores de helicidad, lo que proporciona una masa adicional a los quarks[11] [Han01, Jac05, MÖ1, Mol03].

[10] $h = \vec{s} \bullet \vec{k} / |k|$, donde $\vec{s}$ y $\vec{k}$ son el espín y momento de la partícula.

[11] Los quarks u y d tienen una pequeña masa desnuda de unos ~ 5 MeV, pero debido a la rotura de la simetría quiral su masa aumenta a $\sim$350 MeV.

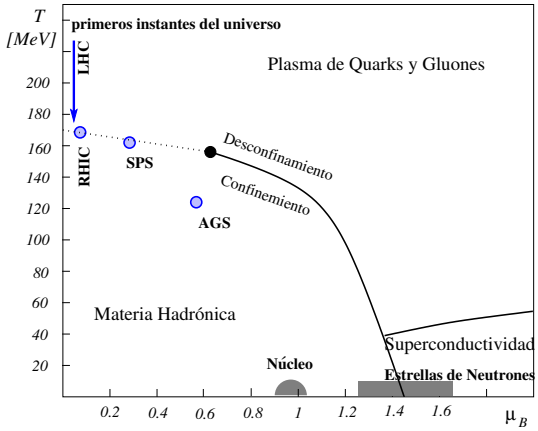

Figure 5: Diagrama de fases de QCD. La línea continua indica una probable transición de primer orden. La línea de puntos indica una posible región con una transición de crossover, continua pero rápida. El círculo negro indica un punto crítico (posiblemente localizado en $\mu_B \sim 700$ MeV) donde una fase de segundo orden podría tener lugar. Fases exóticas pueden existir a altas densidades, como por ejemplo en estrellas de neutrones. Se muestran las condiciones de freeze-out químico alcanzadas en experimentos de iones pesados en el AGS, el SPS y el RHIC. La flecha a alta temperaturas y bajo μ_B indica el comportamiento esperado de la materia en el LHC para energías superiores al freeze-out, siguiendo un camino similar al tomado por la materia durante los primeros instantes del universo [Fri04].

Materia densa y caliente: El plasma de gluones y quarks

QCD describe la interacción entre objetos coloreados, pero necesitamos la ayuda de la termodinámica para poder entender las propiedades de un sistema de partículas elementales grande, una materia de quarks y gluones. Las propiedades termodinámicas de un sistema son frecuentemente presentadas en la forma de un *diagrama de fases*. Éste es un diagrama en función de algunos *parámetros de control*, donde las diferentes fases de una sustancia ocupan distintas regiones. El ejemplo más común es el del agua, cuyos parámetros de control son la temperatura T y la presión P. El agua se describe normalmente en tres fases, líquida, gaseosa y sólida[12]. Hay curvas de transición especiales $P(T)$ que describen la transición de una fase a otra, y también, en el caso del agua, hay un punto crítico donde las tres fases coexisten. En el diagrama de fases para la materia de quarks y gluones, los parámetros de control son la temperatura y el *potencial bario-químico* μ_B.

En reacciones de partículas elementales, un barión qqq se crea o se destruye junto con un anti-barión $\bar{q}\bar{q}\bar{q}$ simultáneamente, no habiendo cambio del valor total de B. Para sistemas abiertos donde B puede variar, el potencial termodinámico más conveniente es $\Omega(T, V, \mu_B) = E - T \cdot S - \mu_B \cdot B$. El equilibrio termodinámico se alcanza cuando Ω es mínimo, interpretándose μ_B en un sistema en equilibrio como el incremento de E por unidad de B.

[12]Hay más fases sólidas pero como ejemplo sólo presentamos éstas tres.

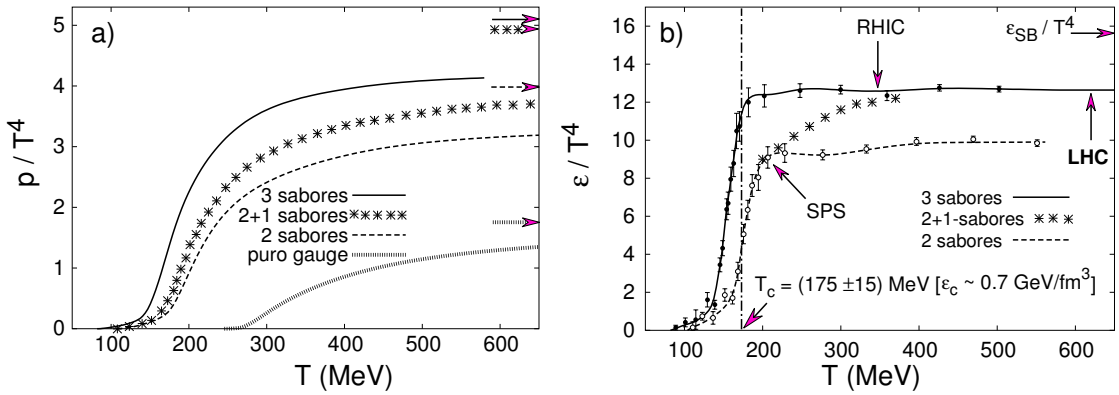

Figure 6: La presión (a) y la densidad de energía (b) en QCD con 0, 2 y 3 sabores de quarks ligeros y 2 sabores de quarks ligeros más un sabor de quark pesado (extraño). Las flechas en la parte derecha de las ordenadas muestran el valor del límite de Stefan-Boltzmann para un gas ideal de quarks y gluones [ALI04].

La materia nuclear podría pasar por varias fases cuando la temperatura y la densidad de energía ϵ aumentan. La materia nuclear ordinaria está caracterizada por bajas temperaturas y $\mu_B \simeq m_{proton} \simeq 940$ MeV. En cuanto aumentamos la temperatura o la densidad de energía, alcanzamos una fase conocida como gas de hadrones, donde los nucleones interactúan creando hadrones, principalmente piones. Si T y ϵ aumentan aún más, se predice una transición a un sistema desconfinado de quarks y gluones (líneas de Fig. 5). Esta transición corresponde a una situación donde los quarks y los gluones evolucionan de un estado confinado (un gas de hadrones) a un estado desconfinado (un gas de quarks y gluones en interacción). Cuando el QGP se forma, la presión del vacío se desvanece y la simetría quiral se restaura aproximadamente, siendo la masa de los quarks en el plasma la masa desnuda.

Análisis de QCD en red predicen que la transición se produce para $T_c \approx 175$ MeV $\approx 10^{12}$ Kelvin, como se muestra en Fig. 6 [Han01, Jac05, ALI04, Fri04, Mol03]. Esta transición corresponde a una densidad de energía de $\epsilon \approx 1$ GeV/fm^3, casi un orden de magnitud más grande que en el caso de la materia ordinaria. El cambio significativo en el comportamiento del sistema ocurre en un limitado intervalo de temperatura ($\Delta T \sim 20$ MeV). Las transiciones de fase se caracterizan por su *orden de transición,* que corresponde al orden de la derivada del gran potencial Ω, que diverge para un valor crítico del parámetro de control. Las transiciones de fase se caracterizan por una discontinuidad de las derivadas del potencial cuando el parámetro de control alcanza el valor crítico. En transiciones de primer orden hay una coexistencia entre las dos fases alrededor del valor crítico. Si no hay una discontinuidad, entonces no hay transición de fase sino un *crossover* [Mol03]. El orden de la transición de la materia nuclear ordinaria al QGP no se conoce. Si sólo hubieran gluones en el medio nuclear, la transición sería de primer orden, pero si se consideran tres quarks ligeros o dos ligeros y uno pesado, la transición puede ser de segundo orden o un

rápido crossover[13]. A altas temperaturas y baja densidad de bariones, análisis de QCD en red parecen indicar que la transición es un suave crossover. Además, puede que haya un punto crítico de segundo orden en el diagrama de fases que conecta la transición de primer orden a alta densidad de bariones con el la región de crossover, como se muestra en Fig. 5.

En el universo primordial, el QGP pudo haber existido $10^{-4} - 10^{-5}$ s después del Big Bang, correspondiendo a una densidad neta de bariones de $\mu_B = 0$. Este valor puede ser aproximadamente alcanzado en colisiones de iones pesados como se explica en la siguiente sección. Para bajas temperaturas y grandes densidades bariónicas, se puede observar en el diagrama de fases ilustrado en Fig. 5 una transición a una fase de materia de color superconductora, en la cual los quarks forman *pares de Cooper*. Esta fase podría estar presente en el núcleo de estrellas de neutrones.

Generación de QGP: Colisiones de iones pesados ultrarrelativistas

Las colisiones de iones pesados como S, Au o Pb a energías relativistas son el medio para producir un sistema grande denso y caliente, donde el plasma de gluones y quarks pueda formarse. Durante los últimos 20 años, esta transición se ha estudiado en experimentos de iones pesados con blanco fijo en los aceleradores AGS y SPS [BNL, CER], con energías en el centro de masas de 5 y 17 GeV por nucleón, respectivamente. Desde el año 2000 el colisionador RHIC en BNL produce colisiones Au-Au a $\sqrt{s} = 130$ y 200 GeV por nucleón [RHI]. En el futuro próximo, oficialmente a partir del verano de 2007, el colisionador LHC del CERN producirá colisiones Pb-Pb a $\sqrt{s} = 5500$ GeV por nucleón [LHC]. Gracias a los programas experimentales pasados y presentes, se han encontrado algunas evidencias de la formación del QGP. Hablaré más sobre estos descubrimientos en el capítulo 2.

A tales energías, ambos iones se ven como dos discos en su dirección de movimiento, debido a la contracción de Lorentz producida por sus velocidades ultrarrelativistas (Apéndice B). Se pueden distinguir diferentes fases durante la colisión:

1. *Pre-equilibrio*: Los nucleones pasan uno a través del otro, produciéndose interacciones entre partones. Debido a la alta densidad del medio nuclear, los partones liberados colisionan varias veces, perdiendo parte de su energía inicial en la región de interacción. Una "bola de fuego" de quarks y gluones en interacción se expande en la región de rapidez media ($y \simeq 0$, Apéndice B), donde la densidad de bariones desaparece, mientras que las regiones hacia delante y hacia atrás de la colisión ($y > 0$) son relativamente ricas en bariones, los cuales proceden de los restos de los

[13] Sólo se consideran los quarks más ligeros u, d y s. De hecho, los más pesados no pueden ser producidos en el plasma dado que su masa es un orden de magnitud mayor que T_c.

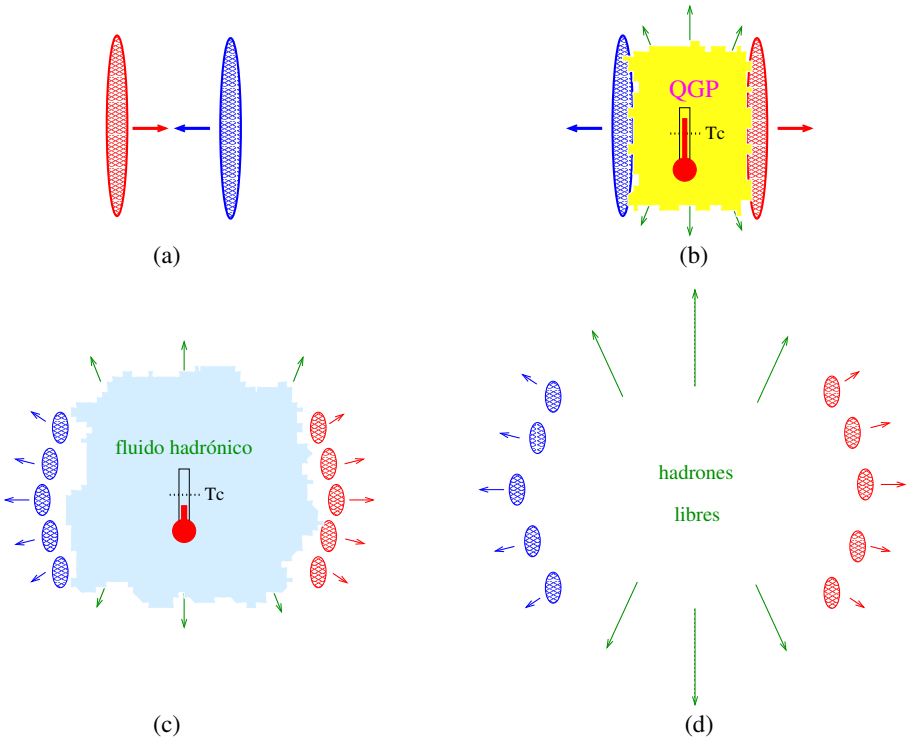

Figure 7: Vista esquemática de las varias fases por las que pasa una colisión de iones pesados ultrarrelativistas. Los termómetros indican la temperatura a la cual el equilibrio térmico podría ser alcanzado.

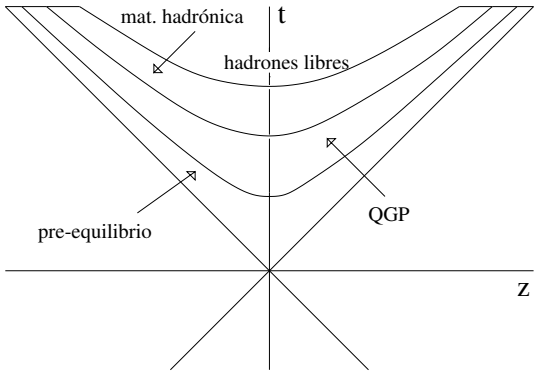

Figure 8: Evolución que sigue una colisión nuclear de alta energía según Bjorken [Bjo83].

núcleos (Fig. 7). En este momento se pueden producir partones energéticos que en su estado final crean jets y pares $c\bar{c}$. Estos productos son interesantes como sondas de estados posteriores de la colisión, dado que interaccionan con el medio nuclear.

2. *Equilibrio químico y térmico*: La materia nuclear alcanza el equilibrio mediante la dispersión de los partones en el medio, transcurrido un cierto tiempo τ_0 desde el comienzo de la colisión. Las densidades de energía que se alcanzan en las colisiones en el CERN y BNL están bien por encima de los valores críticos; en el SPS $\epsilon \sim 1 - 3.5$ GeV/fm^3 [Abr00] y en el RHIC $\epsilon \sim 15$ GeV/fm^3 [Adc04]. Así pues, si el medio en interacción se termaliza, el QGP puede ser producido. Esta fase evoluciona expandiéndose según las leyes de la hidrodinámica.

3. *Hadronización y freeze-out*: El plasma en expansión se enfría rápidamente alcanzando la temperatura de transición en poco tiempo. La materia formada evoluciona del QGP a un gas de hadrones[14], momento conocido como *freeze-out químico*. El gas hadrónico resultante continua expandiéndose y enfriándose hasta que la interacción entre los hadrones es insuficiente para mantener el equilibrio térmico; este proceso se conoce como *freeze-out térmico*. A partir de este momento, los hadrones ya no interaccionan más entre ellos; finalmente serán detectados con el momento y energía que tenían en el freeze-out térmico.

Cualquier información acerca del QGP o el gas de hadrones en equilibrio térmico o químico debe de ser inferida de la propiedades de las partículas que quedan después del freeze-out térmico. Algunas señales como la producción de fotones, de partículas extrañas o de J/ψ pueden dar información de los estados anteriores al freeze-out (capítulo 2).

Motivación de la tesis

Esta tesis está dedicada a la física de fotones en el experimento ALICE del LHC, y particularmente al estudio del funcionamiento del espectrómetro electromagnético PHOS y al desarrollo de algoritmos de identificación de fotones y jets.

Los fotones son una de las señales más interesantes para comprender las colisiones de iones pesados, dado que proporcionan información no perturbada sobre la materia densa y caliente producida en las colisiones, y sólo interactúan electromagnéticamente (no les afecta la interacción fuerte). Los fotones son producidos en las diferentes fases descritas en la sección precedente. En el pre-equilibrio son producidos mediante interacciones de partones energéticos vía los procesos $g+q \rightarrow \gamma+q$ (Compton) y $\bar{q}+q \rightarrow \gamma+g$ (aniquilación), procesos que más tarde llamaremos sucesos γ-jet. Estos fotones son llamados *fotones rápidos* y dan información acerca del partón producido en el proceso; los fotones también

[14] Alrededor de T_c se espera que haya una fase mixta de QGP y gas de hadrones coexistiendo.

son radiados por el medio termalizado, dando información sobre la temperatura de la materia nuclear.

En el capítulo 2, se describirán brevemente las diferentes señales experimentales estudiadas en los experimentos pasados presentes y futuros del CERN y BNL, concentrándonos en la física de fotones.

El experimento ALICE (A Large Ion Collider Experiment) del colisionador LHC (Large Hadron Collider) se describe en el capítulo 3. El LHC producirá colisiones protón-protón (pp) y Pb-Pb a 14 y 5.5 TeV por nucleón, respectivamente. Entre los experimentos del LHC, ALICE fue especialmente diseñado para estudiar colisiones Pb-Pb, las cuales son interesantes para investigar las propiedades del QGP. ALICE está compuesto de sub-detectores cuyas características principales serán descritas. También se describe el software desarrollado para este experimento, AliRoot.

El único detector de fotones aprobado en ALICE, localizado en la región de rapidez media, es el espectrómetro de fotones PHOS (PHOton Spectrometer). Se ha estudiado el funcionamiento de este detector en el capítulo 4. PHOS es un espectrómetro de alta resolución, compuesto por un calorímetro de cristales de $PbWO_4$ y un veto de partículas cargadas. Se estudió la respuesta del detector en diferentes condiciones: baja multiplicidad de partículas y colisiones de iones pesados; la influencia de los diferentes materiales que se colocarán entre el punto de interacción y el detector también se ha tenido en cuenta.

El capítulo 5 está dedicado a la identificación de fotones con PHOS. Éste detector realiza la identificación de fotones con alta pureza, mediante la medida del tiempo de vuelo, detectando partículas cargadas con el veto y mediante análisis de la forma de la cascada que producen las partículas en el calorímetro. Se presentan varios métodos de identificación de partículas: uno basado en el Análisis de los Componentes Principales de la cascada (PCA) y otro basado en la dispersión de la forma de las cascadas energéticas.

Finalmente, los capítulos 6 y 7 tratan la identificación de procesos energéticos. En el capítulo 6, se produce con el generador de sucesos PYTHIA la distribución esperada de fotones rápidos en ALICE, producidos por los procesos Compton y de aniquilación, junto con otras fuentes de fotones como los fotones de desintegración de mesones neutros y de bremsstrahlung. Nos interesa una medida precisa de los fotones rápidos que los distinga de los fotones producidos por esas otras fuentes, por ello se ha desarrollado un método de identificación adicional, el Método de Corte por Aislamiento (ICM). Se aplican estos métodos de identificación y se construye la distribución final de fotones que se espera medir en PHOS en un año de toma de datos en ALICE, con los errores estadísticos y sistemáticos correspondientes.

En el capítulo 7 se estudia la identificación de sucesos γ-jet. Los fotones rápidos generados tienen un partón asociado en retroceso, que se hadroniza produciendo un jet. Una vez que se ha identificado el fotón rápido, se aplica un algoritmo que relaciona el fotón y el jet, el cual es detectado en ALICE en la Cámara de Proyección Temporal (TPC) y si se

aprueba, en el detector EMCal (ElectroMagnetic Calorimeter). Este partón puede sufrir la influencia del QGP, que produce el efecto conocido como *jet-quenching* (sección 2.3.1), modificando las propiedades finales del jet. Finalmente, se ha estudiado la sensibilidad del método de etiquetado de jets mediante fotones rápidos con la finalidad de utilizar los jets etiquetados con fotones para medir el jet-quenching.

Chapter 1

Ultra-relativistic heavy-ion physics at the LHC

High-energy physics is devoted to the study and description of the elementary-components of matter and of the interactions that rule them. In particular, ultra-relativistic heavy-ion physics is interested in the collective phenomena of elementary-particles under high pressure and temperature conditions, as those assumed to exist during the first moments after the Big Bang. When such conditions are achieved, the strong interaction theory predicts that nuclear matter undergoes a phase transition from confined quarks of normal nuclear matter to almost free quarks, creating a weakly interacting matter called the Quark-Gluon Plasma (QGP). Such extreme conditions can be reached in heavy-ion collisions (HIC) at the ultra-relativistic energies achieved at colliders like RHIC and in the near future at LHC. It is not an easy task to demonstrate that a phase transition has been produced and to describe the properties of the new phase. Among the different observables used in heavy-ion collisions to study nuclear matter properties, photons are particularly interesting because they are produced in the hot and dense matter and escape without interacting, giving direct information about their creation conditions.

In this chapter, I survey the strong interaction theory and its study by heavy-ion collisions. Finally, I give the motivation of this thesis.

1.1 Matter, particles and interactions

Our world, according to the Standard Model, is composed of two kinds of particles, the matter components and the particles responsible of the interaction between particles [Her98, Nov00, Han01]. The components of matter are *fermions,* particles with spin 1/2. There are two types: *quarks* q with *flavors* u, d, s, c, b, t and their *anti-flavors*, all with fractional charge $\pm 1/2\, e$ or $\pm 2/3\, e$; and *leptons,* $e^{\pm}$, $\mu^{\pm}$, $\tau^{\pm}$, $\nu_{e,\mu,\tau}$ and $\bar{\nu}_{e,\mu,\tau}$. The particles carriers of the interaction are *bosons*, with spin 0 or 1: the photons γ, responsible

of the electromagnetic interaction, the bosons $W^{\pm}$ and Z^0, carriers of the electro-weak interaction, and the gluons g, carriers of the strong force.

Quarks are confined in normal nuclear matter in quantum states called *hadrons*. Hadrons are classified as *baryons*, particles formed by the combination of three valence quarks[1], and mesons, a combination of a valence quark and anti-quark. Protons and neutrons are baryons with valence quarks (uud) and (udd) respectively, and pions, π^+ with valence quarks $(u\bar{d})$ and π^- with valence quarks $(d\bar{u})$, are mesons. In hadrons, apart from the valence quarks, there is a sea of $q\bar{q}$ pairs and gluons which contribute to the hadron mass. The quantum number called *baryon number* B differentiates between baryons and mesons, equal to $1/3$ for quarks and $-1/3$ for anti-quarks. Baryons have integer B and mesons have $B = 0$.

Experimentally, no single quark has been directly observed, they are always confined in hadrons. The existence of quarks is demonstrated in high-energy inelastic scattering experiments where electrons collide with *nucleons*. The observed results are consistent with the presence of point-like spin $1/2$ constituents of the nucleon called *partons*. This is quite analogous to backward-angle Rutherford scattering of α-particles off atoms which demonstrated the existence of the nucleus. In high energy e^+e^- collider experiments, rather well collimated jets of particles emerge from the interaction region which are explained as a single progenitor quark scattered in the collision. From now on, I will refer to this process as a *jet*. Furthermore, the existence of gluons is confirmed by the observation of particle collisions in which three jets emerge. One of them must result from a high-energy gluon radiated from one of the scattered quarks in the collision.

An analogy of the quark-gluon interaction is provided by the *Quantum Electrodynamics* theory (*QED*), which describes the force between electrically-charged particles such as electrons in terms of exchange of photons. The force between two charges is described by the potential

$$V_{QED} = \frac{A}{r}, \tag{1.1}$$

where A is proportional to the product of the charges and r is the distance between them.

The *Quantum Chromodynamics* theory (*QCD*) describes the properties of the strong interaction, the fundamental force that keeps quarks confined. According to QCD, the quantum number *color* acts like the charge in the electromagnetic interaction, with gluons as the carriers that maintain quarks together in hadrons. There are three different colors, (*red*, *blue* and *green*) and their corresponding anti-colors. As a consequence of the *SU(3)* structure of the theory, there are eight colored gluons. However, there are no free colored objects in nature similar to the free charges of QED. The fact that hadrons are not colored is known as *color confinement*. Following the QED analogy, single gluon exchange can

[1]Valence quarks are those which give to the particle the quantum numbers (but only a part of the mass).

be used to give an accurate description of the force but only at small distances. At large distances, the situation becomes much more complicated. As a matter of fact, in addition of interacting with q and $\bar{q}$, gluons can interact among themselves, because they carry a color charge. At variance, photons are electrically neutral and hence do not self-interact in first order processes. Lattice QCD shows that the potential between a $q\bar{q}$ pair is given approximately by

$$V_{q\bar{q}} = -\frac{A(r)}{r} + Kr. \tag{1.2}$$

For small r, the first term in Eq. (1.2) dominates, and is equivalent to a Coulomb-like interaction. Detailed analysis reveals that $A(r) \propto 1/\ln(r^{-1})$, implying that the interaction between quarks becomes weaker as their separation decreases. In the limit $r \to 0$ the quarks interaction vanishes: this property is known as *asymptotic freedom.* As r increases, the potential becomes stronger, and consequently the energy to take out a quark from a hadron should be infinite, but once the energy provided to separate quarks is about twice the rest mass of the quark, it is possible to break the hadron by creating a $q\bar{q}$ pair. This mechanism explains hadron production in high-energy collisions.

A simple description of the strong interaction, the *Bag Model,* relies on the concepts of color confinement and asymptotic freedom. This model assumes that massless quarks move freely within a spherical hadron of radius R, but are prevented from escaping out by the vacuum pressure. QCD predicts that the ground-state energy expectation value of vacuum is not zero but $\langle \psi\bar{\psi} \rangle \approx -(240\ \text{MeV})^3$, leading to the *chiral symmetry breaking.* Chiral symmetry implies that if quarks were massless, they would exist only in one of the two possible *helicity* eigenstates $h = \pm 1/2$[2]. However, quarks moving in the bag have a *bare mass* and only for the lighter ones, u and d, chiral symmetry is an approximated symmetry. In normal nuclear matter, quarks are in a superposition of both helicity eigenvalues due to the vacuum pressure, which gives an additional mass to the quarks[3] [Han01, Jac05, MÖ1, Mol03].

1.2 Hot and dense matter: The Quark-Gluon Plasma

QCD describes the interaction between single colored objects but to understand the properties of a large elementary-particle system as quark-gluon matter, we need the help of thermodynamics. Thermodynamical properties of a system are often presented in the form of a *phase diagram.* A phase diagram is a plot in function of some *control parameters*, where the different phases of a substance occupy different regions. The most common example is the phase diagram of water, whose control parameters are the temperature T

[2] $h = \vec{s} \bullet \vec{k} / |k|$, where $\vec{s}$ and $\vec{k}$ are the spin and momentum of the particle.

[3] Quarks u and d have a small bare mass of about ~ 5 MeV, but due to chiral symmetry breaking their mass is increased to ~ 350 MeV inside hadrons.

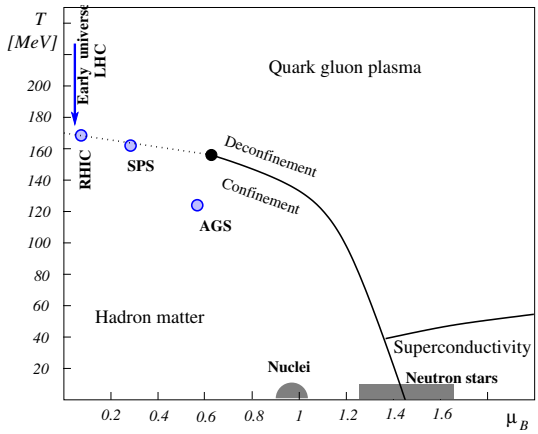

Figure 1.1: Phase diagram of QCD. The solid lines indicate likely first-order transitions. The dotted line indicates a possible region of a continuous but rapid crossover transition. The black filled circle indicates the second-order critical endpoint of a line of first-order transitions, (might be located at $\mu_B \sim 700$ MeV). More exotic phases can exist at high densities, for example in the interior of neutron stars. Chemical freeze-out conditions reached in heavy-ion experiments at AGS, SPS and RHIC are also shown. The arrow at high T and low μ_B indicates the expected behavior of matter at LHC energies before freeze-out, taking a similar path than the early universe [Fri04].

and the pressure P. Water is commonly described having three phases, liquid, gas and solid[4]. There are transition curves $P(T)$ that describe the transition from one phase to the other, and also for the case of water, there is a critical point where the three phases coexist.

In the phase diagram for nuclear matter displayed in Fig. 1.1, the control parameters are the temperature and the *baryon-chemical potential* μ_B.

In elementary particle reactions, a qqq baryon is always created or destroyed simultaneously with a $\bar{q}\bar{q}\bar{q}$ anti-baryon, with no change of the total value of B. For open systems for which B is allowed to vary, the most relevant thermodynamic potential is the *grand potential* $\Omega(T, V, \mu_B) = E - T \cdot S - \mu_B \cdot B$ [Han01]. Thermodynamic equilibrium is reached when Ω is minimum. For a system in equilibrium, we can interpret μ_B as the increase of E per unity of B.

Nuclear matter may pass through several phases as the temperature and energy density ϵ raise. Low temperatures and $\mu_B \simeq m_p \simeq 940$ MeV characterize ordinary nuclear matter. Increasing the temperature or the energy density leads to a hadronic gas, mainly constituted of pions. If T and ϵ are further increased, a transition to a deconfined Quark-Gluon Plasma (QGP) is predicted (lines in Fig. 1.1). This transition corresponds to a situation where quarks and gluons evolve from a confined state (a hadron gas) to a deconfined state (a gas of interacting quarks and gluons). When the QGP is formed, the vacuum pressure vanishes and the chiral symmetry is approximately restored, so that the

[4]There are several solid phases, but as an example we assume only one.

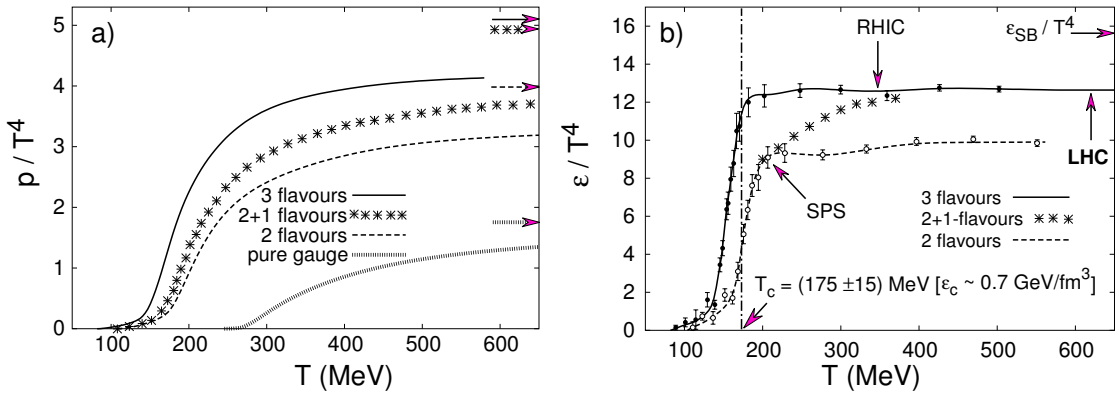

Figure 1.2: The pressure (a) and energy density (b), in QCD considering zero, two and three light mass quarks flavors and two light and a heavier (strange) quark. The arrows on the right-side ordinates show the value of the Stefan-Boltzmann limit for an ideal quark-gluon gas [ALI04].

mass of the quarks in the plasma is their bare mass.

Lattice QCD predicts a phase transition at $T_c = 175 \pm 15$ MeV $\approx 10^{12}$ Kelvin as shown in Fig. 1.2 [Han01, Jac05, ALI04, Fri04, Mol03]. This transition corresponds to an energy density $\epsilon \approx 1$ GeV/fm^3, nearly an order of magnitude larger than in the case of ordinary matter. The significant change happens in a limited temperature range ($\Delta T \sim 20$ MeV). Phase transitions are characterized by the *order of transition*, corresponding to the order of the derivative of the grand potential Ω diverging at the critical point. Phase transitions are characterized by a discontinuity of the Ω derivatives when the control parameter reaches the critical value. In first-order transitions, there is a coexistence of the two phases around the critical value. If there is no discontinuity of the derivatives of Ω, there is no phase transition but a *crossover* [Mol03]. The order of the transition to the QGP is not known. If gluons were the only degree of freedom, the transition would be of first-order. When in addition two or three light quarks or two light quarks and the heavier s-quark are considered, the transition can be of second-order or a fast crossover[5]. At high T and low baryon-chemical potential, lattice QCD results seem to indicate that the transition is a smooth crossover. Furthermore, there might be a second-order critical point in the phase diagram connecting a first-order transition at high density to this crossover, as shown in Fig. 1.1.

In the early universe, the QGP could have existed $10^{-4} - 10^{-5}$ s after the Big Bang, corresponding to a net baryon-chemical potential $\mu_B = 0$. This value can be approximately attained with heavy-ion collisions as explained in the next section. For low T and large baryon-chemical potential, we observe in the phase diagram illustrated in Fig. 1.1 a different phase transition to a color superconducting phase of matter, in which partons form *Cooper-pairs*. This phase might be formed in the core of neutron stars.

[5]We take into account only the lighter quarks u, d and s. As a matter of fact, the heavier ones cannot be produced in the QGP because their mass is an order of magnitude larger than T_c.

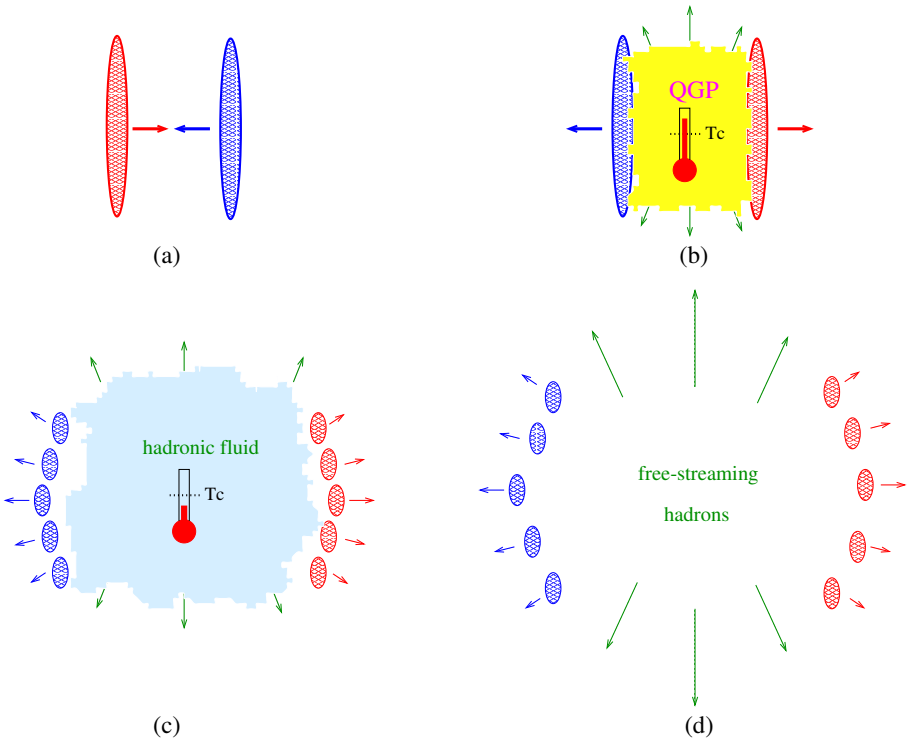

Figure 1.3: Schematic view of the various stages of an ultra-relativistic heavy-ion collision. The thermometers indicate temperatures at which thermal equilibrium might be attained.

1.3 QGP generation: Ultra-relativistic heavy-ion collisions

Collisions of heavy-ions, like S, Au or Pb at relativistic energies are a way to produce a large, dense and hot system in which QGP matter can be formed. Over the past 20 years, the QGP phase transition has been studied by heavy-ion fixed target experiments at the AGS and at the SPS accelerators [BNL,CER], with 5 and 17 GeV center of mass energies per nucleon, respectively. Since year 2000 the RHIC collider at BNL produces Au-Au collisions at $\sqrt{s} = 130$ and 200 GeV per nucleon [RHI]. In the near future, officially from end 2007, the LHC collider at CERN, will produce Pb-Pb collisions at $\sqrt{s} = 5500$ GeV per nucleon [LHC]. Thanks to the past and present experimental programs, some hints of the QGP formation have been found. I will discuss more about these findings in Chap. 2.

During the collision at ultra-relativistic energies, both ions are Lorentz contracted disks along their direction of motion due to their relativistic velocities (Appendix B). Different stages can be distinguished:

1. *Pre-equilibrium*: Nucleons pass through each other, producing parton-parton interactions. Due to the high density of nuclear matter, the released partons can re-scatter several times, loosing part of their initial energy in the interaction region. A "fire ball" of interacting quarks and gluons expands at mid-rapidity ($y \simeq 0$, see

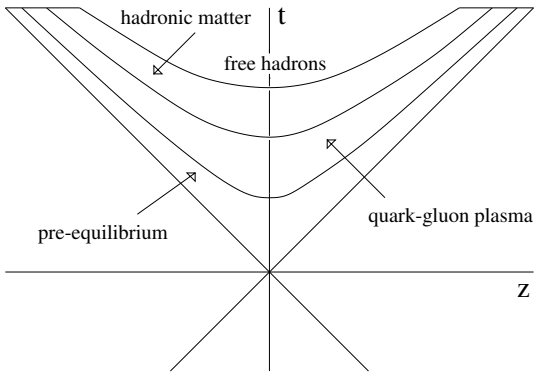

Figure 1.4: Expected evolution of a high energy nuclear collision according to Bjorken [Bjo83].

Appendix B for definition), where the baryon-chemical potential vanishes, while forward and backward regions ($y > 0$), are relatively rich in baryons corresponding to the remnants of the nucleus (Fig. 1.3). At this stage hard partons are scattered and heavy flavour $Q\bar{Q}$ bound states are produced. These products can be used to probe the following stages of the collision through their interaction with the nuclear medium.

2. *Chemical and thermal equilibrium*: The nuclear matter reaches equilibrium at a proper time τ_0 through parton re-scattering in the medium. The energy density ϵ attained in the collisions at CERN and BNL is well above the critical value; at SPS $\epsilon \sim 1 - 3.5$ GeV/fm^3 [Abr00] and at RHIC $\epsilon \sim 5$ GeV/fm^3 [Adc04]. Thus, if the interacting medium is thermalized, the QGP can be produced. This phase evolves according to the laws of hydrodynamics.

3. *Hadronization and freeze-out*: The expanding QGP cools down fast and reaches quickly the transition temperature. It evolves into a hadron gas[6], reaching finally a state known as the *chemical freeze-out*. The resulting hadronic gas continues to expand, cooling down until the interaction rate between the hadrons is insufficient to maintain the thermal equilibrium; this state is known as the *thermal freeze-out*. After this moment, hadrons do not interact anymore and fly freely.

Any information about the QGP or the hadron gas at thermal equilibrium must be inferred from the properties of the particles remaining after the thermal freeze-out. Some signatures such as photons, strange particles and quarkonia bound states, can give information of what happened before the freeze-out as discussed in Chap. 2.

[6]At about T_c, a mixed phase with QGP and hadron gas coexisting is expected.

1.4 Thesis motivation and outline

This thesis is devoted to the investigation of photon physics in the ALICE experiment at the LHC, and in particular to the study of the performance of the photon spectrometer PHOS and to the associated development of particle and jet identification algorithms.

Heavy-ion collisions at ultra-relativistic energies produce different probes in the stages described in the previous section and illustrated in the evolution diagram of Fig. 1.4. These probes provide useful signatures to study the properties of the nuclear matter formed during the collision. In Chap. 2, I review the most interesting signatures studied in the past and those proposed for future experiments at CERN and BNL, giving special attention to photons and *jet-quenching*. I am interested in the study of photons as a probe because they give unperturbed information about the hot and dense matter as they only interact electromagnetically and do not suffer the effects of the strong interaction. *Direct photons,* which are those photons not produced by particle decay, are particularly interesting. *Thermal photons*, defined as those radiated during the equilibrium stage by the thermalized medium, give information on the temperature of nuclear matter. *Prompt photons* are those produced in the pre-equilibrium stage by hard processes. Prompt photon physics is one of the main points of my work. They are produced through hard parton interaction via $g+q \rightarrow \gamma+q$ (Compton) and $\bar{q}+q \rightarrow \gamma+g$ (annihilation) processes, which we call γ-jet processes. These prompt photons give information about the produced recoiling parton, as its original energy and azimuthal direction. Such kind of events are very interesting because the parton may suffer the influence of the QGP medium, which produces the effect known as *jet-quenching*: an energy loss of the parton in the nuclear medium which modifies the final jet properties.

The LHC (Large Hadron Collider) collider will produce proton-proton (pp) and Pb-Pb collisions at 14 and 5.5 TeV per nucleon, respectively. Pb-Pb collisions at those energies will produce the appropriate conditions of temperature and energy density to form the QGP. Among the four LHC experiments, ALICE (A Large Ion Collider Experiment) experiment is specially designed to study the different probes produced in such collisions. The LHC collider and the ALICE experiment are described in Chap. 3. ALICE is composed of different detectors but the most interesting detector for my study is the high energy resolution spectrometer PHOS (PHOton Spectrometer) which is the only approved photon detector at present at mid-rapidity in ALICE. There are other two detectors relevant for my study of prompt photons: the main detector of the central tracking system, the Time Projection Chamber (TPC), devoted to the measurement of charged particles; and the ElectroMagnetic Calorimeter (EMCal), which funding is not approved yet, devoted to the detection of neutral particles. These detectors combined with PHOS enable the possibility of studying γ-jet processes.

The correct detection and identification of photons with PHOS in order to be able to

study the production of direct photons, is an important issue in my work. I participated in beam test experiments where the response of a PHOS prototype was studied. I tuned the simulation parameters to reproduce the results obtained. Then, I studied the performance of PHOS in different conditions that could affect photon measurements: particle environment and the influence of the different material in front of PHOS. This study of the PHOS performance is presented in Chap. 4. PHOS possess excellent photon identification capabilities based on time of flight measurements, charged particle identification and shower shape analysis. We need photon identification methods that provide good hadron rejection, and photon identification efficiency in a wide energy range from 0.5 to 120 GeV. I develop in Chap. 5 identification methods based on the shower shape analysis: the Principal Components Analysis, designed for hadron rejection and the shower dispersion of energetic particles, designed to distinguish high energy photons from high energy neutral pions.

The last part of my thesis is devoted to the development of accurate prompt photon and γ-jet identification algorithms. Prompt photon identification relies on the previous shower shape analysis methods and on an additional method called Isolation Cut Method. This method is required because the existing identification methods can not distinguish prompt photons from decay and bremsstrahlung photons. In order to distinguish them, I developed the Isolation Cut Method, described in Chap. 6 which is based on the idea that a prompt photon of Compton and annihilation processes is produced alone in its direction of motion with no other particles accompanying it. Once the prompt photon is well identified we can proceed to identify the recoiling jet and to study its properties. In Chap. 7, I present an algorithm that links the prompt photon to the jet, which is detected in the TPC and EMCal detectors. With the identified jets, I estimate the sensitivity of the measurement of the jet-quenching effect in one year of ALICE running by comparing the energy distribution of jet particles in *pp* and Pb-Pb collisions.

Chapter 2

Review of experimental observables

The determination of the quark-gluon plasma formation and the study of its properties are formidable tasks. The ephemeral medium under study hadronizes and the final particles arriving to the detectors are the only carriers of information available. There are several signatures that have been studied in heavy-ion experiments and some of them suggest that at CERN and BNL a new kind of strongly interacting matter may have been produced. In this chapter, I review the most interesting results obtained at SPS and RHIC, and I summarize the signatures that could be measured at the LHC. Finally, I devote the last section to photon production, since this signature is the main subject of this thesis.

2.1 Collision geometry of heavy-ion collisions

It is worthwhile to give a brief description of some concepts related to the geometry of the collision as *number of participants*, *centrality* of the collision and *impact parameter*, which are used frequently in this thesis.

The collision is described in terms of the *Glauber model* [Gla70, Wib98]. This model is based on three ideas: ions can be considered as formed by a continuous matter distribution which can be described, for example, by a Woods-Saxon function,

$$\rho(r) = \frac{\rho_0}{1 + \exp\left(\frac{r-r_0}{a}\right)}, \tag{2.1}$$

where r is the distance from a given point of the nuclear matter to the center of the nucleus and the parameters a and r_0 are obtained from electron scattering experiments; nucleons propagate in straight lines when traversing the nucleus; and nucleons interact according to the inelastic scattering cross section σ_{NN} measured in pp collisions.

A useful quantity is the minimal distance b between the center of the two colliding nuclei reached during the collision, known as the *impact parameter*. For a given b, only the nucleons in the overlap region of the two nuclei, called *participant nucleons*, interact and the remaining nucleons, denominated *spectator nucleons,* follow their initial trajectories

without interaction. In a central collision $b = 0$ and the number of participants N_{part} is the total number of nucleons in both nuclei, $2A$. In the case of collisions between large heavy-ions, each nucleon of one nucleus can interact with several nucleons of the second nucleus producing more than $2A$ collisions. The number of *binary collisions* N_{coll} is defined as the total number of collisions of the participant nucleons and can be estimated by the Glauber model. In the absence of nuclear and medium effects, the number of particles produced in a nucleus-nucleus collision should be the number produced in proton-proton collisions, scaled by N_{coll}.

The degree of centrality C of a given subset of collisions characterized by a maximum impact parameter b_c,

$$C = \frac{\int_0^{b_c} 2\pi b db}{\sigma_{AA}}, \tag{2.2}$$

has the meaning of the probability that the collision occurs for $b < b_c$ [Yin04]. Although the impact parameter cannot be directly measured, C can be obtained nevertheless through N_{part}, which is measured in ALICE by the Zero Degree Calorimeters, described in Sec. 3.2.3. In the literature, the term *central collisions* refers to collisions with $0 < C < 0.05 - 0.1$ and *peripheral collisions* are defined as those with $0.9 < C < 1$. Finally, collisions without any selection in b are called *minimum bias collisions*.

2.2 QGP signatures at SPS

The CERN-SPS program was performed with fixed target experiments in which Pb-Pb collisions at $\sqrt{s_{NN}} \simeq 17$ GeV were carried out [CER]. The most striking results from this program were the observation of the previously predicted J/ψ suppression and the measurement of an enhancement of the production of strange particles. A short bibliography of the CERN-SPS heavy-ion programme is Refs. [Abr97, Abr99, Abr00, Aga98, Agg98, Agg00a, Agg00b, Alb95, Alb96, Amb98, Amb99, And99, Ant99a, Ant99b, Bea97, App98, Bea99, Bek95, Esk95, Esk01, Fan02, Kli96, Pei02, Sik99, Len99a, Len99b, Arm02, Sus02, Kad02].

2.2.1 J/ψ suppression

Matsui and Satz argued that a signal of the QGP formation would be the disappearance of quarkonia states like the J/ψ [Mat86]. These states are bound systems formed by charm and anti-charm quarks ($c\bar{c}$). Lattice QCD calculations show that above the critical temperature T_c the heavy-quark potential is effectively screened in the QGP, what means that $c\bar{c}$ bound states melt in the medium. This melting produces a suppression of final $c\bar{c}$ states and an increase of open charm particle production. Figure 2.1 shows the experimental result obtained at SPS of the ratio of the measured J/ψ spectrum to expected one when only ordinary nuclear absorption is taken into account [Abr97, Abr99, Abr00]. A sudden

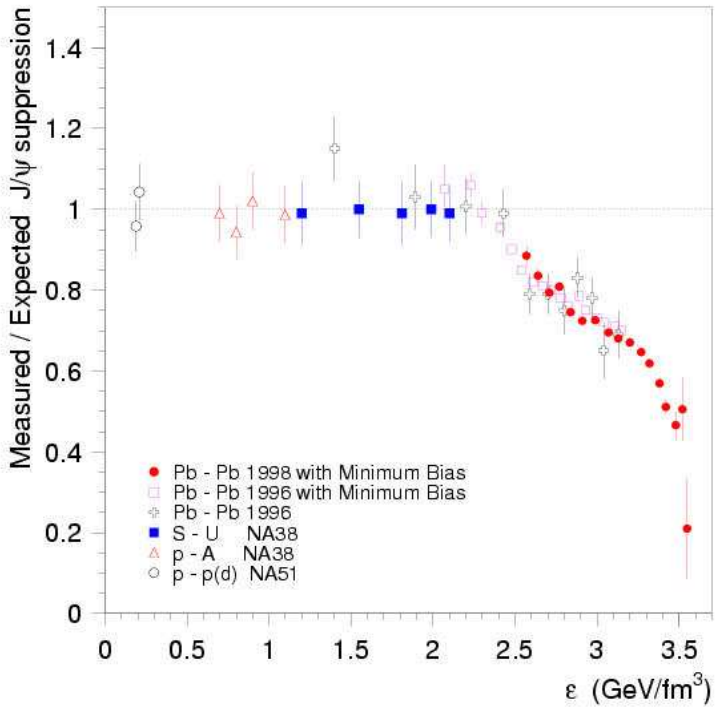

Figure 2.1: Measured J/ψ production yields normalized to the expected yields assuming that the only source of suppression is the ordinary nuclear absorption [Abr99].

change of this ratio happens when the energy density is larger than twice the critical energy density. This ratio is consistently less than one which means that the J/ψ production is suppressed. This suppression effect can be understood as due to the formation of the QGP, although some hadronic models provide plausible alternative explanations [Arm02]. The suppression scenario could change at higher energies like those available at RHIC and LHC, because, due to the large production of charmed quarks, the recombination of $c\bar{c}$ pairs could lead even to an enhancement of their expected production [ALI04].

Experiments at RHIC are studying the behaviour of this signature. From the preliminary results at low statistics, it cannot be concluded that the measured to expected ratio of produced J/ψ particle is different from unity.

2.2.2 Strangeness enhancement

Strangeness production was one of the first proposed signals for the QGP formation. The strangeness content of the colliding nuclei is negligible, and consequently all the measured strange particles are produced in the collision. The strange quark s has a large bare mass $m_s \simeq 170$ MeV/c^2 compared to the bare mass of the lighter quarks u and d, $m_{u,d} \sim 5$ MeV/c^2; thus, the production of particles containing the s-quark via hadronic

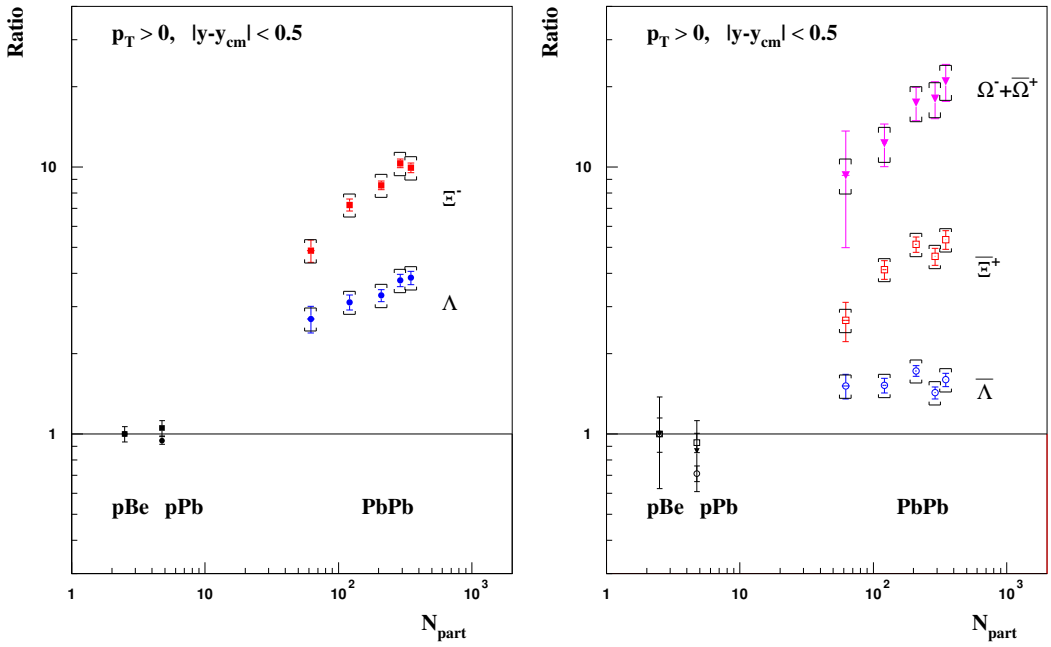

Figure 2.2: Enhancement of strange baryons relative to p-Be collisions, as a function of the number of participants in the collision. The ratio is defined as $\frac{N_{AB}}{N_{part}N_{pPb}}$, where N_{AB} is the number of strange particles in A-B collisions, N_{pPb} is the number of strange particles in p-Pb collisions and N_{part} is the number of participant nucleons [Fan02].

channels is usually suppressed[1]. As $m_s < T_c$, $s\bar{s}$ pairs will be in chemical and thermal equilibrium in the QGP. Strange quarks will hadronize producing an enhancement of the production of strange particles. Figure 2.2 shows the ratio of the measured yields of strange baryons in p-Pb and Pb-Pb to the yield in p-Be collisions at $\sqrt{s_{NN}} \approx 17$ GeV as a function of the number of participants [Fan02]. This ratio is about unity for p-Pb collisions but for Pb-Pb a large enhancement is observed, increasing with the strangeness content of the particles, which could be an indication of the production of the QGP. However, an enhancement of the strangeness production in p-Pb collisions compared to pp collisions has also been observed [Sus02, Kad02]; As in the p-Pb system the QGP formation is not expected, it cannot be claimed that this is the source of the enhancement observed in Pb-Pb collisions; thus, this enhancement cannot be considered at present as a definitive proof of the QGP formation.

Results from RHIC also show an increase of strange particle production as a function of the number of participants [Rit04].

[1] These masses correspond to the quark masses if the chiral symmetry is restored, the breaking of this symmetry gives an additional mass to the quarks, $m_s \approx 500$ MeV/c^2 and $m_{u,d} \approx 350$ MeV/c^2.

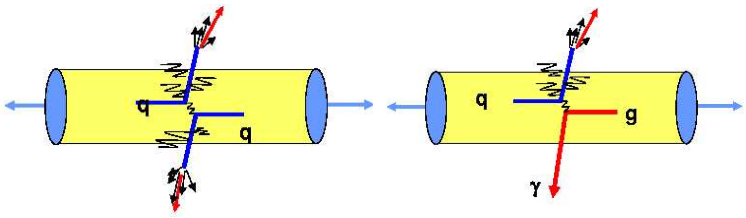

Figure 2.3: Schematic view of parton scattering in heavy-ion collisions. In left frame, two quarks collide and produce two new partons that loose energy in the medium by radiating gluons; they can escape from the nuclear medium and hadronize into jets. In right frame, a gluon-quark scattering produces a photon and a quark; the photon escapes without interacting whereas the quark suffers an energy-loss due to the medium.

2.3 QGP signatures at RHIC

The RHIC-BNL collider [BNL, RHI], has produced Au-Au, pp and d-Au collisions since year 2000 at $\sqrt{s_{NN}} = 130$ and 200 GeV. The experiments carried out at this collider have given rise to important results like the observation of high-momentum particle suppression (jet-quenching), direct photon production and the existence of an anisotropic flow.

2.3.1 High transverse momentum particle suppression: jet - quenching

High-p_T particles are probes that provide information about the propagation of hard partons in the nuclear medium. For pp collisions at RHIC energies, the dominant process of particle production above 2 GeV is hard scattering, a process in which two partons interact energetically producing two new hard partons that hadronize into two opposite jets [Adc04]. In the case of Au-Au collisions, if there would not exist either QGP formation or other effects like the *Cronin effect*[2], we should obtain a high-p_T particle distribution similar to that for pp collisions but scaled by the number of binary collisions. However, scattered partons propagating through a strongly interacting medium lose energy due to strong interactions with the gluons of the medium [Wie04]. After a long path in the medium, the parton may even be stopped. An schematic view of this process is shown in Fig. 2.3.

In order to show the existence of a parton energy-loss, it is useful to define the *nuclear modification factor* R_{AB} associated to the collision of heavy-ions A and B as,

$$R_{AB} = \frac{dN^P_{AB}}{\langle T_{AB} \rangle_C \times d\sigma^P_{NN}}, \tag{2.3}$$

where $\langle T_{AB} \rangle_C$ is the nuclear thickness function for a given centrality C, dN^P_{AB} is the

[2]Enhancement of the hard particle production compared to pp collisions, due to the multiple interaction of partons with nuclear matter before the final hard scattering.

differential yield of a given process P and $d\sigma^P_{NN}$ is the cross section of process P in nucleon-nucleon collisions. If there is no effect that modifies the yield of P, $R_{AB} = 1$ [Adc04].

The PHENIX and STAR collaborations have calculated the nuclear modification factor for Au-Au and d-Au collisions, obtaining a high-p_T particle suppression in Au-Au central collisions, i.e. $R_{AA} < 1$, as Fig. 2.4 shows. In the case of the most central collisions, there is a suppression by a factor 5 at high-p_T for neutral pions and charged hadrons, but for peripheral collisions $R_{AA} \approx 1$; for d-Au collisions there is only a small increase consistent with Cronin effect. It is interesting to note that R_{AA} depends on the particle species. For protons and anti-protons there is almost no suppression at high-p_T[3]; this fact is not fully understood at present.

Another interesting signature related to the parton energy-loss is the back-to-back azimuthal correlation. As reported above, high-p_T particles in pp collisions belong to one of the two jets produced in hard parton scatterings. As these jets are emitted back-to-back in the azimuth, there should be a correlation between the hadrons of the two jets. In Au-Au collisions at RHIC energies, the produced nuclear medium may absorb the jets, modifying in this way the correlation. Unfortunately, jet reconstruction is difficult at the RHIC experiments due to the abundant soft particle environment, and this absorption cannot be shown in a straightforward way. A way to study this correlation is through two-hadron azimuthal angle correlations. The relative azimuthal angle $\Delta\phi$ correlations between the charged particles detected at PHENIX in d-Au collisions and in peripheral (60-90 %) and central (0-10 %) Au-Au collisions are shown in Fig 2.5. The peaks observed at $\Delta\phi = 0$ (near-side) reflect the correlation between hadrons produced within the same jet, while broader peaks observed at $\Delta\phi = \pi$ (away-side) reflect the correlations between pairs of hadrons each produced in one of the two opposite jets. In Au-Au central collisions, the away-side peak disappears at difference with peripheral and d-Au collisions. This suggests that the recoiling jet has been absorbed by the medium.

2.3.2 Anisotropic flow

The collective behavior of propagating particles produced in the interaction gives information about the thermalization of the strongly interacting medium generated. When heavy-ions collide, the nuclear matter momentum distribution has an ellipsoidal shape due to the incomplete overlap of the ions. The subsequent partonic interactions change the initial momentum distribution so that its anisotropy reflects the underlying geometrical anisotropy.

The azimuthal anisotropy of the transverse momentum distribution of a given kind of particle can be used to study the effect of the nuclear medium on the particle distribution.

[3]That is why in Fig. 2.4 the charged hadrons ratio has a maximum and is not flat as the ratio for neutral pions.

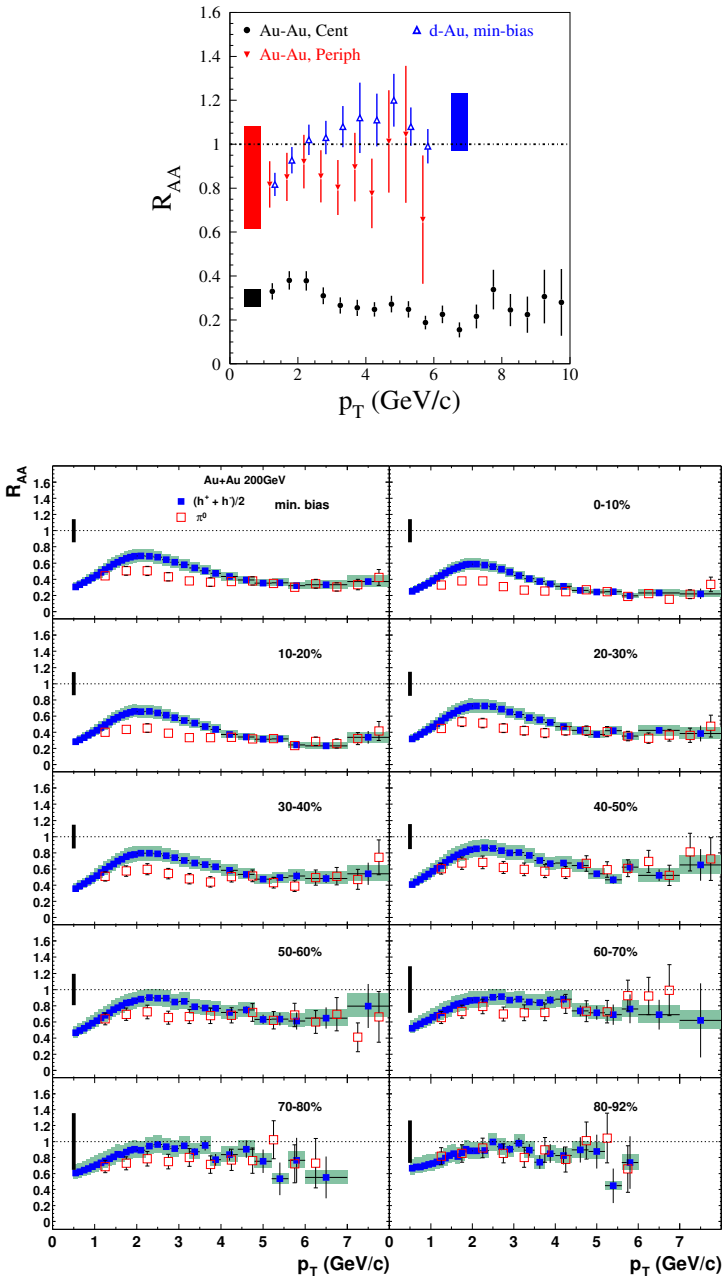

Figure 2.4: Upper figure: $R_{AA}(p_T)$ for π^0 central and peripheral Au-Au collisions and minimum bias d-Au, collisions obtained by the PHENIX collaboration. The shaded boxes show the systematic errors. Lower figures show $R_{AA}(p_T)$ for π^0 and charged hadrons for different collision centralities [Adc04].

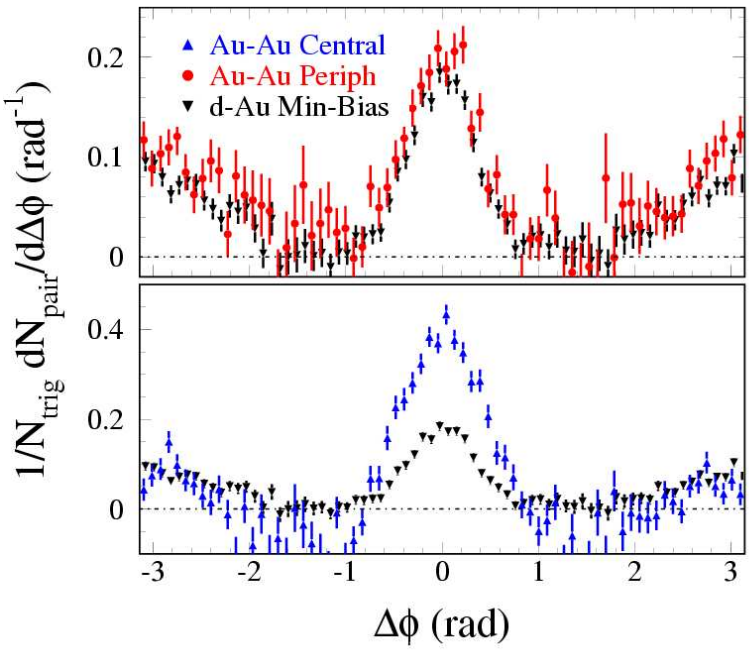

Figure 2.5: Differential yields per relative azimuthal angle $\Delta\phi$ and per trigger particle of pairs of charged hadrons in d-Au, peripheral and central Au-Au collisions. The pairs were selected with the higher-momentum "trigger" particle in the range $2.5 < p_T < 4$ GeV/c and the lower momentum "associated" particle in the range $1 < p_T < 2.5$ GeV/c [Adc04].

The study is performed through the expansion of the azimuthal component of the particle momentum distribution in a Fourier series,

$$\frac{dN}{d\phi} = \frac{1}{2\pi}\left\{1 + 2\sum_n v_n \cos\left[n(\phi - \phi_0)\right]\right\}. \tag{2.4}$$

The harmonic coefficients v_n are called the anisotropy parameters, ϕ the particle azimuthal angle and ϕ_0 is the azimuthal angle of the reaction plane[4]. The first harmonic coefficient v_1 is called the *direct flow* and the second v_2, the *elliptic flow*. Figure 2.6 shows the elliptic flow distribution $v_2(p_T)$ for multi-strange baryons [Cas04]. The agreement between data and hydro-dynamical models between 0 and 2 GeV is very good, suggesting that a local thermalization followed by a collective hydro-dynamic expansion has taken place. At larger p_T, the hydro-dynamical model diverge from the data.

2.4 QGP signatures at LHC

The LHC will produce pp ($\sqrt{s} = 14$ TeV) and Pb-Pb ($\sqrt{s} = 5.5A$ TeV) collisions. Heavy-ion collisions at LHC will be 30 times more energetic than at RHIC; a hotter, larger and more long-lived QGP medium will be formed, which doubtless will lead to unexpected

[4]Plane defined by the beam axis and the impact parameter b.

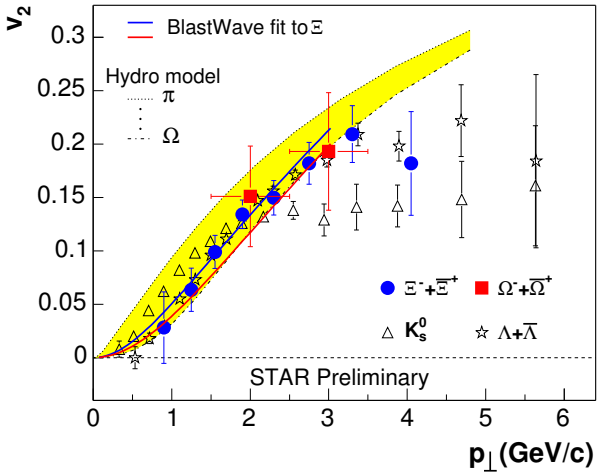

Figure 2.6: Elliptic flow measured by the STAR collaboration for multi-strange baryons, together with hydro-dynamic model predictions [Cas04].

discoveries. The high energy available will enable to extend the study of the known QGP signatures further in energy and will also most likely allow the observation of new phenomena. At LHC, the following facts are predicted [ALI04, Fri04]:

- High-density (saturated) parton distributions determine particle production. A large amount of low-energy partons, mainly gluons, are expected to be produced, so many that they will tend to merge together, producing a lower number of gluons of low energy. This phenomenon, called the *nuclear shadowing effect*, has been observed in electron-nucleus deep inelastic scattering [Esk03]. The loss of low-energy gluons modify the particle production. For example, a reduction of 35 % of the charm cross section per nucleon-nucleon collision in Pb-Pb with respect to the value observed in *pp* collisions at the same c.m.s energy is expected [Dai03].

- Hard processes contribute significantly (94 %) to the total *AA* cross section. At LHC these processes can be calculated with pQCD, and are an ideal tool to characterize the QGP medium. As observed at RHIC, at LHC hard propagating partons will loose part or even their whole kinetic energy by radiating gluons (Figs 2.3). The radiated gluons will emerge almost collinear to jets produced by the escaping partons; the gluon radiation will modify the jet fragmentation function, which will be characterized by a larger abundance of low-energy particles than in the *pp* case. Consequently, jet measurement will be a useful tool to quantify QGP effects at LHC [Acc03].

- Weakly interacting hard probes like direct photons, and eventually Z^0 and $W^{\pm}$, will become accessible, and will give unperturbed information about the nuclear medium, as reported in next section.

- Heavier quarkonia states will be available. At LHC $c\bar{c}$ and specially $b\bar{b}$ states can be produced in the early stages of the collision, before thermalization is reached. As explained in Sec. 2.2.1, quarkonia states are expected to dilute in the QGP. Therefore, the formation of the QGP suppresses the quarkonia production compared to the rate in pp collisions. On the other hand, at LHC energies the plasma itself will produce c and b-quarks, which will favor the recombination of $q\bar{q}$ pairs and consequently may hide the suppression effect but only in the very low-p_T region. At large p_T, where the perturbative production mechanisms are expected to dominate, the suppression effect may be observable.

2.5 Photon Production

Photons are an attractive probe in heavy-ion collisions because they are electromagnetically interacting particles and therefore they do not interact by strong interactions with the nuclear medium. This means that photons probe the state of nuclear matter at the time of their production. Both the photon production rate and momentum distribution depend on the parton momentum distribution in the medium. Unfortunately, a large photon background due to hadrons, specially to π^0 and η mesons, which decay into photons, is produced, and methods to subtract this background have to be developed.

We define as *direct photons* the photons originated in the interaction region that are not produced by particle decay. These photons are of interest because they are produced in the first stages of the collision. We can distinguish two categories of direct photons:

1. *Pre-equilibrium*: The harder part of the photon spectrum, due to the so-called *prompt photons*[5], is produced during the pre-equilibrium stage by parton-parton scattering (Compton and annihilation processes) in the primary nucleon-nucleon collisions (Fig. 2.3-right). Photons produced by parton bremsstrahlung are also considered as direct photons.

2. *Equilibrium*: In the thermally equilibrated plasma, quarks and gluons will radiate *thermal photons* that will populate the soft region of the spectrum up to several GeV, in the LHC case.

To conclude that a thermalized QGP has been produced, we can proceed as follows:

- Measuring direct photon yields. This is a formidable task as the main photon source is neutral mesons decay. Experimentally, the decay background can be determined for example through invariant-mass analysis or isolation methods. Once the background contribution is estimated, the inclusive photon yield to background ratio is

[5]The properties of such photons will be studied in detail in Chapts. 6 and 7.

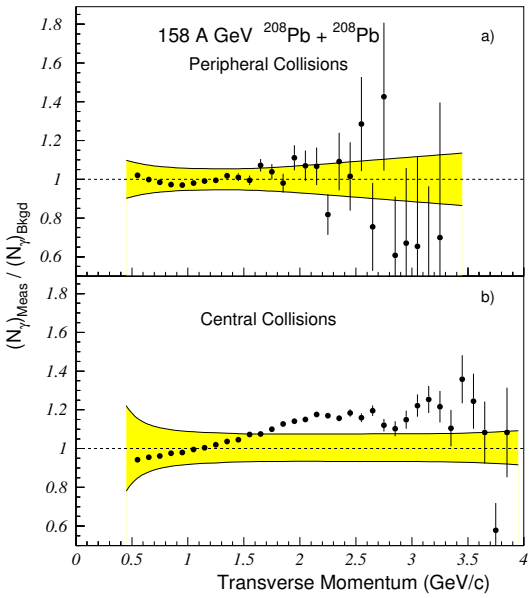

Figure 2.7: Direct photon production normalized to the background obtained at the SPS at $\sqrt{s_{NN}} \simeq 17$ GeV Pb-Pb collisions by the WA98 collaboration, for a) peripheral and b) central collisions [Agg00b].

calculated. If this ratio is larger than one, we can say that the *excess* of photons is due to direct photon production. In addition, if the pre-equilibrium prompt photon yield is also quantified and added to the background, the excess would be due only to thermal photons. This excess may signal the presence of a radiating strongly interacting matter.

- At high energies (larger than 2 GeV at RHIC and than 20 GeV at LHC) the only direct photon production mechanism is the parton-parton scattering. Each prompt photon is associated to a recoiling jet, both with the same energy. The jet fragmentation properties depend on the interaction of the parton with the hot matter and its initial energy. In AA collisions, the measurement of the jet energy and therefore, the measurement of the parton initial energy is difficult due to the large HIC background. Consequently, processes in which a photon is associated to a jet are interesting since the measurement of the prompt photon gives the initial energy of the recoiling parton. The study of high-energy photons and the particle momentum distribution of recoiling jets, may provide a proof of the creation of the QGP.

At SPS (Fig. 2.7) and RHIC (Fig. 2.8) the ratio of the inclusive to background photon spectra has been studied as a function of the centrality of the collision. For central collisions, a photon excess with respect to the total photon yield due to neutral meson decay was observed by the WA98 collaboration [Agg00b]. The SPS results can be interpreted in

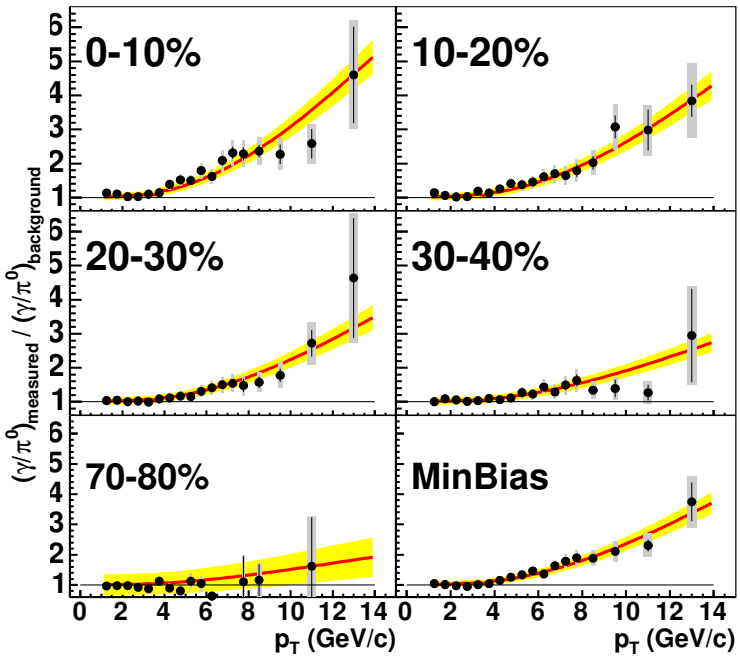

Figure 2.8: Direct photon production normalized to the background obtained at RHIC by the PHENIX collaboration for $\sqrt{s_{NN}} = 200$ GeV Au-Au collisions and for different centralities. The curves represent a pQCD calculation of direct photons in pp collisions normalized to Au-Au collisions, assuming pure point-like scaling. Shaded regions indicate the variation of the pQCD calculation for a change of scale from $p_T/2$ to $2p_T$ [Adl05].

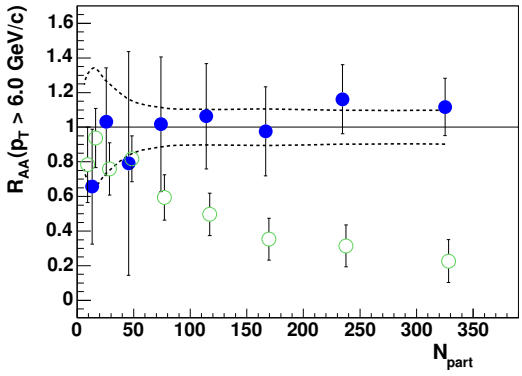

Figure 2.9: R_{AA} as a function of centrality given by N_{part} for direct photons (•) and π^0 (○) yields integrated above 6 GeV. The error bars indicate the total error excluding the error on the number of binary collisions, shown by the dashed lines [Adl05].

a frame different from the QGP if the formation of a hot hadron gas is assumed [Pei02].

Measurements of photon excess at RHIC by the PHENIX collaboration are significantly larger than at SPS, and in good agreement with pQCD calculations as is shown in Fig. 2.8. The PHENIX collaboration has also calculated R_{AA} for photons and π^0 as a function of the number of participants as shown in Fig. 2.9. We see that the photon data are compatible with no suppression compared to pp collisions, behaviour very different of the one observed for hadrons. These measurements suggest that the strong high-p_T hadron suppression observed is a final-state effect due to parton energy-loss in the dense nuclear medium produced [Adl05].

Chapter 3

The ALICE experiment at the LHC

This chapter is devoted to the description of the ALICE experiment. First, a brief description of the LHC and of some relevant beam parameters needed in Chaps. 6 and 7 is given. Next, the ALICE detector layout is reported, and finally, the software currently being developed to simulate and analyze ALICE events is briefly described.

3.1 The LHC accelerator

The Large Hadron Collider (LHC) is a two ring superconducting collider currently under construction which will be installed at CERN, in the 27 km long tunnel of the former electron-positron collider LEP. The expected beginning of data taking is summer 2007 [LHC, CER]. The LHC physics program is mainly aimed at proton-proton (pp) collisions. In addition, shorter running periods, typically one month per year, of heavy-ion collisions (HIC), mainly Pb-Pb, are included in the program. Other projectile-target combinations (p-Pb, Ar-Ar, ...) are also foreseen.

Four experiments will take data at the different interaction points (IP) of the collider, three dedicated mainly to pp collisions: ATLAS, CMS and LHCb [CER]; and ALICE [ALI95] that will be dedicated to heavy-ion collisions, although measurements of pp collisions as a reference for the results obtained in HIC will also be an important part of the ALICE program. CMS has also submitted a strong program dedicated to HIC and ATLAS is studying the proposal of a HIC program.

Protons and nuclei are pre-accelerated before entering the LHC by the following pre-acceleration sequence: ion or proton Linac injectors - PS (Proton Synchrotron) Booster - PS - SPS (Super Proton Synchrotron) - LHC. The expected reachable energy per nucleon in the center of mass for pp collisions is 14 TeV whereas for Pb-Pb collisions is $5.5A$ TeV. One important beam parameter is the luminosity $\mathcal{L}$ which is related to the collision rate

system	$\mathcal{L}$ (cm^{-2} s^{-1})	Time (s)	$\sqrt{s}$ (TeV)
pp	10^{30}	10^{7}	14
Pb-Pb	$0.5 \cdot 10^{27}$	10^{6}	$5.5A$

Table 3.1: Beam parameters for the ALICE experiment [ALI04].

$\Re$, and defined in terms of the latter as

$$\mathcal{L} = \frac{\Re}{\sigma_{int}}, \tag{3.1}$$

where σ_{int} stands for the interaction cross section. The maximum pp luminosity is expected to be around 10^{34} cm^{-2} s^{-1}, but only CMS and ATLAS will be able to work at the maximum luminosity. ALICE will operate at a reduced luminosity of about 10^{30} cm^{-2} s^{-1} in order to avoid pile up in the ITS and TPC detectors (see Sec. 3.2.2). For Pb-Pb collisions the luminosity will be about $0.5 \cdot 10^{27}$ cm^{-2} s^{-1}. In Tab. 3.1, the beam parameters and running conditions for the different colliding systems for the ALICE experiment are summarized [ALI04].

3.2 The ALICE detector

ALICE has been designed to be a general purpose detector, capable of measuring and identifying most of the particles produced in pp and specially Pb-Pb collisions [ALI95, ALI04]. ALICE will allow tracking and identification of particles from quite low p_T (~ 100 MeV/c) up to high p_T (~ 100 GeV/c) in a huge particle multiplicity environment. The detector has been optimized to work at multiplicities up to around 8,000 charged particles per rapidity unit at mid-rapidity, which is the worst scenario predicted for Pb-Pb collisions. Theoretical calculations predict multiplicities in the range of 2,000 to 6,000 charged particles. Extrapolations from RHIC data point to values of about 2,500 as displayed in Fig. 3.1 [Esk01].

3.2.1 Detector layout

ALICE consists of a central detector system, covering the full azimuthal angle range and pseudorapidity $|\eta| < 0.9$, and of several forward and backward detectors.

The central detector system is contained in the large solenoidal magnet of the former L3 collaboration, which will generate a moderate solenoidal field of $B \leq 0.5$ T parallel to the beam axis[1]. The detectors integrating this system are mostly devoted to the study of hadronic signals, dielectrons and photons. It is composed from the interaction

[1]The ALICE global reference frame is: z-axis parallel to the beam axis, pointing toward the Muon Arm and, x and y-axis in the plane transverse to the beam direction.

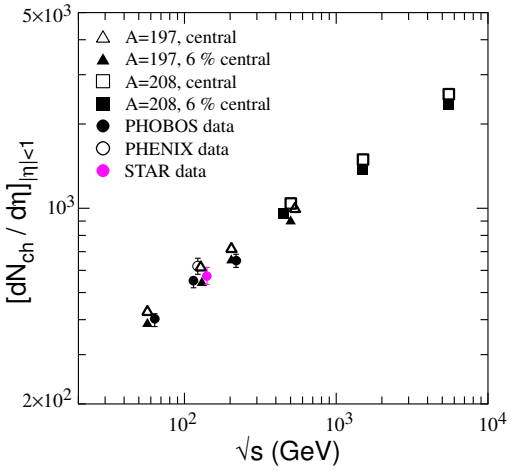

Figure 3.1: Charged particle multiplicity per pseudo-rapidity unit in AA collisions. Square and triangle markers are model predictions. Circle and rhombi markers represent RHIC data [Esk01, Esk00].

vertex to the outer part of the following detectors: six layers of high-resolution silicon detectors called the Inner Tracking System (ITS), surrounding the beam pipe; a Time Projection Chamber (TPC), the main tracking device of the experiment; a Transition Radiations Detector (TRD) designed for electron identification; and a barrel of Time Of Flight detectors (TOF). The central barrel is complemented by two small area detectors: a ring imaging Cerenkov detector covering $|\eta| < 0.6$, and $\Delta\phi = 57.6^{\circ}$ for the identification of high momentum particles (HMPID), and the single-arm high-resolution electromagnetic calorimeter PHOS, designed to work as a PHOton Spectrometer, which covers $|\eta| < 0.12$ and $\Delta\phi = 100^{\circ}$ and consists of an array of lead tungstate crystals.

At large rapidity, there is a muon spectrometer dedicated to the study of muon pairs produced in the decay of quarkonia and which covers the pseudorapidity interval $-4 < \eta < 2.4$, a Photon Multiplicity Detector (PMD), placed opposite to the muon spectrometer, and an ensemble of Forward Multiplicity Detectors (FMD) covering the large multiplicity region (up to $\eta = 5.1$). At zero degrees and about 90 m from the interaction vertex, there are two sets of neutron and hadron calorimeters, designed to measure the impact parameter, called the Zero Degree Calorimeters (ZDC). In addition, a system of scintillation and quartz counters denoted as V0 and T0, will provide fast trigger signals.

In Fig. 3.2, the ALICE layout is displayed. It is still under discussion the construction of an additional electromagnetic calorimeter (EMCal) of large acceptance ($|\eta| < 0.7$, $\Delta\phi = 120^{\circ}$). It would be placed opposite to PHOS as displayed in Fig. 3.3.

In the next sections, a brief description of the aforementioned detectors, excluding PHOS, is given. PHOS is thoroughly described in Chap. 4.

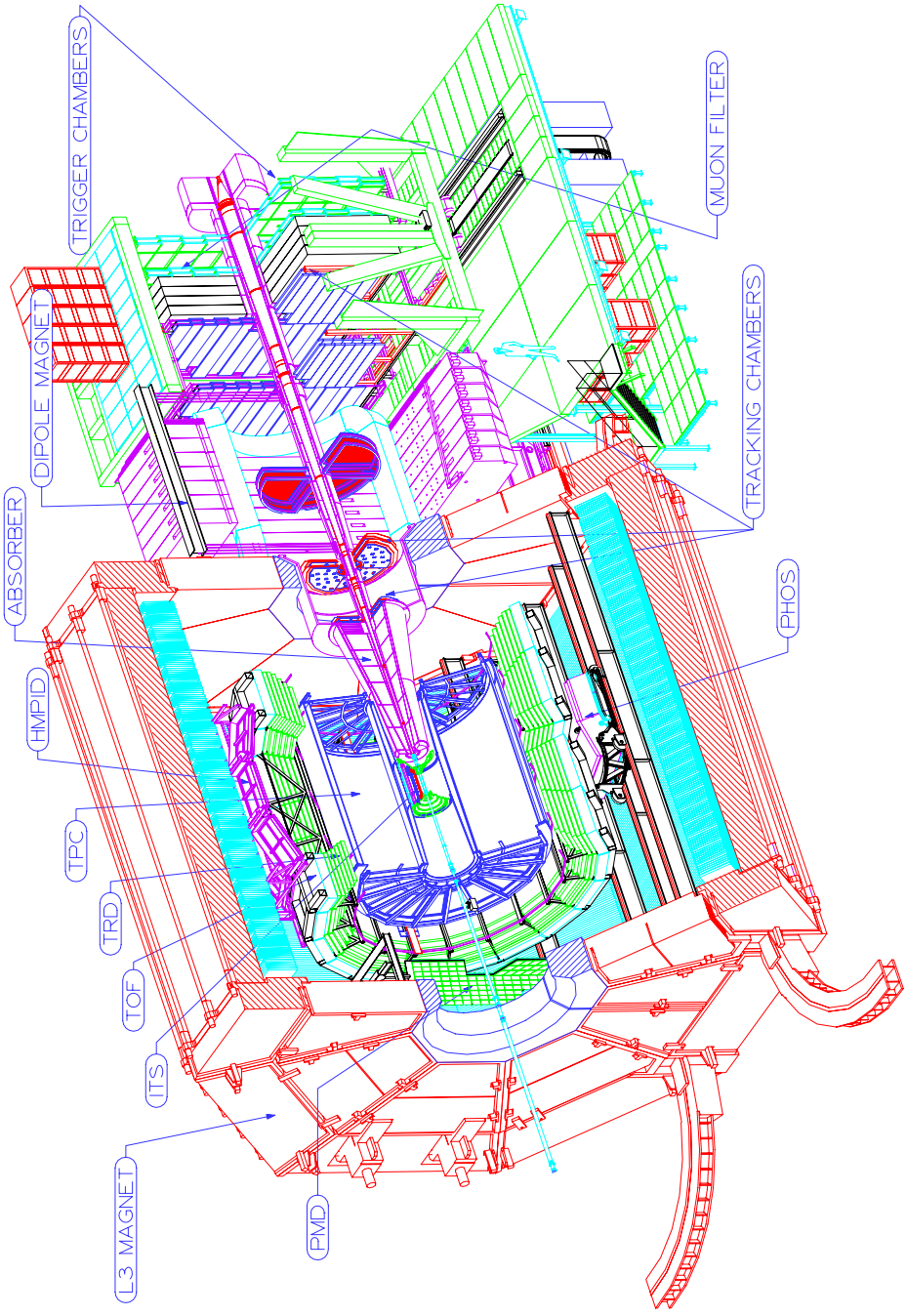

Figure 3.2: Longitudinal view of the ALICE detector without EMCal. A drawing including EMCal is presented in Fig. 3.3.

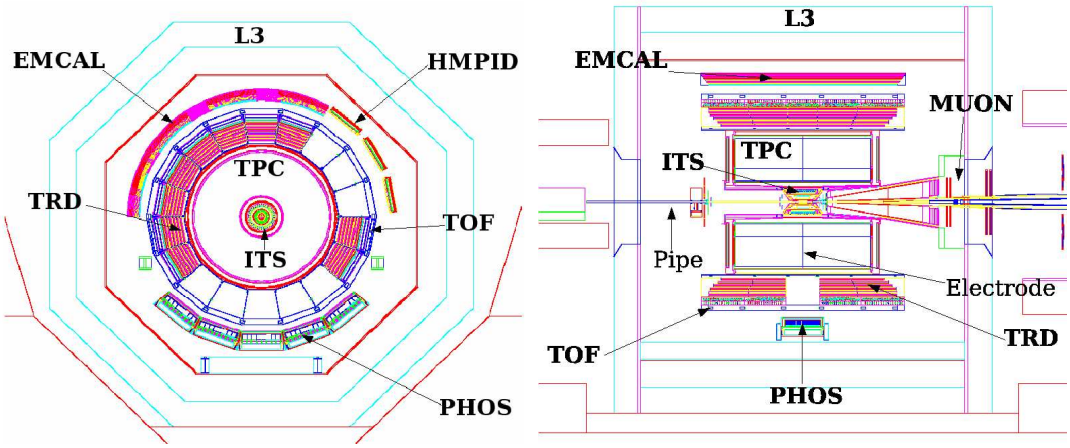

Figure 3.3: Longitudinal and transversal drawings of the ALICE detector including EMCal. TRD and TOF are drawn with holes in the PHOS and HMPID regions; HMPID is displaced respect to its position in Fig. 3.2

3.2.2 Central barrel

We present here the description of the different detectors composing the central barrel.

The ITS system The basic functions of ITS are:

- Determination of the primary vertex and of the secondary vertexes needed for the reconstruction of charmed hadron and hyperon decays, with a spatial resolution better than 100 μm.
- Particle identification and tracking of low momentum particles.
- Improvement of the momentum and angle measurements of the TPC.

ITS consists of six cylindrical layers of silicon detectors. The number and position of the layers are optimized for efficient track finding and impact parameter resolution. The pseudorapidity coverage is $|\eta| < 0.9$ for collisions located within an interaction region of 10.6 cm along the beam direction. The first layer has a more extended coverage, $|\eta| < 1.98$, in order to provide together with the FMD a continuous coverage in rapidity for the measurement of charged particle multiplicities. The outer radius of ITS, $r_{max} = 44$ cm, is determined by the track matching with the TPC and the inner radius, $r_{min} = 4$ cm, is the minimum radius allowed by the size of the beam pipe. The silicon detector characteristic feature is its high granularity, needed for the excellent spatial resolution required.

Due to the high particle density expected of about 80 particles per cm^2, the four innermost layers ($r \leq 24$ cm) must be practically two-dimensional devices. For this reason silicon pixel and silicon drift detectors were chosen. The two outer layers, where the track densities are below one particle per cm^2, will be made of double sided silicon micro-strip detectors.

With the exception of the two innermost pixel planes, all the layers will identify particles via *dE/dx* measurements, a method applicable only in the non-relativistic region. This will give to the inner tracking system a stand alone capability as a low-p_T particle spectrometer [ALI99a].

The Time Projection Chamber The TPC is the main tracking detector of the central barrel. The information provided by this detector added to the information given by the ITS, TRD and TOF detectors, allows to obtain charged particle momenta, particle identification via *dE/dx,* and vertex determination with sufficient momentum resolution and good track separation. The pseudorapidity acceptance of the TPC is $|\eta| < 0.9$.

The TPC is the main tool to investigate hadronic observables in Pb-Pb collisions. Hadronic measurements give information about the flavor composition of the fireball via the spectroscopy of strange and multi-strange hadrons, and about the space-time extent of the fireball at freeze-out via the investigation of two-particle correlations. This detector can achieve with the help the other central barrel detectors a very good momentum resolution needed to study hard probes like heavy quarkonia, charmed and beauty particles and high-p_T jets.

The TPC consists of a cylindrical field cage surrounding the ITS detector, filled with a gas mixture of 90 % of Ne and 10 % of CO_2. Charged particles knock out electrons of the medium which, due to the field, drift from both sides of the central electrode to the end caps of the TPC cylinder where they are detected. The inner radius is $r_{min} = 80$ cm, set by the maximum acceptable particle density of 0.1 particles per cm^2 and the outer radius is $r_{max} = 250$ cm. The overall length along the beam direction is $l = 500$ cm [ALI00b].

The Particle Identification System One of the most characteristic features of ALICE is its capability to identify particles by different techniques. There are four detectors dedicated exclusively to particle identification in the central system:

- TRD. The main goal of the TRD is the identification of electrons with momenta greater than 1 GeV/c, allowing at these energies charged pion rejection which is not possible for the TPC. In addition, together with the ITS and TPC, the TRD will perform: the measurement of electron pairs to study light and heavy meson spectroscopy; the measurement of the production cross section of mesons with a heavy quark through their decay channel into electrons; the measurement of the dilepton continuum originated by Drell-Yan processes; and the identification and separation of J/ψ mesons produced by B disintegration from those produced directly in the collision. The TRD detector surrounds the TPC and covers the same acceptance. This detector consists of six radiator layers, each composed of 100 polypropylene sheets, which produce transition radiation when traversed by relativistic particles,

and of a TEC wire chamber filled with Xe in which the transition radiation is detected [ALI01].

- TOF. This is an array of time of flight detectors, optimized for large acceptance and for momenta from 0.5 to 2.5 GeV/c, a region where the dE/dx technique is no longer effective to separate K and π mesons. The TOF detectors will be placed in the outer part of the TRD, covering the central pseudorapidity region $|\eta| < 0.9$; its inner and outer radii are 3.7 m and 3.9 m, respectively. The TOF system identifies particle masses from their time of flight from the interaction point to the detector. The TOF detector design is based on the Multi-gap Resistive-Plate Chamber (MRPC) technology; its individual modules are gas-filled parallel plate chambers in which there is an uniform and high electric field over their whole sensitive gaseous volume. Any ionization produced by a through going charged particle immediately starts an avalanche which eventually generates a signal in the pick-up electrodes. As there is no time drift associated to the movement of the electrons into a region of high electric field, the time jitter is caused only by fluctuations of the avalanche growth. Tests of several MRPC prototypes show a time resolution better than 40 ps [ALI00a].

- HMPID. This detector is a small system specialized in High Momentum Particle IDentification. This system identifies relativistic particles through the emission of Cerenkov light. The HMPID can measure energies from 1 to 5 GeV, which are essentially related to hard processes. For the RICH detector of the HMPID system, a liquid radiator has been chosen, because liquids have a suitable refraction index at these energies (1-5 GeV) for the measurement of π, p and K mesons. The chosen radiator is $C_6F_4H_4$ because its Cerenkov light is in the far ultraviolet wavelength region ($\lambda <= 200$ nm) and because this is the only liquid transparent to light in this wavelength range. The geometry of the radiator is of the proximity focusing type. As photon detector, a CsI photo-cathode in conjunction with a MWPC will be used. The detector will be composed of seven modules in a calot-like arrangement. HMPID is placed as far as possible from the IP to minimize the density of arriving particles [ALI98].

- PHOS /EMCal. The purpose of these detectors is to measure neutral particles. PHOS is described in detail in Chap. 4. The proposed EMCal (ElectroMagnetic CALorimeter) covers an azimuthal acceptance of 120^o and 1.4 units of pseudo-rapidity, centered at mid-rapidity. It is proposed to be a Pb scintillator sampling calorimeter consisting of 19,152 towers (114×168 in the $\eta \times \phi$ plane), of 25 radiation lengths thickness. The ultimate purpose of the EMCal is to extend the p_T range of the observables studied in ALICE. EMCal will be capable of fast triggering, which is essential for enhancing the sample of extremely high-p_T electrons, π^0 and γ rays. In combination with the ALICE tracking system, EMCal will provide excellent energy

and position resolution for off-line jet reconstruction. It is a crucial device to carry out the ALICE high-p_T physics program [Cor04].

The presence of material due to other detectors should be avoided between the TPC and PHOS or HMPID in order to keep the tracking accurate. It is still under discussion if holes in the intermediate detectors, TOF and TRD, are necessary. In Sec. 4.8, I discuss the effects of the TOF and TRD material in front of PHOS on the neutral particle observables, in the cases of a design with and without holes in those detectors.

3.2.3 Forward detectors

Muon Arm This detector is devoted to the detection of muon pairs coming from particle decay, specially particles of the charmonium and bottomium families (J/ψ, ψ', ...), and its purpose is the observation of the expected suppression of production of those particles [ALI99b].

The dimuon spectrometer consists of the following parts:

- A Front Absorber, made predominantly of carbon and concrete in order to limit the small angle scattering of traversing muons, designed to suppress as much as possible the hadron flux. In addition, it has the purpose of protecting the other ALICE detectors from the secondaries produced in the absorbing material.
- A large area magnetic dipole of 3 Tm integral field, placed out of the L3 magnet.
- A tracking system of high granularity, composed of ten planes of multi-wire chambers, devoted to the measurement of muon trajectories. There are four planes in front of the dipole, two inside it and the remaining four planes in the back side of the dipole. This distribution is the best suited to determine muon trajectories.
- A passive muon filter wall followed by four planes of trigger chambers of the RPC type.
- An inner beam shield designed to protect the chambers from particles produced at large rapidities and their secondaries.

Photon Multiplicity Detector The PMD is a pre-shower detector with fine granularity and full azimuthal coverage in the pseudorapidity range $1.8 < \eta < 2.6$. It will be mounted on the L3 magnet door, at 5.8 m from the IP, in front of the dimuon spectrometer.

The observables measured by the PMD are photon multiplicity and photon spatial distribution. These observables will allow to study the following topics:

- Determination of the reaction plane and probes of thermalization via studies of the azimuthal anisotropy and flow.

- Critical phenomena near the QGP phase boundary leading to fluctuations of global observables as multiplicity, mean transverse momentum and pseudorapidity distributions.

- Signals of chiral symmetry restoration through the measurement of photon and charged-particle multiplicities.

The principle of the pre-shower detector is the following: photons passing through a lead converter initiate an electromagnetic shower and produce large signals on several cells of the sensitive volume of the detector. Hadrons normally affect only one cell and produce a signal corresponding to minimum-ionizing particles. In front of the converter there will be veto detectors that reject charged particles. The thickness of the converter is optimized in such a way that the conversion probability of photons is high and the transverse shower spread is small; so, the shower overlap in a high-multiplicity environment is minimized. The optimal converter thickness is found to be 3 X_0. Behind the converter there will be about 2×10^5 cells filled with a gaseous mixture of Ar and CO_2, each of 1 cm^2 area [ALI99d].

Zero Degrees Calorimeters The ZDC's are in charge of the detection of spectator nucleons and of the measurement of their energy, which is related to the centrality of the collision.

In fixed-target experiments (WA98, NA49) the spectator nucleons, which fly away in the forward direction, are usually intercepted by ZDC detectors placed along the beam axis. In collider experiments, like ALICE, the method is significantly different. Typically, the beams are deflected by means of two separated dipoles at a certain distance from the interaction point, of the order of 50 m in the ALICE case, in order to reach the nominal distance between the beams (188 mm for the LHC). These magnets will also deflect the spectator protons, separating them from the spectator neutrons which basically fly away at zero degree. It is therefore conceptually possible to place between the separation dipoles, at both sides of the IP, a set of two devices, one of them, positioned between the two beams to intercept the spectator neutrons, and the other one, external to the outgoing beam, to collect the spectator protons. These detectors must be extremely compact, because the space between the separating dipoles is very small and the transverse dimensions of the neutron device cannot exceed in any case the distance between the the two beam pipes, and because spectator protons are expected to form a spot separated from the outgoing beam by only a few cm. In addition, they will operate at a high radiation level. Due to these constraints the quartz fiber calorimetry technique has been chosen. Spectator nucleons generate Cerenkov light in quartz fibers that will be collected and detected.

The neutron ZDC will be placed at 116.13 m from IP. At this distance, the neutron spot size will be about 0.6×0.6 cm^2. This device will be made of quartz fibers embedded in a tantalum matrix, and will have dimensions of $7 \times 7 \times 100$ cm^3 which allows to cover the 80 % of the shower generated by spectators neutrons. The fiber diameter is 365 μm. Two calorimeters will be used, one at each side of the IP.

The proton ZDC will be placed at a distance of 115.63 m from IP. At this point, the size of the spectator protons spot is no longer Gaussian because of the influence of the magnets. The 90 % of the protons cross an area of 12.6×2.8 cm^2, centered at 19 cm from the beam axis, on the outgoing beam side. Two devices of $20.8 \times 12 \times 150$ cm^3 made of 550 μm diameter quartz fibers embedded in a brass matrix centered at 19 cm from the beam axis will be constructed [ALI99e].

3.3 Event simulation and reconstruction

The ALICE off-line framework AliRoot [ALI, ALI04], based on the Object Oriented C++ environment ROOT [Roo], allows the reconstruction and analysis of physical data coming from either simulations or measurements. Nevertheless, part of the code is still in FORTRAN, like the Monte Carlo code GEANT 3.21 [GEAa] and the jet simulator PYTHIA [Sjo01b, Sjo01a].

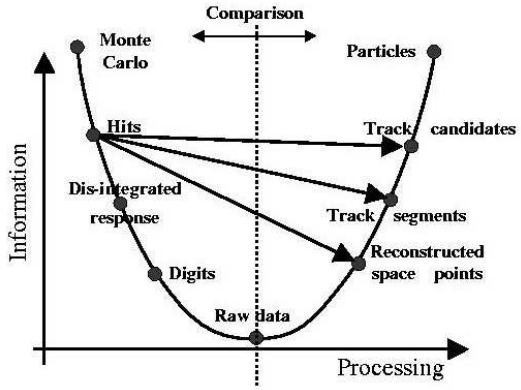

Figure 3.4: Schematic representation of the data processing chain.

The tasks performed in this framework, summarized in Fig. 3.4, are the following:

1. Event Generation: Different generators are employed depending on the physical studies to be performed; for example, PYTHIA is used to generate jets and HIJING [Gyu94] simulates a HIC environment.

2. Event transport: The transport of the generated particles through the detector material is done by the Monte Carlo codes GEANT 3.21, GEANT4 [GEAb] or FLUKA [Fas01]. The energy deposition in the detector is stored in *hits*.

3. Digitalization: The stored *hits* are transformed into a corresponding electric signal *digits* in the detector.

4. Reconstruction, tracking and particle identification from the signals in the detector.

3.3.1 Event generators PYTHIA and HIJING

I briefly describe here some relevant features of the Monte Carlo event generators relevant for the study of the PHOS performance, particle identification capabilities and hard physics.

PYTHIA In the study of hard processes with PHOS we use the generator of leading order processes of the Standard Model PYTHIA 6.203 [Sjo01b, Sjo01a]. The process in which we are interested is prompt photon production. The dominant subprocesses contributing at the parton-level are,

$$\begin{aligned} g + q &\rightarrow \gamma + q, \\ q + \bar{q} &\rightarrow \gamma + g. \end{aligned} \tag{3.2}$$

As main background processes for prompt photon production, hard $2 \rightarrow 2$ QCD subprocesses in the leading pQCD order are considered,

$$\begin{aligned} q + q &\rightarrow g + g, \\ q + q' &\rightarrow q + q', \\ q + \bar{q} &\rightarrow q + \bar{q}, \\ q + g &\rightarrow q + g, \\ g + g &\rightarrow g + g, \\ g + g &\rightarrow q + q'. \end{aligned} \tag{3.3}$$

These processes were simulated for pp collisions at $\sqrt{s} = 5.5$ TeV.

More details about PYTHIA simulations performed in this thesis are given in Chap. 6 and in Appendix C.

HIJING The Heavy-Ion Jet INteraction Generator HIJING 1.36 was employed to take into account the background produced in HIC [Gyu94]. This generator combines a QCD-inspired model of jet production with the Lund string model of jet fragmentation. Binary scaling with Glauber geometry is used to extrapolate to proton-nucleus and nucleus-nucleus collisions. Nuclear shadowing and parton energy-loss are included in the HIJING model and can be selected by the user.

The charged particle density at mid-rapidity in the ALICE barrel acceptance given by HIJING for central Pb-Pb collisions ($b < 2$ fm) at $\sqrt{s} = 5.5A$ TeV is about $(dN/dy)_{y=0} \simeq$

$6,000$ charged particles per rapidity unit, a value rather conservative, close to the most pessimistic value of 8,000 charged particles per rapidity unit, and more than a factor two larger than the value predicted from the extrapolation of RHIC data, $(dN/dy)_{y=0} \simeq 2,500$ charged particles per rapidity unit. Simulations with impact parameter $b < 5$ fm $[(dN/dy)_{y=0} \simeq 3,500$ charged particles per rapidity unit] were also performed to study the influence of particle multiplicity on the PHOS performance.

Chapter 4

Performance of the PHOS detector

The role of PHOS in the ALICE experiment is to detect and identify real photons and to measure with high resolution their 4-momentum in order to carry out the physics program which exploits direct photons and light neutral mesons (π^0 and η mesons mainly) as privileged probes. The unique feature of PHOS of measuring photons over a broad dynamical range in transverse momentum allows to access key information about the soft and hard processes occurring in pp, pA and AA collisions at LHC energies. Although the detection of photons is straightforward, their unambiguous identification among the huge background of other produced particles constitutes a first challenge; a second one is the discrimination between direct and decay photons, which are mixed in a ratio of about one to ten. To respond to these challenges PHOS has been designed with the following requirements:

- A high discrimination power between photons and any other kind of particles: charged and neutral baryons, charged mesons and electrons.

- A high energy and position resolution, and consequently a high mass resolution in the two photon invariant mass spectrum.

- A geometrical acceptance sufficient to measure neutral mesons down to low transverse momenta and to collect statistically-significant data for rare high-momentum particles.

First, I describe the characteristics of PHOS which allow to meet these requirements. Then, I discuss the different steps performed to simulate the PHOS response: hits from the tracking algorithm are converted into digits which in turn are processed by the reconstruction algorithm to produce reconstructed particles. The simulated intrinsic properties of PHOS, matched to data from in-beam measurements, are presented. I also examine how the various parameters are modified in a realistic environment of the ALICE experiment.

4.1 Detector description

The photon spectrometer PHOS is optimized for the measurement, with high energy and spatial resolution, of photons and light neutral mesons (π^0 and η) through their two-photon decay channel. Particles will be efficiently identified over a wide dynamical range, spanning the domain from a few hundreds of MeV/c up to several tens of GeV/c. PHOS, acting as a calorimeter, gives also access to global observables of interest for event characterization, such as the electromagnetic transverse energy and the particle multiplicity at mid-rapidity. PHOS is described in detail in [ALI99c, ALI04]. It consists of an ElectroMagnetic Calorimeter (EMC), and a Charged Particle Veto detector (CPV) [Bli00]. Some pictures of PHOS are given in Fig. 4.1.

- EMC is divided into five modules, consisting of 64×56 (across and along the beam direction, respectively) $PbWO_4$ scintillator crystals. Each crystal is a 18 cm long parallelepiped, equivalent to 20 radiation length units ($X_0[PbWO_4] = 0.89$ cm). Their cross section is 22×22 mm^2 which corresponds to the 90 % of the Molière radius ($r_M[PbWO_4] = 20$ mm). PHOS is located inside the ALICE solenoidal magnet at a distance of 4.6 m from the interaction point and the modules are centered at azimuthal angles of $\pm 40.7°$, $\pm 20.3°$ and $0°$. Each module covers about a quarter of pseudo-rapidity unit, $|\eta| \leq 0.12$ and $17.8°$ in azimuthal angle. The scintillation light is in the visible near UV wavelength range and is detected by 5×5 mm^2 Avalanche Photo-Diodes[1] (APD) coupled to low-noise pre-amplifiers. The calorimeter is operated at $-25°$C (stabilized to $\pm 0.3°$C) to optimize the scintillation light output and to minimize the noise level from the APD. The electronic chain associated to each crystal delivers two energy signals with different amplification factors and one time signal.

- The CPV consist of multi-wire proportional chambers with cathode pad read-out. Each calorimeter module is covered by a CPV module with an active area of $144.6 \times 6.6 \times 1.4$ cm^3 and filled with a gas mixture composed of 80 % Ar and 20 % CO_2. The total thickness of the CPV detector is 5.4 cm. Low-mass construction materials are used to minimize the material thickness. The anode wires of the proportional chamber are placed 7 mm above the cathode along the beam direction with a pitch of 5.65 mm. The cathode is segmented into 56×8 (along and across the beam direction, respectively) rectangular pads of 2.26×1 cm^2 each. The charge induced in the cathode pads by avalanches generated by charged particles is read out by GASSIPLEX chips integrated in the detector front plane.

[1] They are described in detail in the TDR of the CMS-ECAL detector [CMS97].

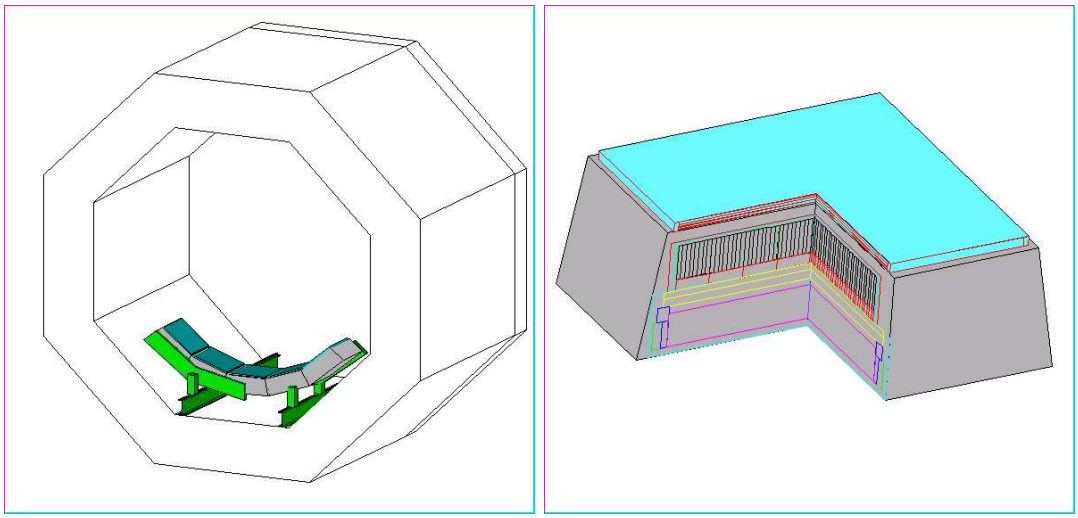

Figure 4.1: View of PHOS as described in AliRoot: PHOS inside the ALICE solenoid magnet (left), one PHOS block (right).

4.2 Prototype beam test results

A prototype PHOS module has been tested in the summers of 2002 and 2003 with pion and electron secondary beams at the CERN PS and SPS synchrotrons. The prototype consisted of 8×8 crystals in 2002 and of 16×16 crystals and a CPV in 2003 as displayed in Fig. 4.2. The crystals had $22\times22\times180$ mm^3 dimensions, one of them is shown in Fig. 4.3. The crystals were wrapped with TYVEC to improve light collection. HAMAMATSU S8148 APD of 5×5 mm^3 sensitive area were used as readout. A plastic scintillator was used to tag charged particles. The set-up of the test is schematically illustrated in Fig. 4.4.

4.2.1 Energy resolution for electromagnetic particles

Energy resolution has been measured by irradiating the array with high-energy electron beams, in the momentum range of 0.6-5 GeV/c at PS and 10-150 GeV/c at SPS. The results obtained are illustrated in Fig. 4.5. The energy resolution ranges from 4 % at 1 GeV/c to 1 % at 100 GeV/c. The experimental energy resolution can be described by the function[2]

$$\frac{\sigma}{E} = \frac{a}{E} \oplus \frac{b}{\sqrt{E}} \oplus c\,, \tag{4.1}$$

where $a = 0.0130 \pm 0.0007$ GeV is the electromagnetic noise, $b = 0.036 \pm 0.002$ GeV$^{1/2}$ is the stochastic term and $c = 0.0112 \pm 0.0003$ is the constant term. Simulations done with the AliRoot package reproduce well the data as can be observed in Fig. 4.5.

[2] $a \oplus b = \sqrt{a^2 + b^2}$

Figure 4.2: The 256 crystal PHOS prototype. A: Detector and cooling system. B: Closed detector with CPV on top. C: Crystal matrix. D: Close-up of the CPV.

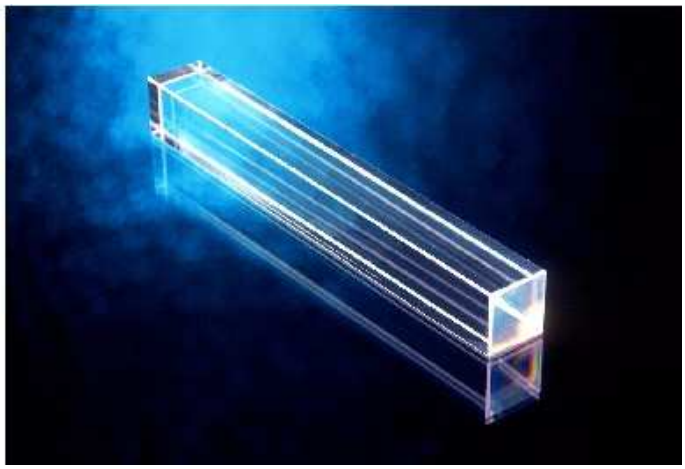

Figure 4.3: $PbW0_4$ PHOS crystal.

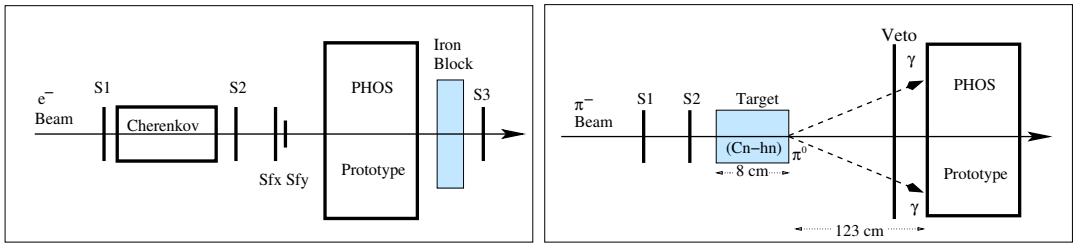

Figure 4.4: Experimental set-up for the test with 8×8 crystal PHOS prototype. Left frame: Electron beam impinging on plastic scintillators S1, S2, and S3, a Cerenkov detector, 2 charged particle position detectors Sfx, Sfy (plastic scintillators of 4 mm transverse size, installed perpendicular to each other) and the prototype. If there is coincidence in S1 $\times$ S2 $\times$ Cerenkov $\times$ Sfx $\times$ Sfy $\times$ $\bar{S3}$ the event on the prototype is most likely an electron. Right frame: Charged pion beam impinging on the scintillators (S1 and S2) and a plastic target. The reaction $\pi^{\pm} + {}^{12}C \rightarrow \pi^0 + X$ is produced and the 2 photons are likely to go into PHOS. If there is coincidence in S1$\times$S2 and anti-coincidence with the veto (multi-wire particle chamber), the event registered in the prototype is most likely a photon.

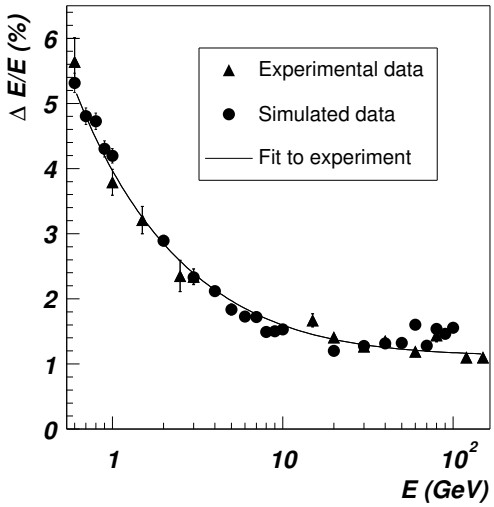

Figure 4.5: Energy resolution for photons. The line represents Eq. (4.1) fitted to the experimental points.

4.2.2 Invariant mass resolution of neutral pions

In the tests carried out at PS, a π^- beam of 6 GeV/c momentum irradiated a carbon target of 8 cm located in front of the PHOS prototype at a distance of 123 cm. The set-up shown in Fig. 4.4-right. At SPS, π^+ beams of 20 and 30 GeV/c momentum were used,

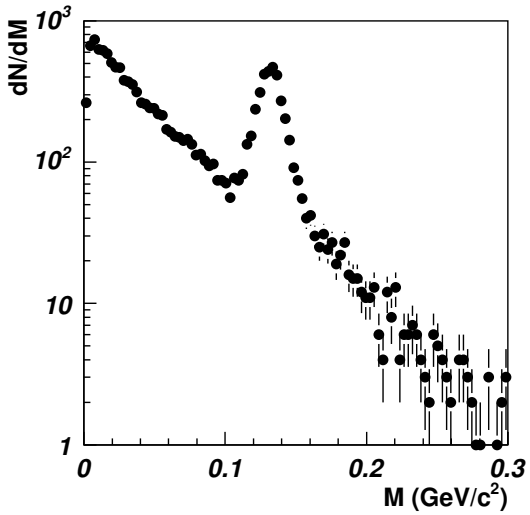

Figure 4.6: Invariant mass distribution of π^0 produced by a 30 GeV/c π^+ secondary beam.

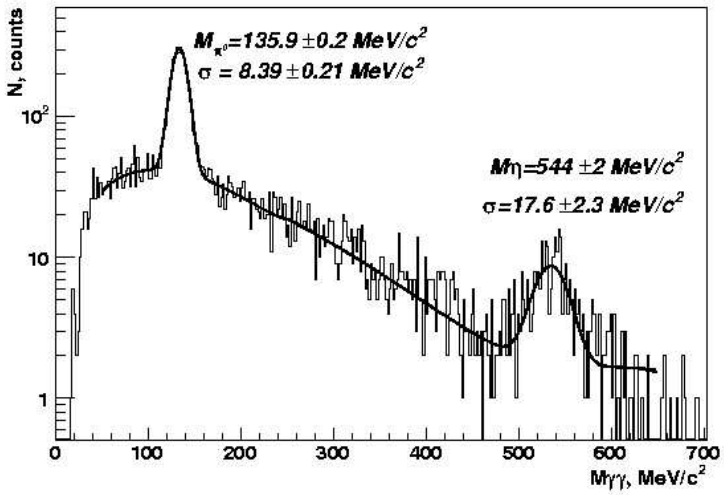

Figure 4.7: Invariant mass spectrum for the inclusive reaction $\pi^- + ^{12}C \rightarrow \pi^0(\eta)\, X$ at 6 GeV/c. The solid line is a fit by a Gaussian distribution plus a cubic polynomial.

and the distance from the carbon target to the PHOS prototype was increased to 4.5 m. We were interested in production of neutral pions via the reaction $\pi^{\pm} + ^{12}C \rightarrow \pi^0 + X$. In Fig. 4.6, the invariant mass distribution of the neutral pairs measured by the PHOS prototype for the 30 GeV/c π^+ beam is shown. A clear peak of 10 MeV/c^2 width centered

at the π^0 mass and superimposed over the combinatorial background is seen. For the 6 GeV pion beam, clear π^0 and η peaks are present (Fig. 4.7).

4.3 Simulation parameters

The exact final geometry of PHOS is implemented in the AliRoot simulation package. The energy deposition in the active materials is calculated by the GEANT3 tracking algorithm and is converted into digitized information similar to experimental raw data. The following steps are performed:

- The algorithm records at each step of the tracking a *hit* composed of the deposited energy, the position, the time and the primary particle which has generated the hit. The deposited energy E_{dep} is converted into a corresponding signal. The mean number of scintillation photons $\langle N_\gamma \rangle$ collected by the APD is calculated as,

$$\langle N_\gamma \rangle = E_{dep} \cdot \widetilde{N_\gamma} \cdot \varepsilon_{\mathrm{APD}} \cdot e^{-At \cdot d} \tag{4.2}$$

  where $\widetilde{N_\gamma} = 4.7 \times 10^4\,\mathrm{GeV}^{-1}$ is the average number of scintillation photons per unit of deposited energy, $\varepsilon_{\mathrm{APD}} = 0.0266$ is the APD photo-efficiency, $At = 0.0045\ \mathrm{cm}^{-1}$ is the attenuation factor of scintillation photons and d is the distance of the hit to the APD. The amplitude $\mathcal{A}$ of the APD signal is calculated from n_γ, randomly selected according to a Poisson distribution with mean value $\langle N_\gamma \rangle$,

$$\mathcal{A} = n_\gamma \cdot G_{\mathrm{APD}} \cdot C \tag{4.3}$$

  where $G_{\mathrm{APD}} = 300$ is the APD photo-electron gain factor and $C = 0.418/\widetilde{N_\gamma}$ is a calibration factor that converts photo-electrons into GeV. Although particles entering the calorimeter develop an electromagnetic shower and thus a huge number of tracks and hits, the PHOS algorithm only stores one hit per primary particle and per active volume. A PHOS hit thus corresponds to the total energy deposited by a given primary particle in a single crystal and the time corresponds to the time at which the particle entered the crystal: a primary particle can generate several hits in different crystals and there can be several hits in a single crystal produced by different primary particles. The energy $E_{\mathrm{d}}^{\mathrm{CPV}}$ deposited by an ionizing particle in the active gas volume of CPV is proportional to the ionization charge Q collected in the nearest anode wire, $Q = BE_{\mathrm{d}}^{\mathrm{CPV}}$. The collected charge is expressed in arbitrary units, and for simplicity B is taken equal to 1. When the track is not perpendicular to the cathode plane, several anode wires can collect the charge which is proportional to the projection of the track onto the CPV cathode plane. The charge distribution

in the cathode plane is calculated according to the electrostatic formula,

$$\sigma(x') = \frac{Q}{\pi} \sum_{i=0}^{\infty} (-1)^i \frac{2i+1}{x'^2 + (2i+1)^2} \tag{4.4}$$

where $x' = x/d$, x is the distance from the point of the anode wire where the charge was deposited to the cathode plane, d is the distance of the anode to the cathode and i is the pad number. This charge distribution function allows us to calculate the charge induced in each pad. For detail see [Bog02]. The CPV hits are calculated from this distribution.

- The simulated deposited energies in the crystals are called *summable digits* and are a copy of the corresponding hits. For hits with a deposited energy lower than a given threshold (we assume $E_{\text{th}} = 1$ MeV) the reference to the primary particle is omitted to reduce the number of primary particles attached to the electronic signal of a single crystal.

- To construct *digits*, related to the electronic signal of a single crystal, first a random Gaussian noise with a mean value of 4 MeV equivalent deposited energy for EMC, and 0.01 charge units for CPV , is added to all active elements, whether they have been hit or not. Summable digits in the same active volume are merged into a single digit by summing all the deposited energies. The time is calculated in a way that mimics the response of a leading-edge discriminator with a rise time of $t_{\text{rise}} = 1$ ns, an energy crossing threshold that defines the time origin, $E_{\text{cross}} = 1$ MeV and a time jitter of $t_{\text{jit}} = 0.5$ ns. Only EMC digits with an energy larger than the 12 MeV noise threshold, and CPV digits with a charge above 0.09 units are recorded. The energies in the EMC are digitized in 16 bits words (which corresponds to a gain of 1.5 GeV/channel and to an overflow at 90 GeV), and the times in 12 bits words (1 ps/channel gain). The charges in the CPV are digitized in 12 bits words (gain of 0.001 units/channel and overflow at 5 units). We define the digit corresponding to a crystal as the set formed by the simulated energy deposited in the crystal, the coordinates of the crystal and the time the crystal was hit.

4.4 Reconstruction algorithm

The reconstruction algorithm treats the EMC and CPV simulated energies (digits) in three steps: production of reconstructed impact points, track segments, and reconstruction of particles. The first step is performed separately on EMC and CPV digits whereas the two last steps combine the information collected by both detectors. The particle identification step could in principle make use of additional information provided by the global tracking

in ALICE. However, this possibility was not yet implemented in the PHOS reconstruction algorithm when most of the particle identification studies were done. Only in Sec. 5.7 we use information from the TPC tracking.

4.4.1 Clustering

The clustering algorithm looks for clusters of neighboring hit crystals to reconstruct the impact point of the particle. Two crystals are considered as neighbors if they have a common side or a common edge. Any crystal with an energy above a chosen threshold and larger than the energy deposited by minimum ionizing particles is taken as a seed of a new cluster. Clusters with several local maxima, which are often produced by overlapping showers, are unfolded following the algorithm described in [ALI99c]. A local maximum is defined as a crystal in the cluster with an energy 30 MeV higher than the energy of the surrounding crystals. The fitting procedure takes into account the measured electromagnetic shower profile. Overlapped clusters are split into a set of reconstructed points with one local maximum, and the energies of individual crystals are shared among the overlapping showers in a proportion given by the fit. The energy E and the position of the clusters in the $(x,\ z)$-plane[3] of the module reference frame, are calculated respectively as the sum of the individual crystal energies e_i, and the energy center of gravity with a logarithmic weight,

$$\bar{s} = \frac{\sum\limits_{\text{digits}} s_i w_i}{\sum\limits_{\text{digits}} w_i}, \tag{4.5}$$

where $\bar{s}$, standing either for $\bar{x}$ or $\bar{z}$, is the coordinate of the cluster center-of-gravity, and s_i, denoting either x_i or z_i, is the coordinate of the individual crystals; the sum extends over all the crystals forming the cluster. The weight w_i is defined by,

$$w_i = \max\left[0,\ p + \log\left(\frac{e_i}{E}\right)\right], \tag{4.6}$$

where p is a parameter empirically determined (4.5 for EMC and 4.0 for CPV). Since the edges of the crystals in a module (except for the central crystal) are not parallel to the momentum of particles emerging from the interaction point, the center of gravity of EMC clusters with energy E is further corrected for the incidence direction $(\theta,\ \phi)$ of the primary particle,

$$\begin{aligned} x' &= x - (A_{inc} + B_{inc} \log E) \sin\phi\,, \\ z' &= z - (A_{inc} + B_{inc} \log E) \cos\theta\,, \end{aligned} \tag{4.7}$$

where the parameters A and B were determined empirically by simulations and are given in Tab. 4.4.1.

[3] x-axis is perpendicular to the beam direction and z-axis is parallel to the beam direction.

A_{inc} (cm)	B_{inc}(cm)
7.02 ± 0.04	0.75 ± 0.01

Table 4.1: Parameters used in Eq. (4.7) and Eq. (4.15) to correct for the incidence angle of the primary particle.

Clusters in EMC are characterized by their multiplicity, which is a function of the particle type, their energy and the selected energy threshold. In Fig. 4.8 the cluster multiplicity is plotted as a function of the energy.

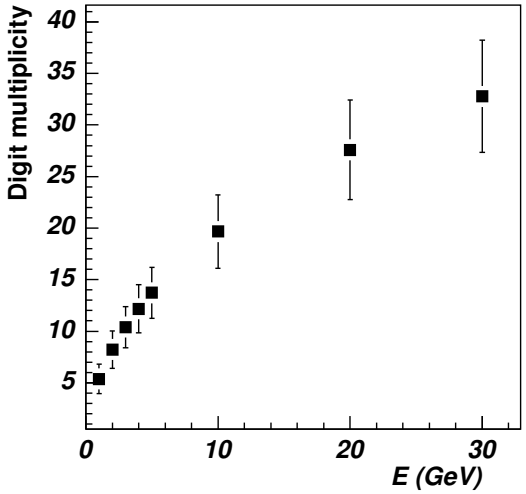

Figure 4.8: Multiplicity of EMC clusters for mono-energetic photons simulated with energy between 1 and 30 GeV. The error bars indicate the width (r.m.s.) of the multiplicity distribution.

A few additional topological parameters which characterize the shape of the clusters are calculated,

- The lateral dispersion d in the (x, z) plane, measured on the surface of the EMC,

$$d = \frac{\sum\limits_{\text{digits}} w_i \left[(x_i - x)^2 + (z_i - z)^2\right]}{\sum\limits_{\text{digits}} w_i}. \tag{4.8}$$

- The shape of the surface defined by the intersection of the cone containing the shower with the front plane of the calorimeter (Fig. 4.9). This surface can be expressed in terms of the covariance matrix,

$$S = \begin{pmatrix} s_{xx} & s_{zx} \\ s_{xz} & s_{zz} \end{pmatrix}, \tag{4.9}$$

where,

$$s_{xx} = \langle (x - \bar{x})^2 \rangle = \frac{\sum\limits_{\text{digits}} w_i x_i^2}{\sum\limits_{\text{digits}} w_i} - \left(\frac{\sum\limits_{\text{digits}} w_i x_i}{\sum\limits_{\text{digits}} w_i} \right)^2 , \tag{4.10}$$

and similar definitions for s_{zz} and s_{zx}. Here $\langle\rangle$ denotes averaging with the logarithmic weights w_i defined by Eq. (4.6), $\bar{x}$ and $\bar{z}$ are the coordinates of the center of gravity of the cluster [Eq. (4.5)] and (x_i, z_i) are the coordinate positions of crystal i. The principal axes of the shower surface are the eigenvectors of the covariance matrix, with eigenvalues λ_1 and λ_2. The geometrical meaning of the principal axes is illustrated in Fig. 4.9.

- The sphericity parameter defined from the eigenvalues λ_1 and λ_2 as,

$$\mathcal{S} = \frac{|\lambda_1 - \lambda_2|}{\lambda_1 + \lambda_2}. \tag{4.11}$$

- The largest fraction of the cluster energy deposited in a single crystal.

- The core energy which is defined as the sum of the energies of the crystal with the largest energy and the neighbour crystals. From the experimentally established shower profile, the fraction of energy deposited by an electromagnetic shower in more distant crystals is less than 2 %. The core energy is thus subject to less fluctuations due to the background or to overlapping showers than the total energy. The time of the cluster is selected as the shortest time among the crystals composing the cluster.

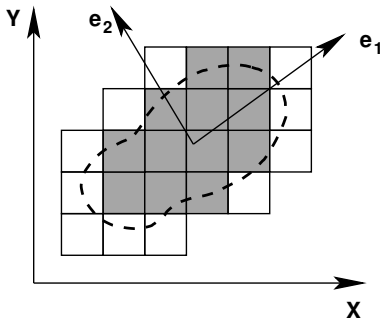

Figure 4.9: Example of a shower profile and its principal axes e_1 and e_2.

A CPV cluster is characterized by the multiplicity induced by a single track, and by its projections N_x and N_z along the x and z directions in the detector reference system given as number of cells. N_x and N_z were measured experimentally during in-beam tests [Bli00], and the reconstruction procedure was tuned to match the experimental data. Typical histograms of N_x and N_z are given in Fig. 4.10.

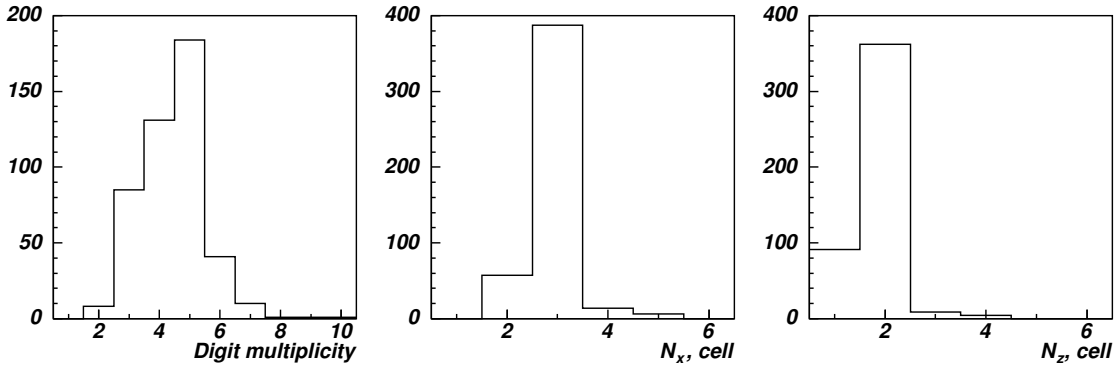

Figure 4.10: Total multiplicity and projections N_x and N_z along the x and z directions of a CPV cluster generated by a single charged track.

4.4.2 Construction of track segments

A track segment in PHOS is composed at most of two reconstructed points, one in CPV and one in EMC. The algorithm searches for all possible pairs of reconstructed points, one in EMC and one in CPV, separated by less than a given distance, taken as $d_{\rm th}^{\rm link} = 10$ cm. For a given EMC reconstructed point, the associated track segment is defined either as the pair constituted by the considered EMC reconstructed point and the closest CPV reconstructed point satisfying the previous condition, or as the EMC reconstructed point alone if there is none CPV point within that distance. A CPV reconstructed point can only be in a single track segment, i.e. can only be attached to a single EMC point.

The simulation, digitization and reconstruction algorithm is illustrated in Fig. 4.11.

4.4.3 Particle identification

Every track segment constitutes the seed of a reconstructed particle. Its energy is taken as the energy of the EMC reconstructed cluster and its momentum is taken either along the direction passing through the EMC and the CPV reconstructed impact points or the direction passing through the EMC impact point and the interaction vertex if there is no CPV impact point in the track segment. The type of the particle is determined according to the parameters characterizing the track segment. Photons are classified in three quality classes, defined with respect to purity. The purity is defined as the ratio of the number of reconstructed particles identified as photons actually produced by photons to the total number of reconstructed particles identified as photons. The following criteria are used for particle identification:

- TOF. The time elapsed between the interaction and the impact of the particle on the calorimeter is calculated from the timing information of the reconstructed points. A variable threshold, depending on the cluster energy and on the particle identifica-

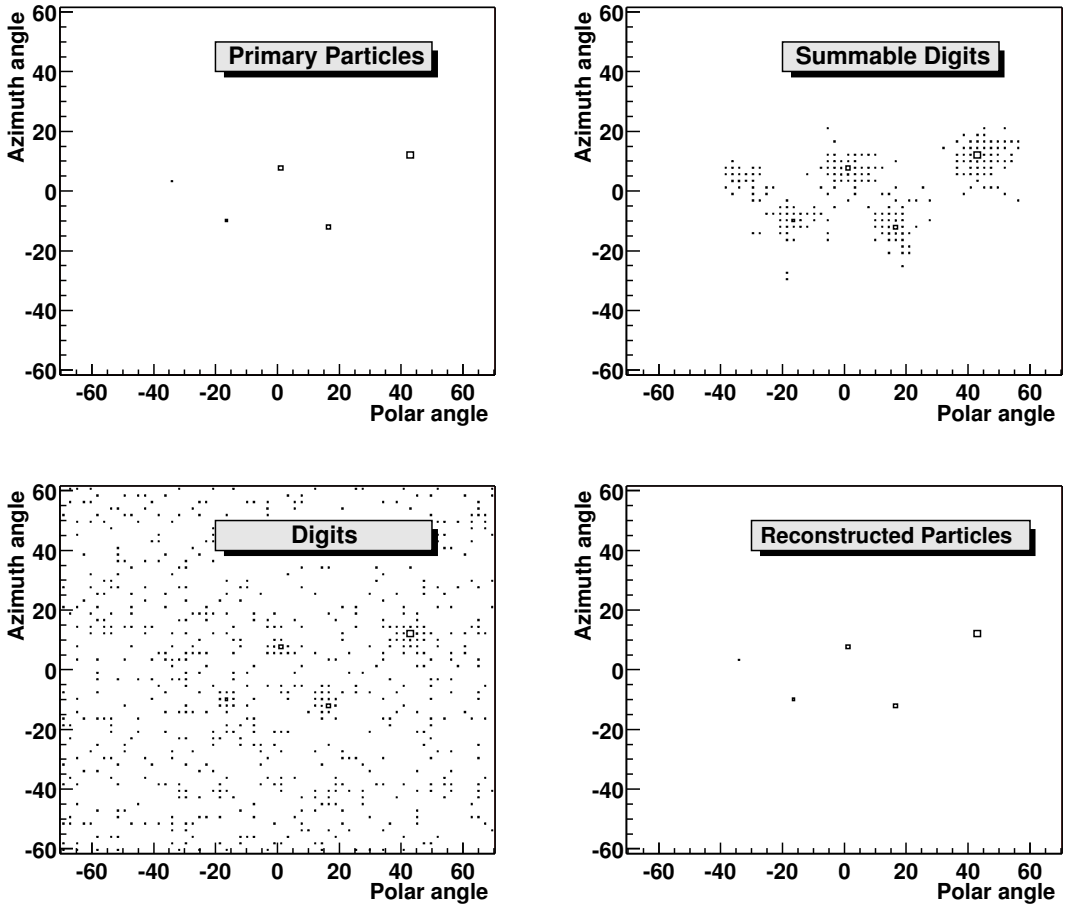

Figure 4.11: Event display for a EMC module represented in its local coordinate system (angles in degrees). The generated event (upper left) contained 5 photons with energy between 1 and 10 GeV. The corresponding crystals with summable energies (upper right), crystals with deposited energy (lower left) and the reconstructed impact points (lower right) are calculated with the PHOS-AliRoot simulation algorithm as explained in the text.

tion quality desired, defines the time boundary between fast particles (photons and electrons) and slow particles (any other massive particle).

- Charged particle rejection. In the case of track segments composed of both EMC and CPV reconstructed points, the distance between the two reconstructed points is compared to a variable threshold depending on the EMC cluster energy and on the desired particle identification quality. Track segments with distance larger or smaller than this threshold are identified as corresponding to neutral particles (photons, neutrons) or charged particles (electrons, charged mesons and protons), respectively.

- Shower shape. The shape of the shower in the calorimeter is a characteristic of the particle type. Two discrimination methods based on the shower shape will be presented below.

More information about particle identification is presented in Chap. 5.

4.5 Detector acceptance

The photon acceptance is defined as the probability that a photon radiated from the interaction point within the rapidity interval $|y| < 0.5$ and azimuthal angle $0 < \phi < 2\pi$ hits PHOS. The PHOS acceptance for photons does depend neither on their transverse momentum nor on their rapidity as seen in Fig. 4.12. The acceptance for π^0- and η-mesons detected in their $\gamma\gamma$ decay channel is defined as the probability that both decay photons hit PHOS when the mesons are radiated from the interaction point within rapidity interval $|y| < 0.5$ and azimuthal angle $0 < \phi < 2\pi$. This acceptance is small at low p_T due to the wide opening angle between the decay photons as observed in Fig. 4.13.

The increase of the acceptance with transverse momentum observed in Fig. 4.14 reflects the decreasing of the relative angle between the decay photons. The π^0 acceptance saturates at $p_T > 20$ GeV/c. The η-mesons acceptance does not reach its maximum value even at 100 GeV/c.

The acceptance as a function of p_T and y in the range $-0.13 < y < 0.13$ can be well fitted by the parametric functions,

$$f(p_T) = (p_0 + p_1 p_T) \exp\left(-\frac{p_T - p_2}{p_3}\right), \quad (4.12)$$

$$g(y) = p_0' - p_1' y^4 \quad (4.13)$$

with the parameters p_i listed in Tabs. 4.2 and 4.3.

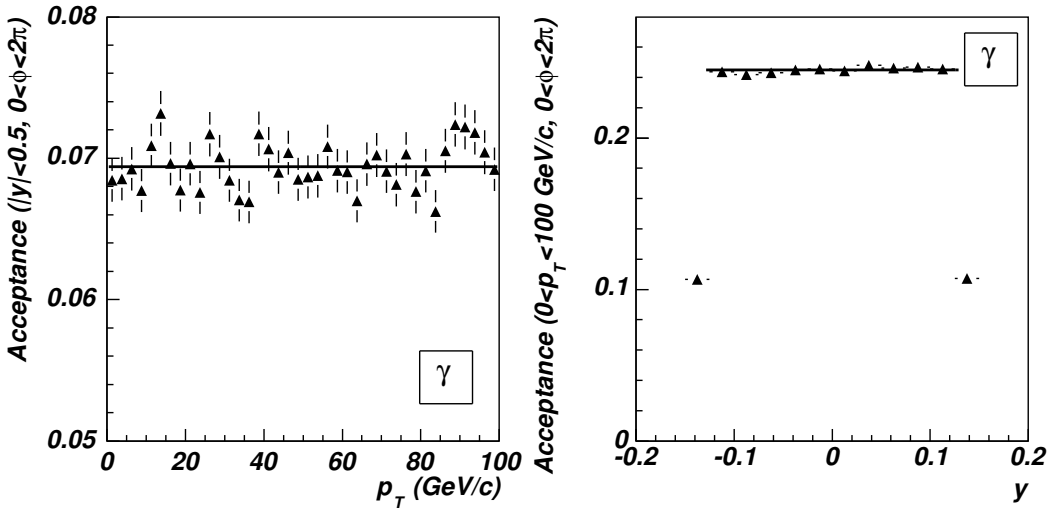

Figure 4.12: Acceptance as a function of p_T (right) and y (left) for γ generated with $0 < p_T < 100$ GeV/c, $0 < \phi < 2\pi$ and $-0.5 < y < 0.5$.

Acceptance vs. p_T	$p_0 \times 10^4$	$p_1(c/\text{GeV})\times 10^4$	p_2 (GeV/c)	p_3(GeV/c)
γ ($p_T < 100$ GeV/c)	694±2			
π^0 ($p_T < 10$ GeV/c)	420±20	13±3	0.55±0.07	1.25±0.16
π^0 ($p_T < 100$ GeV/c)	640±20	0.12±0.27	-14±6	12±4
η ($p_T < 10$ GeV/c)	20±20	13.1±1.5	0.75±0.07	2.3±0.9
η ($p_T < 100$ GeV/c)	196±7	0.52±0.10	2.2±0.8	86.0±9.0

Table 4.2: Parameters of the function $f(p_T)$ of Eq. (4.12) which fits the acceptance vs p_T for γ rays and π^0 and η mesons.

Acceptance vs. y	$p'_0 \times 10^4$	p'_1
γ ($p_T < 100$ GeV/c)	2451±9	
π^0 ($p_T < 10$ GeV/c)	1801±11	393.0±13.0
π^0 ($p_T < 100$ GeV/c)	2324±13	57.0±17.0
η ($p_T < 10$ GeV/c)	348±5	146.0±4.0
η ($p_T < 100$ GeV/c)	828±8	86.0±9.0

Table 4.3: Parameters of the function $g(y)$ of Eq. (4.13) which fits the acceptance vs y for γ rays and π^0 and η mesons.

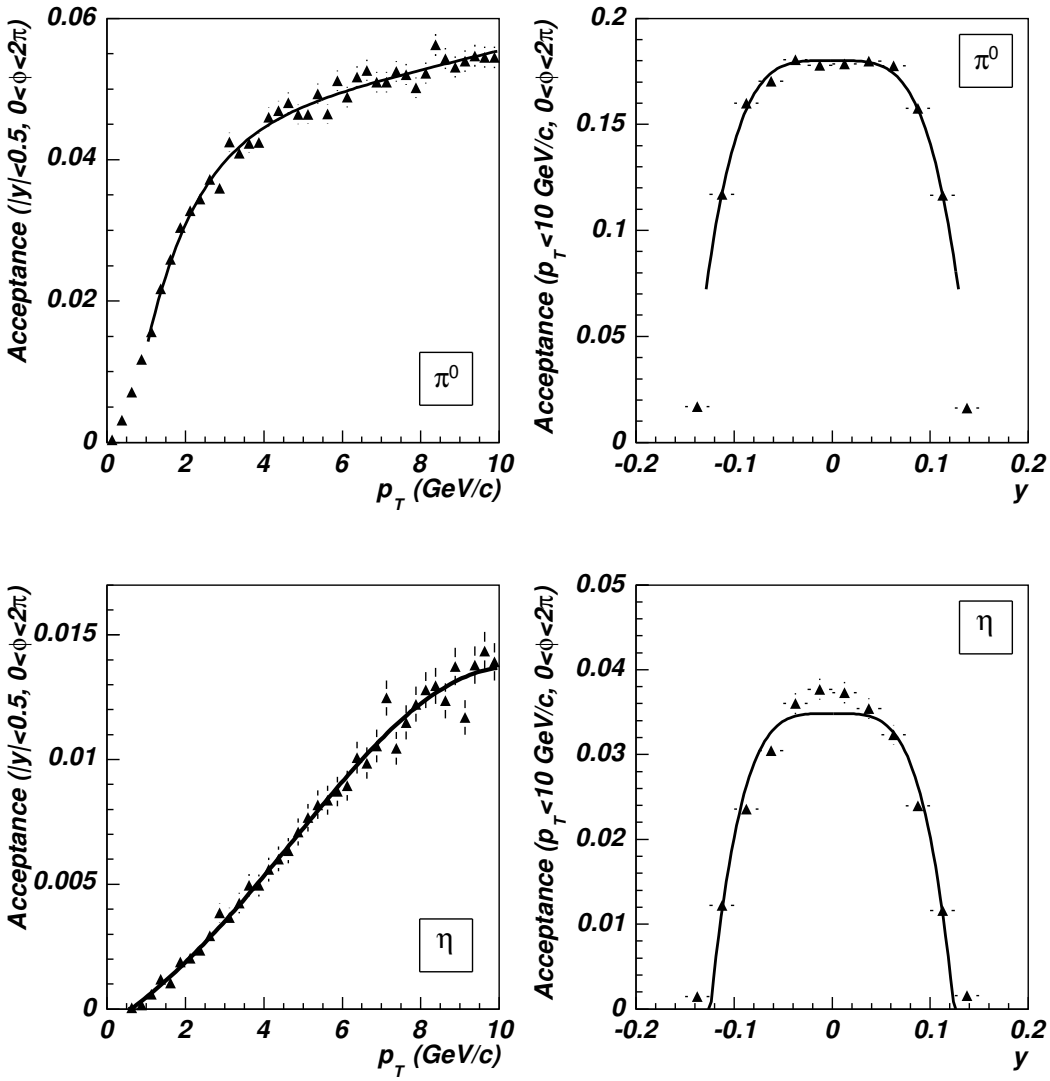

Figure 4.13: Acceptance as a function of p_T (right) and y (left) for low p_T π^0 (up) and η (down). The particles were generated with $0 < p_T < 10$ GeV/c, $0 < \phi < 2\pi$ and $-0.5 < y < 0.5$.

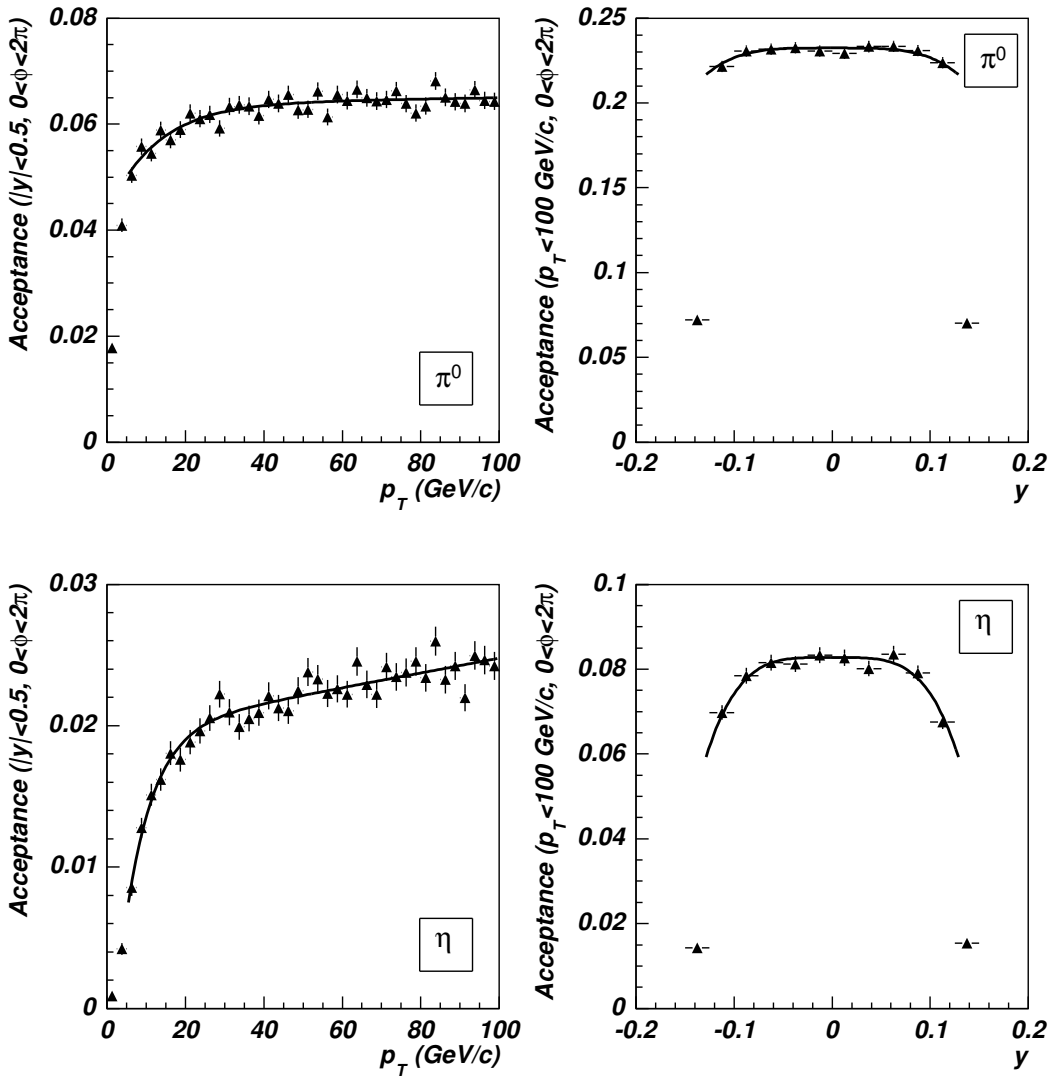

Figure 4.14: Acceptance as a function of p_T (right) and y (left) for high p_T π^0 (up) and η (down) mesons. The particles were generated with $0 < p_T < 100$ GeV/c, $0 < \phi < 2\pi$ and $-0.5 < y < 0.5$.

4.6 Intrinsic performances

I now discuss the response of PHOS to electromagnetic particles and hadrons in a particle free environment and with no other detectors. In the following section we study the response in a dense particle environment (Sec. 4.7) and the effect of the other ALICE detectors (Sec. 4.8).

4.6.1 Response to electromagnetic particles

Among the parameters describing the response of the EMC spectrometer those which play the most important role for photon identification are the energy, position and time-of-flight resolutions. The energy resolution depends on the capability of the spectrometer to collect the energy of the electromagnetic shower, the scintillation efficiency, the light transport through the crystal, the APD photo efficiency and the photo-electron gain-factor. The position resolution depends on the segmentation of the spectrometer and on the energy resolution of the individual EMC crystals.

4.6.1.1 Energy Resolution

The parameters characterizing the energy resolution were tuned to match the calculated response function to measurements performed with electron beams of energy ranging from 0.6 to 4.5 GeV. The central module of an array of 3×3 crystals was irradiated. The energy resolution was determined from the total energy E collected in the array. Figure 4.15-left shows the energy resolution obtained from simulations compared to a fit to the experimental points by Eq. (4.1). The values of the three parameters a, b and c of Eq. (4.1), depend on the simulation parameters and the stochastic term b depends also on the clustering algorithm parameters. The fit values of these parameters are summarized in Tab. 4.4.

	a (GeV)$\times 10^4$	b (GeV$^{1/2}$)$\times 10^4$	$c \times 10^4$
electron beam	220	280	130
static reconstruction	140±300	365±12	67±10
dynamic reconstruction (0.6-10 GeV)	170±20	334±13	71±10
simulation dynamic (0.6-100 GeV)	255±11	272±10	129±2

Table 4.4: Parameters obtained by fitting Eq. (4.1) to the resolution of the energy collected in a 3×3 array of EMC crystals upon the impact of mono-energetic electrons from 0.6 to 4.5 GeV, and of the calculated energy from simulations of mono energetic photons from 0.6 to 10 GeV and from 0.6 to 100 GeV, performed in conditions similar to those of the experiment. In the static reconstruction, the energy was collected in 3×3 array of neighboring crystals whereas in the dynamic reconstruction, the clustering algorithm was applied.

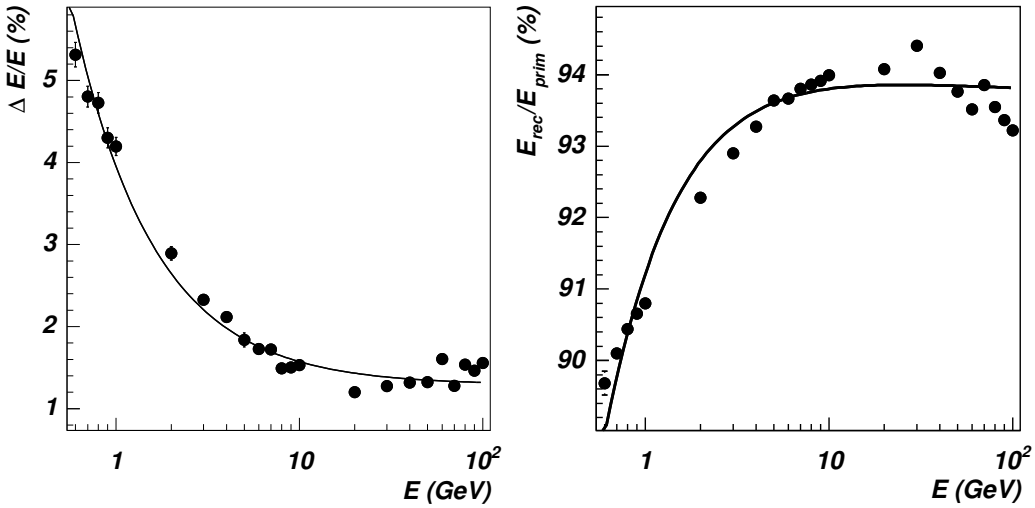

Figure 4.15: Left frame: Energy resolution calculated by simulations of mono-energetic photons (points). The line is a fit to the experimental data by Eq. (4.1). Right frame: Fraction of the energy contained in the cluster obtained by the reconstruction algorithm for simulated mono-energetic photons impinging on the center of a PHOS block (points). The line is a fit to the points by the equation $p_0/E + p_1/\sqrt{E} + p_2$.

When we switched from the static clustering, i.e. summing the energy deposited in the 3×3 array, to the dynamic clustering performed by the reconstruction algorithm, the energy resolution was slightly improved and a lower value of the stochastic term was obtained.

The fraction of the photon energy contained in the cluster found by the reconstruction algorithm was about 94 % on average for photons of energy higher than 10 GeV impinging on the center of a PHOS block as seen in Fig. 4.15. The parameters of the function describing the energy resolution are reported in Tab. 4.4. For photon energies larger than 10 GeV the constant term dominates and the resolution remains about 1.3 %.

We conclude from this study that photons can be satisfactorily measured up to energies of the order of 100 GeV. The yield will decrease below the limit of statistical significance at higher energies according to the LHC running conditions and expected cross sections extrapolated from the systematics (see Ref. [Aph02] and Chap. 6).

4.6.1.2 Position Resolution

The impact position in PHOS was reconstructed by calculating the position of the center of gravity of the reconstructed cluster as described in Sec. 4.4.1. This position was further corrected for the incidence direction of the impinging photon according to the Eq. (4.7).

The shift of the reconstructed impact point with respect to the photon impact onto the EMC surface was simulated for several photon energies, from 1 to 50 GeV and photon incidence angles, $\alpha = 0°$, $3°$, $6°$ and $9°$. Figure 4.16 shows the difference between the

reconstructed point $x_{\rm rec}$ and the impact coordinate $x_{\rm in}$ versus $\sin\alpha$. The dependence with $\sin\alpha$ of the shift $x_{\rm rec} - x_{\rm in}$ was parametrized as,

$$x_{\rm rec} - x_{\rm in} = t_{\rm eff} \sin\alpha, \tag{4.14}$$

where $t_{\rm eff}$ is the effective maximum depth at which the shower develops in the crystal for oblique photon tracks. The energy dependence of $t_{\rm eff}$ is observed in Fig. 4.16 and is described by the function

$$t_{\rm eff} = A_{inc} + B_{inc} \log E, \tag{4.15}$$

where the photon energy E is measured in GeV and parameters A_{inc} and B_{inc} are given in Tab. 4.4.1.

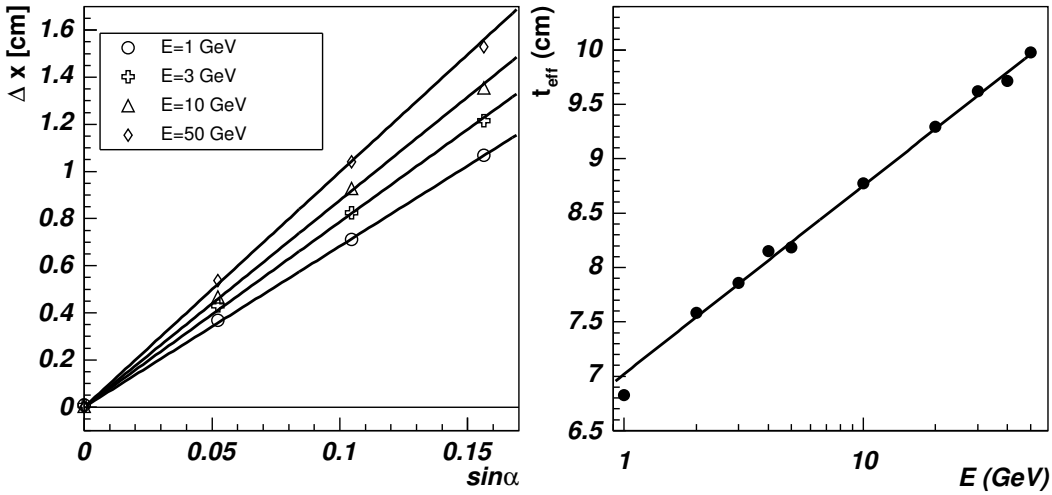

Figure 4.16: Left frame: Difference between the reconstructed impact point position $x_{\rm rec}$ and the impact coordinate $x_{\rm in}$ in a PHOS module versus the $\sin\alpha$ for incidence angles $\alpha = 0°$, $3°$, $6°$ and $9°$ and for photon energies of 1, 3, 10 and 50 GeV. Right frame: Dependence of the effective maximum depth of the shower with photon energy.

The position of the reconstructed points was corrected for the obliquity effect according to Eq. (4.7).

The width of the $x_{\rm rec} - x_{\rm in}$ distribution, which defines the spatial resolution, was studied for several incidence angles and photon energies and the results are shown in Fig. 4.17. The improvement of the position resolution with the photon energy is mostly a consequence of the increase of the cluster multiplicity and thus of the more accurate determination of the cluster center of gravity. The position resolution depends strongly on the incidence angle. The function

$$\sigma_{x,z} = \sqrt{A_{x,z}^2 + \frac{B_{x,z}^2}{E}} \tag{4.16}$$

was fitted to the simulated position resolution for photons from the interaction vertex illuminating entirely a PHOS module; this is equivalent to an incidence angle with the perpendicular to the surface of the EMC modules continuously distributed between 0° and 8.75°. The parameters obtained by fitting Eq. (4.16) to the position resolution for photons between 1 and 50 GeV and for the different incidence angles plotted in Fig. 4.17 are reported in Tab. 4.5.

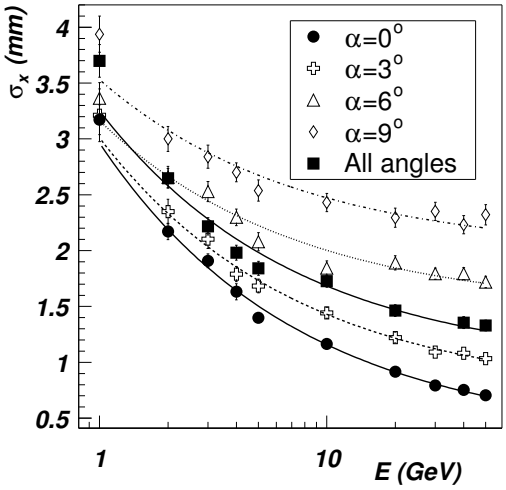

Figure 4.17: Position resolution versus the photon energy for incidence angle $\alpha = 0°$, 3°, 6°, 9° and for a uniformly distributed incidence angle.

α	A_x (cm)	B_x (cm GeV$^{1/2}$)
0°	0.032	0.264
3°	0.070	0.231
6°	0.147	0.170
9°	0.198	0.155
random $(0-9°)$	0.096	0.229

Table 4.5: Parameters A_x and B_x of Eq. (4.16) for the incidence angles $\alpha = 0°$, 3°, 6° and 9° as well as for uniformly distributed incidence angles.

4.6.2 Response to hadrons

Hadrons produced at LHC energies are minimum-ionizing particles (MIP). Therefore, they deposit in the EMC a constant energy that depends only on the amount of traversed material. The average value of the energy deposited in a single EMC module has been estimated to be about 227 ± 3 MeV from GEANT3 simulations of charged pions with energy between 0.5 and 10 GeV, emitted from the ALICE IP and irradiating one EMC module as shown in Fig. 4.18. However, about the 51 % of the hadrons deposit an energy

larger than 350 MeV and therefore give a trigger for the calorimeter and develop a shower through hadron-nucleus interactions.

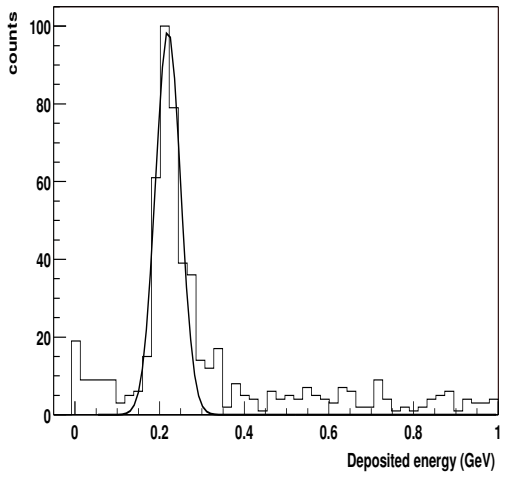

Figure 4.18: Energy deposited in a single EMC module calculated by GEANT3 simulations by charged pions of energy between 0.5 and 10 GeV, emitted from the ALICE IP and irradiating one EMC block.

With anti-protons and anti-neutrons, the situation is particular, since these particles annihilate inside the crystals and may deposit more energy than protons and neutrons. As the annihilation of anti-nucleons produces most likely charged pions, we do not expect that anti-nucleons deposit the 2 GeV energy corresponding to the mass of the two annihilated baryons. Moreover, since anti-nucleons travel a given distance before annihilating (the nuclear interaction length in $PbWO_4$ is 19.5 cm), the impact position obtained from the clustering algorithm for oblique tracks is different from the true impact position. This effect deteriorates the identification of anti-protons by correlating hits in the CPV and EMC.

The response of PHOS to hadrons depends on several factors like the hadron type and energy and the detector occupancy by other particles. The spectrum of primary hadrons can be obtained by unfolding the spectrum of reconstructed hadrons with the help of the reconstructed energy E_{rec} versus the primary energy E_{prim}; however, this unfolding has not been done yet.

4.6.3 Time of flight

At the time this study was done no TOF measurement existed; therefore, we based our study exclusively on simulations. The TOF resolution depends on the jitter of the time of the trigger (START signal) and the time given by the EMC crystal (STOP signal). In our simulations we have neglected the jitters of the start time. With these assumptions

a resolution of 500 ps is achieved which compares well with the TOF resolution achieved with the PHENIX calorimeter [Aph03].

The TOF resolution required to discriminate photons and electrons from massive particles can be deduced from Fig. 4.19. The application of the TOF criterion to identify photons rejects heavier particles with an efficiency which depends on the TOF resolution. This is illustrated by the spectra of identified photons for different TOF resolutions presented in Fig. 4.20.

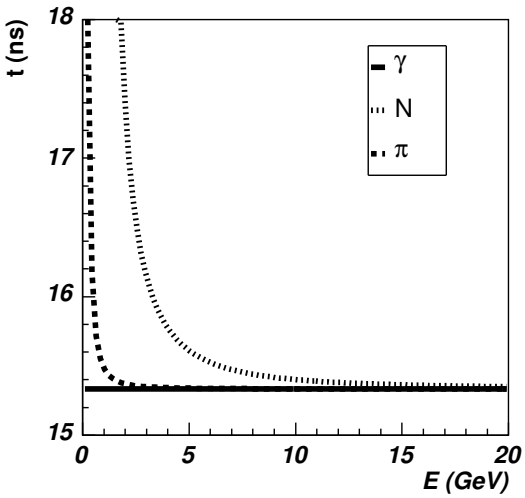

Figure 4.19: Time of flight of photons, π-mesons and nucleons from the interaction point to the PHOS surface versus their energy.

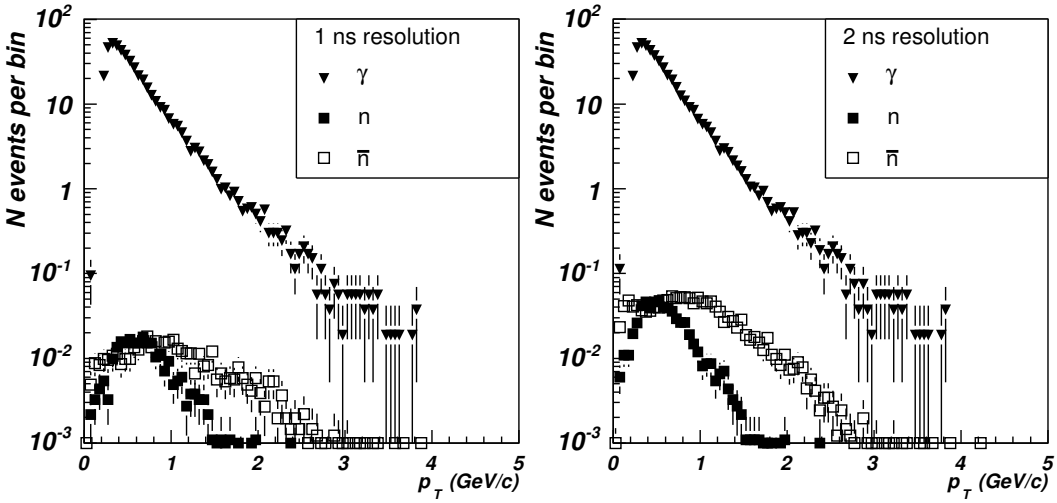

Figure 4.20: Spectra of photons (▼), neutrons (■) and anti-neutrons (□) generated by central Pb-Pb HIJING events, identified as low purity photons by the TOF criterion (see Sec. 5.2) for time resolutions of 1 and 2 ns.

4.6.4 CPV performance

The CPV detector is sensitive to any particle that ionizes the CPV gas volume. Therefore, the CPV can detect charged particles with almost any momentum. The only parameter characterizing the response of the CPV is the position resolution of charged particle tracks passing through the detector.

The impact position on the CPV is reconstructed directly as the center of gravity of the cluster of neighboring pads with non-zero deposited energy. In-beam tests were carried out at the CERN PS accelerator with beams of different charged particles (electrons, hadrons and muons) in the momentum range 1 - 5 GeV/c [Bli00]. To measure the position resolution experimentally, a gas strip-detector with position resolution of 60 μm was used as a reference detector. The effective spatial resolution of CPV was measured to be $\sigma_x = 0.138$ mm and $\sigma_z = 0.154$ mm. AliRoot simulations reproduce the coordinate resolution of the CPV as observed in Fig. 4.21.

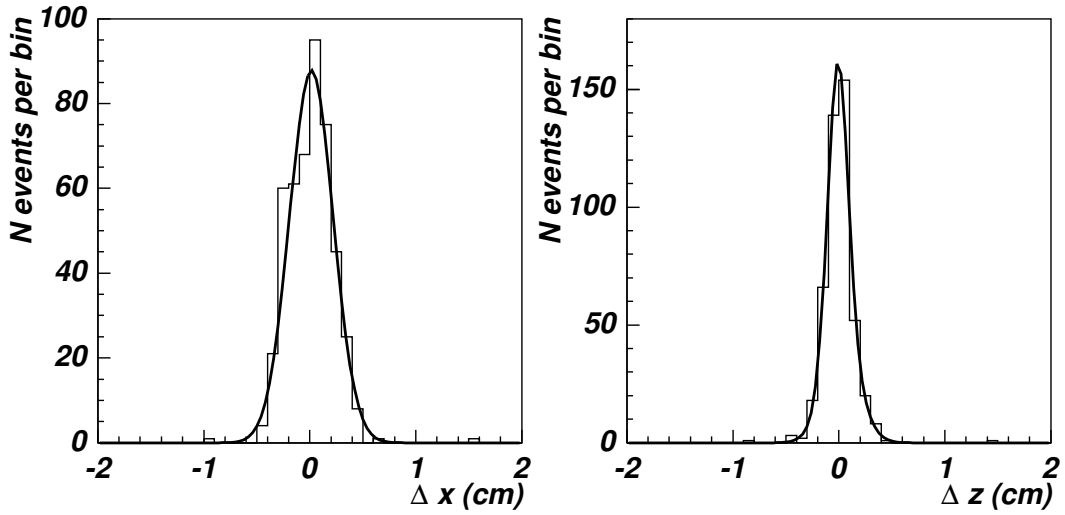

Figure 4.21: Difference between the exact and reconstructed impact point on the CPV. The plot for the x-axis (across the anode wires) is fitted by a single Gaussian distribution, and for the z-axis (along the anode wires) is fitted by a sum of two Gaussian distributions [Bli00].

4.7 Modifications due to the heavy-ion environment

In the high particle multiplicity environment created in ALICE by heavy-ion collisions, the energy and position resolution of EMC will deteriorate. The importance of this degradation depends obviously on the occupancy of the EMC, the larger the occupancy the more probable the overlapping of electromagnetic and hadronic showers. This effect has been studied by embedding mono-energetic photons in a central heavy-ion collision event. The central event was generated by HIJING with the charged particle density at

central rapidity taken as 8,000. The energy resolution and the fraction of reconstructed energy are displayed in Fig. 4.22. Because of shower overlapping, the energy resolution is noticeably degraded in the heavy-ion environment, specially for low energy photons. The new parameters fitting the energy resolution versus the photon energy by Eq. (4.1) are

$$a = 0.00(6)\ \text{GeV}, \quad b = 0.0593(12)\ \text{GeV}^{1/2}, \quad c = 0.0136(2). \tag{4.17}$$

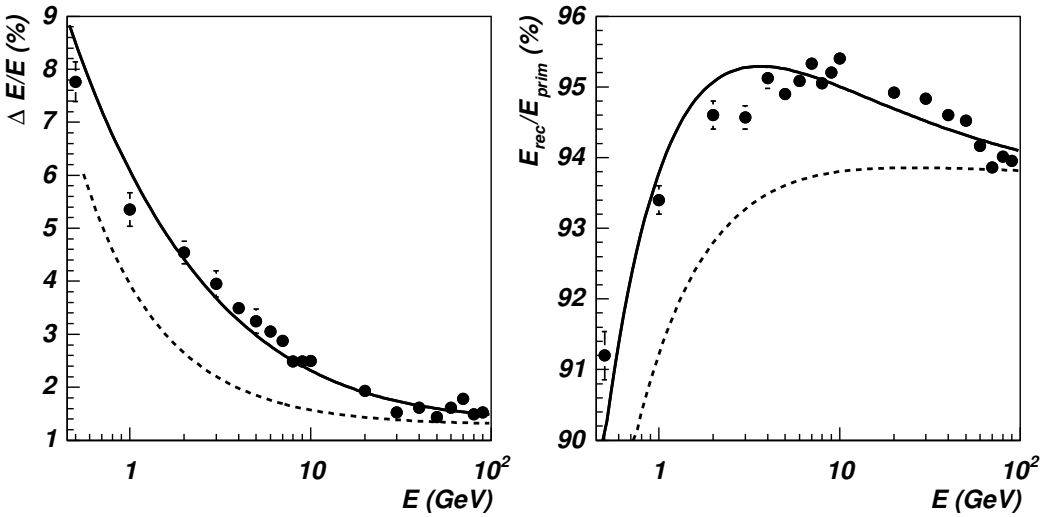

Figure 4.22: Energy resolution (left) and fraction of energy contained in the cluster (right) found by the reconstruction algorithm for simulated mono-energetic photons impinging on the center of a PHOS block and embedded in a central heavy-ion collision environment with charged particle density at mid-rapidity of 8,000. The dashed curves represent the values obtained for photons in a particle free environment. Solid lines on the left and right figures are a fit to the points by Eq. (4.1) and equation $p_0/E + p_1/\sqrt{E} + p_2$, respectively.

4.8 Modifications due to the ALICE environment

The performance of PHOS in ALICE will be worse than standalone due to several effects like conversion of photons in the material between the interaction point and PHOS and production of secondary particles out of the IP. Two detector configurations have been considered, one in which there are no detectors between the TPC and PHOS, called the configuration with holes, and a second one in which the TRD and TOF are present in front of PHOS, called the configuration without holes. In Ref. [Del01] the study of the influence on the energy resolution of material in front of PHOS for the configuration with holes is presented. Writing the ratio of the resolution with the material of the configuration with

	without holes	with holes
Radiation Length	$0.5X_0$	$0.2X_0$
Absorption Length	$0.14\lambda_I$	$0.05\lambda_I$

Table 4.6: Radiation and absorption length average values obtained from Fig. 4.23, not taking into account the contribution from the central TPC electrode at $\theta = 90^o$.

holes and without any material (PHOS standalone) as:

$$\frac{\sigma_{\rm E}^{\rm w}}{\sigma_{\rm E}^{\rm wo}} = 1 + d, \tag{4.18}$$

we find that the degradation parameter d scales approximatively with two times the interaction probability, $d \sim 2P_{\rm I}$. The interaction probability is related to the material thickness X by:

$$\begin{aligned} P_{\rm I}^{\gamma} &= 1 - e^{-\frac{X}{X_0}\frac{7}{9}} \text{ for photons,} \\ P_{\rm I}^{\rm e} &= 1 - e^{-\frac{X}{X_0}} \text{ for electrons.} \end{aligned} \tag{4.19}$$

As there are also issues concerning the configuration with holes, we have studied how the material of TRD and TOF detectors in front of PHOS will affect its response function [Cam01]. In Fig. 4.23, we show the absorption and radiation length as a function of the polar angle θ for both configurations and in Tab. 4.6 we list the average values of these two quantities. The irregularities seen in the figure are mainly due to ITS in the configuration with holes and to the TRD frame in the configuration without holes. The contribution of the frame of the central electrode of the TPC is clearly seen as a peak at $\theta = 90^o$ of more than one radiation length. If we neglect the contribution from this electrode, we conclude that the absorption and radiation lengths in the configuration without holes are about 2.5 and 2.8 times larger than in the configuration with holes, respectively.

In the following figures, the effect of the additional material in the configuration without holes is shown. In Fig. 4.24 the number of reconstructed particles in PHOS is plotted for both configurations. In the configuration without holes, we clearly observe a decrease of the number of reconstructed particles due to the absorption in the TRD and TOF material. In Figs. 4.25 and 4.26 we represent the photon and π^0 reconstructed spectra up to 10 GeV for both configurations for central HIJING events (Pb-Pb collisions at $5.5A$ TeV, $b < 2$ fm). In the configuration without holes, we lose about 20 % of the photon detection efficiency and 20-40 % of the π^0 detection efficiency when we compare with the configuration with holes. For high-energy photons from 10 to 40 GeV, the effect of the TRD and TOF material is similar to the one observed at lower energies, as seen in Fig. 4.27.

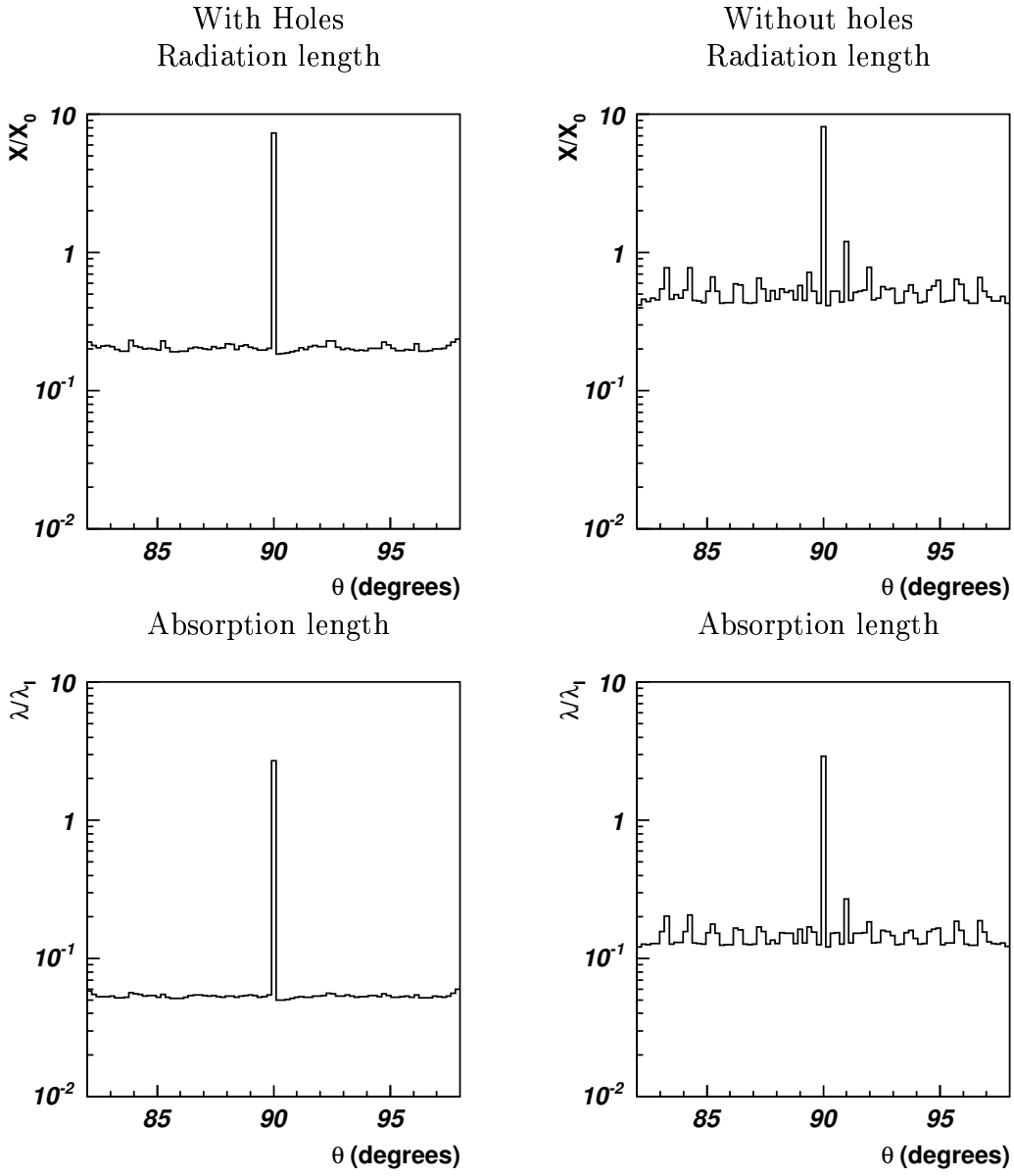

Figure 4.23: Amount of material in radiation (upper) and absorption (lower) length units from the IP to the PHOS blocks as a function of the polar angle θ for the configurations with (left) and without (right) holes.

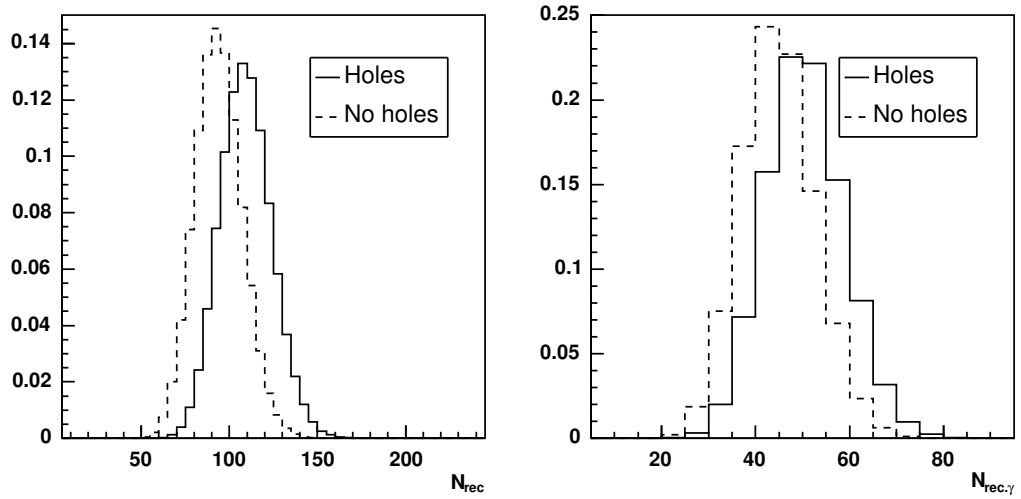

Figure 4.24: Distributions of all reconstructed particles (left) and reconstructed photons (right) in PHOS for central HIJING events of Pb-Pb collisions at $5.5A$ TeV and for the configurations with (solid line) and without (dashed line) holes.

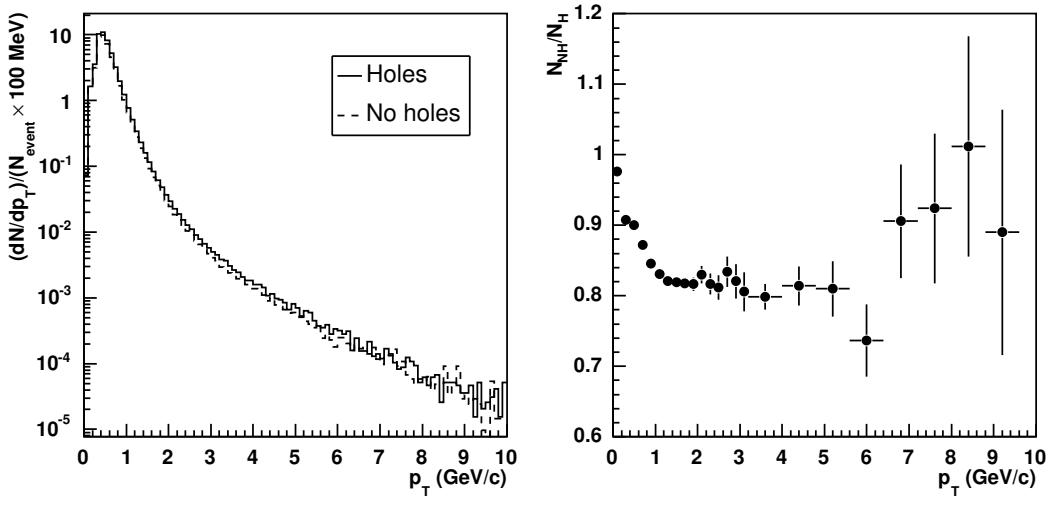

Figure 4.25: Left frame: Number of reconstructed photons per event (central Pb-Pb collisions at $5.5A$ TeV) for the configurations with (solid line) and without (dashed line) holes. Right frame: Ratio of the reconstructed spectra in the configuration without holes to that in the configuration with holes.

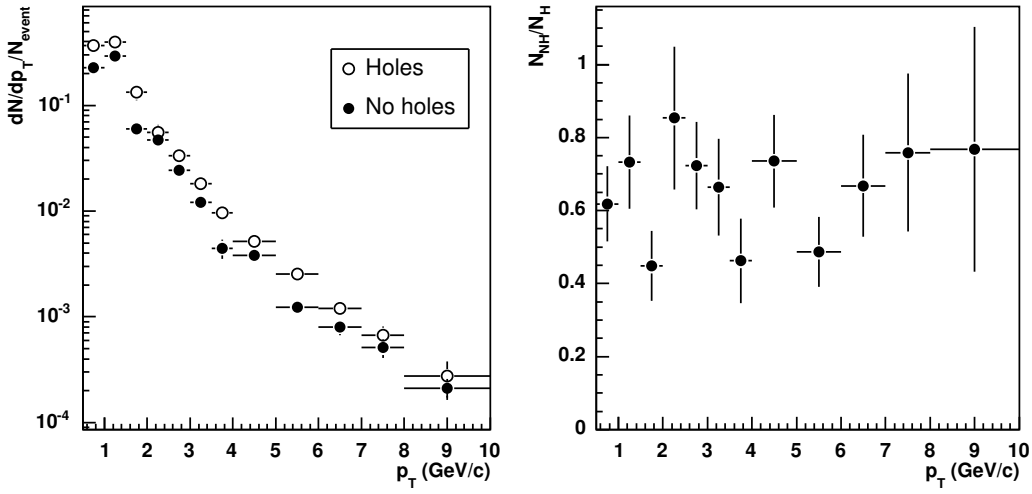

Figure 4.26: Left frame: Spectrum of reconstructed π^0 per event (central Pb-Pb collision at 5.5A TeV) for the configurations with (○) and without (●) holes. Right frame: Ratio of the reconstructed spectra for the configurations with and without holes.

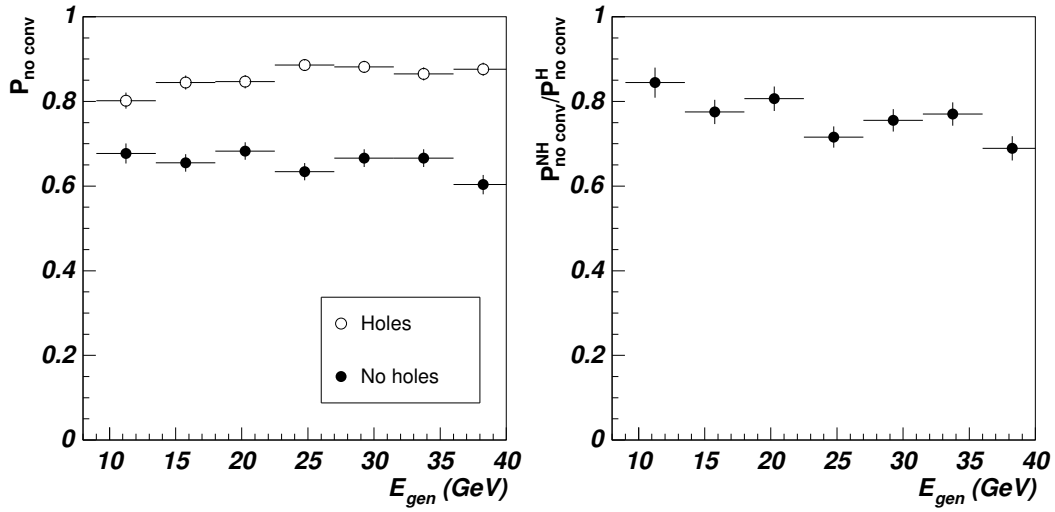

Figure 4.27: Left frame: Probability that high-p_T photons do not convert in the material in front of PHOS, calculated as the ratio of the number of photons that arrive to PHOS to the number of generated photons for the configurations with (○) and without (●) holes. Right frame: Ratio of the non conversion probabilities for the configurations without and with holes. Photons have been generated with energy uniformly distributed from 10 to 40 GeV.

In which follows, the ALICE environment refers to the configuration with holes except in Sec. 5.7 where I discuss how high-energy photons converting into $\gamma \rightarrow e^+e^-$ in the TRD and TOF material can be identified.

4.9 Conclusions

The PHOS detector has a good capability of detecting and identifying photons, electrons and π^0-mesons, and of measuring their 4-momenta with high resolution.

PHOS simulations reproduce in beam experimental data as confirmed by the comparison of simulated and measured energy resolution of PHOS arrays. Reconstruction algorithms of PHOS have been tuned to reduce systematic errors in measuring the impact coordinates and energy of the reconstructed clusters. A HIC environment produces a degradation of the photon energy resolution of a few percent. The ALICE environment produces the absorption of about 10 % and 30-40 % of photons for the configurations with and without holes, respectively.

Chapter 5

Particle identification

I discuss in this chapter the details of particle identification with PHOS and I present several methods of particle identification that rely on the three different identification procedures described in Sec. 4.4.3, which are treated in length below.

5.1 Charged particle identification with the CPV

Showers in the PHOS electromagnetic calorimeter (EMC) can be initiated by both photons and charged particles. Electromagnetic charged particles (electrons or positrons) produce electromagnetic showers in the calorimeter, while charged hadrons produce hadronic showers and signals of minimum ionizing particles. The CPV capability to identify showers produced by charged particles rely on the matching of the positions of the reconstructed points in the CPV and in the electromagnetic calorimeter. We simulated uniform energy distributions from 0 to 100 GeV of electrons, charged pions and photons in the ALICE environment. We calculated the width σ of the distributions of the relative distance $\Delta x_{CPV-EMC}$ between both reconstructed points and we found that σ is less than 1 cm for electrons and larger than 1 cm for pions, as shown in Figs. 5.1 and 5.2. In these figures, the main contribution comes from high-energy particles, which are hardly deflected by the magnetic field, and thus the distributions are centered in the x-axis origin (axis across the beam). For electrons with energies around 1 GeV, the $\Delta x_{\text{CPV-EMC}}$ mean value is about 5 cm and decreases with the energy. The relevant efficiencies of charged particles are shown in Fig. 5.3. The probability of misidentifying photons as charged particles is about 10 % in the whole energy range due essentially to photon conversion into e^+e^- pairs in the material in front of PHOS, as found in Sec. 4.8. The probability of electron identification as charged particles is only about 90 % due to bremsstrahlung in the material before the CPV. The probability of identification of charged pions as charged particles is still lower than in the case of electrons because pions are minimum ionizing particles and deposit only part of their energy in the EMC.

The behaviour of electromagnetic particles and hadrons is different because electro-

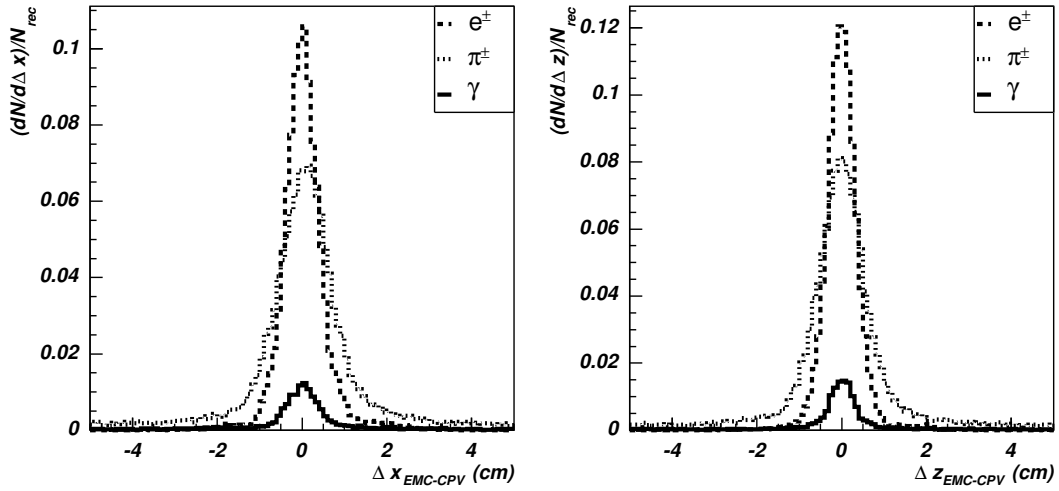

Figure 5.1: Distribution of the distance between the EMC and the CPV reconstructed points, projected onto the EMC surface on the axes across the beam (left) and along the beam (right). The simulations were performed within a realistic ALICE environment and the particles were generated with a uniform energy distribution from 0 to 100 GeV. The distributions normalized to the total number of reconstructed points are shown for e^+e^- pairs from converted single photons (solid line), single e^+ and e^- (dashed line) and single π^+ and π^- (dotted line).

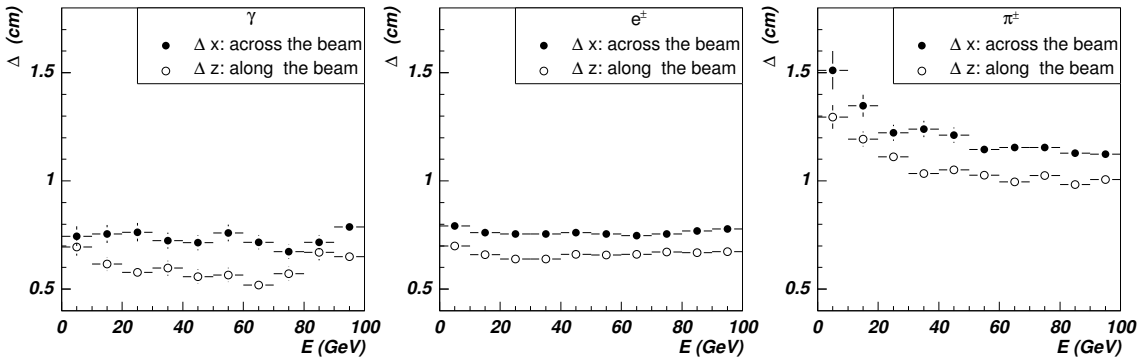

Figure 5.2: Widths of the distributions of the distance between the reconstructed points in the EMC and the CPV (see caption of Fig. 5.1 for more details), across (•) and along (○) the beam direction versus the reconstructed energy for e^+e^- pairs from converted single photons (left), single e^+ and e^- (middle) and single π^+ and π^- (right). The vertical error bars are the uncertainty of the width obtained by a Gaussian fit to the distributions.

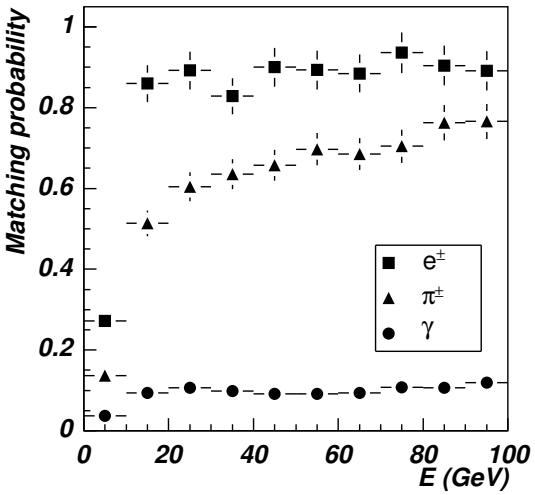

Figure 5.3: Probability to accept the EMC reconstructed impact point as a charged particle versus the incident particle energy for photons (circles), electrons (squares) and charged pions (triangles).

axis	a	b	c
x	0.64	0.44	0.30
z	0.54	0.14	0.42

Table 5.1: Parameters of Eq. (5.1) obtained by fitting the standard deviation of the distance between the reconstructed points in the CPV and EMC of Fig. 5.4.

magnetic particles deposit essentially all their energy in the EMC while hadrons deposit only a small fraction of it. To identify charged hadrons we have to rely on the distance between the impact points in the CPV and the EMC. The standard deviation of this distance for pions, shown in Fig. 5.4, can be parametrized as

$$\sigma_i = a_i + \exp(b_i - Ec_i)\,, \tag{5.1}$$

where σ is expressed in centimeters, the reconstructed energy E in GeV, the index i stands for x or z, and the parameters a, b and c are given in Tab. 5.1.

Neutral particles are identified with a purity level. Three different levels of purity were defined: low, medium and high which correspond to the conditions,

$$\begin{aligned} |x_{\mathrm{EMC}} - x_{\mathrm{CPV}}| &> \kappa\sigma(\Delta x), \\ |z_{\mathrm{EMC}} - z_{\mathrm{CPV}}| &> \kappa\sigma(\Delta z), \end{aligned} \tag{5.2}$$

with $\kappa = 1$, 2 and 3 for low, medium and high purity levels, respectively.

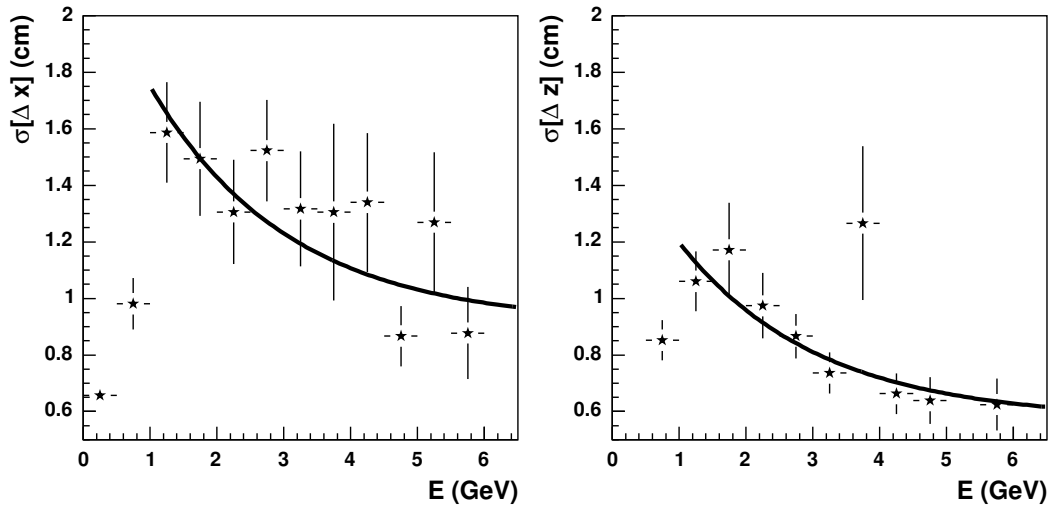

Figure 5.4: Standard deviation of the distance between the reconstructed impact points in the CPV and EMC along the x-axis and z-axis (along the beam) for charged pions produced with a uniformly distributed energy from 0 to 100 GeV vs the reconstructed energy. The lower points between 0 and 1 GeV correspond to minimum ionizing particles which have larger energy and therefore smaller widths.

5.2 Time of flight discrimination

A reconstructed particle is classified as photon-like if its time of flight is consistent with that of a photon, i.e. 15.3 ns. Two identification purity levels of photon-like particles are considered, high-purity (TOF $<$ 16.5 ns) and low-purity (TOF $<$ 17.0 ns)[1].

5.3 Shower shape analysis by the PCA approach

The shower generated in the calorimeter is characterized by the following seven parameters, defined in Sec. 4.4.1: lateral dispersion, ellipse axes, sphericity, core energy, largest fraction of energy deposited in a single crystal and multiplicity. Although we could define selection criteria on this multidimensional surface, it would be a tedious task with no guarantee of finding an absolute minimum. A set of seven statistically independent parameters, referred to as the principal components, can be obtained by diagonalizing the covariance matrix of the original seven parameters. Showers produced by different kind of particles can be identified in the space of the principal components following an approach known as the Principal Component Analysis (PCA) [Bru79]. The two most significant components, i.e. the two components corresponding to the largest eigenvalues of the covariance matrix, are used to identify showers in the 2-dimensional space defined

[1]For the CPV and PCA criteria we define a third purity level, medium. When we combine the three criteria and define the medium purity level, the TOF criterion is the same for medium and low purity levels.

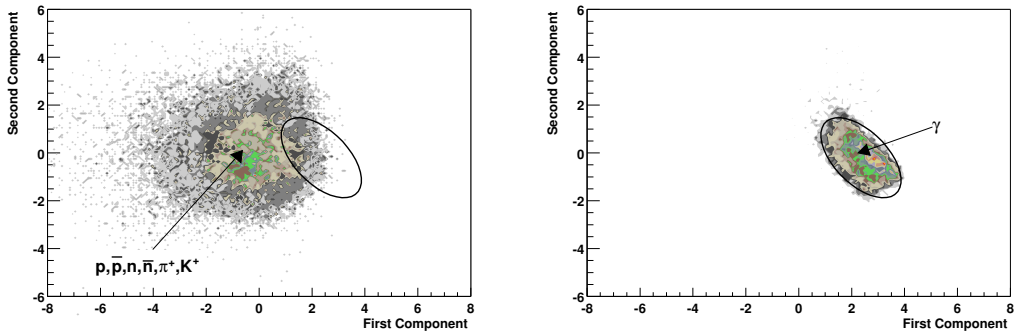

Figure 5.5: Scatter plots in function of the two first principal components for showers of single photons (right hand side) and charged pions, charged kaons, protons, anti-protons, neutrons and anti-neutrons (left hand side plot) of transverse momentum uniformly distributed between 0.5 and 100 GeV/c. The contours on the figures correspond to photon identification with a 95 % of efficiency and a 79 % of purity.

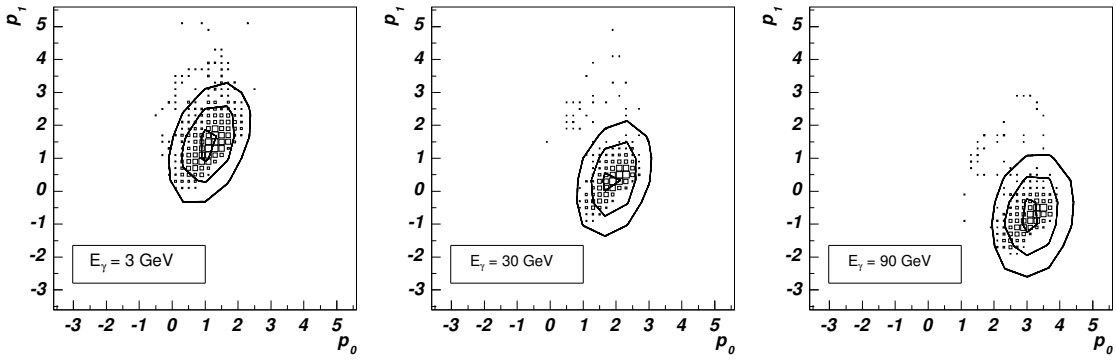

Figure 5.6: Photon shower distribution in the space defined by the two first principal components (p_0, p_1). Photon showers of three energies have been considered: 3, 30 and 90 GeV. The three different ellipses in each plot are the contours corresponding to high (smallest ellipse), medium and low (largest ellipse) purity.

by these components, as displayed in Fig. 5.5.

I defined contours depending on the EMC cluster energy and on the level of purity desired which are shown in Fig. 5.6. Showers inside these contours are tagged as photons, and those outside them as different from photons.

The distributions of Fig. 5.6 were fitted by 2-dimensional Gaussian functions

$$f(p_0,\, p_1) = \exp[-R(p_0,\, p_1)]\,,$$
$$R(p_0,\, p_1) = \left(\frac{p_0 - x_0}{a}\right)^2 + \left(\frac{p_1 - y_0}{b}\right)^2 + C\frac{(p_0 - x_0)(p_1 - y_0)}{a \cdot b}\,, \tag{5.3}$$

where the parameters a, b, c, x_0 and y_0 as a function of the reconstructed energy are shown in Fig. 5.7. These parameters were fitted by the function $f(E) = q_0/\sqrt{E} + q_1 E + q_2 E^2 + q_3$, with the values of q_i given in Tab. 5.2.

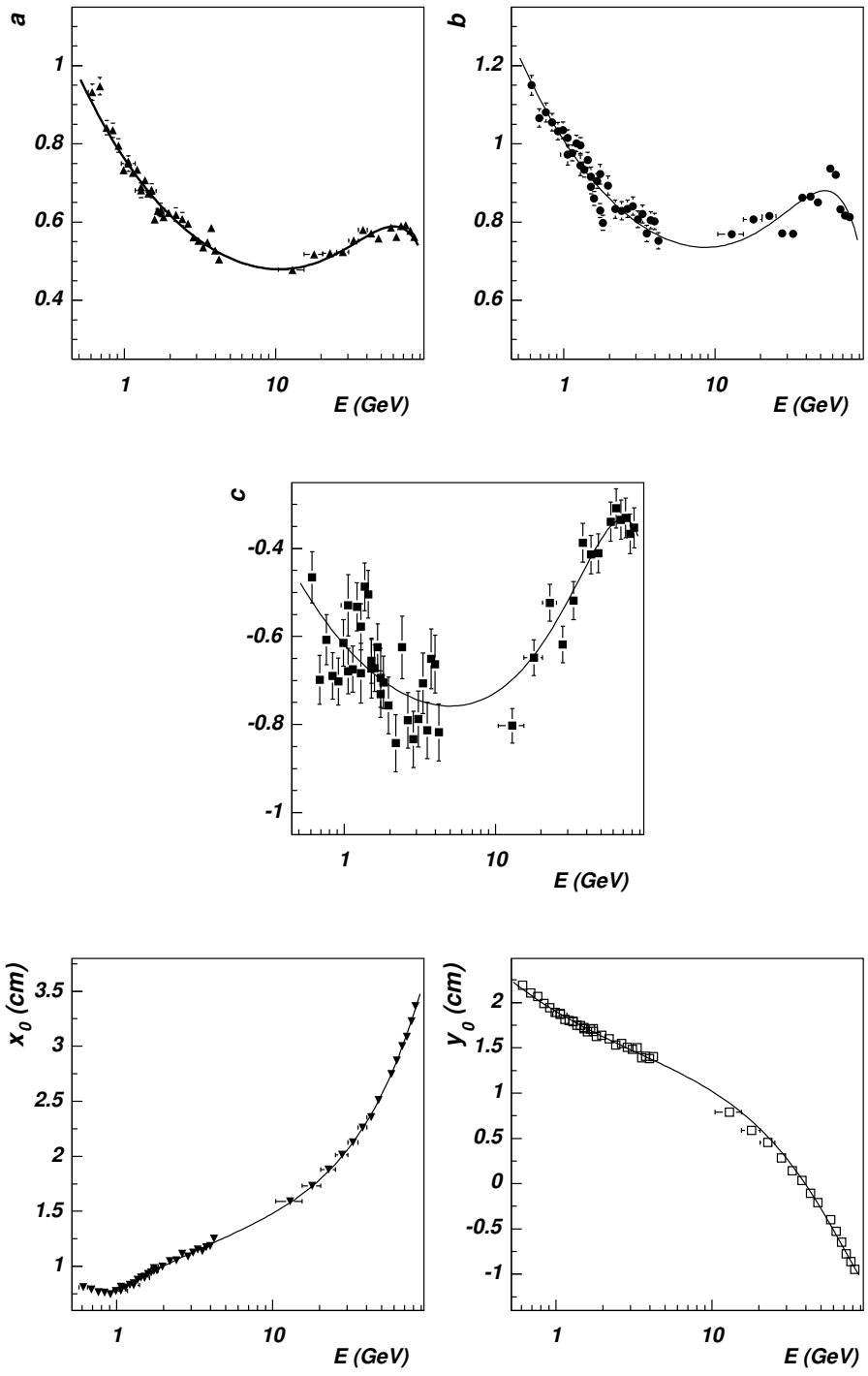

Figure 5.7: Parameters a, b, c, x_0 and y_0 characterizing the PCA ellipse for photons vs reconstructed photon energy. Points were fitted by the function $f(E) = q_0/\sqrt{E} + q_1 E + q_2 E^2 + q_3$, the q_i are given in Tab. 5.2.

	q_0	q_1	q_2	q_3
a	0.52	$8.4 \cdot 10^{-3}$	$-6 \cdot 10^{-5}$	0.23
b	0.47	$8.3 \cdot 10^{-3}$	$-5.6 \cdot 10^{-5}$	0.42
c	0.36	$1.4 \cdot 10^{-2}$	$-8 \cdot 10^{-5}$	-0.99
x_0	-0.75	$1.9 \cdot 10^{-2}$	$4 \cdot 10^{-6}$	1.49
y_0	0.91	$-3 \cdot 10^{-2}$	$1.1 \cdot 10^{-4}$	1.03

Table 5.2: Parameters obtained by fitting the PCA photon ellipse parameters a, b, c, x_0 and y_0 of Fig. 5.7 by the function $f(E) = q_0/\sqrt{E} + q_1 E + q_2 E^2 + q_3$.

The three classes of photon identification purity levels defined, high, medium and low, correspond to reconstructed particles in a region of the $(p_0,\ p_1)$ space defined by:

$$R(p_0,\ p_1) < \kappa/2, \tag{5.4}$$

with $\kappa = 1$, 4 and 9 for high, medium and low purity photons, respectively. These values of R correspond to a distance of 1, 2 and 3 standard deviations of the shower point to the center of the contour in the $(p_0,\ p_1)$ space, respectively.

5.4 Particle identification probabilities

5.4.1 Single photons

The identification probability was defined as the ratio of the spectrum of reconstructed particles identified as photons to the spectrum of all reconstructed particles. The three identification criteria (CPV, TOF and PCA) were applied simultaneously and the probability for three purity classes defined above were obtained[2]. These probabilities, given in Fig. 5.8 as a function of the energy, were calculated for photons of energy uniformly distributed in two different energy ranges: from 0.5 to 5 GeV and from 0.5 to 120 GeV. In these simulations, the other ALICE detectors were not present.

5.4.2 Photons in a heavy-ion environment

The high occupancy of PHOS in heavy-ion collisions induces a significant number of overlapping showers. In central HIJING Pb-Pb collisions ($b < 2$ fm), about a third of the EMC reconstructed points are associated to more than one primary particle, as observed in Fig. 5.9. To avoid identification ambiguities in the simulations, we have assigned to each reconstructed point the primary particle that contributes with the largest fraction of energy to it.

[2]Low purity = TOF low purity + CPV low purity + PCA low purity.
Medium purity = TOF medium purity + CPV medium purity + PCA medium purity.

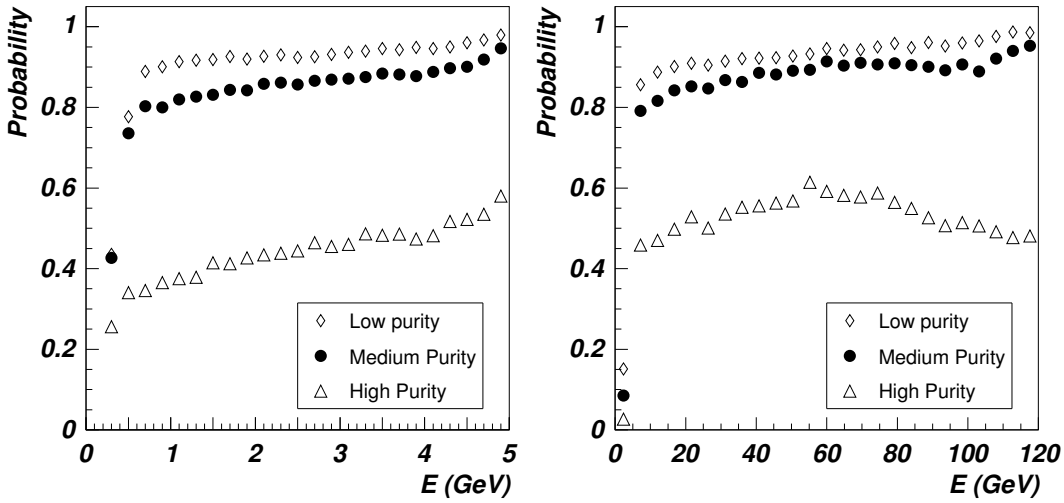

Figure 5.8: Photon identification probability with low (◇), medium (●) and high (△) purity levels for single photons of $E < 5$ GeV (left) and $E < 120$ GeV (right) as a function of the reconstructed photon energy.

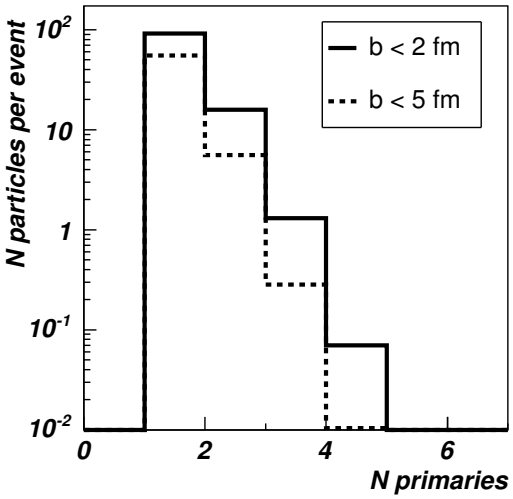

Figure 5.9: Average number of reconstructed particles for central HIJING events (Pb-Pb collisions at $5.5A$ TeV) as a function of the number of primary particles associated with one reconstructed particle in the EMC. Two impact parameter regions are considered: $b < 2$ fm (solid line) and $b < 5$ fm (dashed line).

5.4.2.1 Low-energy photons in a heavy-ion environment

The photon identification probability was calculated for each of the TOF, CPV and PCA criteria separately and for the three criteria combined for particles in the reconstructed energy range $0 < E < 5$ GeV. To evaluate the contamination of the identified photon spectrum, we considered charged pions, protons, neutrons and their anti-particles.

The identification probability by TOF shown in Fig. 5.10 indicates that TOF measurements alone cannot discriminate photons from nucleons for reconstructed energies larger than 1.5 GeV. This threshold is higher for anti-nucleons because they deposit additional energy through their annihilation. Charged π-mesons could not be discriminated from photons for energies higher than 0.5 GeV.

Concerning the CPV criterion, charged particles were efficiently discriminated from neutral particles for reconstructed energies higher than 1 GeV, as illustrated in Figs. 5.11 and 5.12. Soft hadrons are so significantly deflected by the magnetic field that the distance of their impact point in CPV and EMC is sufficiently large to produce their misidentification as photons. We observe that neutral particle identification probabilities are well below 100 %. This is due to a mismatch in the tracking between the CPV and the EMC produced by the HIC environment. This effect increased with the particle multiplicity of the event; for $b < 2$ fm the probability of misidentifying neutral particles was about a 10 % worse than for $b < 5$ fm.

The probability of identifying photons by the PCA criterion showed a minimum at about 1.5 GeV; hadrons were misidentified as photons with a high probability for reconstructed energies lower than 0.5 GeV but for higher energies the probability was small as seen in Figs. 5.13 and 5.14. The PCA identification criterion was efficient for reconstructed energies $E > 1$ GeV, although a strong dependence of the identification probability on the particle multiplicity was observed. I explain the shape of this probability below.

The comparison of the identification probabilities obtained for each of the three identification criteria alone allows us to conclude that the TOF criterion was the most efficient for energies $E < 1$ GeV. The CPV criterion rejected charged hadrons for $E > 1$ GeV, while the PCA criterion rejected charged and neutral hadrons for $E > 1$ GeV.

In Figs. 5.15 and 5.16 the results for the three identification criteria combined are plotted. We observe that the probabilities of identifying photons have a maximum at low energies and then decrease reaching a minimum at about 1.5 GeV. These probabilities are quite different from the probabilities obtained by merging photons of energy uniformly distributed with HIJING events, shown in Fig. 5.17. This difference is due on one side to the shape of the photon spectrum in HIJING events which is exponential and on the other side to the overlapping clusters produced in HIJING events. In these figures we observe a maximum of the identification probability at low energies and a decrease with energy

High purity = TOF high purity + CPV high purity + PCA high purity.

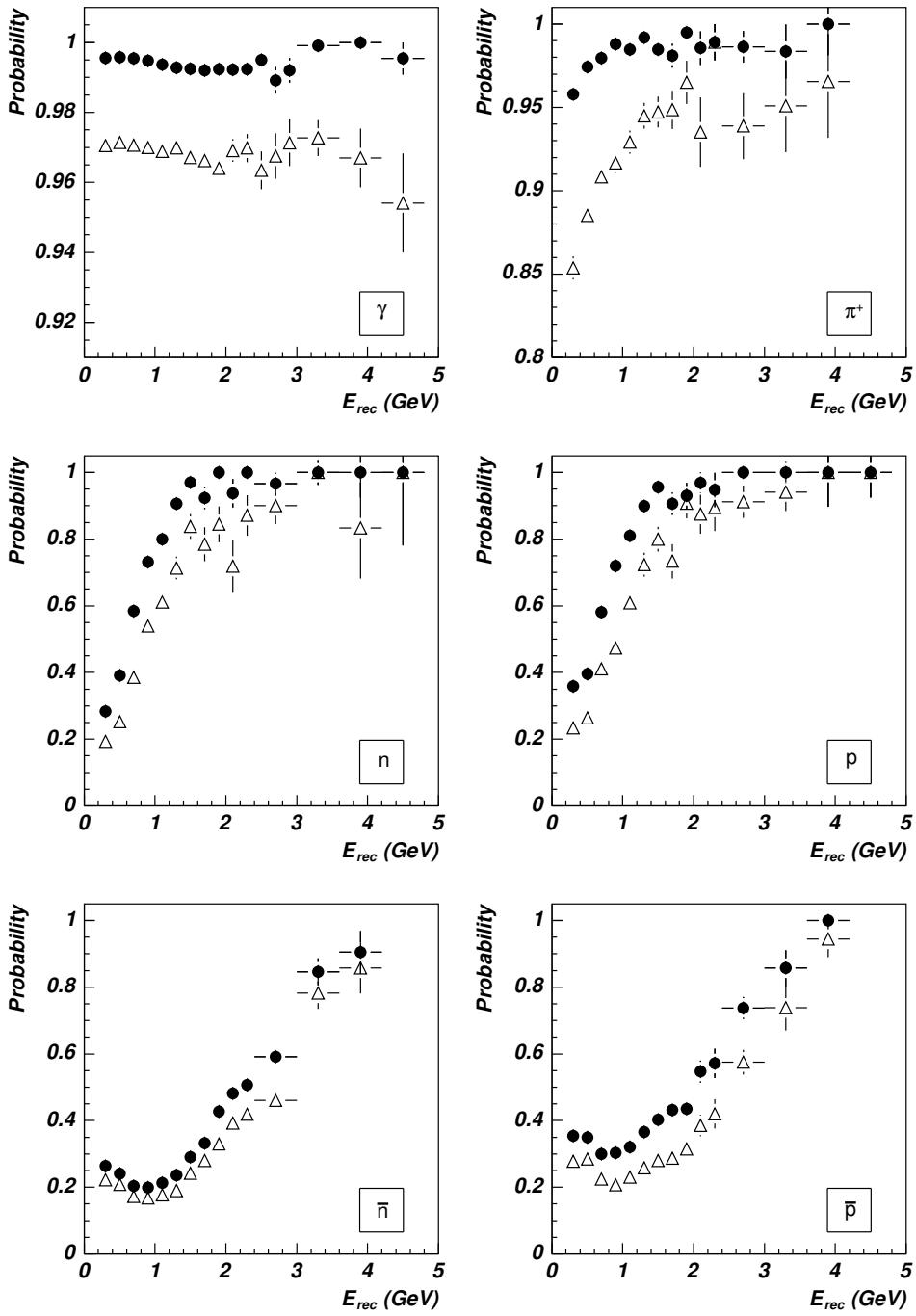

Figure 5.10: Probability of identifying a particle as a photon with high (△) and low (•) purity level by the TOF criterion as a function of the reconstructed energy for γ, n, $\bar{n}$, p, $\bar{p}$ and $\pi^{\pm}$ generated by HIJING simulations for Pb-Pb collisions at $5.5A$ TeV and $b < 5$ fm. Similar results obtained for $b < 2$ fm.

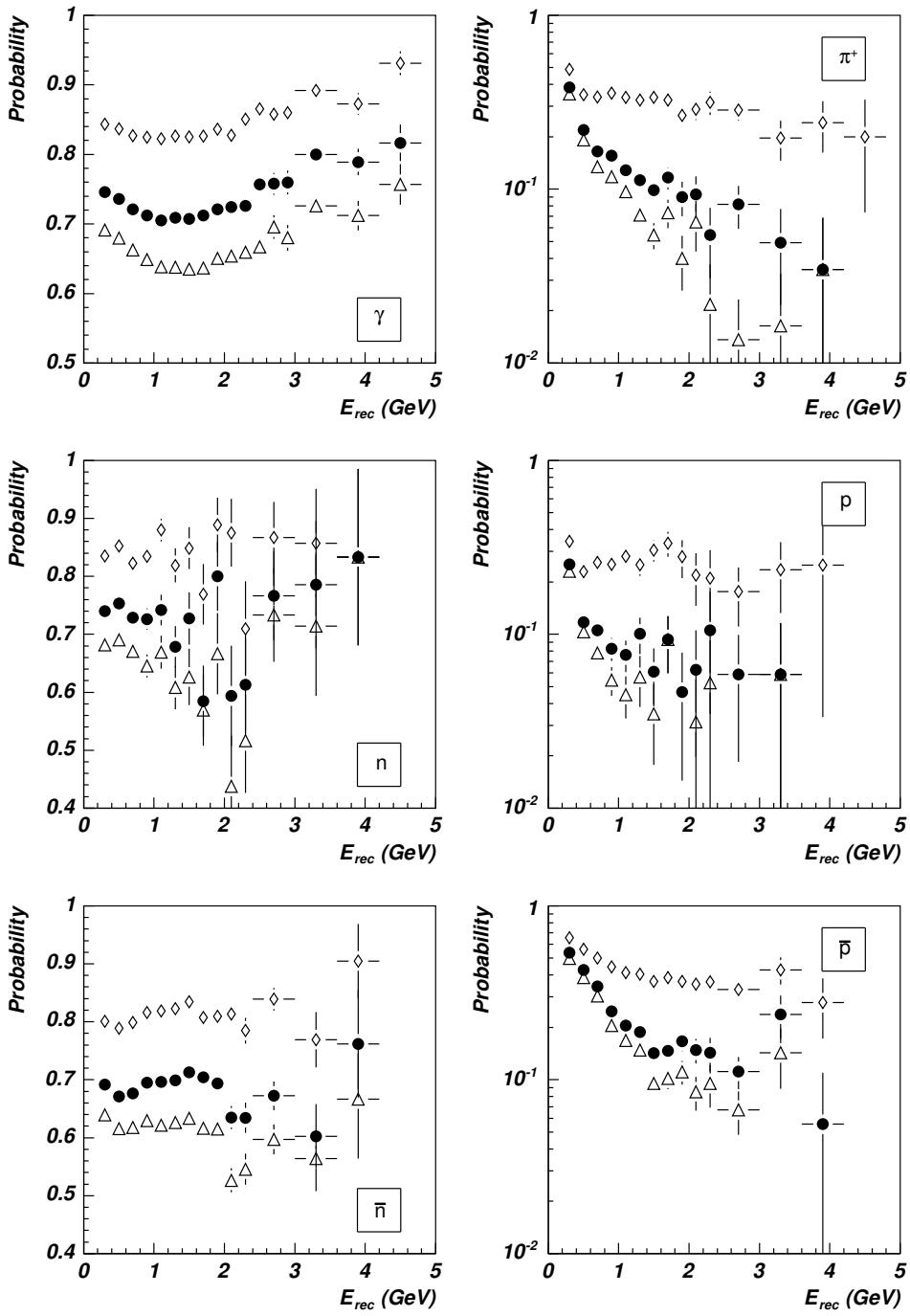

Figure 5.11: Probability of identifying a particle as a photon with high (△), medium (•) and low (◇) purity level by the CPV criterion as a function of the reconstructed energy for γ, n, $\bar{n}$, p, $\bar{p}$ and $\pi^{\pm}$ generated by HIJING simulations for Pb-Pb collisions at 5.5A TeV and $b < 5$ fm.

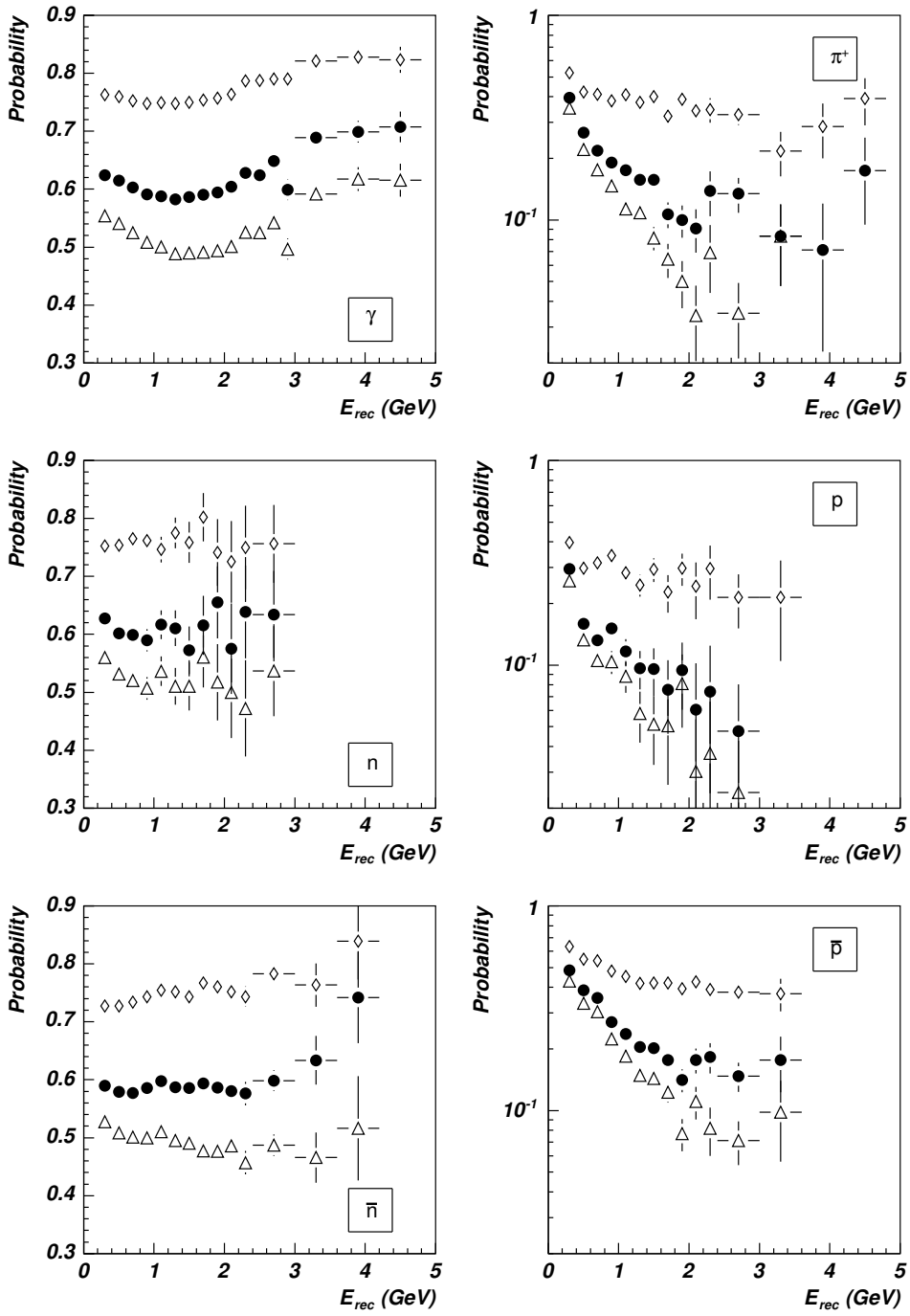

Figure 5.12: Probability of identifying a particle as a photon with high (△), medium (•) and low (◇) purity level by the CPV criterion as a function of the reconstructed energy for γ, n, $\bar{n}$, p, $\bar{p}$ and $\pi^{\pm}$ generated by HIJING simulations for Pb-Pb collisions at 5.5A TeV and $b < 2$ fm.

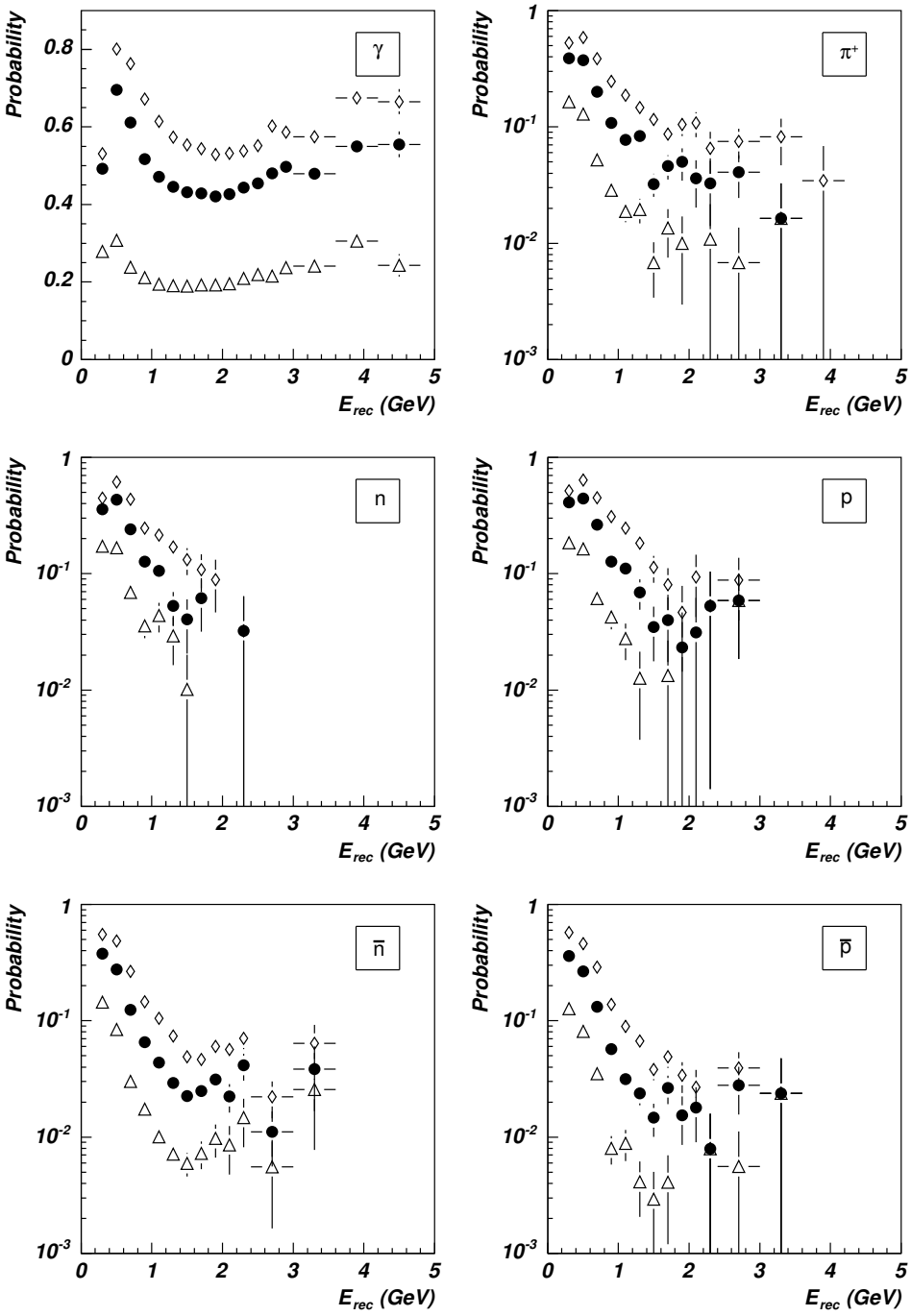

Figure 5.13: Probability of identifying a particle as a photon with high (△), medium (•) and low (◇) purity level by the PCA criterion as a function of the reconstructed energy for γ, n, $\bar{n}$, p, $\bar{p}$ and $\pi^{\pm}$ generated by HIJING simulations for Pb-Pb collisions at $5.5A$ TeV and $b < 5$ fm.

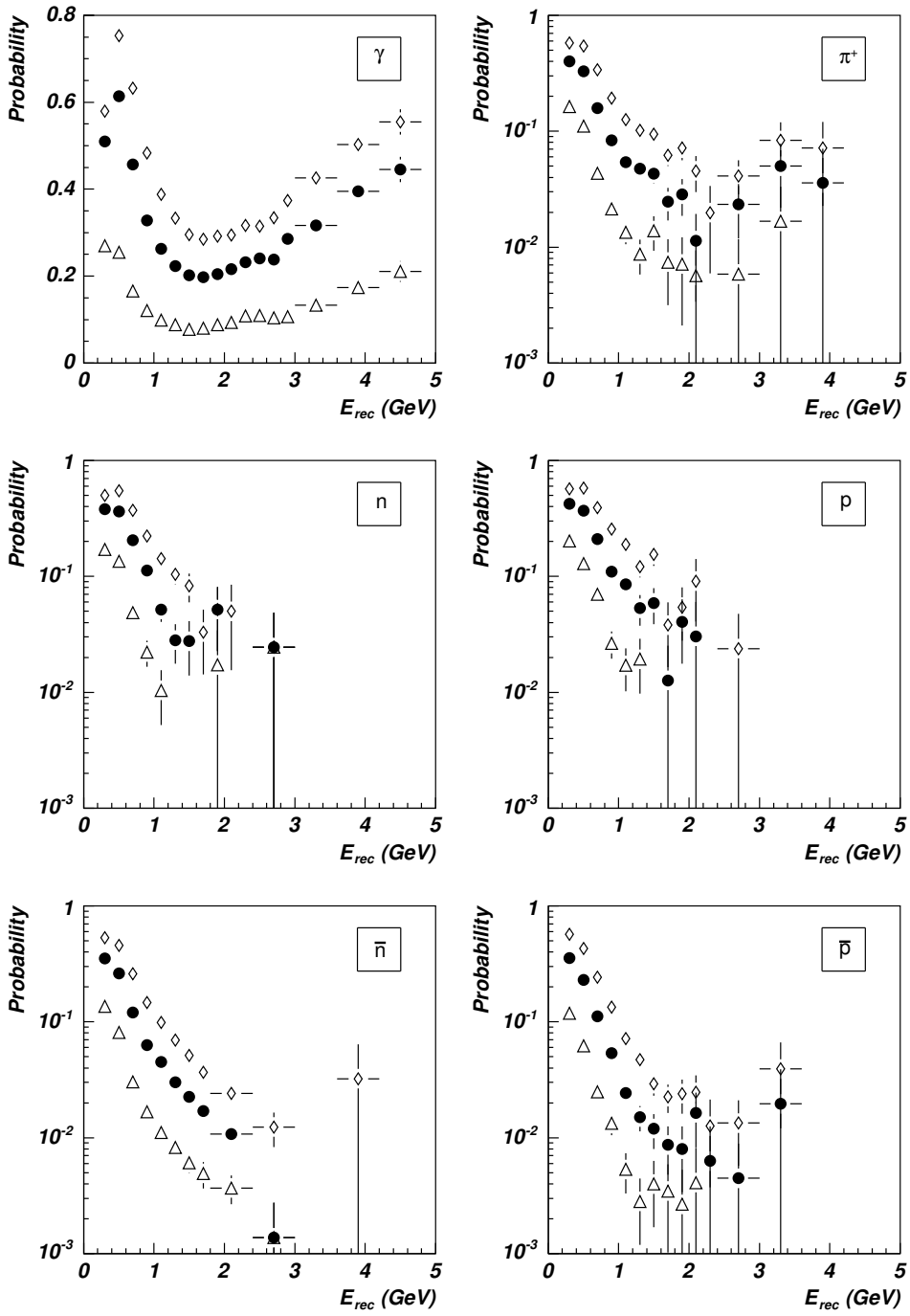

Figure 5.14: Probability of identifying a particle as a photon with high (△), medium (•) and low (⋄) purity level by the PCA criterion as a function of the reconstructed energy for γ, n, $\bar{n}$, p, $\bar{p}$ and $\pi^{\pm}$ generated by HIJING simulations for Pb-Pb collisions at $5.5A$ TeV and $b < 2$ fm.

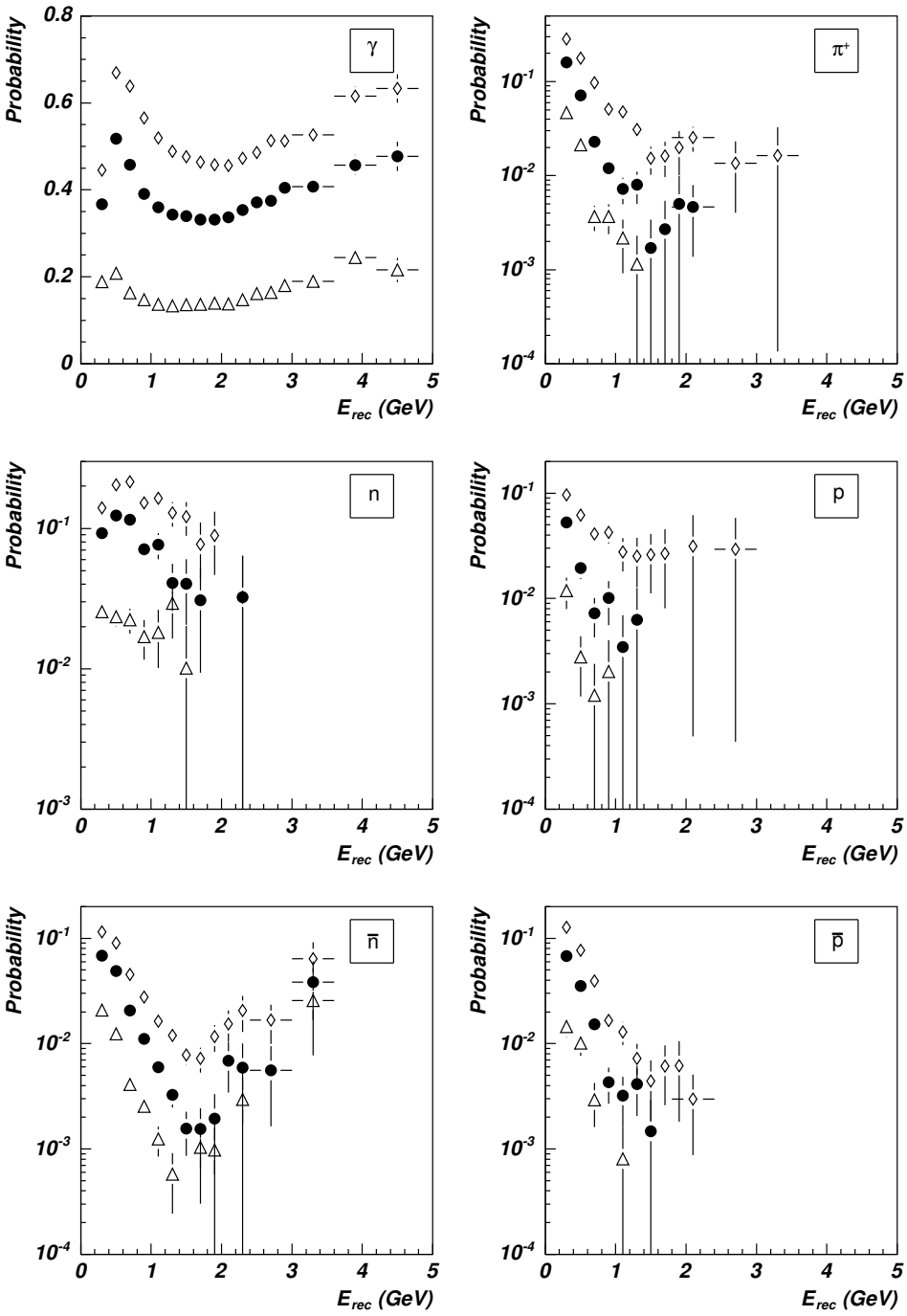

Figure 5.15: Probability of identifying a particle as a photon with high (△), medium (•) and low (◇) purity level by the TOF, CPV and PCA criteria as a function of the reconstructed energy for γ, n, $\bar{n}$, p, $\bar{p}$ and $\pi^{\pm}$ generated by HIJING simulations for Pb-Pb collisions at $5.5A$ TeV and $b < 5$ fm.

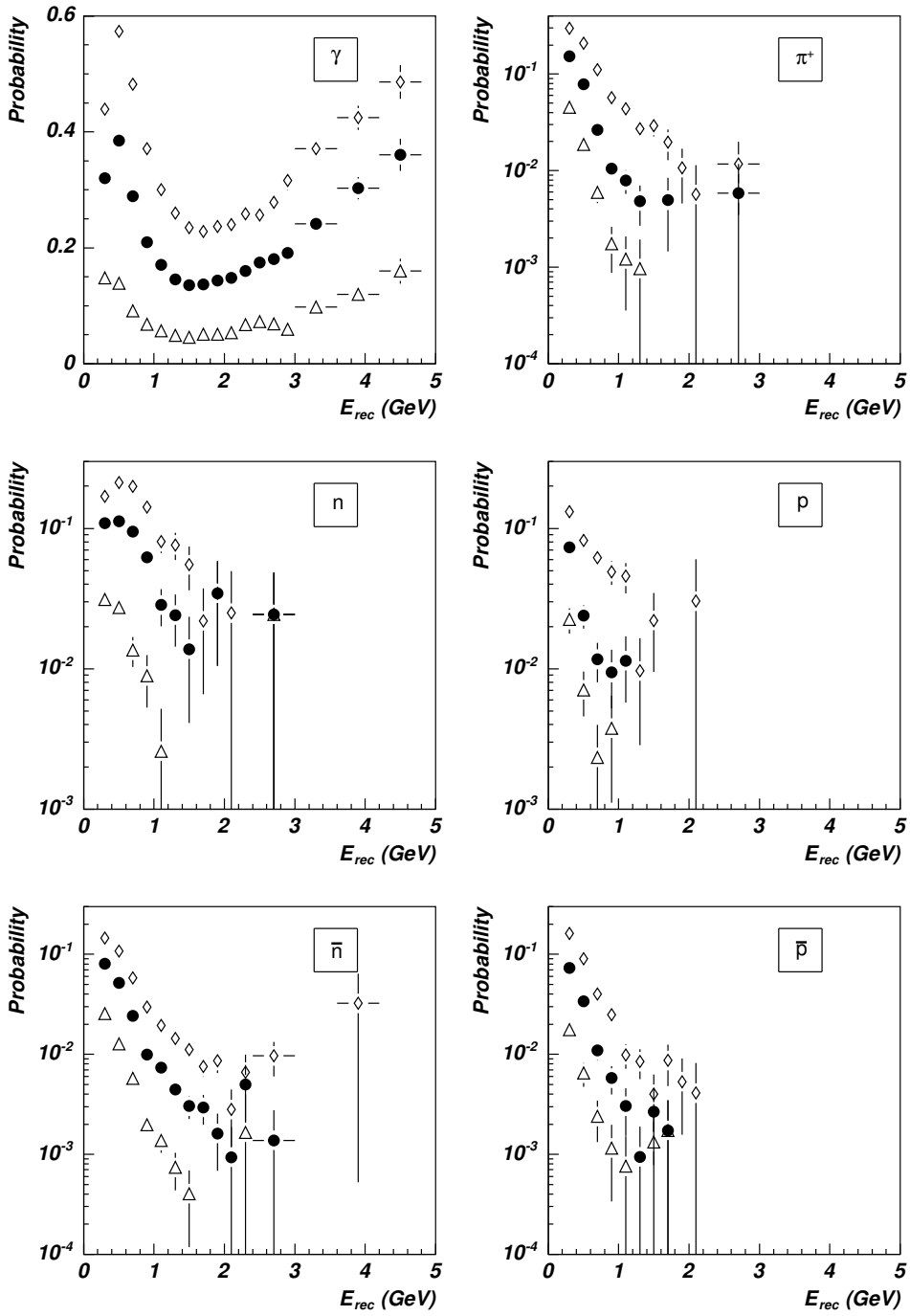

Figure 5.16: Probability of identifying a particle as a photon with high (△), medium (•) and low (⋄) purity level by the TOF, CPV and PCA criteria as a function of the reconstructed energy for γ, n, $\bar{n}$, p, $\bar{p}$ and $\pi^{\pm}$ generated by HIJING simulations for Pb-Pb collisions at $5.5A$ TeV and $b < 2$ fm.

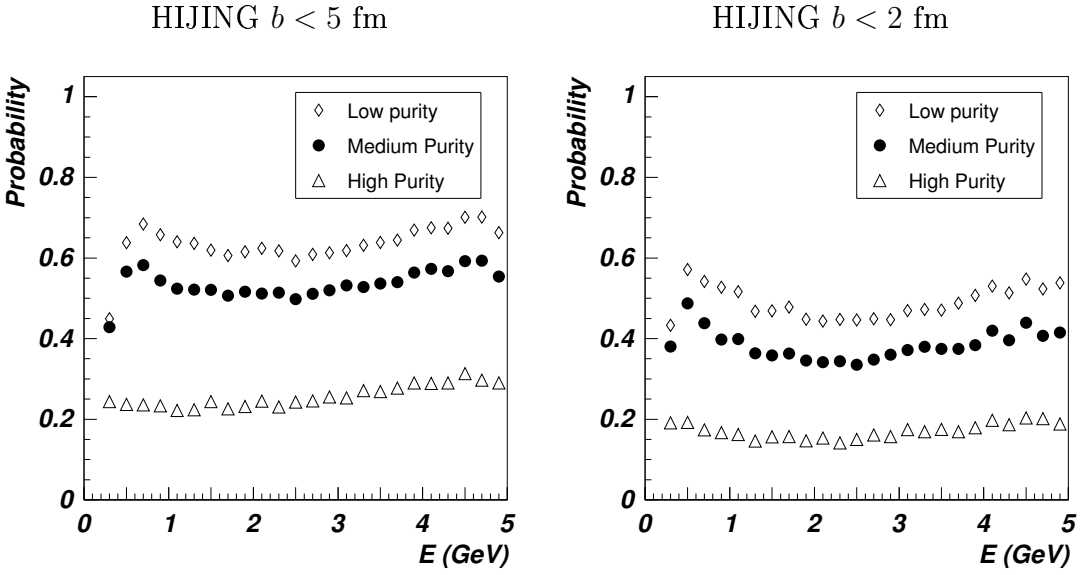

Figure 5.17: Probability of identifying photons generated with energy uniformly distributed from 0 to 5 GeV and merged with HIJING events as a function of the reconstructed energy with high (△), medium (•) and low (◇) purity level, for TOF, CPV and PCA criteria simultaneously required. Results for impact parameters $b < 5$ fm (left) and $b < 2$ fm (right) are shown.

which is more pronounced for HIJING events. This decrease was due to the overlapping of showers of different particles which produced reconstructed particles with higher energy than the original particle and photons identified as hadrons. Consequently, the probability denominator which is the number of clusters generated by photons, was enhanced at higher energies. In the case of single HIJING events, the probability decreased with the energy even faster due to the exponential shape of the HIJING photon spectrum. This effect was small and saturated for uniform energy photon distributions, but for exponential photon spectrum, the comparatively lower number of high energy photons produces an abrupt drop of the probability.

The purity $\mathcal{P}$ of the identified photons was defined as the ratio of the number of reconstructed particles actually generated by photons to the total number of particles identified as photons. Similarly, the hadron contamination was defined as the ratio of the number of reconstructed particles identified as photons but generated by hadrons to the total number of particles identified as photons; obviously $\mathcal{C} = 1 - \mathcal{P}$. About $97 - 99\%$ of all the particles identified as photons are indeed photons. The contamination of photons is displayed in Fig. 5.18.

5.4.2.2 High-energy photons in a heavy-ion environment

The identification of high-energy photons in a HIC environment was studied with built-up test cases, simulated by mixing single hard photons of energy generated by a uniform distribution between 0.5 to 120 GeV with central Pb-Pb HIJING events ($b < 2$ fm and

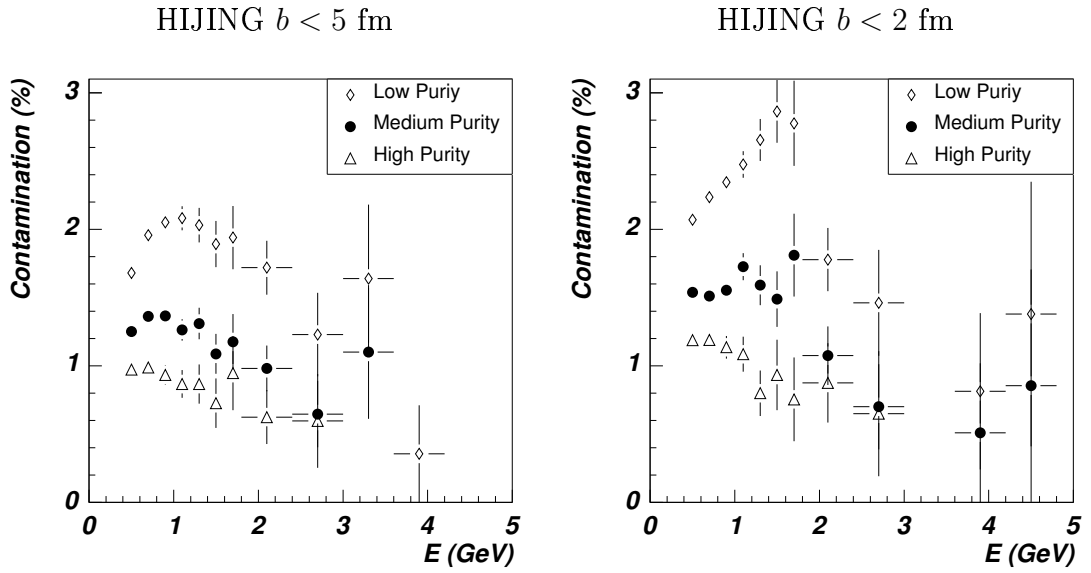

Figure 5.18: Hadron contamination of the spectrum of reconstructed particles identified as photons in HIJING events with $b < 5$ fm (left) and $b < 2$ fm (right) with high ($\triangle$), medium ($\bullet$) and low ($\diamond$) purity level.

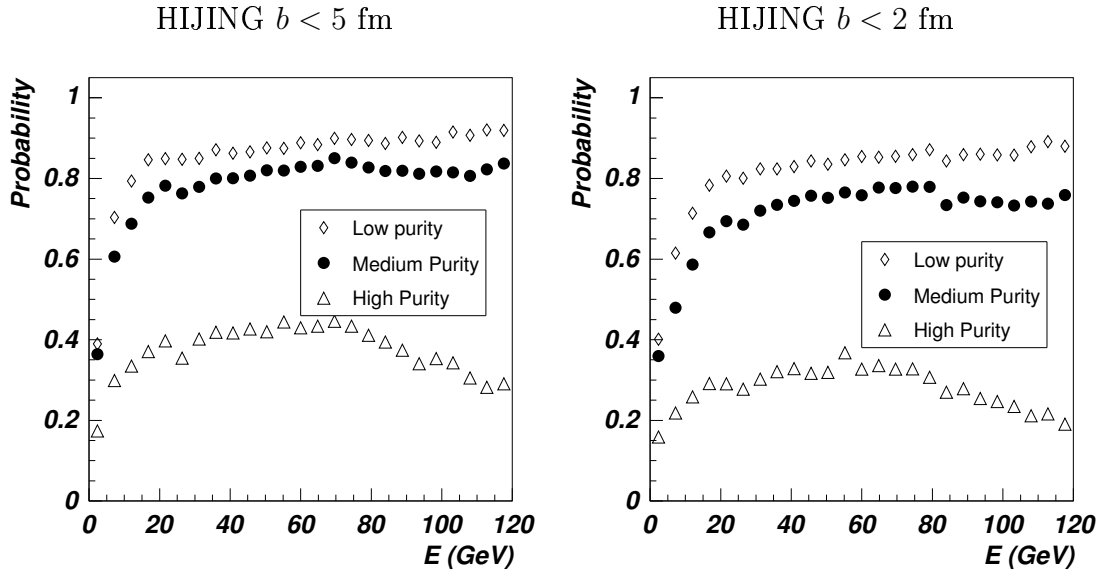

Figure 5.19: Probability of identifying with high ($\triangle$), medium ($\bullet$) and low ($\diamond$) purity level photons of energy uniformly distributed from 0.5 to 120 GeV and embedded in HIJING Pb-Pb collision events at $5.5A$ TeV with $b < 5$ fm (left) and $b < 2$ fm (right), with TOF, CPV and PCA criteria simultaneously required.

$b < 5$ fm). The identification probabilities of hard photons for heavy-ion collisions are plotted in Fig. 5.19. The hard photon identification probability decreased a 10 % with respect to the single particle case due essentially to the failure of the CPV criterion.

5.5 Detection of π^0 in PHOS

5.5.1 Invariant mass analysis of neutral pions

Neutral mesons were identified by an invariant-mass analysis of their two decaying photons measured in PHOS. The average mass resolution at the π^0 mass is 3 - 7 MeV/c^2 depending on the π^0 energy, as shown in Fig. 5.20. The probability of reconstructing π^0 by invariant mass analysis was evaluated from π^0 of energy uniformly distributed between 0.5 and 100 GeV impinging within the PHOS acceptance. The reconstruction probability was studied for photons satisfying the following conditions:

- Without any condition (denoted as a raw efficiency);
- Only photons which hit crystals separated at least two cells from the EMC edge are considered;
- Photon pairs with invariant mass satisfying $|M_{\gamma\gamma} - M_{\pi^0}| < 2\sigma_{M_{\gamma\gamma}}$;
- Photon pairs of energies E_1 and E_2 satisfying $\alpha = |E_1 - E_2| / (E_1 + E_2) < 0.8$;
- Photons identified with either low, medium or high purity level.

The probability obtained for each of these conditions as a function of the energy is plotted in Fig. 5.21. We conclude from Fig. 5.21 that the π^0 spectrum can be measured in PHOS with a fairly good efficiency up to a π^0 transverse momentum $p_T < 30$ GeV/c. Beyond this momentum, the efficiency drops steeply and almost vanishes above $p_T = 50$ GeV/c. This decreasing of the efficiency at high-π^0 energies can be explained by the impossibility of unfolding overlapping showers in which both decay photons merge into a single reconstructed impact point.

5.5.2 Invariant mass analysis of neutral pions in a heavy-ion environment

The high π^0 multiplicity existing in a heavy-ion environment generates a combinatorial background in the invariant-mass spectrum constructed by combining in pairs all the detected photons in the same event. The background underlying the π^0 peak must be subtracted to obtain the π^0 yield. In central Pb-Pb HIJING collisions generated for impact parameter $b < 2$ fm, no peak at the π^0 mass was observed for pairs of $p_T < 10$ GeV/c

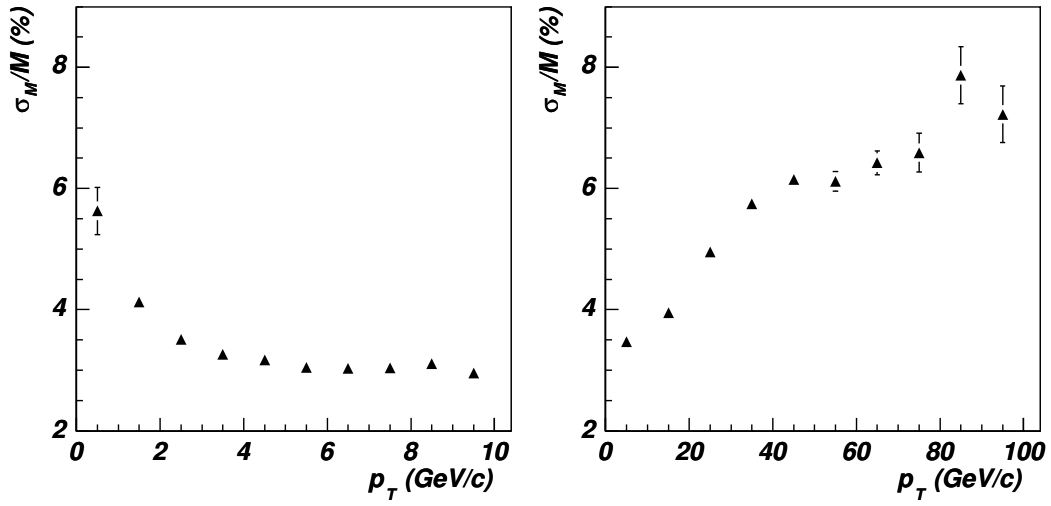

Figure 5.20: Invariant mass resolution calculated for π^0 of energy uniformly distributed between 0.5 and 100 GeV.

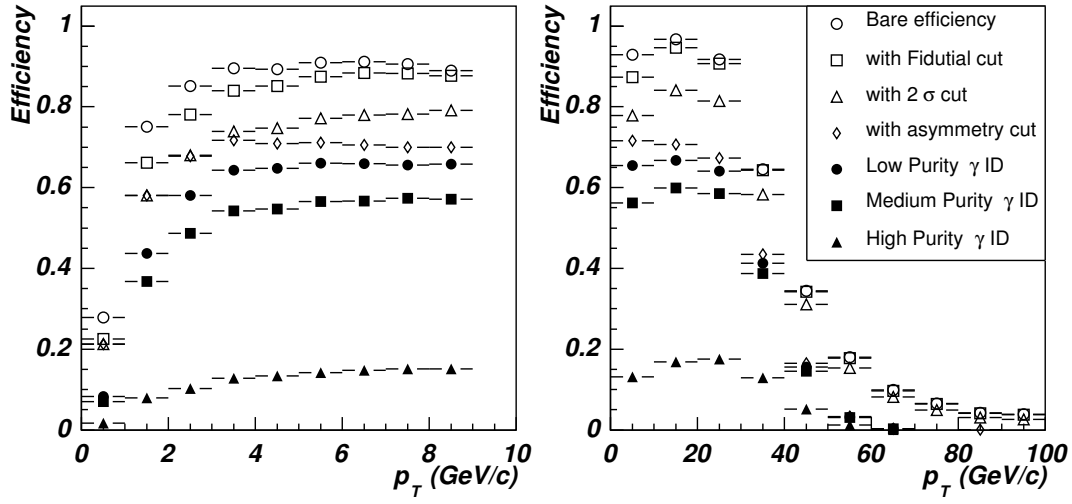

Figure 5.21: Probability of reconstructing π^0 by invariant-mass analysis with different conditions.

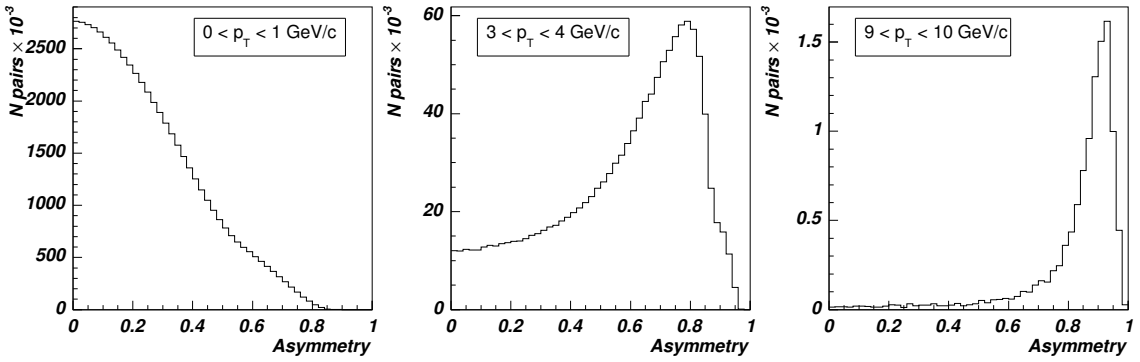

Figure 5.22: Energy asymmetry parameter α calculated for reconstructed photon pairs generated by HIJING simulations of central Pb-Pb collisions ($b < 2$ fm) with transverse momenta $0 < p_T < 1$ GeV/c (left), $3 < p_T < 4$ GeV/c (middle) and $9 < p_T < 10$ GeV/c (right).

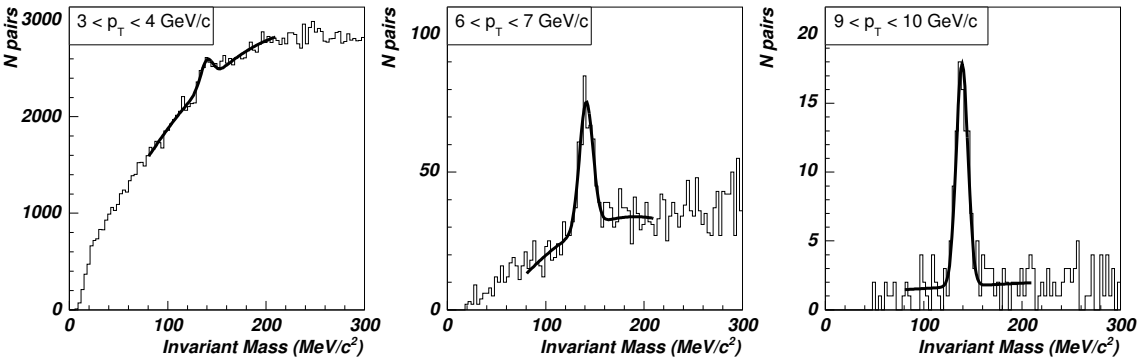

Figure 5.23: Invariant mass spectra of particle pairs with asymmetry $\alpha < 0.75$ and with transverse momentum in the ranges $3 < p_T < 4$ GeV/c (left), $6 < p_T < 7$ GeV/c (middle) and $9 < p_T < 10$ GeV/c (right) generated by HIJING simulations of central Pb-Pb collisions ($b < 2$ fm)

due to the high combinatorial background produced by hadron contamination. This contamination can be suppressed by imposing conditions on the asymmetry parameter. The asymmetry distribution of π^0 is uniform because their decay is isotropic. However, the asymmetry distribution for identified photon pairs in a HIJING event exhibited a strong enhancement at large asymmetries and for large transverse momentum of the pair, as seen in Fig. 5.22. This behaviour can be attributed to asymmetric pairs in which one of the particles identified as photons was in fact a contaminating hadron. The elimination of pairs with asymmetries $\alpha > 0.75$ reduced the combinatorial background significantly while the π^0 peak was suppressed by only 25 %, as seen in Fig. 5.23. The π^0 p_T spectrum obtained after eliminating pairs of high asymmetry was close to the generated π^0 spectrum as observed in Fig. 5.24.

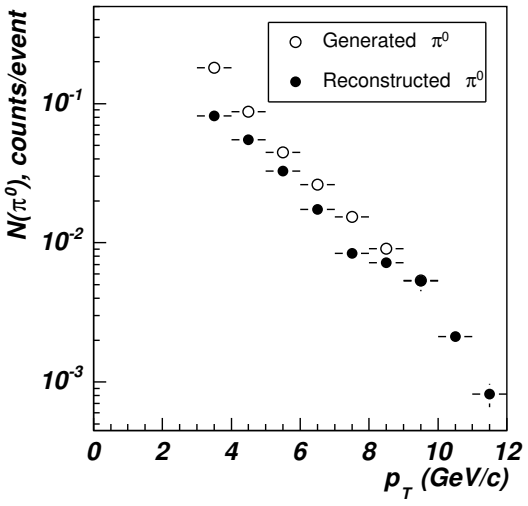

Figure 5.24: p_T spectrum of generated and reconstructed π^0 per HIJING event ($b < 2$ fm).

5.6 Event by event photon and π^0 identification at high-energy

At high momenta, π^0 are identified as photons because their decay photons merge into a single electromagnetic shower. We developed several approaches to discriminate high-p_T π^0 from photons based on the shower-shape analysis.

5.6.1 One-dimensional shower-shape analysis

Additional parameters need to be introduced to separate γ and π^0. The most helpful parameter to discriminate γ and π^0 is the second moment M_{2x} of the cluster, i.e. the largest eigenvalue of the covariance matrix ($M_{2x} = \lambda_1^2$ with $\lambda_1 \geq \lambda_2$, see Sec. 4.4.1) which is plotted in Fig. 5.25. At moderate E_{π^0} the M_{2x} distributions for photon and π^0 were well separated with only a slight overlap, while at higher p_T they merged into each other. To separate photons and π^0-mesons, the optimal cut M_{2x}^0 of the second moment distributions that maximizes the ratio of correctly identified to misidentified particles was determined. To get a reasonably high value of the identification probability, we restricted the search of this optimal cut to the interval between the mean values of the photon and π^0 moments and required a misidentification probability smaller than 3 %. The value of M_{2x}^0 was different for photons and π^0. This value as a function of the reconstructed energy is shown in Fig. 5.26. In this figure, M_{2x}^0 for photons was fitted by the equation

$$M_{2x}^0(\gamma) = p_0 \cdot \exp\left[\frac{(E - p_1)^2}{2 \cdot p_2^2}\right] + p_3, \tag{5.5}$$

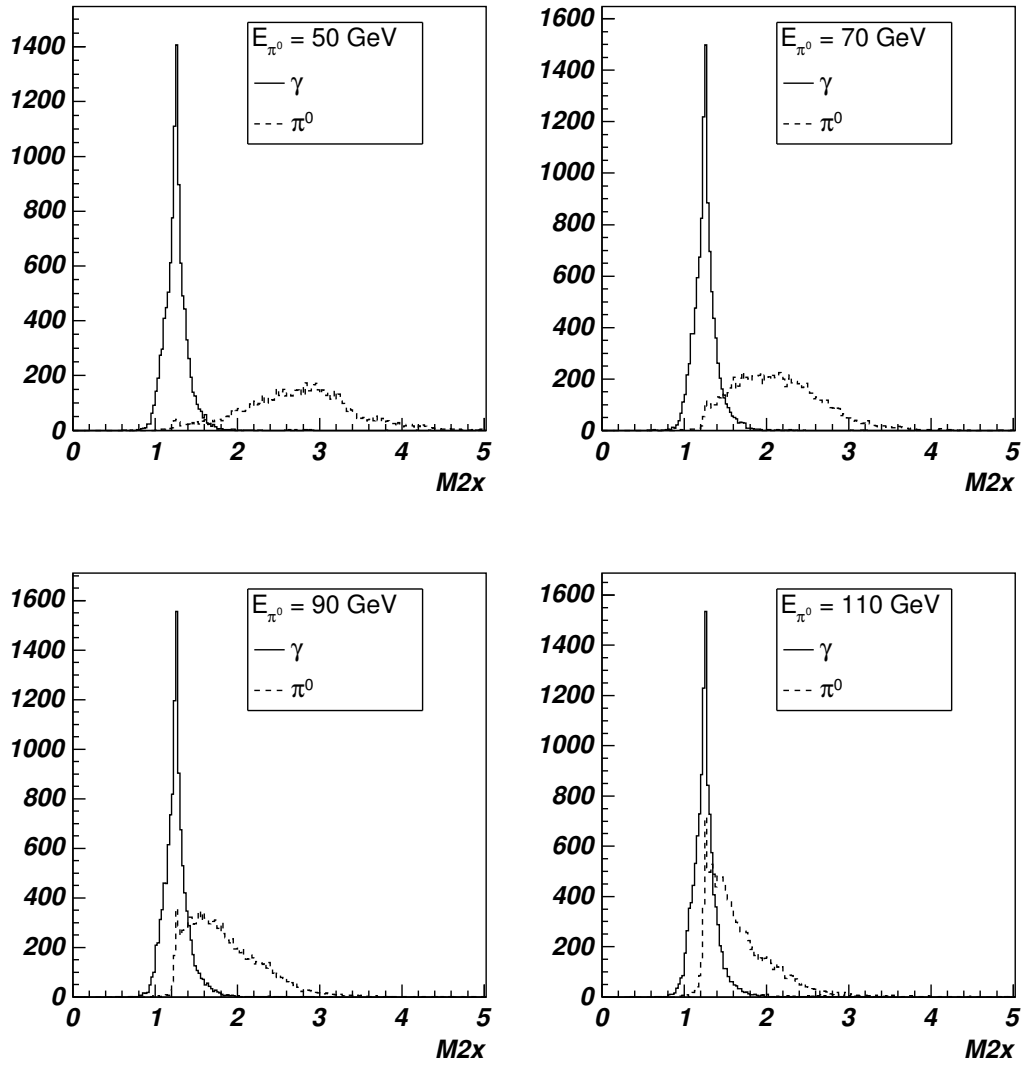

Figure 5.25: M_{2x} for photons (solid line) and π^0 (dashed line) of 50, 70, 90 and 110 GeV of energy.

and M^0_{2x} for π^0 was fitted by a straight line. The p_i parameters of Eq. (5.5) for photons and of the linear fit for π^0 are given in Tab. 5.3.

The photon identification probability, $P(\gamma,\ \gamma)$, was defined as the fraction of single-photon events with moment $M_{2x} < M^0_{2x}(\gamma)$, and the misidentification probability of π^0 as photons, $P(\gamma,\ \pi^0)$, as the fraction of π^0 events with $M_{2x} < M^0_{2x}(\gamma)$. Similarly the π^0 identification probability, $P(\pi^0,\ \pi^0)$, and the misidentification probability of photons as π^0, $P(\pi^0,\ \gamma)$, were defined as the fraction of π^0 and single photons with $M_{2x} > M^0_{2x}(\pi^0)$, respectively. These probabilities are shown in Fig. 5.27. The ratios $P(\gamma,\ \pi^0)/P(\gamma,\ \gamma)$ and $P(\pi^0,\ \gamma)/P(\pi^0,\ \pi^0)$ shown in Fig. 5.28 indicate that the misidentification probability is a few percent of the probability of correct identification at moderate p_T, and not higher than 10-20 % at $p_T = 120$ GeV/c. We obtained similar probabilities for high-energy γ and π^0 merged in a HIC environment.

	p_0	p_1	p_2	p_3
γ	0.17	54	9	1.3
π^0	1.5	$1.2 \cdot 10^{-3}$		

Table 5.3: Parameters obtained by fitting the M^0_{2x} by Eq. (5.5) for high-energy photon identification and by a straight line for hard-π^0 identification.

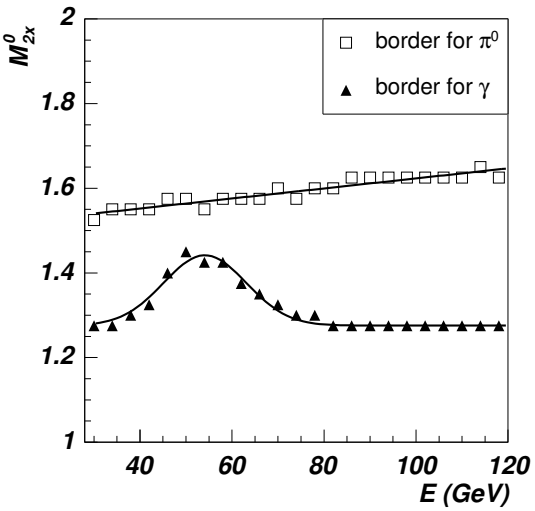

Figure 5.26: M^0_{2x} threshold employed to separate photons from π^0 (▲) and π^0 from photons (□) as a function of the reconstructed energy. The photon threshold was fitted by Eq. (5.5) and the π^0 threshold was fitted by a straight line, with parameters given in Tab. 5.3.

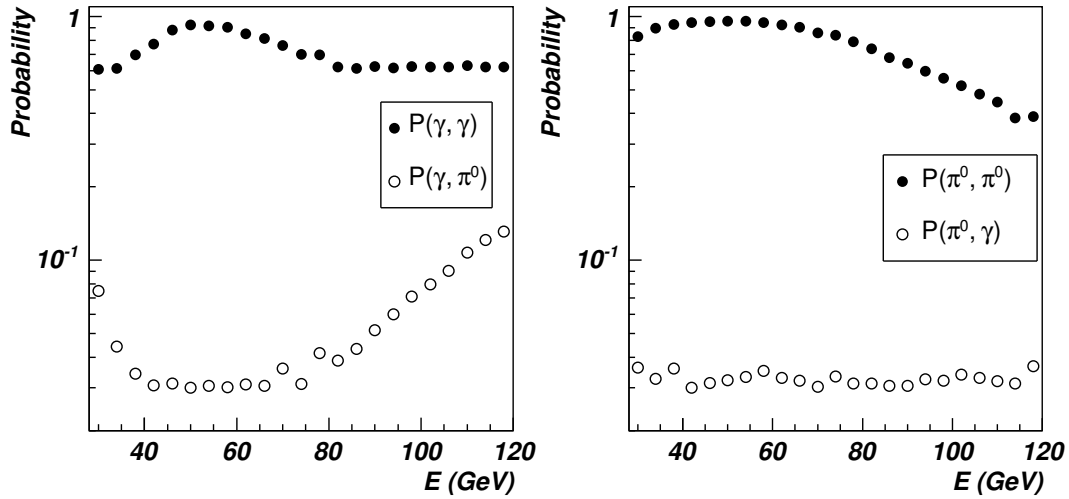

Figure 5.27: Probabilities of correct photon identification and π^0 misidentification as photon (left plot), and of correct π^0 identification and photon misidentification as π^0 (right plot).

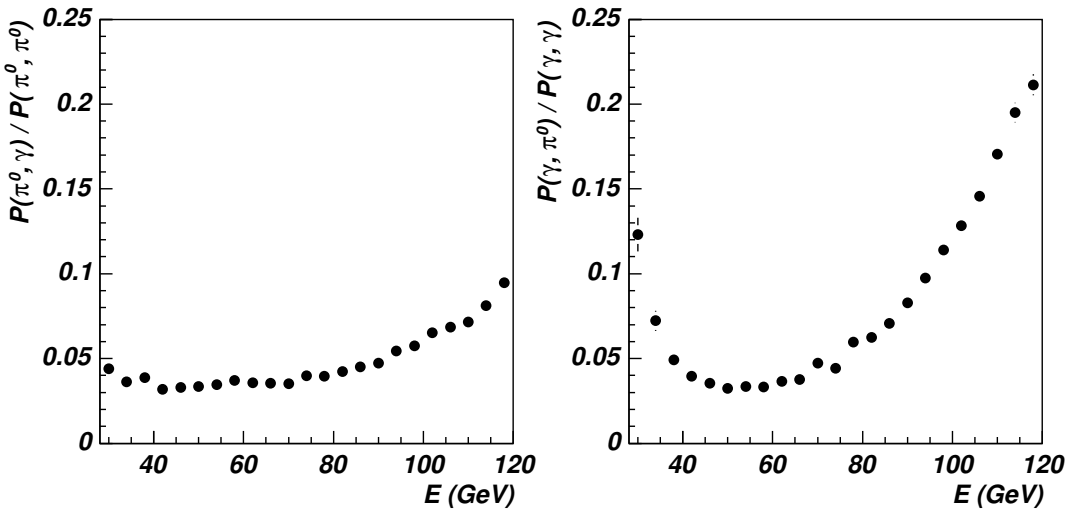

Figure 5.28: Ratios $P(\gamma, \pi^0)/P(\gamma, \gamma)$ (left plot) and $P(\pi^0, \gamma)/P(\pi^0, \pi^0)$ (right plot).

	q_0	q_1	q_2
a	0.95	$7.6{\cdot}10^{-3}$	$-7.1{\cdot}10^{-5}$
b	3.4	-0.041	$1.7{\cdot}10^{-4}$
c	0.36	0	0
x_0	-6.1	0.11	$-3.8{\cdot}10^{-4}$
y_0	4.7	-0.09	$3.8{\cdot}10^{-4}$

Table 5.4: Parameters obtained by fitting the different ellipse parameters of Fig. 5.30 by the function $f(E) = q_2E^2 + q_1E + q_0$.

5.6.2 Identification of photons and π^0 by PCA

A different approach to distinguish photons and π^0-mesons, based on the PCA described in Sec. 5.3, was investigated. Scatter plots of showers of π^0-mesons of 46, 66 and 90 GeV of energy and scatter plots of photon showers of 40, 60 and 80 GeV of energy versus the two most significant principal components are shown in Fig. 5.29. The ellipses were obtained as described in Sec. 5.3. The π^0 distributions shown in Fig. 5.29 were fitted by Eq. (5.3) with parameters depending on the reconstructed energy, plotted in Fig. 5.30. The ellipse parameters for low, medium and high purity levels were fitted to a parabola with coefficients given in Tab. 5.4. Photon and π^0 showers were well separated at low energies but at higher energies their scatter plots in the principal component space overlapped.

The probabilities of correct identification and misidentification $P(\gamma, \gamma)$, $P(\pi^0, \pi^0)$, $P(\gamma, \pi^0)$ and $P(\pi^0, \gamma)$ are defined as in Sec. 5.6.1 and are shown in Figs. 5.31 and 5.32 for π^0 generated with energy uniformly distributed from 30 to 120 GeV.

Identification of photons and π^0 by PCA in a heavy-ion environment I studied the π^0 identification probability in a heavy-ion environment by the PCA as described in

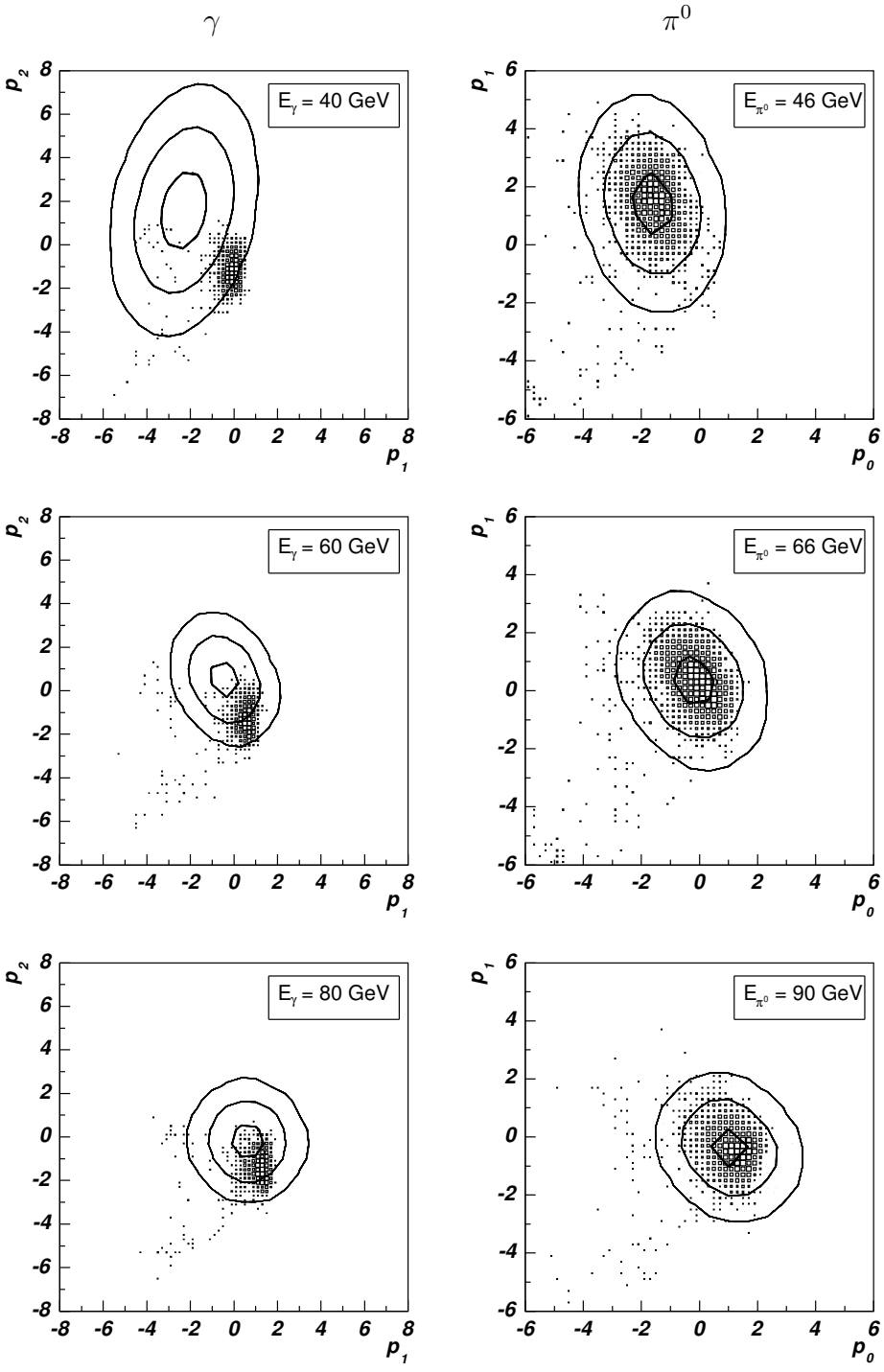

Figure 5.29: Scatter plots for γ showers of energies 40, 60 and 80 GeV (left) and π^0 showers of energies 46, 66 and 90 GeV (right) as a function of the the first two principal components obtained by the PCA. The three different ellipses show the high, medium and low purity contours for π^0 identification.

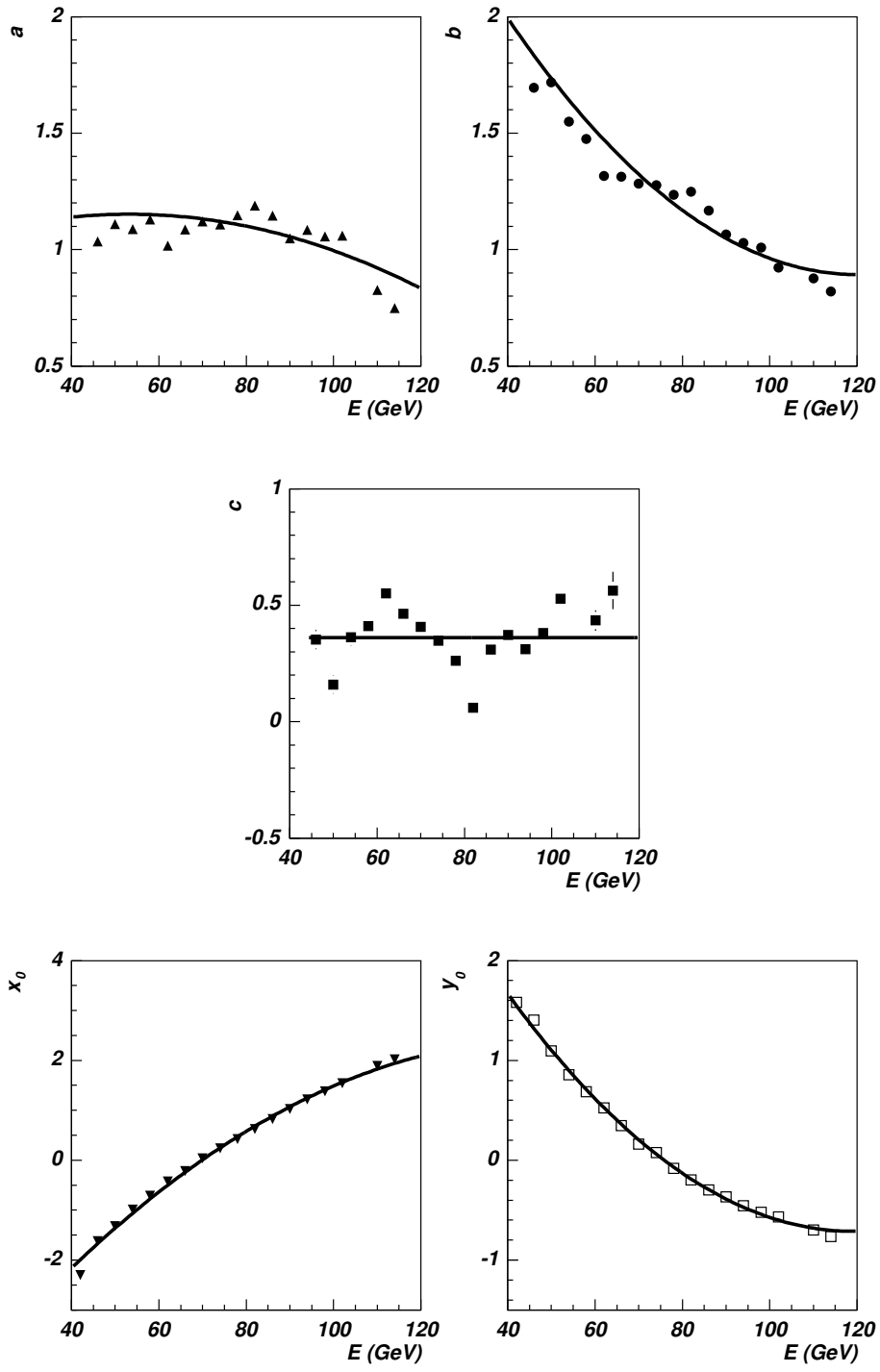

Figure 5.30: PCA ellipse parameters a, b, c, x_0 and y_0 vs reconstructed energy for π^0. Points were fitted to a parabola; the fitted parameters q_i are given in Tab. 5.4.

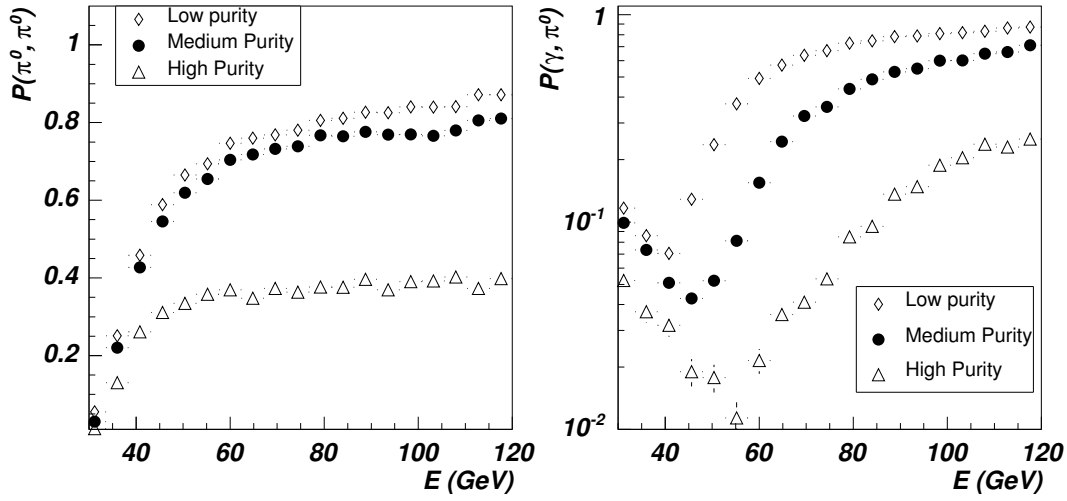

Figure 5.31: Probability of correct single π^0 identification (left) and misidentification as photons (right) by PCA for high ($\triangle$), medium ($\bullet$) and low ($\diamond$) identification purity levels.

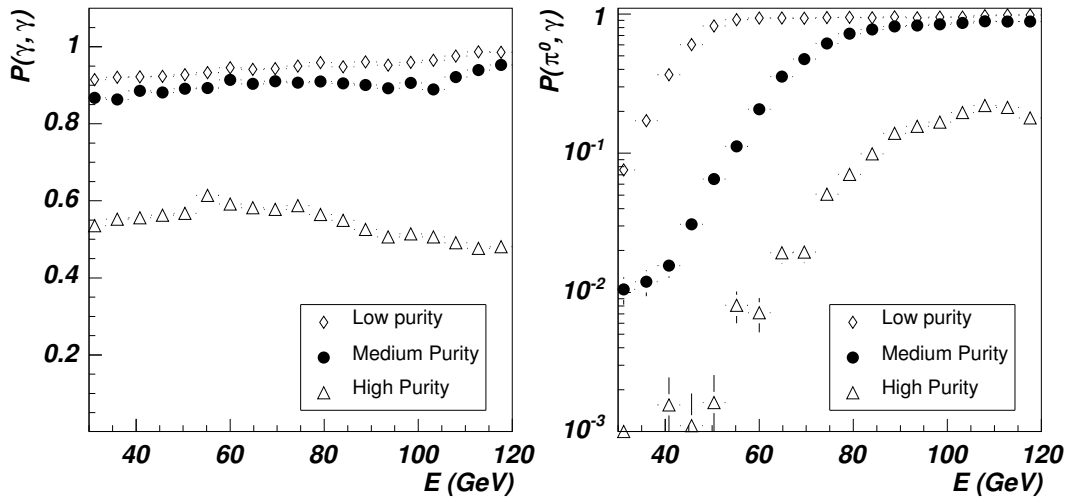

Figure 5.32: Probability of correct single photon identification (left) and misidentification as π^0 (right) by PCA for high ($\triangle$), medium ($\bullet$) and low ($\diamond$) identification purity levels.

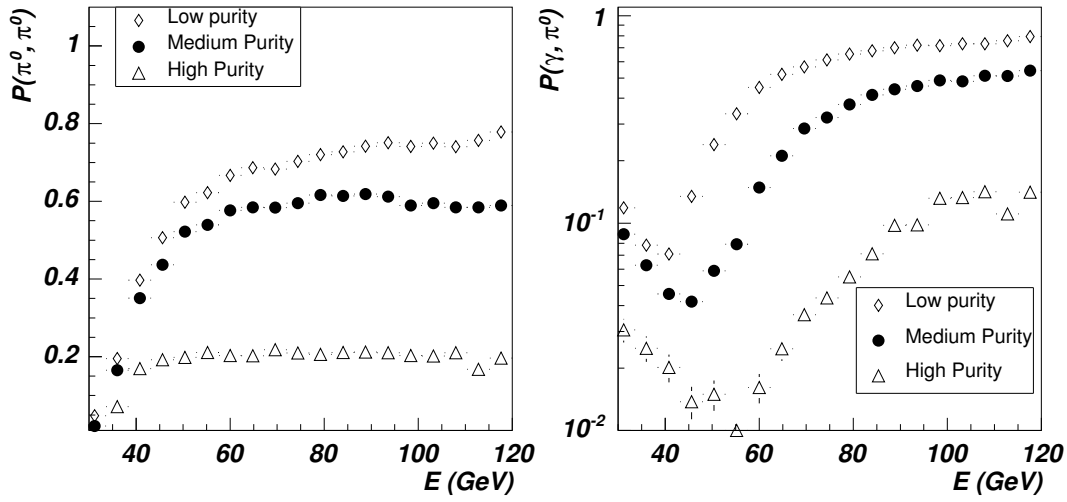

Figure 5.33: Probability of correct π^0 identification (left) and misidentification as photons (right) by PCA for π^0 embedded in a HIC environment (central HIJING events for Pb-Pb collisions at $5.5A$ TeV, $b < 2$ fm) with high ($\triangle$), medium ($\bullet$) and low ($\diamond$) purity levels.

Sec. 5.4 for hard photons. Events with a π^0-meson with transverse momentum uniformly distributed in the range $30 < p_T < 120$ GeV/c were merged with HIJING events for central Pb-Pb collisions. The probability of correct π^0 identification and of π^0 misidentification as photons are shown in Fig. 5.33, and the probability of correct photon identification and of photon misidentification as π^0 are shown in Fig. 5.34. These probabilities are about a 10 % smaller than those for single photon and π^0 identification due essentially to CPV matching failure (as remarked in Sec. 5.4.2.2) for single hard photons, which means that the high detector occupancy existing in a heavy-ion environment does not modify significantly the capability of discriminating hard π^0 from photons by the PCA analysis.

5.6.3 Recognition of photons and π^0 by a neural network

The discrimination of photons and π^0-mesons was also studied in the Artificial Neural-Network (ANN) approach [Pet94] which emerged as a powerful tool for different applications in high-energy physics, [Pet90, Pet91, Bha90, Sca90, Mag97, Ase02].

The PHOS reconstruction program provides sets of photon clusters characterized by the signal amplitudes and coordinates of all the crystals in the cluster. The approach to γ and π^0 recognition by the ANN-method developed by the PHOS group of the IHEP is based on a few characteristic variables which carry major information about the cluster profile. An energy profile tensor Q_{ij} of 2×2 dimension is defined for each cluster as follows

$$Q_{ij} = \sum_k x_i^{(k)} x_j^{(k)} E_k \ , \tag{5.6}$$

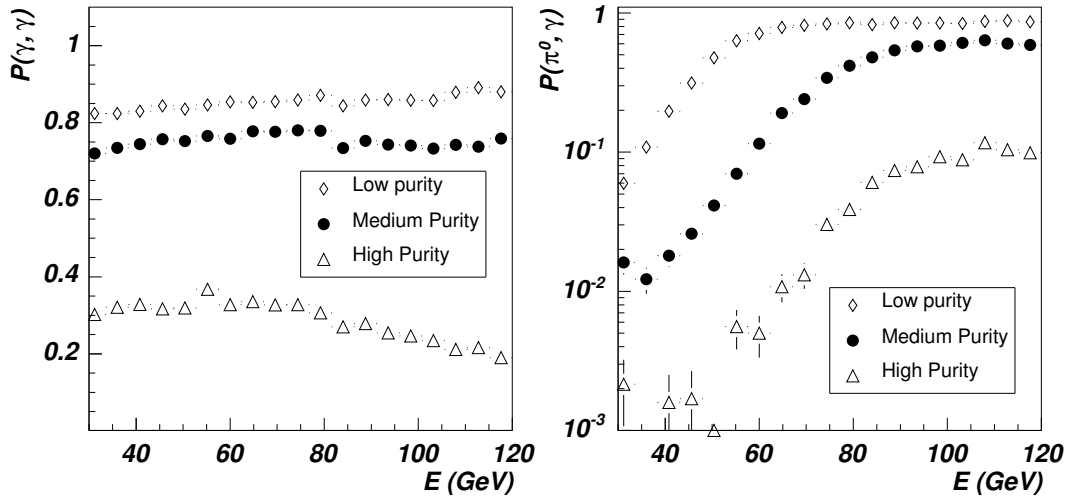

Figure 5.34: Probability of correct photon identification (left) and misidentification as π^0 (right) by PCA for simulated photons embedded in a HIC environment (central HIJING events for Pb-Pb collisions at $5.5A$ TeV, $b < 2$ fm) with high ($\triangle$), medium ($\bullet$) and low ($\diamond$) purity levels.

where index k runs over the cluster crystals, $i, j = 1, 2$ and $\vec{x}^{(k)} = (x_1^{(k)}, x_2^{(k)})$ is the vector of the crystal coordinates in units of the crystal transverse size. The tensor of Eq. (5.6) is similar to the cluster covariance matrix given in Eq. (4.9), apart from the linear energy weights and the lack of averaging. This energy-profile tensor depends on the number of photon showers contained in the cluster as well as on the angle of the photon with the detector surface. To reduce as much as possible this latter dependence, the calculation of the matrix Q_{ij} was made after transforming the cluster crystal coordinates to a system centered in $\vec{X}_0$, defined as the center of the crystal of the cluster with the maximum signal. This transformation is defined by the angle Θ between the normal to the surface of the PHOS module and the direction of the photon as,

$$\vec{x} \rightarrow R(-\phi_0) \cdot E_c(\Theta) \cdot R(\phi_0) \cdot \left(\vec{x} - \vec{X}_0\right) + \vec{X}_0 \ , \tag{5.7}$$

where $\vec{x} = (x_1, x_2)$ is the position vector of the crystal and R and E_c are the rotation and the transformation matrices, respectively:

$$R(\phi_0) = \begin{pmatrix} \cos\phi_0 & \sin\phi_0 \\ -\sin\phi_0 & \cos\phi_0 \end{pmatrix}, \quad E_c = \begin{pmatrix} \cos\Theta & 0 \\ 0 & 1 \end{pmatrix} \tag{5.8}$$

and ϕ_0 is the polar angle of $\vec{X}_0$ in the PHOS module coordinate system.

After the transformation, the two eigenvalues (λ_1, λ_2) and eigenvectors (e_1, e_2) of the

matrix Q_{ij} were ordered as $\lambda_1 \geq \lambda_2$. The matrix Q was reduced to the diagonal

$$Q = \begin{pmatrix} \lambda_1 & 0 \\ 0 & \lambda_2 \end{pmatrix} \tag{5.9}$$

in the coordinate system defined by the eigenvectors. In this new coordinate system, the moments M_{mn} were calculated according to

$$M_{mn} = \sum_k (x_1^{(k)})^m \cdot (x_2^{(k)})^n \; E_k \; , \tag{5.10}$$

where index k runs over the cluster crystals. It should be mentioned that the invariant mass $M_{\gamma\gamma}$ of two photons can be expressed in terms of the moments M_{mn} [Bit81, Bog04]. The angle ϕ between the eigenvector $\vec{e_1}$ and the vector $\vec{X_0}$ is a useful variable for the analysis by the ANN method. This variable helps to improve the quality of γ and π^0 discrimination in the peripheral region of PHOS modules. The input vector $\vec{P}^{(\mathrm{in})}$ for ANN was composed of the following variables: the energy E of the cluster, the eigenvalues λ_1 and λ_2, the momenta M_{10}, M_{30}, M_{40} and M_{04}, the distance d between the hit of the two photons at the PHOS surface, the invariant mass $M_{\gamma\gamma}$ and the angle ϕ. The ANN for γ and π^0 discrimination was composed of the three layers shown in Fig. 5.35: input, hidden and output. The input layer consisted of N nodes, where N is the dimension of the vector $\vec{P}^{(\mathrm{in})}$; the hidden layer was built of $2N+1$ nodes; finally, a one-node output layer provided the response S_{NN} used for the final event classification.

The network was trained with samples of clusters from direct photons and from background (clusters produced by overlapped photons from π^0 decay). Each sample contained 10,000 clusters. Upon training the net, we tested its efficiency with two statistically independent samples, each consisting of 30,000 events. The data for the analysis were simulated with AliRoot v.3.06.02. Single photons and neutral pions were emitted from the interaction point with uniformly distributed transverse momentum in the range $0 < p_T < 120$ GeV/c within the solid angle defined by the azimuthal and polar angle range $210^\circ < \phi < 330^\circ$ and $80^\circ < \theta < 100^\circ$, respectively. The solid angle of the emitted particles was chosen to be a bit larger than the subtended by PHOS to avoid border effects. A noise with $\sigma_{\mathrm{noise}} = 10$ MeV was added to the energies deposited in single crystals and a 50 MeV threshold was applied to the sum of signal and noise. The neighbour crystals were grouped into clusters. Only clusters with total energy greater than 500 MeV were accepted.

The achieved γ and π^0 discriminating power of the ANN after network training is shown in Fig. 5.36 for the event feature vectors $\vec{P}^{(\mathrm{in})} = (E, \lambda_1, \lambda_2, M_{30}, M_{04}, \phi)$. This figure shows the probability $P(\gamma, \gamma)$ of correct photon identification and $P(\gamma, \pi^0)$ of π^0 misidentification as a photon in the energy interval from 3 GeV to 120 GeV, as well as

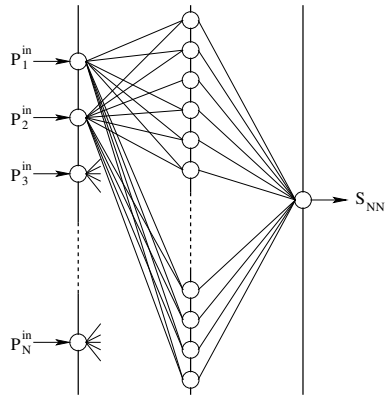

Figure 5.35: Architecture of the ANN employed for γ and π^0 discrimination.

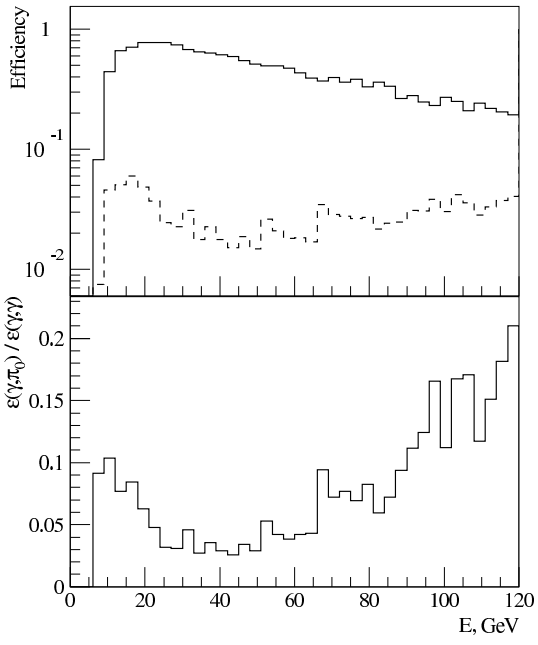

Figure 5.36: Probability $P(\gamma,\gamma)$ of correct photon identification (solid lines, upper plot) and misidentification $P(\gamma,\pi^0)$ of π^0-mesons as photons (dotted lines, upper plot), and the ratio $P(\gamma,\pi^0)/P(\gamma,\gamma)$ (lower plot).

the π^0 background suppression coefficient $P(\gamma,\pi^0)/P(\gamma,\gamma)$. In this figure it is seen that the probability of misidentification of a neutral pion as a photon is a few percent in the energy range from 3 to 120 GeV and that the correct photon identification probability in this energy range is relatively high.

5.6.4 Methods comparison

The ANN and the one-dimensional shower-shape analysis have similar background suppression coefficients in the energy range $40 < E < 120$ GeV. The one-dimensional shower shape analysis gives the best correct photon identification probability but identifies more π^0 as photons than the ANN, specially in the energy region $70 < E < 120$ GeV where the probability increases from 3 % at 70 GeV to about 15 % at 120 GeV while the misidentification probability given by the ANN varies between 2 % and 5 %. Both methods produce a better neutral pion rejection for $E > 70$ GeV than the PCA approach for any identification purity level. We may improve the results of the PCA approach by looking for the best ellipse in the two principal component space for discriminating γ and π^0 as a function of the energy, similarly to the search of the best M^0_{2x} limit done for the one-dimensional shower-shape analysis.

The identification probabilities obtained with the ANN and the one-dimensional shower shape analysis for PHOS are better than those found for the electromagnetic calorimeters of the STAR experiment, where the misidentification probability $P(\gamma,\pi^0)$ was estimated to be 15 % at 20 GeV and 45 % at 40 GeV [Min94], and the CMS experiment, for which $P(\gamma,\pi^0)$ is about 50 % at 20 GeV and between 55 to 60 % at 100 GeV [Rei00]; concerning photon and π^0 discrimination, PHOS is more efficient than those experiments.

5.7 Identification of high-energy photons converted into electron pairs

The presence of the TRD and TOF detectors in front of PHOS will perturb the photon yield detected in PHOS, as discussed in Sec. 4.8. Photons interact with the material of these detectors and produce conversion electrons ($\gamma \rightarrow e^- e^+$). I discuss here how high-energy photons converted into electron pairs can be identified, and how important is the conversion effect due to the TRD and TOF detectors. The need of a configuration with holes in TRD and TOF to obtain reliable data with PHOS is discussed.

5.7.1 Converted photons reconstruction

The electrons created by a photon converted in the material between the TPC and PHOS can be identified because there is no matching track in the TPC pointing to the hit in

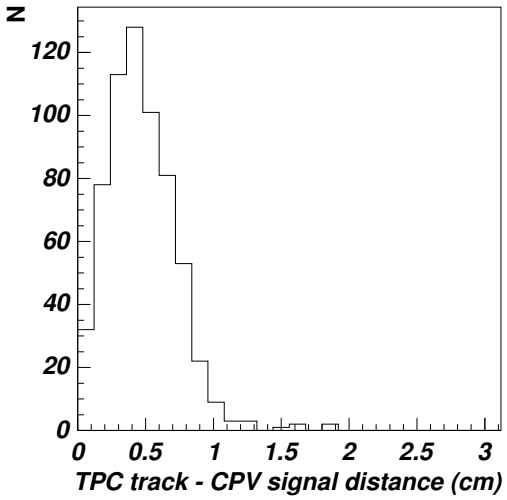

Figure 5.37: Distribution of the distance between the outer track in the TPC and the impact point in the CPV for electrons with energy uniformly distributed between 10 and 40 GeV.

the CPV of PHOS produced by those electrons. To minimize random matching in the heavy-ion environment, it is important to control accurately the matching criteria. For this purpose, electrons with energies between 10 and 40 GeV were simulated and the distance between the TPC track and CPV signal was studied. The distribution of the distance between the endpoint of the track in the TPC and the hit on the CPV is shown in Fig. 5.37. Although according to this figure, the maximum distance is about 2 cm, we have set the maximum to 4 cm in the matching algorithm to ensure that low-energy electrons which are more bent by the magnetic field are not rejected. More accurate simulations are needed to find the optimum value of the maximum matching distance.

In order to study the reconstruction of electrons produced by photon conversion, I generated photons with energy uniformly distributed between 10 and 40 GeV for the setups with and without holes. Particles identified as charged particles by the CPV but not detected by the TPC and identified as photons by the PCA were tagged as *conversion electrons*. In this section, particles are identified as photons with low purity level; electrons are identified as low purity photons by the PCA and as charged particles by the CPV and the TPC. The probability of identifying conversion electrons as single photons is about 50-60 % in the energy range $E < 40$ GeV, as seen in Fig. 5.38.

In order to recover the original photons from the conversion electrons, the invariant mass of all possible pairs of identified conversion electrons was calculated. If the invariant mass was small, the pair came likely from a photon of energy close to the total energy of the pair. If only an isolated conversion electron was detected, we assumed that both electrons flied so close to each other that PHOS could not separate them, and the energy of this isolated electron was taken as the energy of the parent photon. In Fig. 5.39, the invariant mass distribution of the conversion pairs is displayed, without and with a HIC

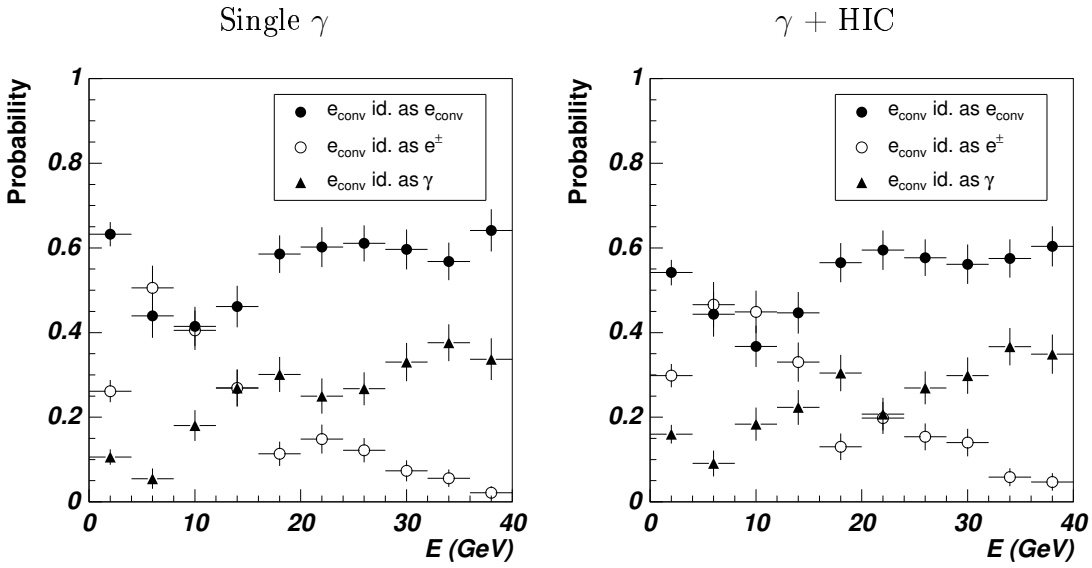

Figure 5.38: Probability of identifying electrons produced by conversion of photons in the material in front of PHOS as conversion electrons (•), electrons (○) and photons (▲). Results are shown for simulations of single photons with a uniform energy distribution from 10 to 40 GeV (left) and single photons merged with central HIJING events for Pb-Pb collisions at $5.5A$ TeV and $b < 2$ fm (right).

environment. In the first case the invariant mass distribution peaks at 0-0.2 MeV/c^2 for reconstructed energies between 10 and 40 GeV. In the case of a HIC environment, the invariant mass distribution is broader and we identified as photons conversion pairs of invariant mass smaller than 20 MeV/c^2.

5.7.2 Photon identification in PHOS

The photon identification probability is shown in Figs. 5.40 and 5.41 for the configurations without and with holes, respectively. Photons, conversion pairs and electrons were identified in PHOS as photons as stated above. From these figures and Fig. 4.27 we conclude:

- In the configuration with holes, about 10 % of the photons suffer conversion somewhere between the IP and the CPV. Conversion electrons produced in the TPC are mostly tagged as electrons.

- In the configuration without holes, about 30 % of the photons are converted into electrons, of which 20 % are converted in the TRD and TOF. Between 10 and 20 % of the photons can be recovered by conversion pair identification. If we add the identified conversion pairs to the identified photons, the identification probabilities for the configuration with and without holes are close.

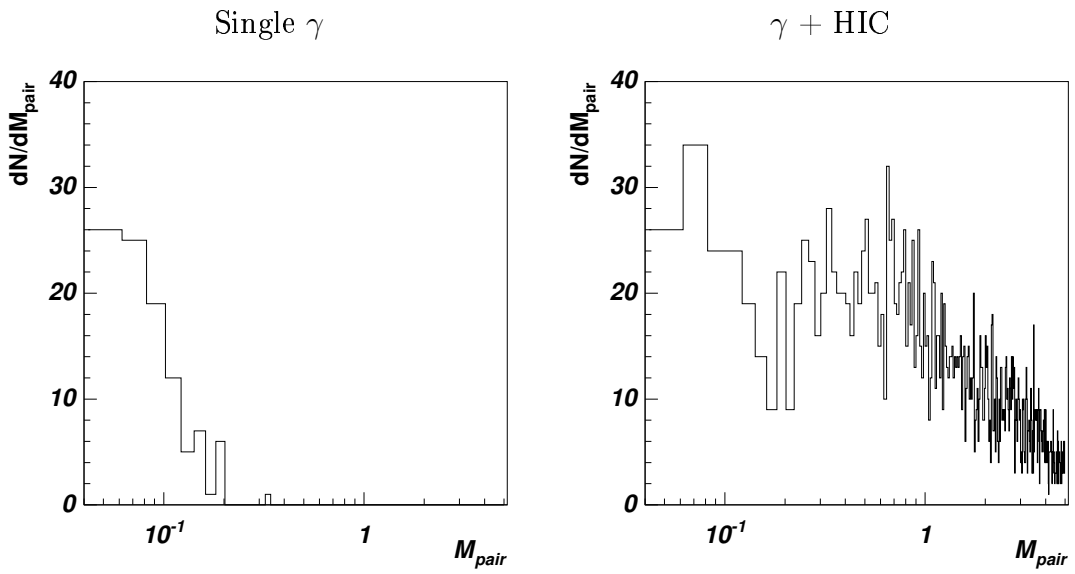

Figure 5.39: Invariant mass of conversion electron pairs with energies between 10 and 40 GeV for simulated single photons (left) and simulated photons merged with a HIC environment (right).

The ratio of the number of identified photons to the sum of identified photons and conversion pairs is plotted in Fig. 5.42. We see in this figure that for single photons in the configuration without holes the inclusion of conversion pair identification improves the photon identification by 20 %. For photons merged with HIC events, although apparently about 15 % of the photons are additionally recovered by including conversion pairs, what it is actually identified as additional photons is mostly contaminating particles from the HIC background.

5.7.3 Neutral pion detection in PHOS

In this section, I study neutral pion identification along the lines of the previous section. Simulated π^0 mesons in the energy range 10-40 GeV for the setups with and without holes were generated. Pions were identified through: the invariant mass of photon pairs; the invariant mass of photons and conversion pairs; and by shower shape techniques, identifying overlapped photons as neutral pions. Figure 5.43 shows the identification probability of photon pairs from π^0 decay in the invariant mass window $0.1 < M_{pair} < 0.17$ MeV/c^2. In the energy range from 10 to 30 GeV, the identification probability was about 70-80 % for the setup with holes and about 50-60 % for the setup without holes. To identify π^0 in a HIC environment by the pair invariant mass, a more restrictive window was necessary. With $0.12 < M_{pair} < 0.15$ MeV/c^2 and an opening angle window as defined in Sec. 7.2.2, the pair identification probability was reduced to 30-40 %, as shown in Fig. 5.44 for the setup without holes and in Fig. 5.45 for the setup with holes. We can summarize these results as follows:

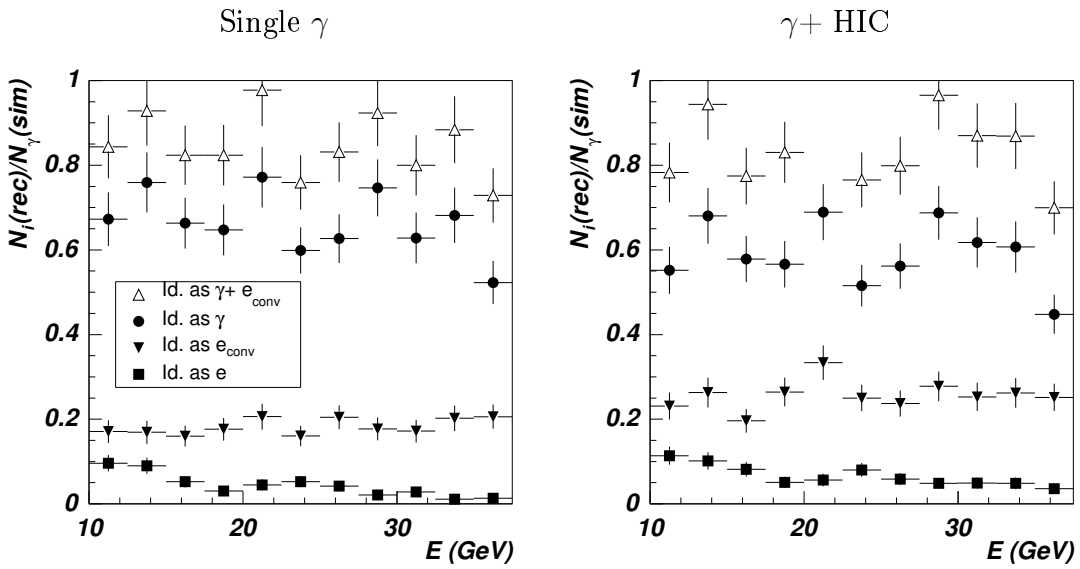

Figure 5.40: Probability of identifying photons as photons, conversion pairs or electrons for the setup without holes for single photons (left), and photons merged with HIJING events(right).

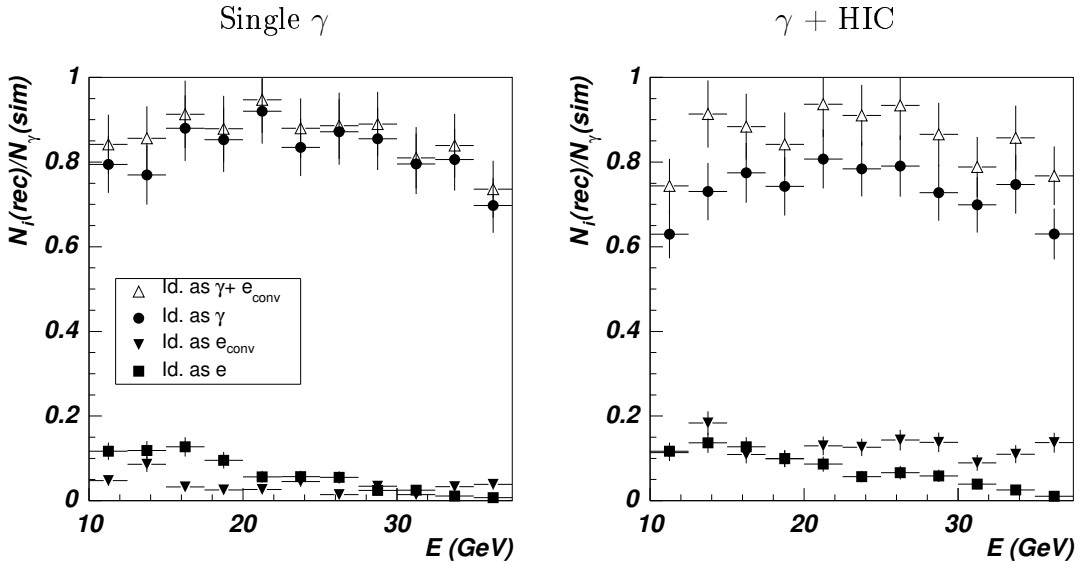

Figure 5.41: Probability of identifying photons as photons, conversion pairs or electrons for the setup with holes for single photons (left) and photons merged with HIJING events (right).

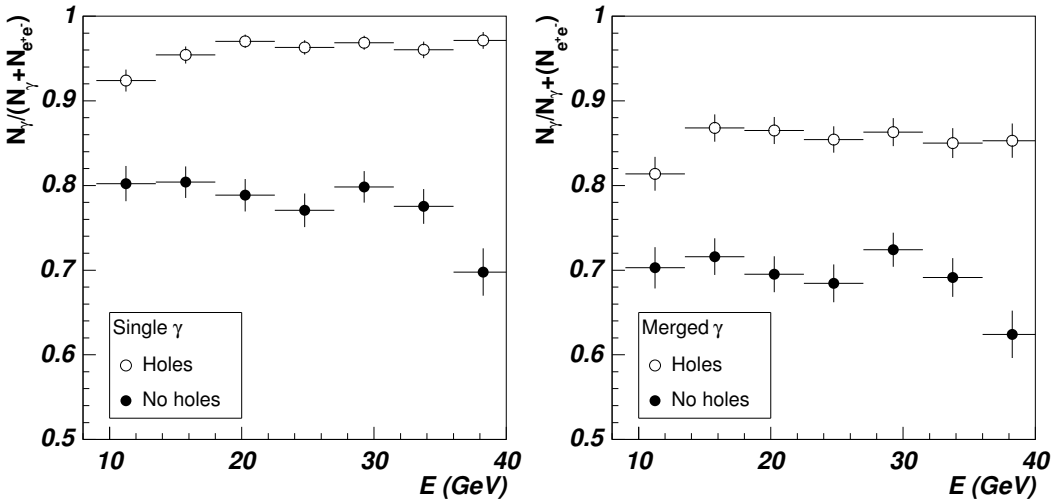

Figure 5.42: Ratio of particles identified as photons to particles identified as photons or conversion electron pairs with invariant mass smaller than 20 MeV for the setups with and without holes, for single photons (left) and photons merged with HIJING events (right).

- There is no significant improvement of the π^0 identification probability by the inclusion of converted pairs for the setup with holes.
- In the case of the configuration without holes, the inclusion of conversion pairs improves the single π^0 identification probability from about 20 % obtained without considering conversion pairs to about 40 %. In the case of a HIC environment, the neutral pion identification probability improves from about 15 % to about 30 %.

The ratio of the identification probabilities determined without and with conversion pair identification, shown in Fig. 5.46, indicates that the inclusion of converted pairs increases the single π^0 identification probability by about a 40 % for the setup without holes but by only a few percent for the setup with holes. In the case of a HIC environment, the apparent improvement is actually due to background identified as conversion pairs.

5.8 Conclusions

I have developed particle identification methods that allow to identify and measure the momentum of photons, electrons and π^0 mesons with PHOS in the energy range form 0.5 to 120 GeV; charged hadrons are efficiently rejected in this energy range.

I have also investigated methods to recover photons converted into electron-positron pairs. They seem to be most useful for proton-proton collisions in the ALICE configuration without holes.

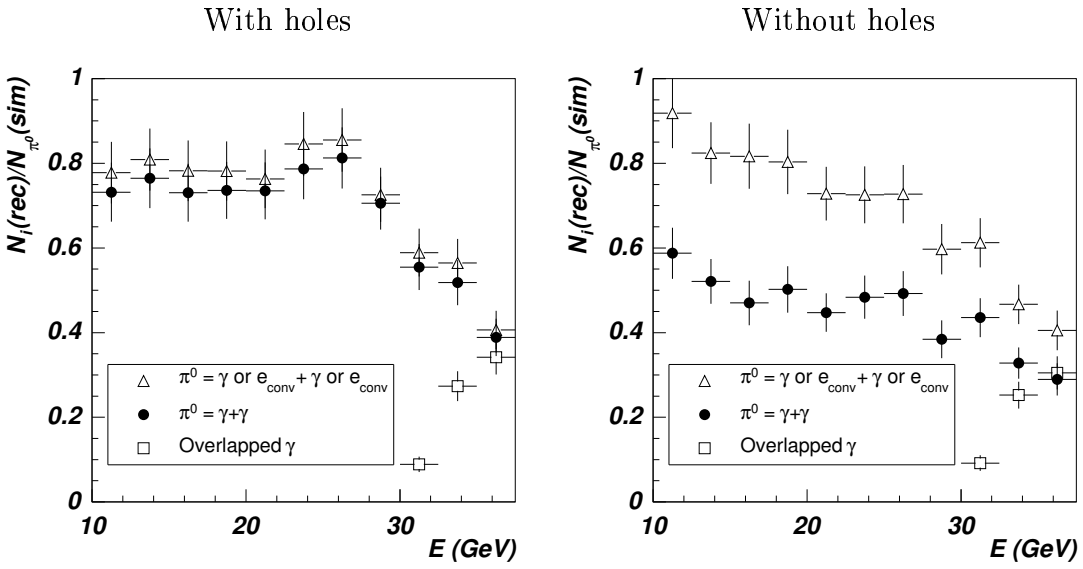

Figure 5.43: Probability of identifying single neutral pions by the invariant mass analysis with the invariant mass window $0.1 < M_{pair} < 0.17$ MeV/c^2, and by the shower shape analysis (overlapped clusters), for the configurations with holes (left) and without holes (right). The probability for the invariant mass analysis for photon pairs (•) and for photons and pairs of conversion electrons (○) is given.

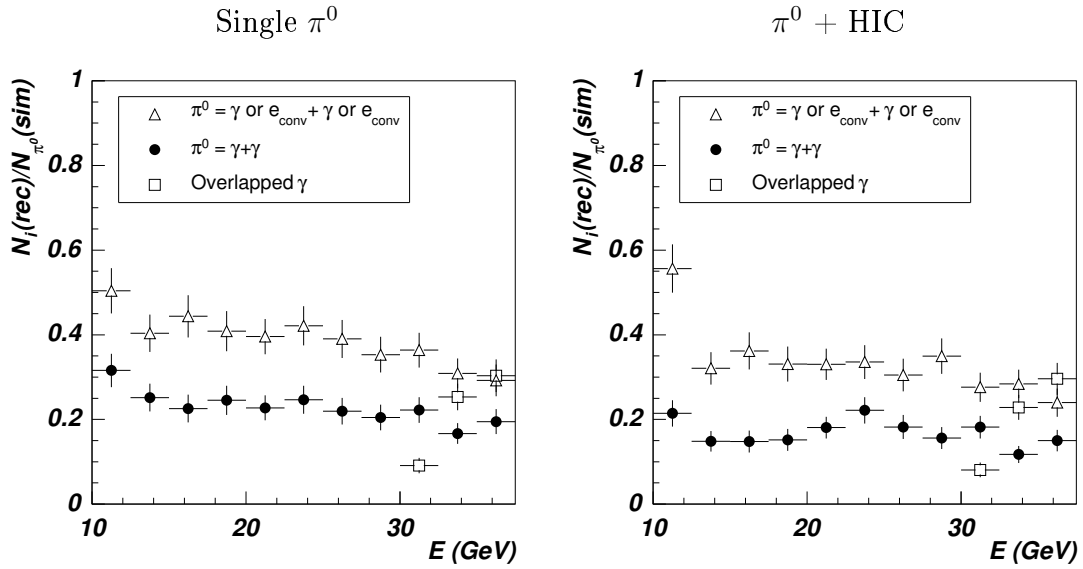

Figure 5.44: Probability of identifying neutral pions by the invariant mass analysis for $0.12 < M_{pair} < 0.15$ MeV/c^2 and opening angle defined in Sec. 7.2.2 and by the shower shape analysis (overlapped clusters), for the setup without holes. The probability for the invariant mass method for photon pairs (•) and for photons and pairs of conversion electrons (○) for single π^0 (left) and π^0 merged with HIJING events (right) is given.

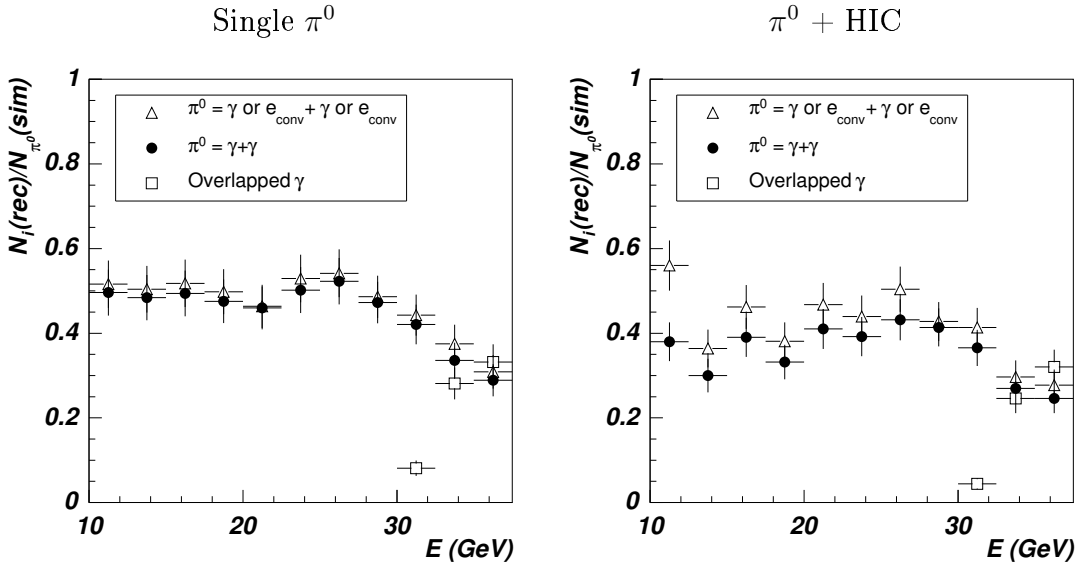

Figure 5.45: Probability of identifying neutral pions by the invariant mass analysis for $0.12 < M_{pair} < 0.15$ MeV/c^2 and opening angle defined in Sec. 7.2.2 and by shower shape analysis (overlapped clusters), for the setup with holes. The probability for the invariant mass method for photon pairs (•) and for photons and pairs of conversion electrons (○) for single π^0 (left) and π^0 merged with HIJING events (right) is given.

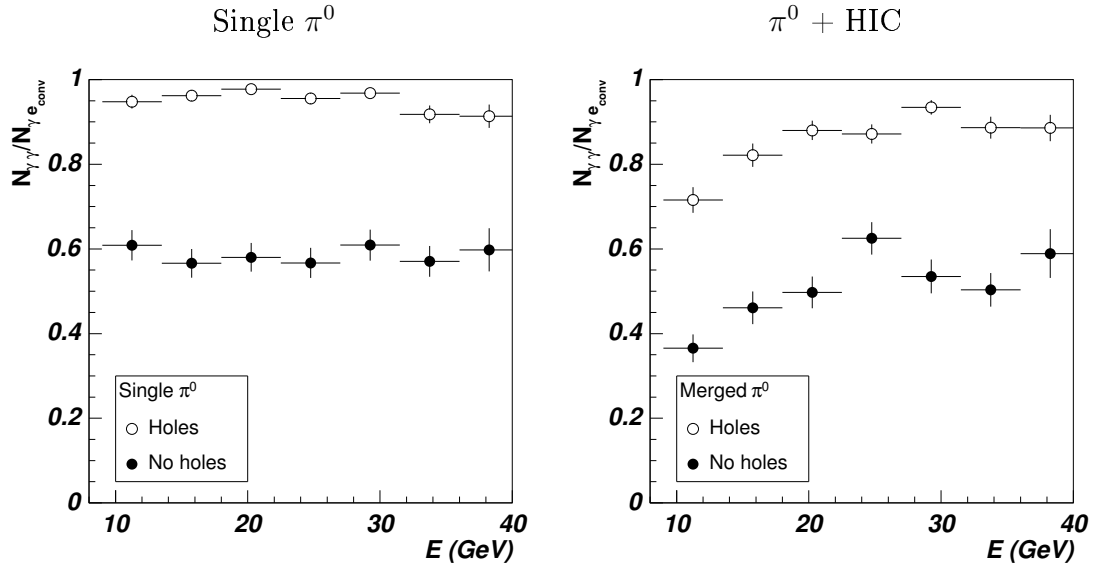

Figure 5.46: Ratio of neutral pions identified by the invariant mass of photon pairs to neutral pions identified by both photon pairs and of photons and pairs of conversion electrons for the configurations with (○) and without (•) holes for single π^0 (left) and π^0 merged with HIJING events (right).

Chapter 6

Prompt photon identification

In this chapter, I present some methods for identifying prompt photons produced in hard parton scattering based on shower topology analysis and isolation criteria. Prompt photons are of particular importance because they have an associated jet in their opposite direction. Prompt photons identified in PHOS trigger their search of the corresponding jet. These jets carry information about the production of a strongly interacting matter, as reported in the next chapter.

6.1 Event simulation and detection main reconstruction features

In this section, I present simulations of prompt photon and jet detection which are the basis of this and next chapter. Prompt photons are detected by PHOS whereas charged particles streaming from jets are detected by the ALICE central tracking system, the TPC, and neutral particles in the EMCal (if available).

Concerning the event generation, prompt photon production was calculated in the leading order of the Standard Model. The dominant parton-level processes contributing to γ-jet events are given by Eq. (3.2). These processes were simulated by the event generator PYTHIA, described in Sec. 3.3.1, for pp collisions at $\sqrt{s} = 5.5$ TeV. Since the production cross sections drop very quickly with p_T, events were sampled in the following $\langle p_T \rangle$[1] bins: $[20, 40]$, $[40, 60]$, $[60, 80]$, and $[80, 100]$ GeV/c. To obtain the continuous differential cross sections over the whole p_T-range, these four samples were combined with weights corresponding to their cross sections as calculated by PYTHIA. In order to enrich the sample with events in the PHOS acceptance, we restricted the event generation: the prompt photon rapidity in the final event center-of-mass system satisfied $|\eta_\gamma| < 0.2$, and the azimuthal angle range was $200° < \phi_\gamma < 340°$. Particles were generated in a solid angle

[1]Here $\langle p_T \rangle$ refers to the transverse momentum of the hard $2 \to 2$ processes in their center-of-mass system.

somewhat wider than the detector acceptance to avoid boundary effects. We performed also a few γ-jet simulations with quasi mono-energetic photons ($\Delta E_\gamma = 0.1$ GeV) of 5, 10, 20, 40, 60 and 80 GeV, to test with high statistics the jet reconstruction capability of our algorithm at well defined jet energies (Sec. 7.3).

Events with two jets in the final state, called jet-jet events, are a significant source of background. They were simulated by hard QCD $2 \rightarrow 2$ processes in the leading pQCD order [Eq. (3.3)]. These processes contribute to the background through fragmentation in π^0-mesons whose decay photons may be detected in PHOS as single electromagnetic showers which mimic prompt photons. Among the background contributions, the bremsstrahlung process has also to be considered. To simulate a continuous p_T spectrum of π^0-mesons from 20 to 100 GeV/c, we generated hard QCD events in eight bins of 10 GeV/c width in the $\langle p_T \rangle$ range from 30 to 100 GeV/c and in four more bins of 50 GeV/c width in the $\langle p_T \rangle$ range from 100 to 300 GeV/c. The full p_T spectrum was taken as the combination of these event samples weighted by their corresponding cross sections. The generation of hard QCD processes was restricted in the outgoing parton center-of-mass system to $|y_{parton}| < 0.2$ and in the outgoing jets center-of-mass system to $|\eta_{jet}| < 0.15$, without any azimuthal angle limitation. In the jet-jet case, we needed to apply a more severe restriction in rapidity than in the γ-jet case because due to the small size of PHOS the background statistics is too low in wide rapidity ranges. The values of the cross sections and the number of γ-jet and jet-jet events generated are given in Tab. C.1.

To simulate Pb-Pb collisions events we assumed that a Pb-Pb collision is equivalent to a *pp* collision plus a heavy-ion underlying event. Thus, *pp* collisions generated by PYTHIA, were merged with heavy-ion events produced by HIJING for Pb-Pb collisions at $\sqrt{s_{NN}} = 5.5A$ TeV and impact parameter $b < 2$ fm.

The simulations were done for the ALICE environment with holes in the TRD and TOF detectors.

The aim of our investigation is to develop an algorithm capable of identifying prompt photons and γ-jet events, and rejecting most misidentified jet-jet events. There are significant discrepancies between the event generators PYTHIA, HERWIG and NLO calculations. In the present state of knowledge, there is no definitive argument in favor of any of these generators. In such circumstances, we assume that PYTHIA is a reasonable choice to demonstrate the validity of our approach.

6.1.1 Expected experimental rates

The p_T distributions obtained from simulations were normalized to the number of events expected in a standard year of LHC running, given in Tab. 3.1. As we simulated p_T bins with different number of events, we proceeded in the following way:

Centrality (%)	f_C	$\langle T_{AA}\rangle_C$ (mb^{-1})
5	0.05	26.0
10	0.1	23.2
Minimum bias	1	5.58

Table 6.1: Values of the nuclear overlap functions and of the centrality factor as a function of the Pb-Pb collision centrality, taken from [Arl03].

- The raw distributions N_i were normalized to the number of simulated events N_{Evt} in each $\langle p_T\rangle$ bin and to the cross sections assigned by PYTHIA (Appendix C). Finally, the different distributions were combined to obtain the differential cross section as a function of p_T.

- The differential cross section was multiplied by the integrated luminosity expected in a year of running; the luminosity $\mathcal{L}$ and the running time are listed in Tab. 3.1. Here, we follow a quite standard procedure described in detail in [Aph02] and [Arl03], known as "binary scaling". For Pb-Pb collisions, the *pp* PYTHIA events are scaled to the average number of *NN* collisions by multiplying the corresponding differential *pp* cross section by the product of the nuclear overlap function $\langle T_{AA}\rangle_C$ for the appropriate centrality class *C,* by the centrality factor f_C and by the geometrical cross section $\sigma_{AA}^{geo} = 7745$ mb as postulated in Eq. (133) of [Arl03], i.e.

$$\left(\frac{d^2\sigma_{AA}^{PYTHIA}}{dp_T dy}\right)_C = \langle T_{AA}\rangle_C \cdot \sigma_{AA}^{geo} \cdot f_C \cdot \frac{d^2\sigma_{pp}^{PYTHIA}}{dp_T dy} \tag{6.1}$$

  The appropriate values of the nuclear overlap function and f_C are listed in Tab. 6.1. We consider minimum bias collisions.

This procedure leads to the expected spectra of prompt photons (γ-jet) and γ-like (jet-jet) in *pp* and Pb-Pb collisions at $5.5A$ TeV detected in PHOS during a standard year of LHC running, displayed in Fig. 6.1. We denote as photon-like any photon which is not prompt, including bremsstrahlung and decay photons from jet-jet events. The decay photons from jet-jet events may be detected in PHOS either as single or as overlapped[2]. Due to the PHOS geometry, overlapped clusters are produced predominantly by π^0 of energy beyond 40 GeV (see Fig. 6.2). All these photons constitute a background for prompt photon identification and contribute predominantly to the inclusive photon spectrum. Figure 6.3 shows the separate contribution of the spectrum of jet particles arriving to PHOS (single and overlapped photons produced by π^0 decays, bremsstrahlung and other hadrons). From this figure, the change of behaviour of the photon-like spec-

[2]An energetic π^0 decays into two photons whose opening angle is too small. In such a case, the two showers cannot be separated by PHOS, creating a single cluster. We call this kind of event overlapped photon or one-cluster π^0.

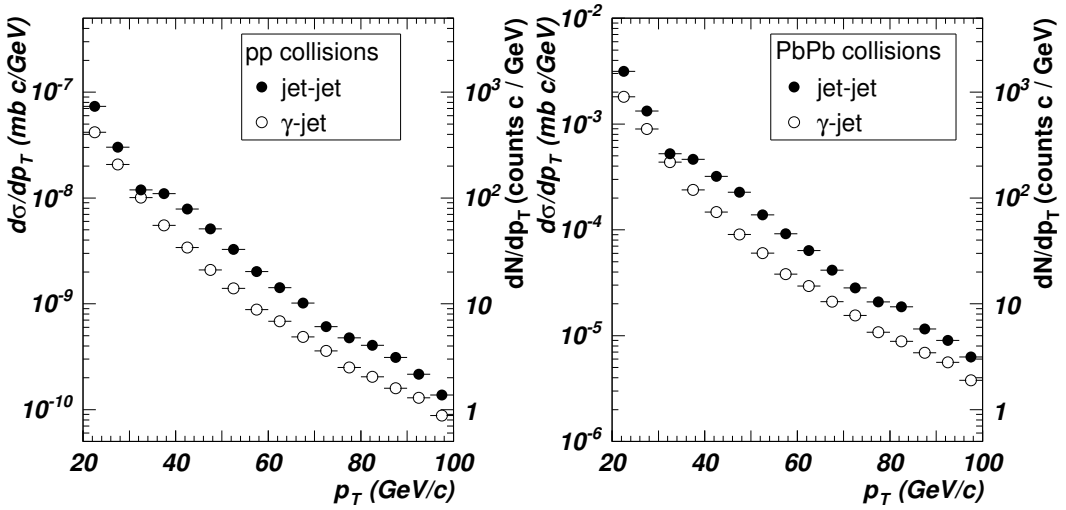

Figure 6.1: Spectra of prompt photons (γ-jet events, $\circ$) and γ-like (single and overlapped photons from jet-jet events, $\bullet$) detected in PHOS, for pp (left) and minimum bias Pb-Pb (right) collisions at $\sqrt{s_{NN}} = 5.5A$ TeV. Differential cross sections are given on the left y-axis of the plots and the expected number of particles on the right y-axis. Both quantities are determined for a standard LHC running year.

trum at 30-40 GeV/c observed in Fig. 6.1 can be explained. Below 30-40 GeV/c, the contribution of overlapped decay photons is not important while for higher energies one-cluster π^0 mesons produce the main contribution; the addition of both spectra produces the observed behaviour.

6.2 Particle identification with PHOS

In this section, prompt photon identification and rejection of hard π^0 contamination are discussed. The identified prompt photon spectrum expected to be measured in one running period is presented.

Two different procedures to select prompt photons were applied: the Shower Shape Analysis (SSA) described in Chap. 5, and the Isolation Cut Method (ICM). The former identifies photons by analysing the shape of the shower, and the latter tags and identifies a photon as prompt if it appears isolated, i.e. without charged particles in its vicinity.

For this study, we used the simulated PYTHIA (pp) and PYTHIA + HIJING (Pb-Pb) events described in Sec. 6.1, but we performed a full-fledged Monte Carlo simulation of the transport of particles in PHOS. Also, we used the information of the charged particles collected in the acceptance of the ALICE central tracking system (only in ICM), but applying the fast reconstruction method described in Sec. 7.1.2.

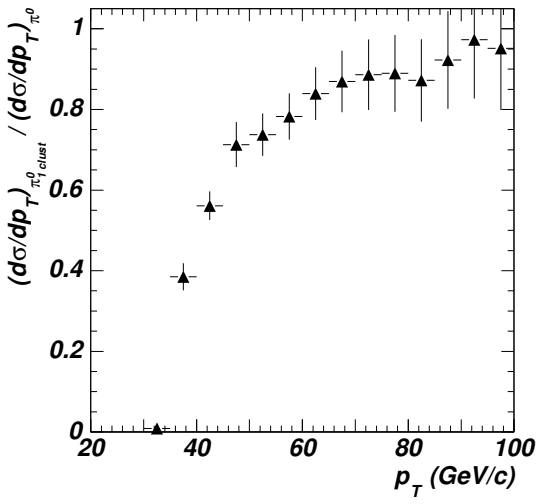

Figure 6.2: Ratio of the one-cluster π^0 detected in PHOS to the total generated π^0 spectrum.

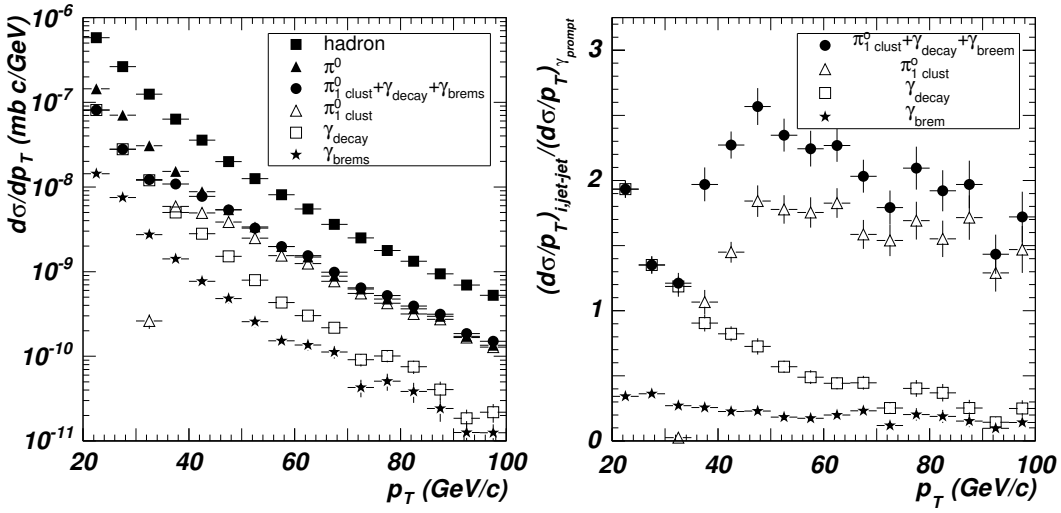

Figure 6.3: Left frame: Spectra of different particles detected in PHOS streaming from a jet-jet event in pp collisions at $\sqrt{s} = 5.5$ TeV; (▲) total hard π^0; (△) one-cluster π^0 detected in PHOS; (□) photons from decay (not overlapped); (•) one-cluster π^0 plus photons from decay plus photons from bremsstrahlung; (■) total hadron spectrum; (★) photons from bremsstrahlung. Right frame: Ratio of generated photon-like particles in jet-jet events to prompt photon in γ-jet events: one-cluster π^0 (△); two-cluster π^0 (□); photons from bremsstrahlung (★); the sum of these three contributions (•).

6.2.1 Shower shape analysis (SSA)

The photon spectra of γ-jet and jet-jet events were identified with different identification purity levels by the PCA analysis and the one-dimensional shower-shape analysis[3] (methods described in Secs. 5.3 and 5.6.1, respectively). Figure 6.4 shows the identified photon spectrum with medium purity level detected in PHOS during one LHC running period. The identification probabilities, calculated as the ratio of the identified to the simulated spectra of Fig. 6.1, is about 90 % for *pp* collisions and about 75 % for Pb-Pb collisions for medium purity photons, as observed in Fig. 6.5. In the case of one-cluster π^0, the misidentification probability ranges from 0 to 40 % (Fig. 6.6-upper) and for hadrons it ranges from 5 to 15 % (Fig. 6.7-upper). The π^0 background from jet-jet events, quantified as the photon to π^0 ratio shown in the lower part of Fig. 6.6, remains still too high. If we require high purity level photons and hard dispersion, the improvement of rejection is accompanied by an unacceptable reduction of the photon identification efficiency. To improve the situation, new identification procedures have to be developed.

6.3 Isolation Cut Method

Prompt photons are produced in parton collisions in which the final state photon and parton are emitted back-to-back. As there is no hadron from the parton jet flying in the same direction as the photon, the latter should appear isolated[4]. However, the underlying event generated by the heavy-ion collision may perturb this ideal topology. To overcome this difficulty, we developed two isolation cut methods. Both methods search for hadrons inside a cone centered around the direction (η_0, ϕ_0) of high-p_T photon candidates ($p_T >$ 20 GeV/c) identified by the SSA. The cone size is given by

$$R = \sqrt{(\phi_0 - \phi)^2 + (\eta_0 - \eta)^2}. \tag{6.2}$$

In Fig. 6.8, multiplicity distributions for γ-jet and jet-jet events as a function of p_T are shown for both *pp* and Pb-Pb collisions. The multiplicity depends on the cone size and on the event type. For γ-jet events in *pp* collisions, there is almost no particle inside the cone, independently of the energy of the prompt photon but for jet-jet events there is a clear dependence of the multiplicity with the jet energy. Thus, applying p_T cuts to the particles in a cone around a photon candidate helps to distinguish between γ-jet and jet-jet events. Following this idea, we developed two different selection criteria to decide if a photon candidate is isolated and should be tagged as a prompt photon:

[3] Denoted as "hard dispersion" in the legend of figures and in text.

[4] This is not true for next to leading order processes like bremsstrahlung. However, PYTHIA predicts that such processes are suppressed compared to the other processes of Fig. 6.3. This statement might have to be revised considering recent studies [Arl04], which suggest that at high p_T the bremsstrahlung could be a dominant process ($p_T < 50$ GeV/c).

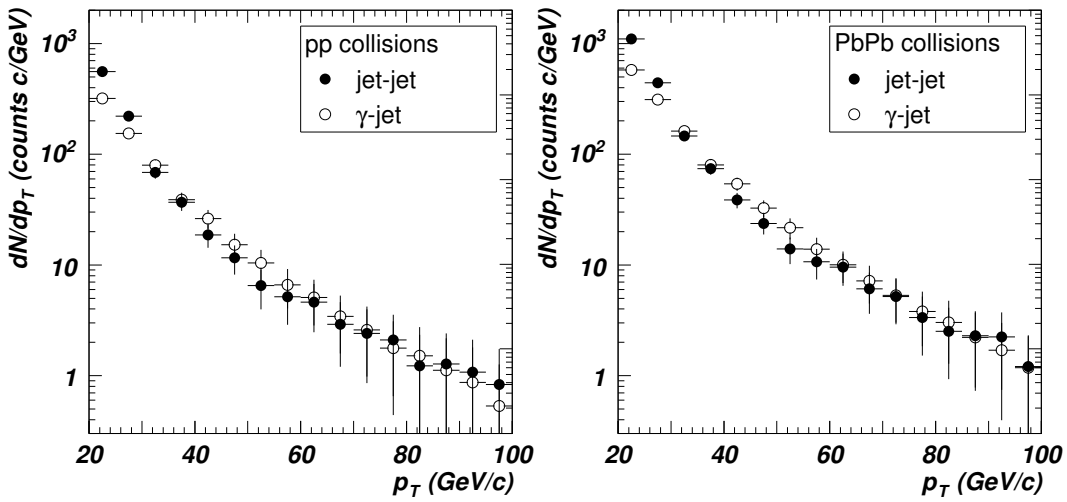

Figure 6.4: Identified medium purity photon spectra in jet-jet (•) and γ-jet events (○) with shower shape analysis in pp (left) and Pb-Pb (right) collisions at $5.5A$ TeV for the expected luminosity in a standard LHC running year.

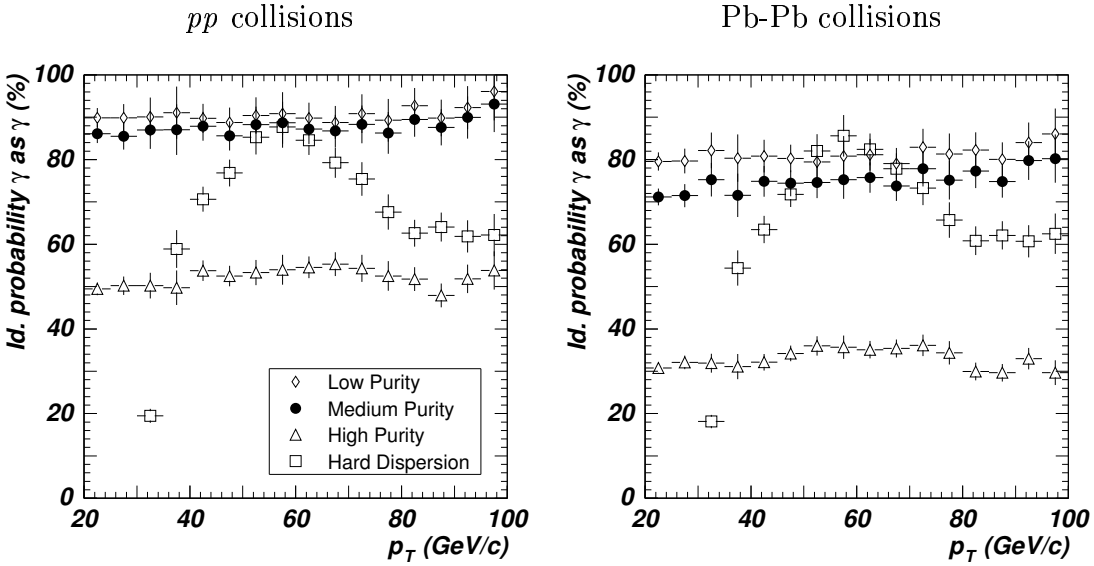

Figure 6.5: Identification probabilities in PHOS of prompt photons from γ-jet events by the shower shape analysis for pp (left) and Pb-Pb (right) collisions. The different identification purity levels defined for PHOS have been considered. The assumed beam energy is $\sqrt{s} = 5.5A$ TeV.

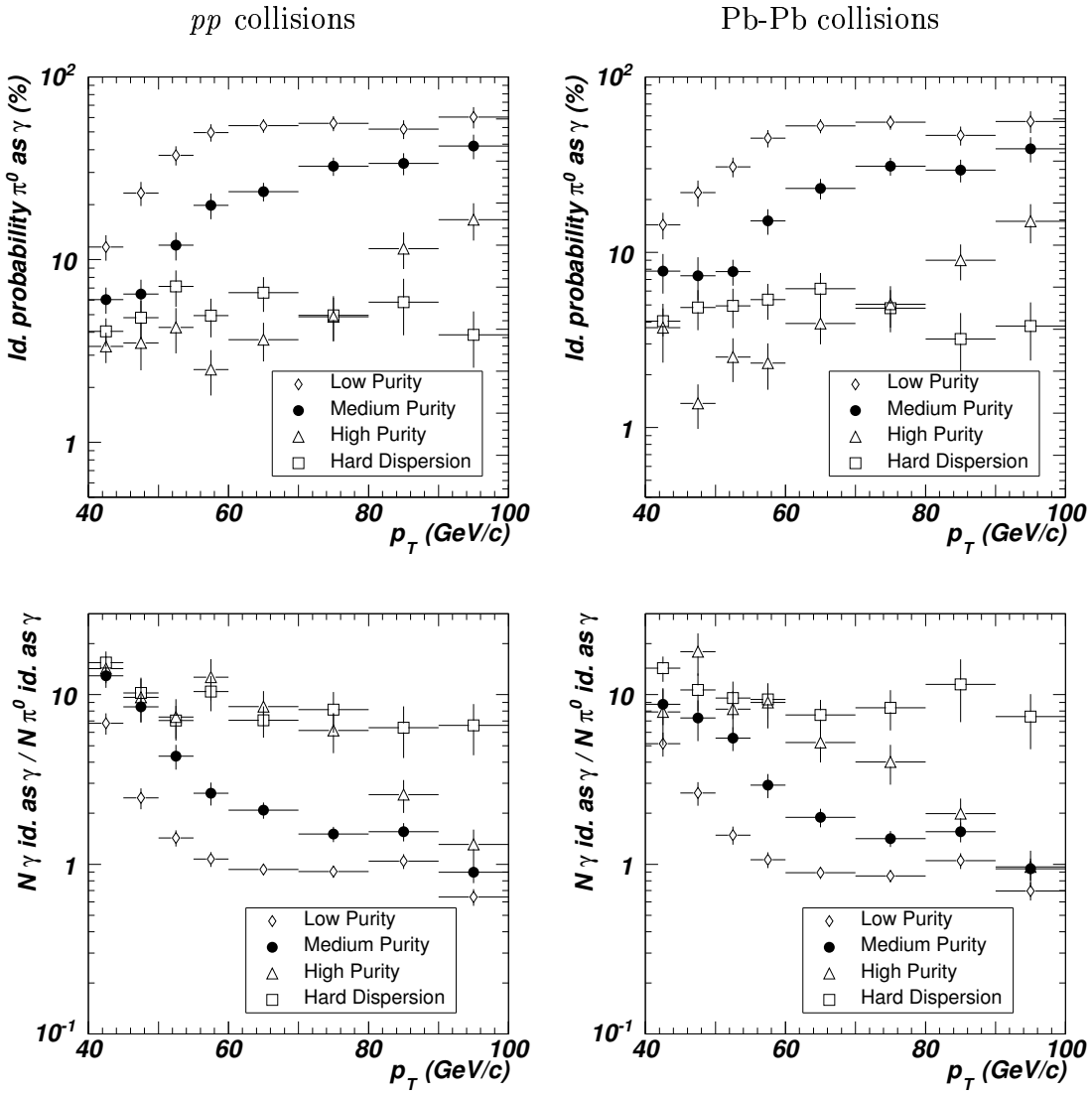

Figure 6.6: Upper frames: Misidentification probability of one-cluster π^0 from jet-jet events as a photon by the shower shape analysis for *pp* (left) and Pb-Pb (right) collisions. Lower frames: Ratio of correctly identified photons in γ-jet events to one-cluster π^0 identified as photons in jet-jet events. The small fraction of jet-jet events with a leading π^0 detected in PHOS is the origin of the large statistical errors.

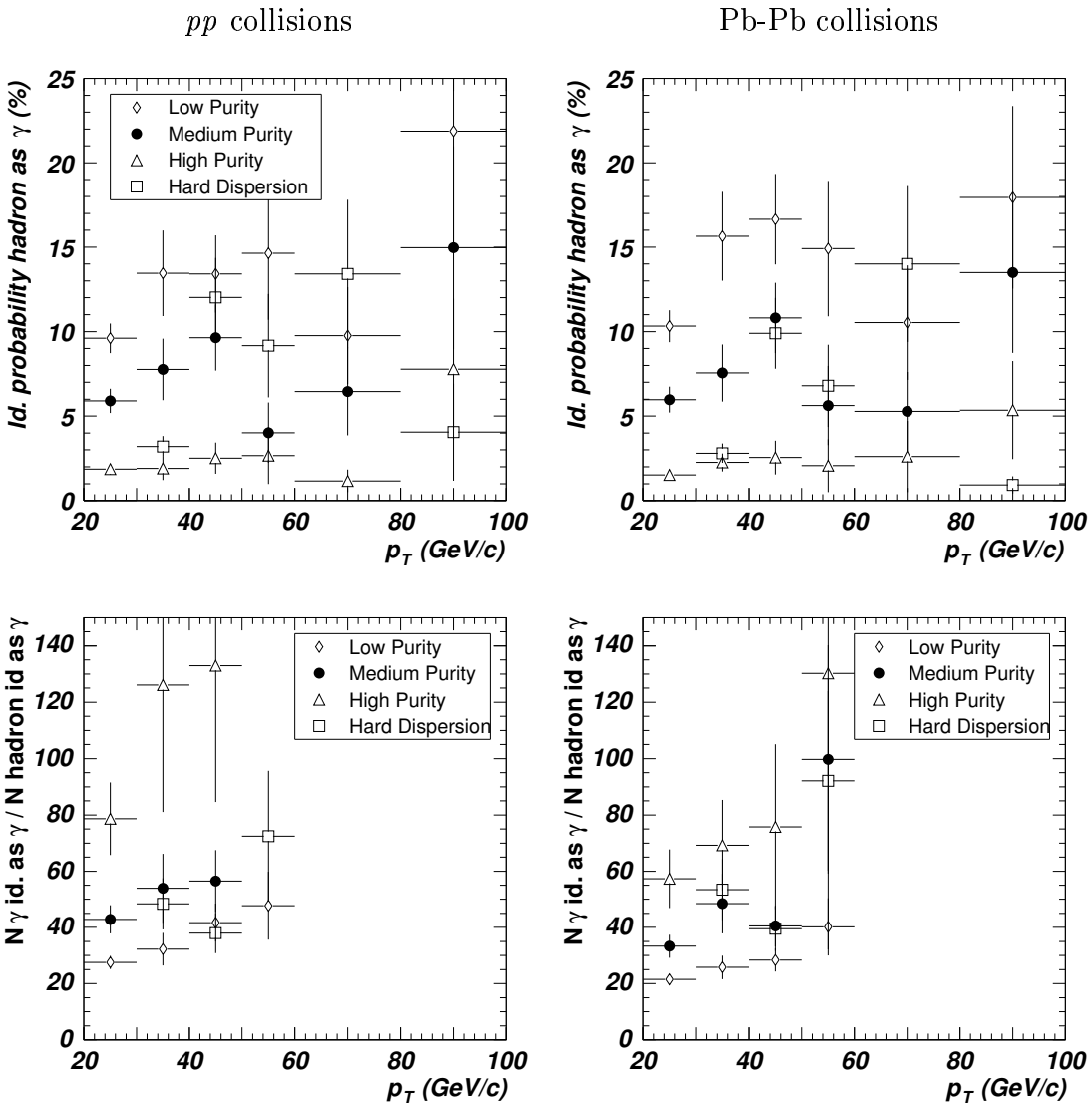

Figure 6.7: Upper frames: Probability of identifying in PHOS a charged hadron from a jet-jet event as a photon by the shower shape analysis for *pp* (left) and Pb-Pb (right) collisions. Lower frames: Ratio of correctly identified photons in γ-jet events to hadrons identified as photons in jet-jet events. The small fraction of jet-jet events with a leading hadron detected in PHOS is the origin of the large statistical errors shown.

R	$p_T^{th} = 2$ GeV/c	$p_T^{th} = 4$ GeV/c	$p_T^{th} = 6$ GeV/c
	pp collisions		
0.1-0.8	100 %	100 %	100 %
	Pb-Pb collisions		
0.1	83 %	98 %	100 %
0.2	50 %	93 %	98 %
0.3 - 0.8	23-0.3 %	84-34 %	95-74 %

Table 6.2: Ratio of the isolated to the total number of particles in γ-jet events ($20 < E_\gamma < 100$ GeV) obtained by the ICM for several p_T thresholds and cone sizes (without considering detector response) for pp and Pb-Pb collisions.

1. No hadron with p_T above a given threshold is found in the cone. We call this method standard ICM.

2. The sum of the transverse momentum of all hadrons inside the cone is smaller than a given threshold. We call this method ICMS (ICM with threshold on the Sum).

6.3.1 Isolation cut method with particle p_T threshold (ICM)

We studied the ICM efficiency for cone sizes in the range $0.1 < R < 0.8$ and particle thresholds of $p_T^{th} = 2$, 4 and 6 GeV/c.

In a first step, we applied this method without taking into account the detector response. We defined the isolation efficiency as the ratio of the number of candidates tagged by the ICM as prompt photons to the total number of candidates, where candidate particles are those with $p_T > 10$ GeV/c. In the case of γ-jet events produced in pp collisions, the efficiency was near 100 % for any threshold value. However, in the case of Pb-Pb collisions the efficiency stayed constant with p_T but varied significantly with the cone size independently of the p_T threshold. When this method was applied to jet-jet events, an important dependence of the efficiency with p_T and the parton energy was found. At low z values ($z = p_{T,i}/E_{parton}$), the efficiency was constant and significantly lower than unity, but close to $z = 1$ all the events were found to be isolated. The larger z the smaller the fragment multiplicity. Table 6.2 shows the ICM efficiencies for γ-jet events for different R and p_T thresholds. Results for jet-jet events are shown for pp and Pb-Pb collisions in Figs. 6.9 and 6.10, respectively.

In a second step, we applied the ICM method to reconstructed events filtered through the TPC and PHOS acceptance and response. The different jet energy bins were added weighted by their corresponding cross sections. The ICM efficiency was defined as the ratio of the number of isolated low-purity photons to the total number of low purity-photons. The dependence of the ICM efficiency with the energy of the photon candidate is shown for jet-jet events in Fig. 6.11 for $R = 0.1$ and 0.2 and $p_T^{th} = 2$, 4 and 6 GeV/c.

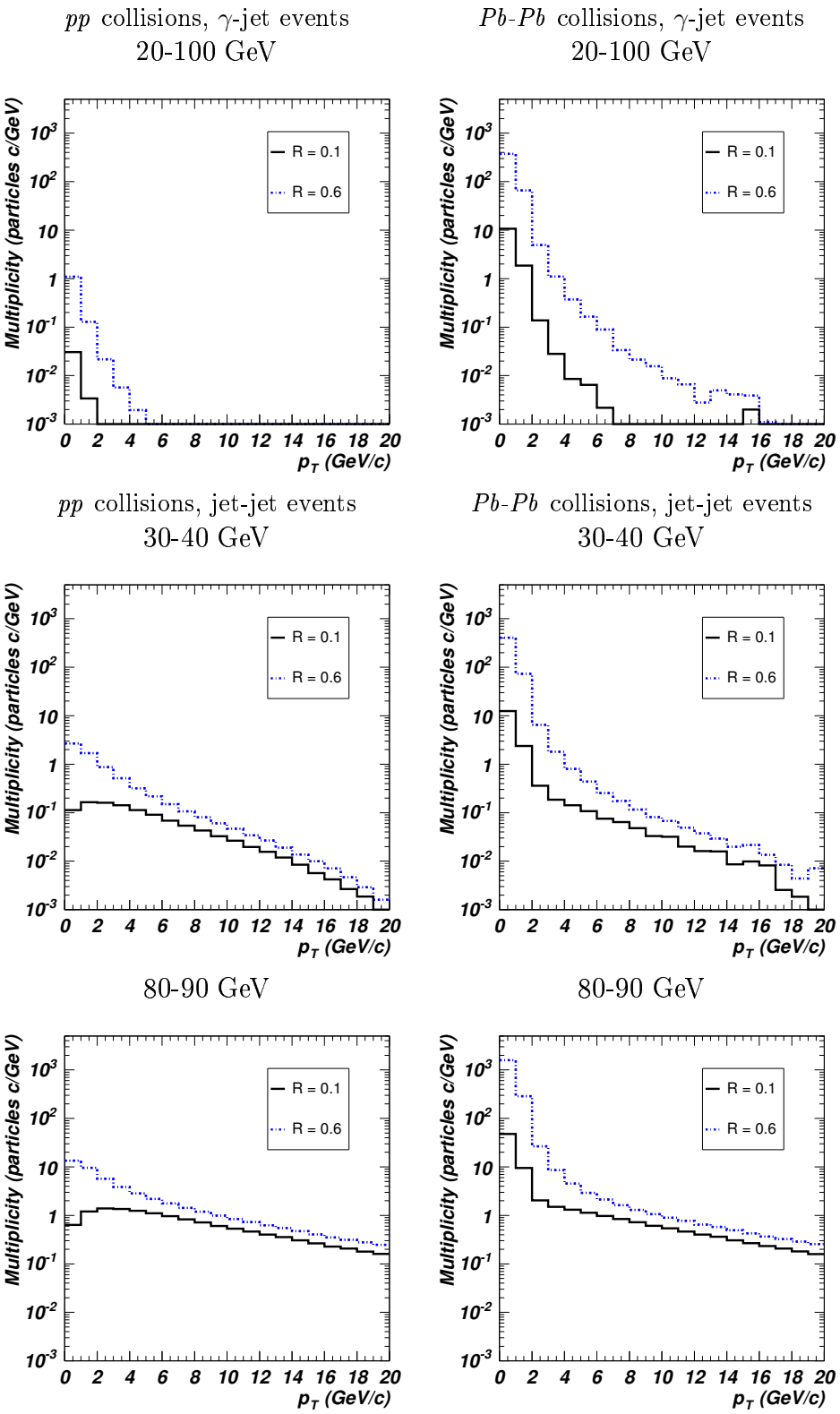

Figure 6.8: p_T particle distribution inside cones of size $R = 0.1$ (solid line) and 0.6 (dotted line) around particles with p_T larger than 10 GeV/c. The results are not corrected either for detector response or acceptance. Upper figures are distributions around 20-100 GeV prompt photons (γ-jet events), middle and lower figures for 30-40 GeV and 80-90 GeV jet particles (jet-jet events), respectively. Left and right figures are for *pp* and Pb-Pb collisions, respectively.

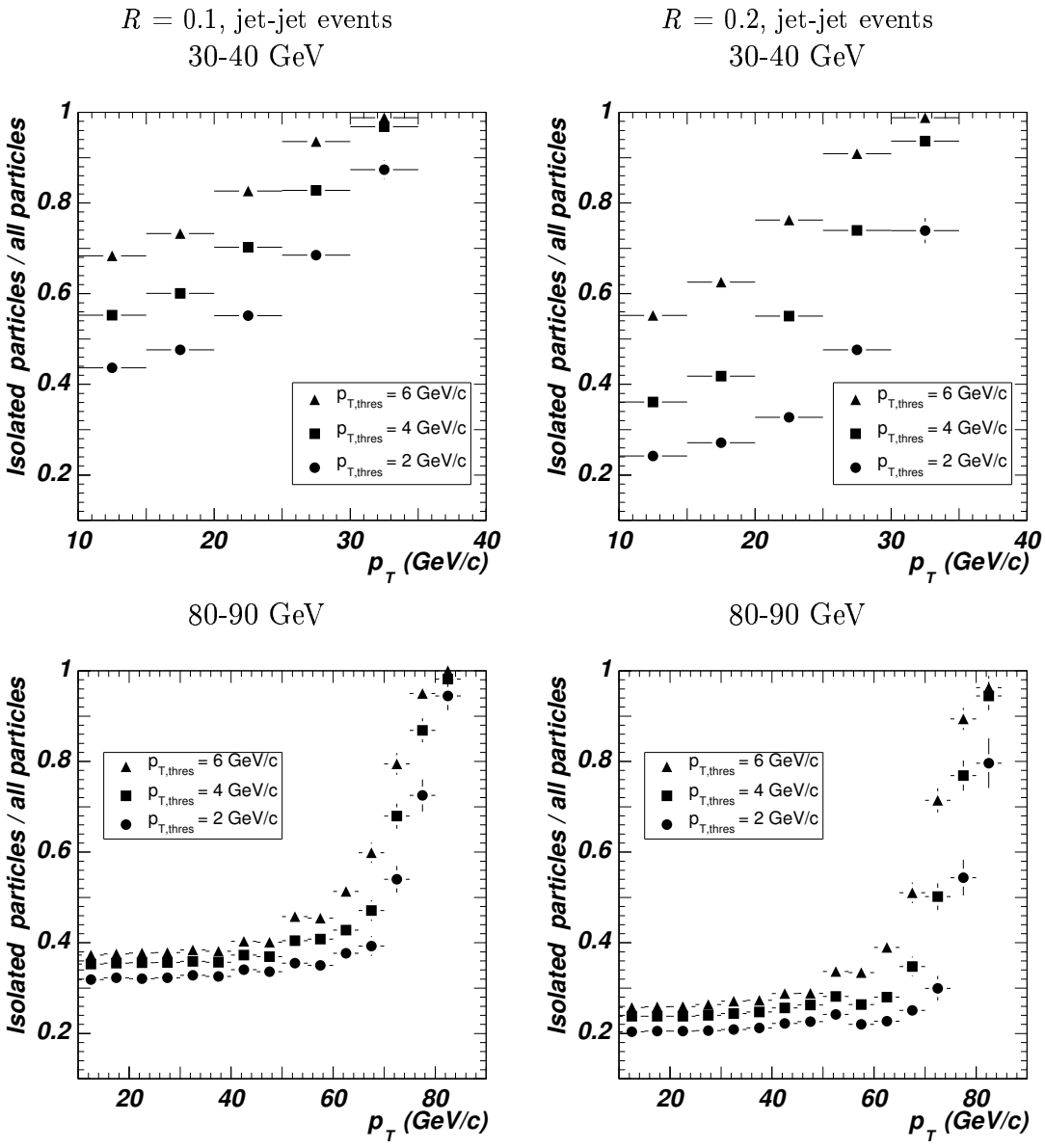

Figure 6.9: Ratio of the isolated to the total number of particles as a function of the particle p_T for the ICM and for several p_T thresholds, for pp collisions. Two cone sizes were considered, $R = 0.1$ (left) and 0.2 (right). The results correspond to prompt photon candidates with $p_T > 10$ GeV/c without considering detector response and acceptance. Upper and lower figures display the results for 30-40 GeV and 80-90 GeV jet-jet events, respectively.

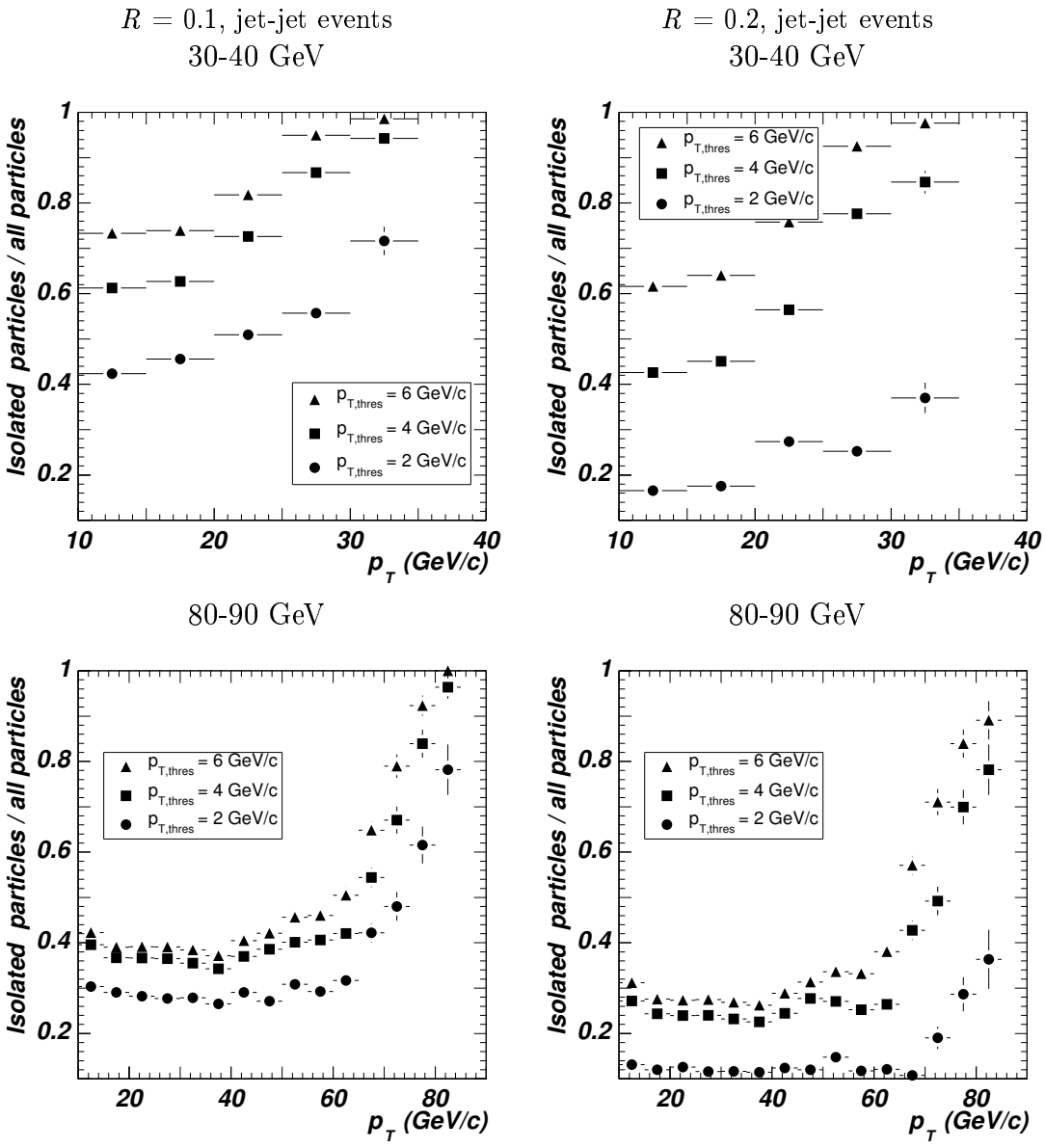

Figure 6.10: Ratio of the isolated to the total number of particles as a function of the particle p_T for the ICM and for several p_T thresholds, for Pb-Pb collisions. Two cone sizes were considered, $R = 0.1$ (left) and 0.2 (right). The results correspond to prompt photon candidates with $p_T > 10$ GeV/c without considering detector response and acceptance. Upper and lower figures display the results for 30-40 GeV and 80-90 GeV jet-jet events, respectively.

R	$p_T^{th} = 2$ GeV/c	$p_T^{th} = 4$ GeV/c	$p_T^{th} = 6$ GeV/c
	pp collisions		
	γ-jet events		
0.1 - 0.8	100 %	100 %	100 %
	jet-jet events		
0.1	20 %	42 %	56 %
0.2	16 %	41 %	56 %
0.3 - 0.8	16 %	41 %	56 %
	Pb-Pb collisions		
	γ-jet events		
0.1	80 %	98 %	99 %
0.2	50 %	95 %	99 %
0.3 - 0.8	34 - 8 %	93 - 84 %	98 - 97 %
	jet-jet events		
0.1	15 %	39 %	56 %
0.2	7 %	37 %	54 %
0.3 - 0.8	4 - 1 %	36 - 31 %	54 - 53 %

Table 6.3: ICM integrated efficiency for pp and Pb-Pb collisions.

The ratio of the integral of the isolated low purity-photon spectrum to the integral of the total low-purity photon spectrum is reported in Tab. 6.3 for different values of the cone size and p_T^{th}, applied to γ-jet and jet-jet events. The following features were found:

- γ-jet events: In pp collisions the ICM efficiency was close to 100 % independently of the cone size and of the p_T threshold. On the other side, there was an important dependence of the efficiency on R and p_T^{th} for Pb-Pb collisions; the larger the cone size the worse the isolation efficiency, and the higher the p_T threshold is the better the isolation efficiency. No dependence of the isolation efficiency with the photon energy was observed.

- jet-jet events: The ICM gave a smaller probability of misidentifying a one-cluster π^0 as a photon in Pb-Pb than in pp collisions. The misidentification probability increased with the p_T threshold and is quasi independent of the cone size for large p_T thresholds. The dependence of the misidentification probability with the p_T threshold was strong, ranging from about 50-60 % for $p_T^{th} = 6$ GeV/c to about 15-20 % for $p_T^{th} = 2$ GeV/c for pp collisions and from about 40-60 % for $p_T^{th} = 6$ GeV/c to about 5-20 % for $p_T^{th} = 2$ GeV/c for Pb-Pb collisions.

The ratio of the γ-jet signal to the jet-jet background is reported in Tab. 6.4 and Fig. 6.12. In the case of pp collisions, this ratio rises slightly with R for $p_T^{th} = 2$ GeV/c but for Pb-Pb collisions, this ratio shows a maximum at $R = 0.3$. For the largest p_T thresholds ($p_T^{th} = 4$ and 6 GeV/c), the signal to background ratio is smaller than for the lower p_T threshold

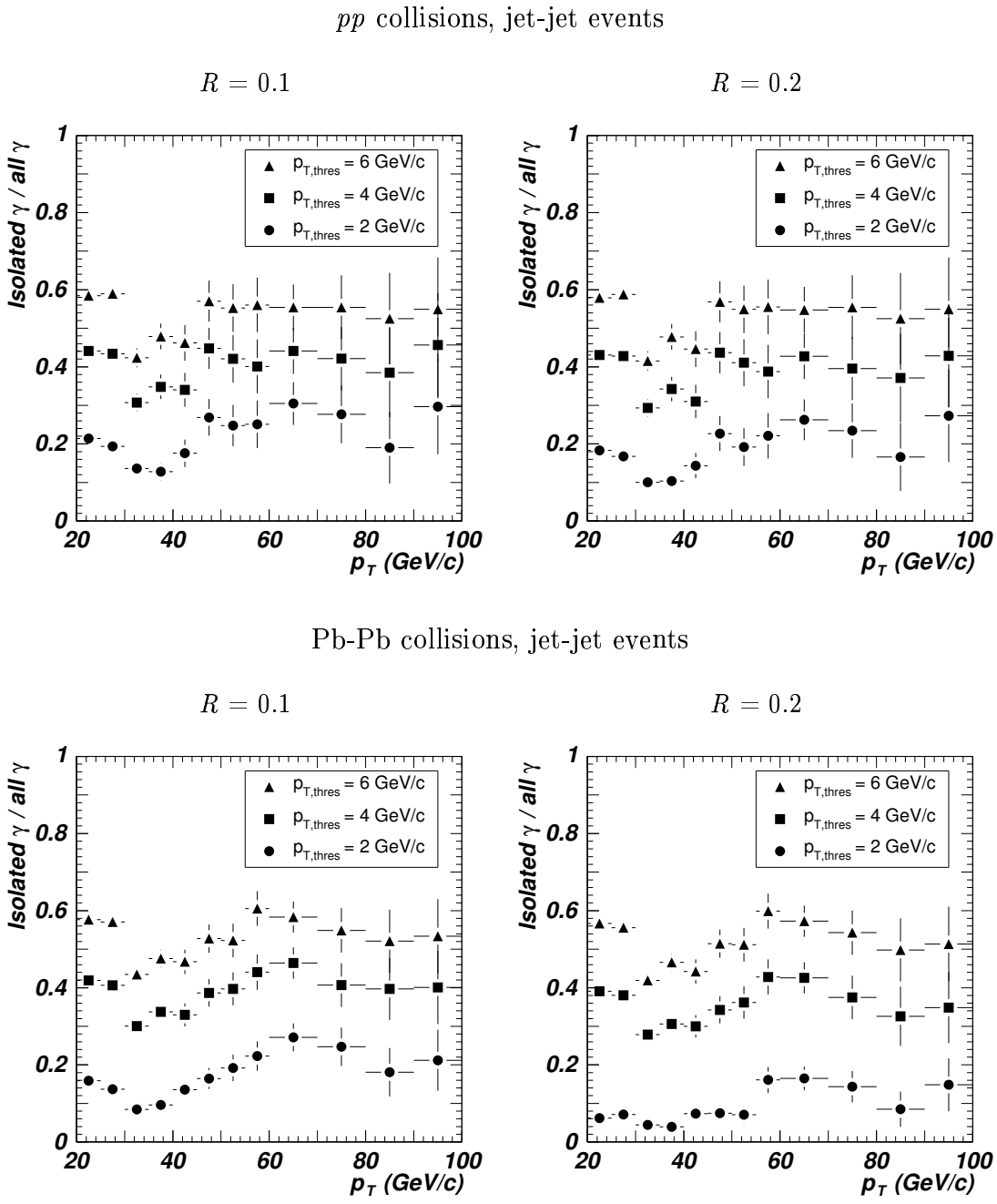

Figure 6.11: Misidentification efficiency of ICM identified prompt photons as function of the photon p_T for $R = 0.1$ (left) and $R = 0.2$ (right) cone sizes and 2, 4 and 6 GeV/c p_T thresholds. This efficiency was defined as the ratio of the isolated to the total photon spectra for low purity photons. Upper and lower figures show the misidentification efficiency for pp and Pb-Pb collisions, respectively.

R	$p_T^{th} = 2$ GeV/c	$p_T^{th} = 4$ GeV/c	$p_T^{th} = 6$ GeV/c
	pp collisions		
0.1	3	1.4	1
0.2	3.5	1.4	1
0.3 - 0.8	3.6-3.7	1.4	1
	Pb-Pb collisions		
0.1	3	1.4	1
0.2	4.2	1.4	1
0.3 - 0.8	4.6 - 3	1.5	1

Table 6.4: Signal (γ-jet) to background (jet-jet) ratio obtained by the ICM method for pp and Pb-Pb collisions. R and p_T^{th} are the cone size and particle momentum threshold.

($p_T^{th} = 2$ GeV/c) and the dependence with R disappears. The optimum values of the ICM parameters were found to be $R = 0.2$ and $p_T^{th} = 2$ GeV/c. We did not consider $R = 0.3$ because in this case the ICM efficiency was reduced to less than 50 % for Pb-Pb collisions and the signal to background ratio was not much better than in the case of $R = 0.2$.

6.3.2 Isolation cut method with total p_T sum threshold in cone (ICMS)

The ICMS method is based on the value of the sum of the transverse momentum of all the particles found in a given cone around the photon candidate. This sum is denoted as Σ_{p_T}. We studied the efficiency of this method for threshold values of 0.7, 1, 2 and 3 GeV/c for pp collisions, and for threshold values between 5 and 50 GeV/c for Pb-Pb collisions. It emerged that for Pb-Pb collisions Σ_{p_T} was not the appropriate parameter to compare the results obtained for different cone sizes because Σ_{p_T} varied strongly with R as displayed in Fig. 6.13. We found that a more appropriate parameter was the momentum sum density Σ'_{p_T} defined as

$$\Sigma'_{p_T} = \frac{\Sigma_{p_T}}{R^2 \times f(R)}, \tag{6.3}$$

where $f(R)$ is a factor that takes into account the response functions and acceptance of the various detectors involved. $f(R)$ is equal to one when detector response and acceptance are not considered, otherwise is given by the empirical formula $f(R) = 0.95 - 1.5 \times R$, deduced from the data reported in Tab. 6.5.

As in the previous section, we applied the ICMS to all generated particles. We observed a similar behavior than in the case of the ICM method. Table 6.6 shows the ICMS efficiencies for different R and p_T thresholds in the case of γ-jet events. Results for jet-jet events for pp and Pb-Pb collisions are shown in Figs 6.14 and 6.15.

By applying this method to reconstructed events, we calculated the ICMS efficiency for

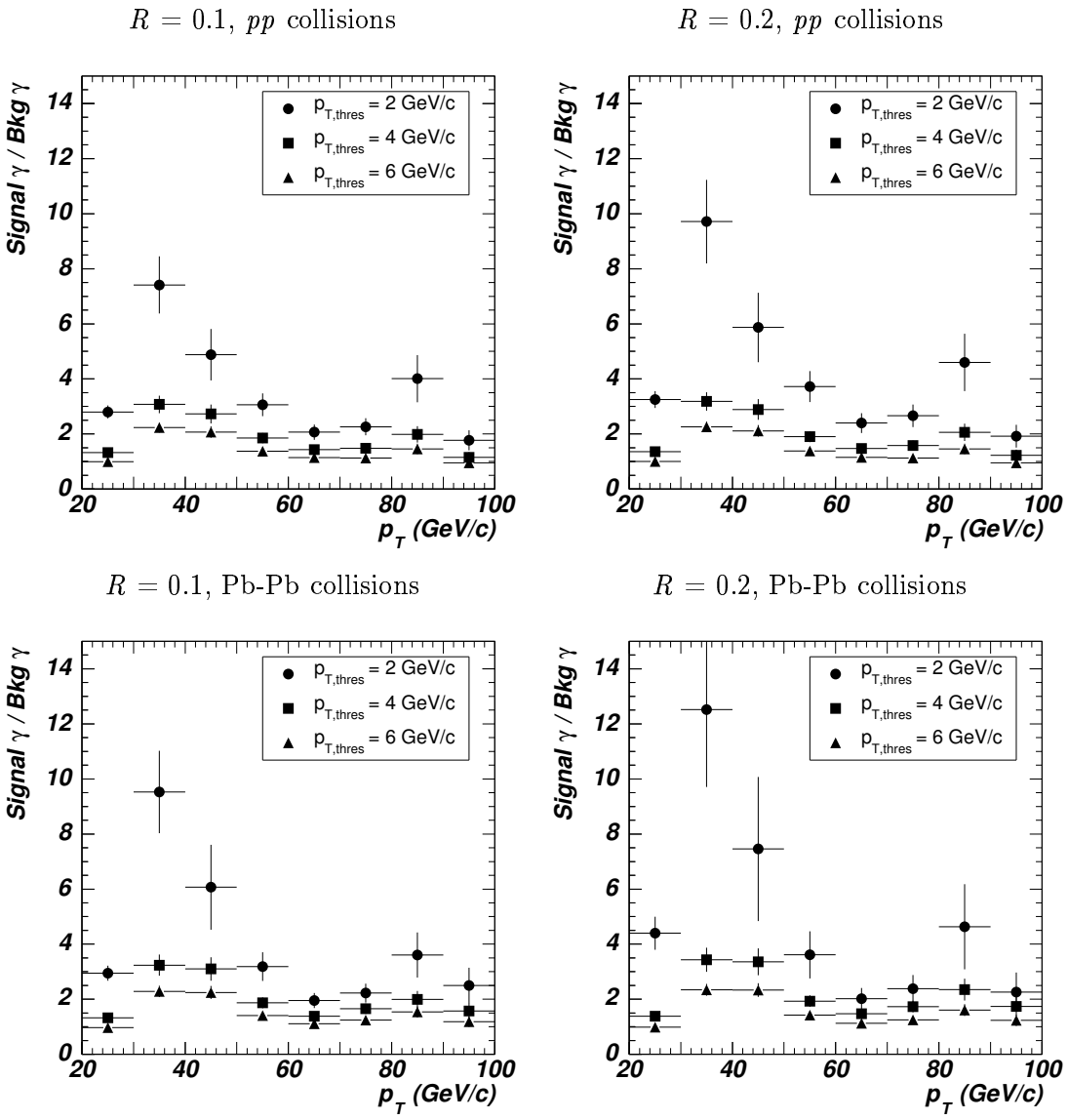

Figure 6.12: Signal (identified prompt photons by SSA low purity and ICM from γ-jet events) to background (identified prompt photons by SSA low purity and ICM from jet-jet events) ratio as a function of p_T, for $R = 0.1$ (left) and 0.2 (right), and p_T^{th} of 2, 4 and 6 GeV/c. Upper and lower frames correspond to pp and Pb-Pb collisions, respectively.

	$R = 0.1$	$R = 0.2$	$R = 0.3$
Generated particles	10 GeV/c	40 GeV/c	91 GeV/c
Detected particles	8 GeV/c	26 GeV/c	43 GeV/c

Table 6.5: Mean value of the Σ_{p_T} distributions shown in Fig. 6.13 as a function of the cone size for all the generated particles and restricted to detected particles.

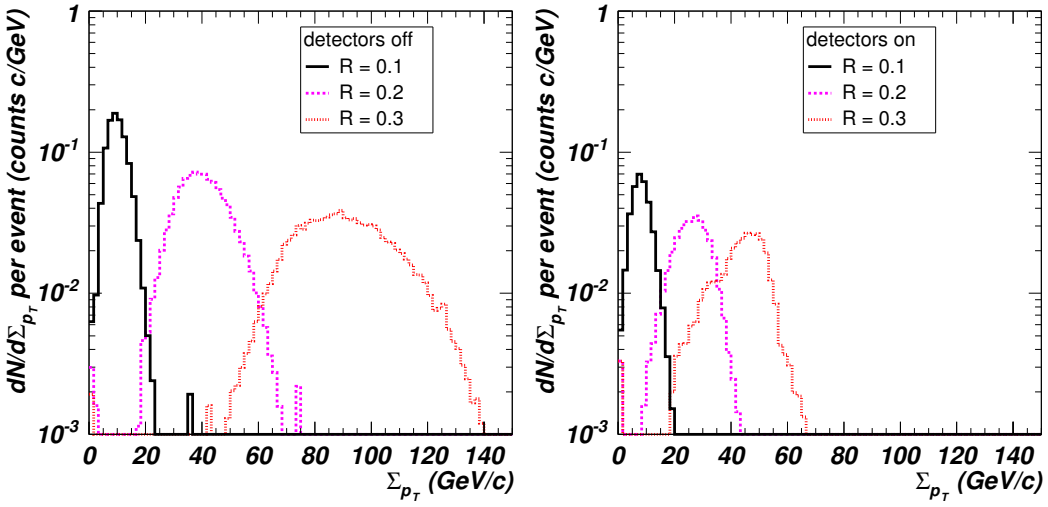

Figure 6.13: p_T sum of all particles inside cone sizes of $R = 0.1$, 0.2 and 0.3 in HIJING events. In the left figure, all the simulated particles (charged and neutral) were considered, i.e. the acceptance and response of detectors were not taken into account. In the right figure, only the particles in the cone detected in the TPC (charged) and PHOS (neutral) were considered.

	$R = 0.1$	$R = 0.2$
Σ_{pT}(GeV/c)	pp collisions	
0.7	97 %	92 %
1	99 %	96 %
> 2	100 %	100 %
Σ'_{pT}(TeV/c)	Pb-Pb collisions	
0.8	30 %	18 %
0.9	41 %	34 %
1	52 %	51 %
1.1	63 %	67 %

Table 6.6: Ratio of isolated and total number of particles for γ-jet events ($20 < E_\gamma < 100$ GeV) obtained with the ICMS method for several p_T thresholds and cone sizes and without considering detector response for pp and Pb-Pb collisions.

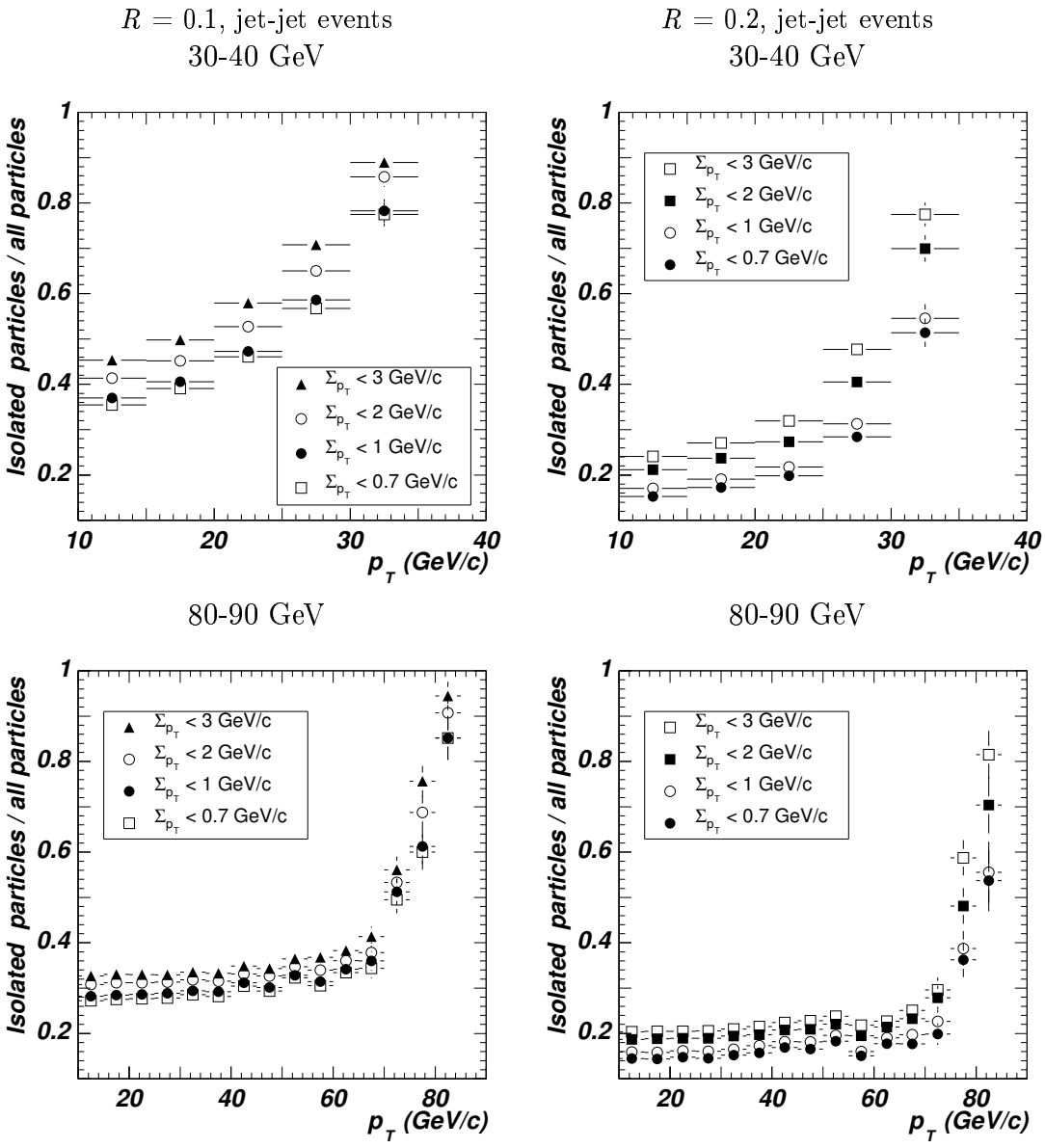

Figure 6.14: Ratio of the isolated to the total number of particles as a function of p_T, for the ICMS method and several Σ_{p_T} thresholds in the case of pp collisions. Two cone sizes were considered, $R = 0.1$ (left) and 0.2 (right). In these figures, we show the results for jet particles with $p_T > 10$ GeV/c, without detector response functions and without acceptance limitations. Upper and lower figures correspond to 30-40 GeV and 80-90 GeV jet-jet events, respectively.

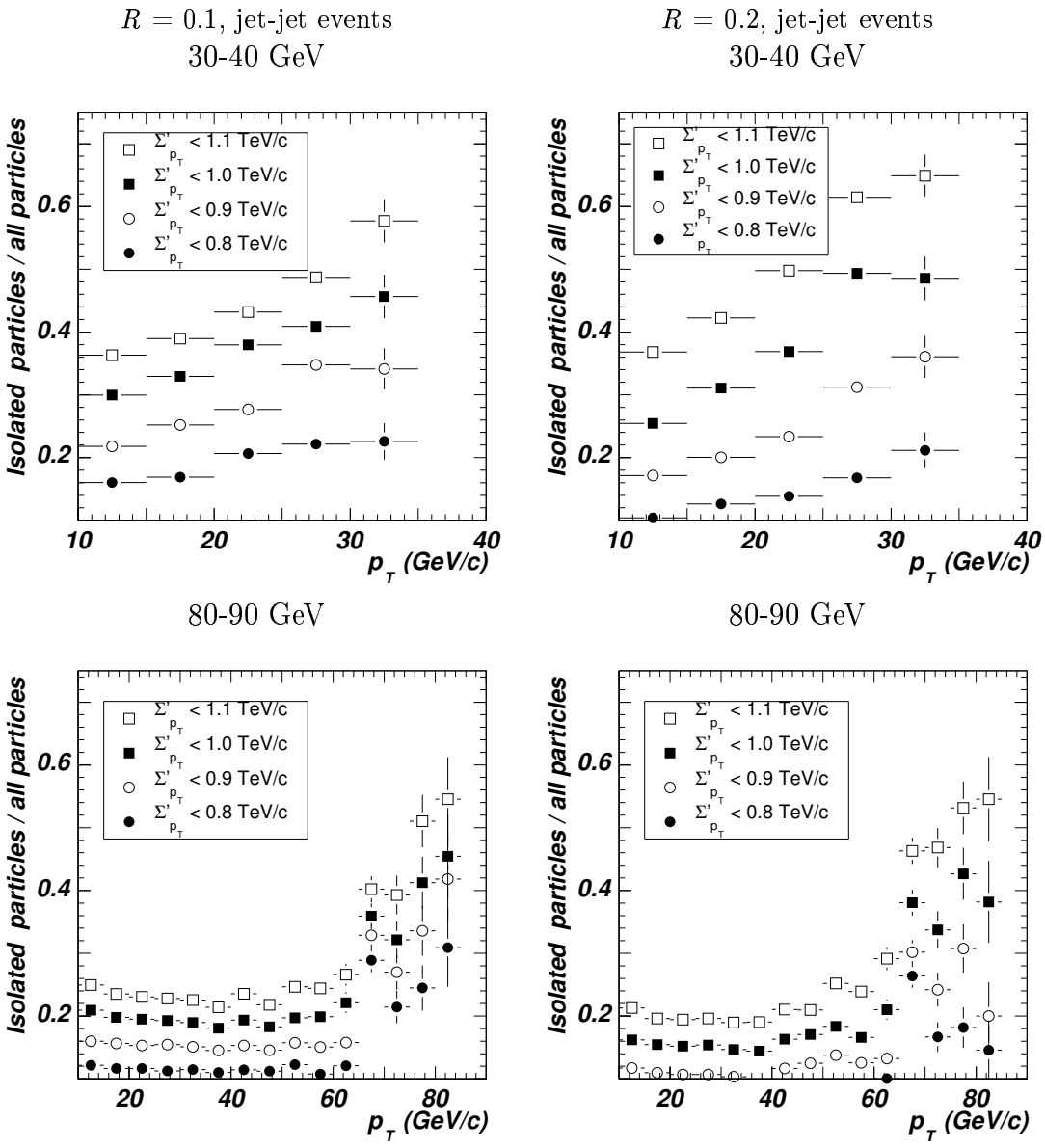

Figure 6.15: Ratio of the isolated to the total number of particles as a function of p_T, for the ICMS method and several Σ_{p_T} thresholds in the case of Pb-Pb collisions. Two cone sizes were considered, $R = 0.1$ (left) and 0.2 (right). In these figures, we show the results for jet particles with $p_T > 10$ GeV/c, without detector response functions and without acceptance limitations. Upper and lower figures correspond to 30-40 GeV and 80-90 GeV jet-jet events, respectively.

the different values of the cone size and Σ_{p_T} or Σ'_{p_T} reported in Tab. 6.7. The dependence of the ICMS efficiency with the energy of the photon candidate for jet-jet events, and for $R = 0.1$ and 0.2 and the most convenient Σ_{p_T} or Σ'_{p_T} thresholds, is shown in Fig. 6.16. The following features are observed:

- γ-jet events: In the case of *pp* collisions, the ICMS efficiency was close to 100 % for any threshold, independently of the cone size. On the other side, for Pb-Pb collisions an important dependence on both R and Σ'_{p_T} was found: the larger the cone size and the lower Σ'_{p_T} the better the isolation efficiency. For example, for $\Sigma'_{p_T} < 1$ TeV/c the efficiency was about 50 % independently of the cone size. No dependence with the photon energy was observed.

- jet-jet events: In *pp* collisions, the ICMS probability of misidentifying one-cluster π^0 as photons depended slightly on the cone size, and strongly on the p_T threshold; for example, the probability was about 8-4 % for $\Sigma_{p_T} < 1$ GeV/c and about 22-15 % for $\Sigma_{p_T} < 3$ GeV/c in the $0.1 < R < 0.3$ range. In the case of Pb-Pb collisions, there was an important dependence on both parameters: the misidentification probability ranged between 12-28 % for $\Sigma'_{p_T} < 1$ TeV/c but ranged between 17-52 % for $\Sigma'_{p_T} < 1.2$ TeV/c in the $0.1 < R < 0.3$ range. We obtained the best π^0 rejection for the smallest p_T. The ICMS probability of misidentifying a one-cluster π^0 as a photon was also almost independent of the p_T of the photon candidate.

The γ-jet signal to jet-jet background ratio is reported in Tab. 6.8 and Fig. 6.17. This ratio increases with R and decreases with Σ_{p_T} for *pp* collisions. In the case of Pb-Pb collisions, the ratio decreases with R and shows a small dependence on Σ'_{p_T}, with a maximum at $\Sigma'_{p_T} \sim 1$ TeV/c. The optimum values of the ICMS parameters were deduced from this pattern; for *pp* collisions, the chosen parameters were $R = 0.2$ and $\Sigma_{p_T} < 0.7$ GeV/c; although the signal to background ratio was somewhat better for $R = 0.3$ we selected $R = 0.2$ to compare with the ICM method; for Pb-Pb collisions, we obtained the best signal to background ratio for $R = 0.1$ and $\Sigma'_{p_T} < 0.9$ TeV/c.

6.3.3 Comparison between the two ICM methods

By comparing the signal to background ratios obtained with the ICM and ICMS methods the following conclusions are obtained:

- In the case of *pp* collisions, a threshold on Σ_{p_T} is more efficient than a simple threshold on p_T. A γ-jet identification probability of 100 % and a jet-jet misidentification probability of 3 % is obtained by the ICMS method with $R = 0.2$ and $\Sigma_{p_T} < 0.7$ GeV/c to be compared with a γ-jet identification probability of 100 % and a jet-jet misidentification probability of 16 % obtained by the ICM with $R = 0.2$ and $p_T^{th} = 2$ GeV/c.

pp collisions			
Σ_{p_T}(GeV/c)	$R = 0.1$	$R = 0.2$	$R = 0.3$
γ-jet			
any	100 %	100 %	100 %
jet-jet			
0.7	6.1 %	3.2 %	2.1 %
1.0	7.9 %	4.5 %	3.8 %
2.0	15 %	10 %	8.6 %
3.0	22 %	16 %	15 %
Pb-Pb collisions			
Σ'_{p_T}(TeV/c)	$R = 0.1$	$R = 0.2$	$R = 0.3$
γ-jet events			
0.7	18 %	11 %	14 %
0.8	28 %	21 %	24 %
0.9	36 %	34 %	36 %
1.0	48 %	49 %	54 %
1.1	56 %	62 %	73 %
1.2	64 %	77 %	92 %
jet-jet events			
0.7	4.8 %	5.8 %	8.3 %
0.8	7.2 %	9.1 %	14 %
0.9	8.5 %	15 %	20 %
1.0	12 %	20 %	28 %
1.1	15 %	25 %	37 %
1.2	17 %	35 %	52 %

Table 6.7: Integrated ICMS efficiency for reconstructed pp and Pb-Pb events in PHOS and TPC.

Σ_{p_T}(GeV/c)	$R = 0.1$	$R = 0.2$	$R = 0.3$
pp collisions			
0.7	9.5	18	27
1.0	7.4	13	15
2.0	4.0	5.8	6.8
3.0	2.6	3.6	4.0
Σ'_{p_T}(TeV/c)	$R = 0.1$	$R = 0.2$	$R = 0.3$
Pb-Pb collisions			
0.7	2.2	1.1	0.97
0.8	2.3	1.3	0.99
0.9	2.4	1.3	1.0
1.0	2.2	1.4	1.1
1.1	2.2	1.4	1.1
1.2	2.1	1.3	0.99

Table 6.8: γ-jet signal to jet-jet background ratio of the isolated photon integrated spectrum to the total photon integrated spectrum for reconstructed pp and Pb-Pb collisions in PHOS and TPC obtained by the ICMS method.

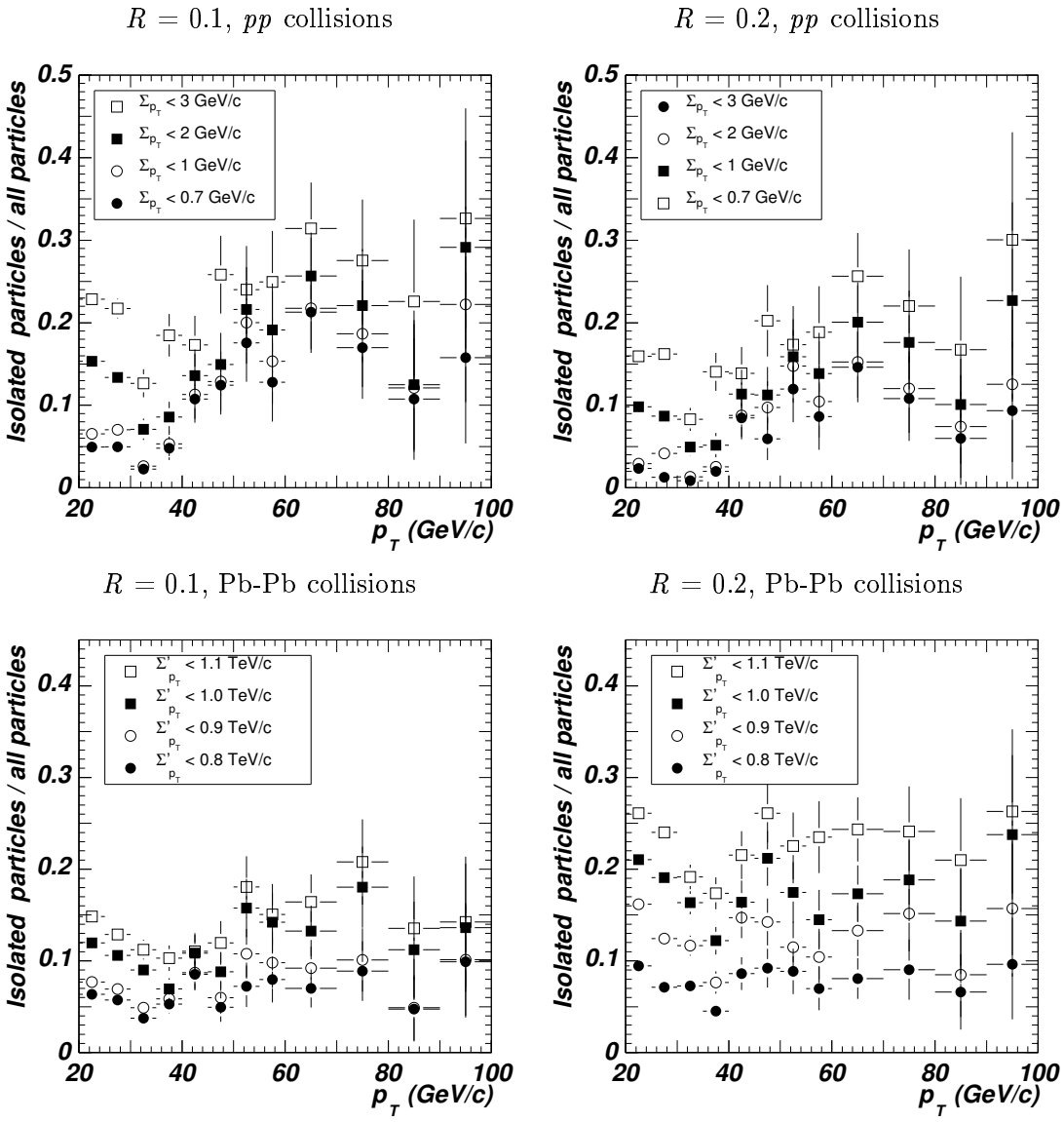

Figure 6.16: Prompt photon misidentification efficiency of ICMS as a function of the candidate p_T for $R = 0.1$ (left) and $R = 0.2$ (right) and for different Σ_{p_T} or Σ'_{p_T} for pp (upper figures) and Pb-Pb collisions (lower figures), respectively.

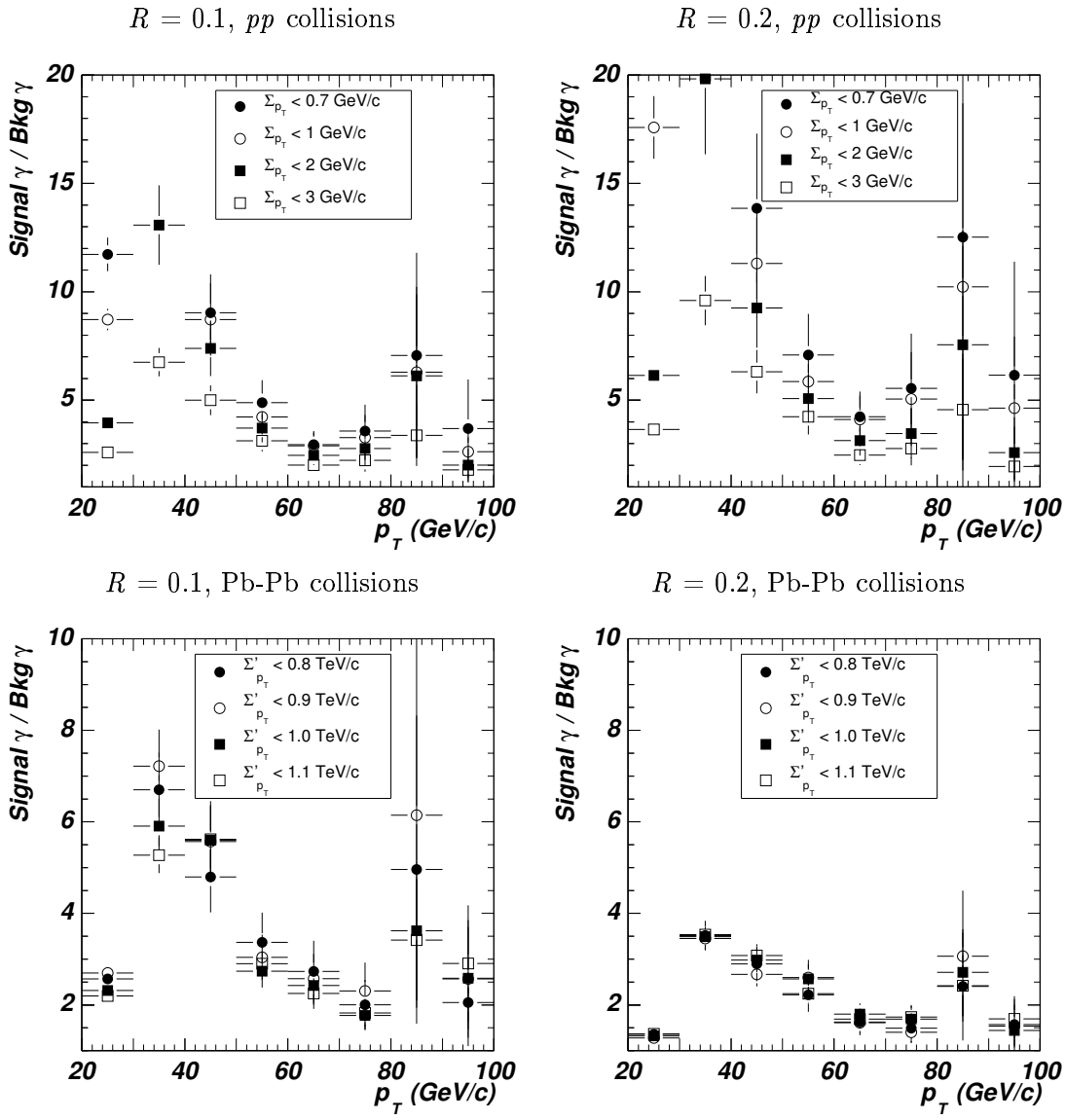

Figure 6.17: Signal to background ratio as a function of p_T for $R = 0.1$ (left) and 0.2 (right), and $\Sigma_{p_T} = 0.7$, 1, 2 and 3 GeV/c for pp collisions (upper frame) and $\Sigma'_{p_T} = 0.8$, 0.9, 1 and 1.1 TeV/c for Pb-Pb collisions (lower frame).

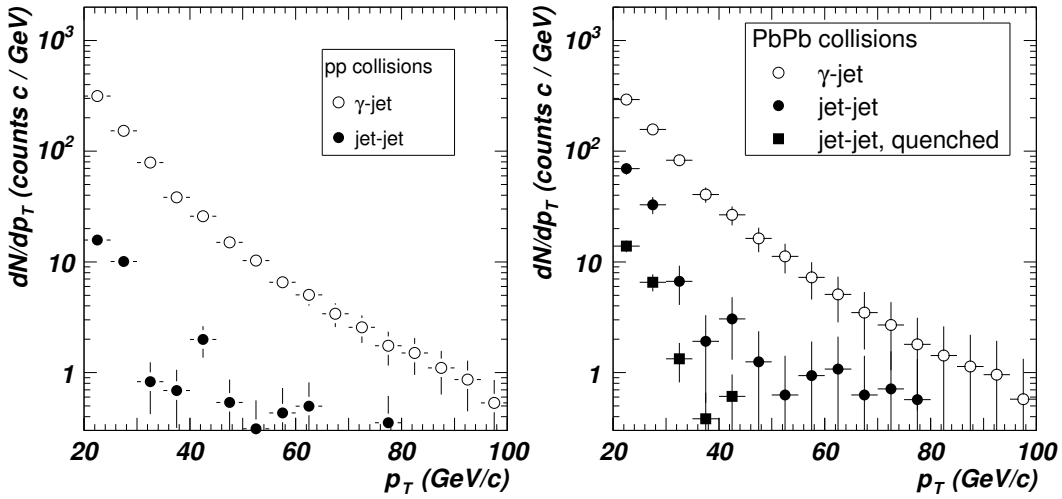

Figure 6.18: Spectra of prompt photons identified in ALICE during a LHC running year with statistical errors by medium purity SSA and ICM methods for jet-jet (•) and γ-jet events (○) for *pp* (left) and Pb-Pb (right) collisions at $5.5A$ TeV. A quenching factor of 5 for γ-like events is assumed for Pb-Pb collisions (■). ICMS has been employed for *pp* collisions and ICM for Pb-Pb collisions.

- In the case of Pb-Pb collisions, the ICM method gave a better identification probability than the ICMS method. A γ-jet identification probability of 50 % and a jet-jet misidentification probability of 7 % was obtained by the ICM with $R = 0.2$ and $p_T^{th} = 2$ GeV/c to be compared with a γ-jet identification probability of 36 % and a jet-jet misidentification probability of 8.5 % obtained by the ICMS method with $R = 0.1$ and $\Sigma'_{p_T} < 0.9$ TeV/c.

The identified prompt photon spectra obtained by the ICM and ICMS methods are presented in Fig. 6.18; they should be compared to the spectra obtained by the SSA method given in Fig. 6.4: we conclude that a sufficient background rejection is achieved by ICMS for *pp* collisions and by ICM for Pb-Pb collisions. It has been observed at RHIC that the hadron spectrum is quenched by a factor 5 [Adc04]. If this quenching holds for ALICE, the jet-jet contribution would be lowered by this factor, leading to a signal to background ratio of 20 instead of 4 as given in Tab. 6.4. The quenched results are displayed in Fig. 6.18 for $R = 0.2$ and $p_T^{th} = 2$ GeV/c.

6.4 Final prompt photon spectrum

We constructed the prompt photon spectrum expected to be measured during one LHC running period with its statistical and systematic errors. We added the identified prompt photon spectrum from γ-jet events to the remaining spectrum from jet-jet events to obtain the total identified prompt photon spectrum N_γ^{id}. From the known identification prob-

abilities, we can reconstruct the original prompt photon spectrum in the following way: Let N_γ be the original prompt photon spectrum, N_{π^o} the original π^o spectrum, N_h the original hadron spectrum, ε_i^{pid} the identification probability of the particle i as a photon by SSA and ε_i^{icm} the identification probability of particle i as prompt photon by ICM, where i can be a photon, a one-cluster π^0 or any other hadron. We can write

$$N_\gamma^{id} = N_\gamma \varepsilon_\gamma^{pid} \varepsilon_\gamma^{icm} + N_{\pi^o} \varepsilon_{\pi^o}^{pid} \varepsilon_{\pi^o}^{icm} + N_h \varepsilon_h^{pid} \varepsilon_h^{icm}, \tag{6.4}$$

which can be rearranged as,

$$N_\gamma^{id} = N_\gamma (\varepsilon_\gamma^{pid} \varepsilon_\gamma^{icm} + \frac{N_{\pi^0}}{N_\gamma} \varepsilon_{\pi^o}^{pid} \varepsilon_{\pi^o}^{icm} + \frac{N_h}{N_\gamma} \varepsilon_h^{pid} \varepsilon_h^{icm}) = \zeta N_\gamma. \tag{6.5}$$

In the studies discussed in the previous sections, we deduced the various factors (the ICM misidentification probabilities for π^o and hadrons are the same) and calculated the correction factor ζ for the different identification criteria (PID photon classes, cone sizes and p_T thresholds). The PID systematic error around the average value was calculated as the dispersion of the corrected spectra obtained for the different identification criteria. This systematic error was added quadratically to the average background spectra in order to obtain the total systematic error. The statistical error was calculated from the photon statistics as $\sqrt{N_\gamma}$.

The final spectra of identified photons compared with the original spectra are shown in Fig. 6.19. In Fig. 6.20, similar spectra are shown for Pb-Pb collisions which were calculated by assuming that hadrons are quenched by a factor 5 as observed at RHIC. This assumption reduces the systematic error.

6.5 Conclusions

We developed an algorithm to identify prompt photons generated in pp and Pb-Pb collisions in the ALICE experiment. Prompt photons were identified efficiently in PHOS with the help of a shower shape analysis, capable of rejecting hadrons, and by the isolation cut method which rejects π^0 mesons efficiently. We estimated the identified prompt photon spectrum from the expected ALICE statistics during a standard year of LHC running.

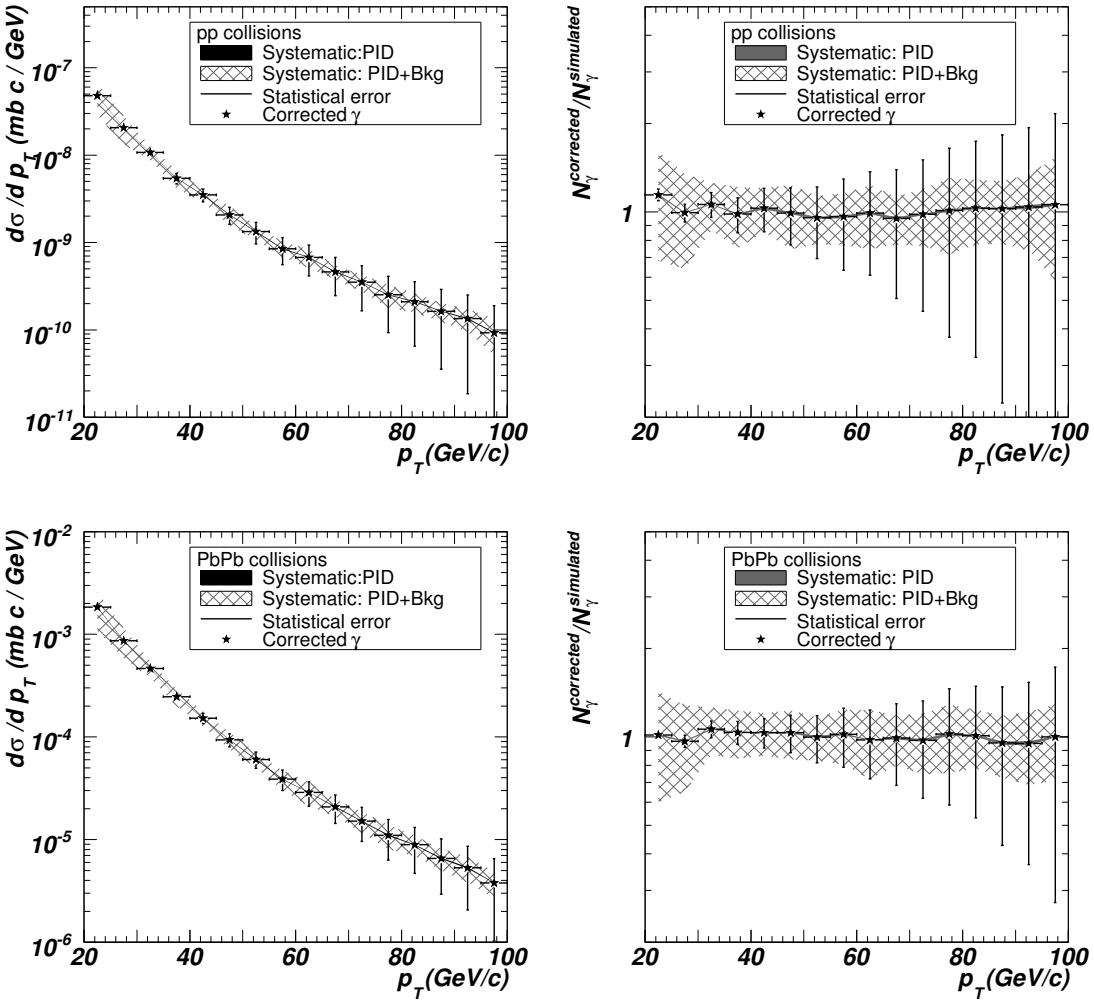

Figure 6.19: Left frames: Simulated final prompt photon spectrum measured in ALICE during a LHC running year with statistical and systematic errors. Right frames: Ratio of the final prompt photon spectrum to the original simulated spectrum for pp (upper figures) and Pb-Pb (lower figures) collisions at $5.5A$ TeV incident energy.

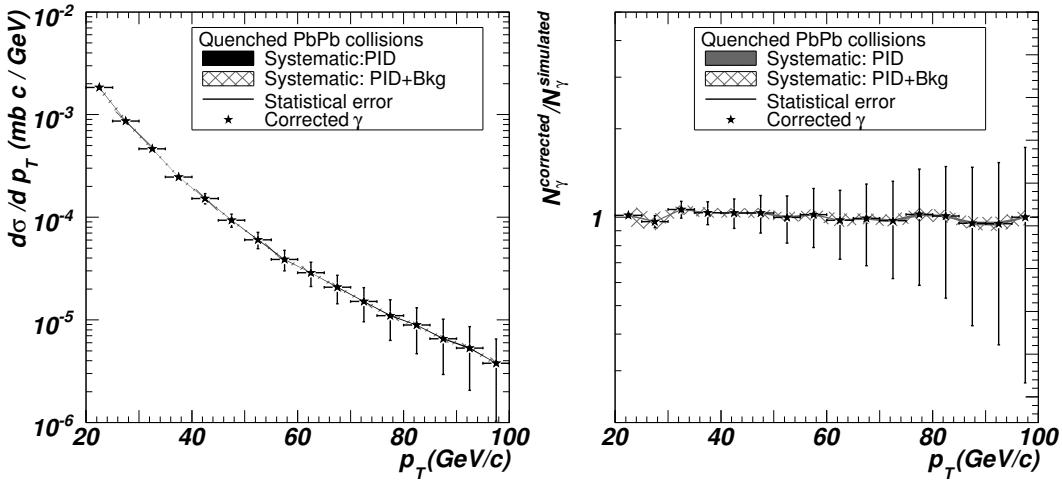

Figure 6.20: Left frame: Simulated final prompt photon spectrum measured in ALICE during a LHC running year with statistical and systematic errors. Right frame: Ratio of the corrected prompt photon spectrum and the original simulated spectrum. We assumed a quenching factor of 5 for the hadron spectrum in Pb-Pb collisions at $5.5A$ TeV incident energy.

Chapter 7

Photon-tagged jets identification

In this chapter, I discuss an algorithm for identifying photon-jet events and for reconstructing hadron jet features. The simulations described in the previous chapter were employed associated to a fast reconstruction algorithm of the generated particles. In the jet reconstruction procedure, two experimental situations were considered: i) only charged particles are detected (EMCal is not present) and ii) neutral particles can also be detected (EMCal is present).

7.1 Response of the detectors

The goal of the studies presented in this chapter was to assess the performance of our photon-jet identification algorithm. A fast detector simulation was used because a complete event simulation with particle transport and reconstruction would imply an unaffordable computing time; more elaborate simulations will be performed during the ALICE physics data challenge. In a fast simulation framework, we rely only on the properties of the final state particles generated by PYTHIA and on the knowledge of the response functions of the various detectors involved.

In this section, the response functions assumed for the detectors involved in our analysis, PHOS, EMCal and the central tracking system are described.

7.1.1 The photon detectors PHOS and EMCal

PHOS and possibly EMCal will be the detectors dedicated to photon detection in the ALICE experiment at mid-rapidity. As a first approximation in this investigation, the EMCal and PHOS responses were assumed to be identical.

The energy and impact position of PYTHIA generated particles were smeared according to Gaussian distributions of width equal to the energy and position resolutions obtained in Sec. 4.6. Only particles depositing in PHOS and EMCal an energy greater than 0.5 GeV were taken into account.

7.1.2 Charged particle detector

In the case of charged particles, the fast reconstruction was performed with parameterized responses of ITS [ALI99a] and TPC [ALI00b] to long-lived charged particles. In this fast reconstruction, charged particles were assumed to be detected with an angular resolution $\Delta\alpha/\alpha = 2\,\%$ and a momentum resolution $\Delta p/p = 2\,\%$. These resolutions were the main parameters of the Gaussian smearing applied to the momentum. After smearing, the particle energy was recalculated to ensure that the particle mass was conserved. A detection probability of 80 % within the ranges $|\eta| < 0.7$ and $p_T > 150$ MeV/c and vanishing outside these ranges was assumed as suggested in [Kow02].

7.2 Jet selection procedure

We identified photon-jet events by the following γ-tagging algorithm:

1. Search in each event for the most energetic prompt photon identified in PHOS.

2. Search for the jet leading particle[1], charged hadron or neutral pion with the highest p_T value, detected by the central tracking system or EMCal and emitted almost back-to-back to the photon, i.e. with $\Delta\phi$ close to 180°. As leading neutral pions decay into two photons, they can be measured by considering all the photon pairs in the event with a relative angle between a maximum and minimum angle defined by the decay kinematics and with an invariant mass in the range $120 < M_{\gamma\gamma} < 150$ MeV/c^2. An additional condition to be satisfied by the leading particle is that its p_T value must be at least the 10 % of the photon energy.

3. Reconstruct the jet as the ensemble of all particles contained inside the cone defined by Eq. (6.2) with axis aligned along the leading particle direction. We took here $R = 0.3$ and 0.5 (2.0) GeV/c for pp (Pb-Pb) collisions as the particle p_T threshold.

4. Finally, the event is identified as a photon-jet event if the ratio of the reconstructed energies of the jet and the prompt photon falls inside a selection window.

7.2.1 Aspects of γ- jet selections

Since jet particles can be detected only if they go through the central tracking system or the EMCal acceptance, only a fraction of jet particles is usually measured. In this case, the jet energy is only partially reconstructed which provokes the rejection of such a jet candidate.

[1] Jets have always some particles that can carry a significant proportion of the jet energy (in average 40%).

Since the prompt photon and the parton of a γ-jet event are emitted in opposite directions in their center of mass, the jet and the photon directions should be correlated in azimuthal and axial angles. However, the relative angle between the parton and the photon in the laboratory system depends on the velocity of the parton-photon center of mass and therefore the correlation in pseudo-rapidity is destroyed as seen in Fig. 7.1. As the azimuthal angle is a Lorentz invariant, the correlation in azimuthal angle is conserved in the laboratory system. The relative azimuthal angle $\Delta\phi$ of γ-jet events is peaked at 180° and its width depends on the detector acceptance and resolution and on the energy of the event. We tuned our algorithm to select photon-leading particle pairs satisfying the angular condition $0.9\,\pi < \Delta\phi < 1.1\,\pi$.

If the leading particle of a given event falls out of the detector acceptance, the algorithm finds a wrong leading particle. Such a misidentification produced a peak at low values of the $p_{T,l}/E_\gamma$ ratio of the jet leading particle distribution, as shown in Fig. 7.2, where $p_{T,l}$ and E_γ are the momentum of the identified leading particle and the energy of the photon, respectively. Fake leading particles can be rejected by imposing the condition $p_{T,l}/E_\gamma > 0.1$. When this selection condition was added to the previous jet selection conditions, the probability of finding the jet associated to a prompt photon for a γ-jet event was about 50 %, determined only by the detectors acceptance.

7.2.2 Detection of π^0 leading particles

π^0 candidates to leading particles were identified by detecting both decay photons in EMCal and selecting a window in the $\gamma\gamma$ invariant mass around the π^0 rest mass as described above. Unfortunately, the $M_{\gamma\gamma}$ distributions has a huge combinatorial background, in particular in the case of Pb-Pb collisions, as observed in Fig. 7.3. Additional selection conditions based on kinematics were therefore necessary.

The opening angle between the two photons originated in a π^0 decay is given in the laboratory system by Eq. (B.8). This angle is minimum for symmetric decays ($\alpha = 0$, see Appendix B). By comparing the opening angle distributions of simulated π^0 and of all the photon pairs identified in Pb-Pb collisions, shown in Fig. 7.4, we deduced an empirical maximum opening angle for the π^0 given by

$$\theta_{max} = 0.4 \cdot e^{-0.25 \cdot E} + 0.025 - 2 \cdot 10^{-4} \cdot E. \tag{7.1}$$

The condition $\theta \leq \theta_{max}$ selected most of the π^0 decay photon pairs and rejected almost all the uncorrelated photon pairs. The calculated $M_{\gamma\gamma}$ distributions for all the photon pairs and for pairs satisfying the opening angle condition, shown in Fig. 7.3, illustrate the power of this condition to reduce the combinatorial background. This reduction, however, is not sufficient for our needs and we required the additional condition that the invariant mass be in the interval $120 < M_{\gamma\gamma} < 150$ MeV/c^2. The efficiency of a set

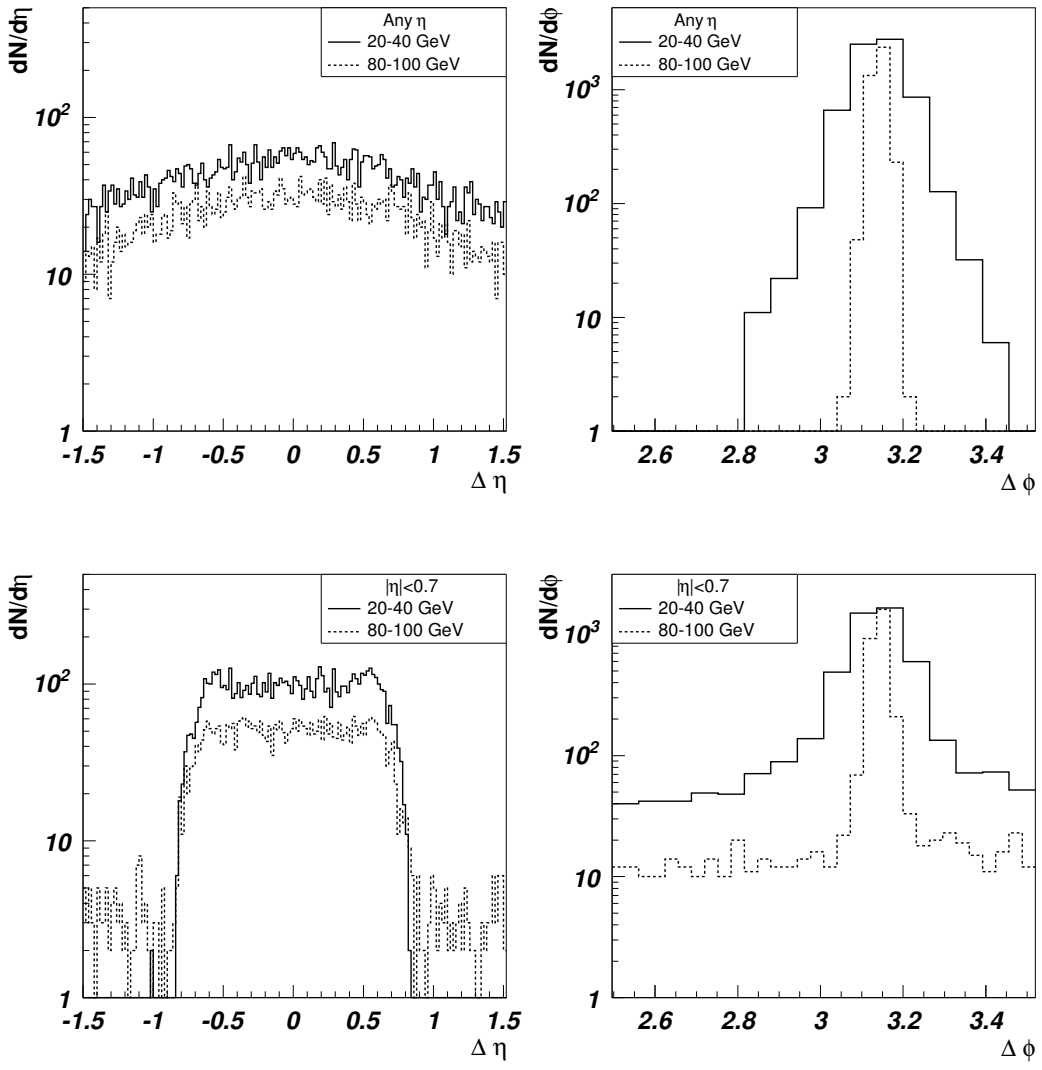

Figure 7.1: Angular correlations between prompt photons and their corresponding jet leading particles as a function of $\Delta\eta = \eta_l - \eta_\gamma$ (left) and $\Delta\phi = \phi_l - \phi_\gamma$ (right), for simulated γ-jet events in the energy ranges 20-40 GeV and 80-100 GeV for pp collisions. Jet particles in lower figures were filtered through the acceptance $|\eta| < 0.7$.

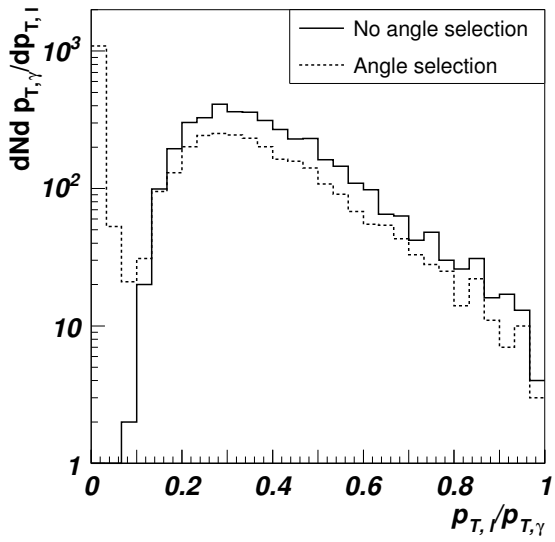

Figure 7.2: Leading particle distribution of γ-jet events as a function of the $p_{T,l}/E_\gamma$ ratio for pp collisions and jet energies in the range 80-100 GeV. The dotted line is for the selected leading particles falling inside the acceptance of the detectors and opposite in ϕ angle to the prompt photon. The solid line is for the leading particles without detector acceptance restriction.

of conditions (opening angle, invariant mass and leading particle) was estimated as the ratio of the number of simulated π^0 to the whole number of photon pairs produced in the heavy-ion event satisfying them, shown in Fig. 7.5. This ratio was between 1 and 1.2 for π^0 of energies greater than 5 GeV for pp collisions and greater than 10 GeV for Pb-Pb collisions. This ratio is greater than one because the opening angle limit eliminates some pairs corresponding to true π^0 decays. It is also observed in Fig. 7.5 that the combinatorial background produces a fast decrease of the signal/noise ratio for Pb-Pb collisions at low energies.

7.3 Jet reconstruction

Jets were reconstructed starting from the seed provided by their leading particle. Particles found in the cone around the leading particle defined by Eq. (6.2) were assigned to a jet if their transverse momentum surpasses a given threshold. Again, a fraction of jet particles may be lost due to the limited detector acceptance, and only jets of reconstructed energy comparable to the energy of their corresponding prompt photon were selected in the end.

In our jet finding algorithm, two experimental configurations were considered,

- Charged particles are detected in the central tracking system and neutral particles in EMCal; this configuration is labelled TPC+EMCal in figures and text;

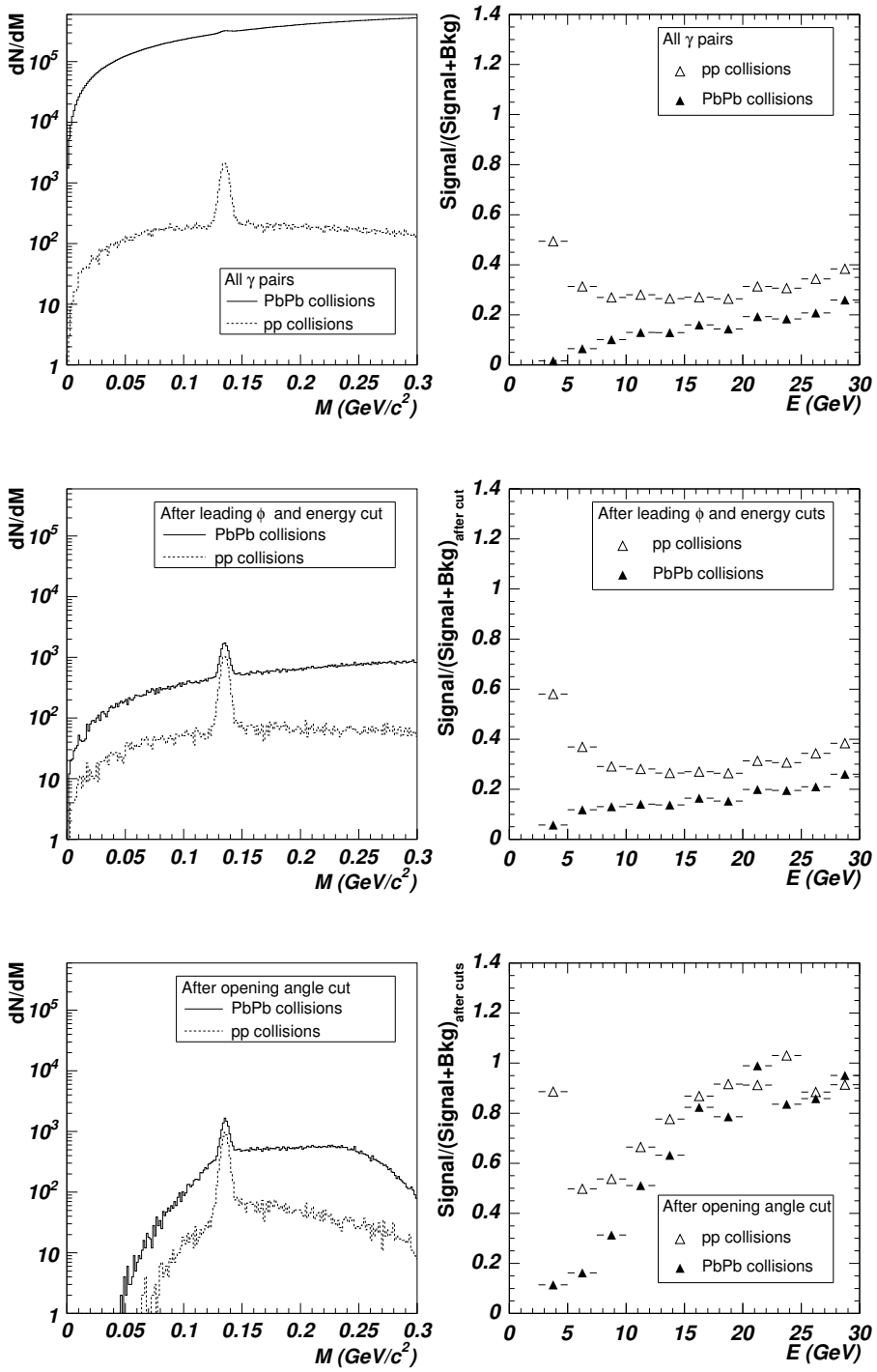

Figure 7.3: Left frames: Invariant mass distributions of all photon pairs in the event (upper figures), of pairs satisfying the ϕ and leading particle energy cut (middle figures) and with in addition the opening angle restriction (lower figures), for pp (dashed line) and Pb-Pb (solid line) collisions at $5.5A$ TeV. Right frames: Ratio of the simulated π^0 number to the selected photon pair number in the event, for pp ($\triangle$) and Pb-Pb ($\blacktriangle$) collisions at $5.5A$ TeV. γ-jet events with jet energy in the range from 20 to 100 GeV were considered.

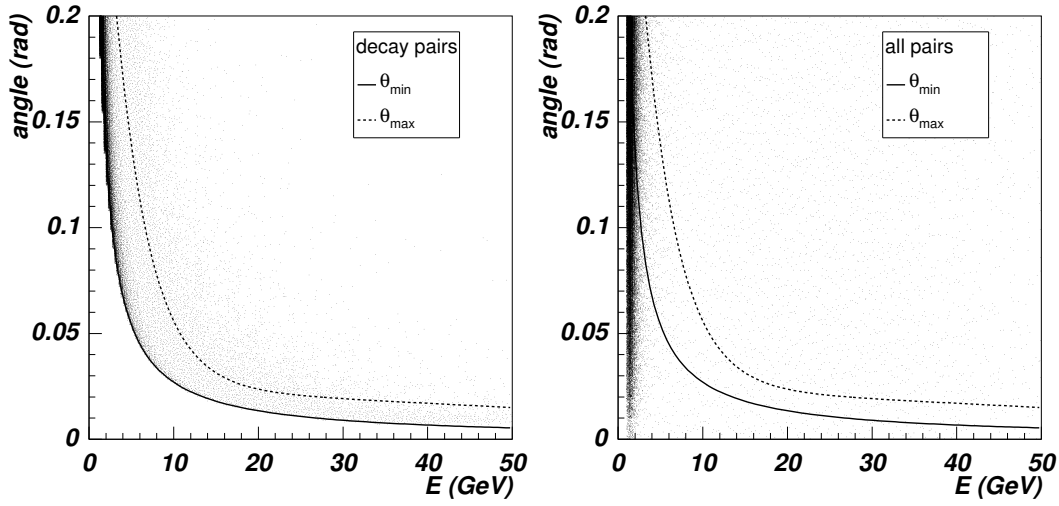

Figure 7.4: Relative angle of photon pairs in the energy window 80-100 GeV as a function of their energy for γ-jet events from simulated Pb-Pb collisions. Left: Opening angle of π^0 decay photon pairs (no restriction in detector acceptance). Right: Opening angle of all photons pairs. The lines limit the opening angle window selected; the lower line was obtained from the decay kinematics, the upper one was empirically chosen to select most of π^0 decay pairs.

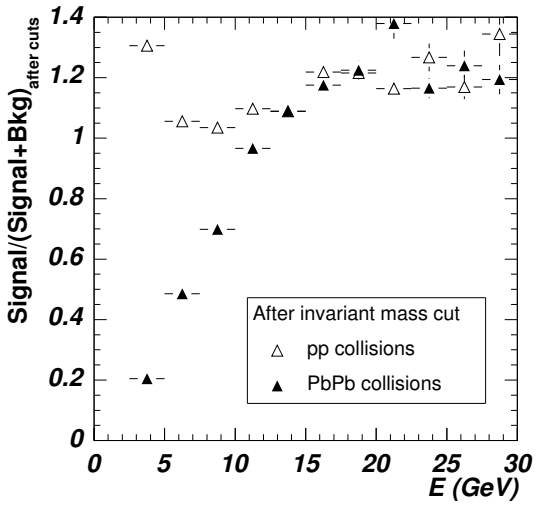

Figure 7.5: Ratio of the number of simulated π^0 to the total number of photon pairs satisfying the opening angle, invariant mass and leading particle selection conditions for pp ($\triangle$) and Pb-Pb ($\blacktriangle$) collisions at $5.5A$ TeV. γ-jet events in the jet energy range from 20 to 100 GeV were considered.

- Only the central tracking system is available and consequently only charged particles can be detected; this configuration is labelled TPC in figures and text.

We compare in Fig. 7.6 the ratio of the measured jet transverse momentum $p_{T,j}$ to the energy of the corresponding prompt photon E_γ for pp collisions, for various photon energies and for the two detector configurations under study. We took a p_T threshold of 0.5 GeV/c. In the TPC+EMCal configuration, the jet energy was well reconstructed and was nearly equal to the energy of the corresponding prompt photon. In the case without EMCal, as the energy carried away by neutral particles cannot be detected, the $p_{T,j}/E_\gamma$ distribution is rather flat. The jet reconstruction was better for higher jet energies. This result is independent of the cone size, which was taken as 0.3 along this study.

In the case of Pb-Pb collisions, the background is very important and the $p_{T,j}/E_\gamma$ distributions were wide and peaked at values greater than 1 as exhibited in Fig. 7.7. We required a higher p_T threshold than for pp collisions in order to remove as much background as possible. If a threshold of $p_T > 2$ GeV/c is required (only to calculate the energy of the jet), the distribution features (peak position and width) resemble to those obtained for pp collisions, at least for high jet energies, as observed in Fig. 7.8. Although the width was still large for 20 GeV/c jets, the requirement of a higher p_T threshold produced a lost of essential information about the jet (2 GeV/c is already the 10 % of the jet energy). Consequently, we systematically required a p_T threshold of 0.5 GeV/c for pp collisions and of 2 GeV/c for Pb-Pb collisions in the calculation of the jet energy. Nevertheless, in the construction of the jet fragmentation function in the next sections, we considered all detected particles inside a cone with $p_T > 0.5$ GeV/c.

A photon-jet event observed in the setup including EMCal is well identified if the ratio $p_{T,j}/E_\gamma$ is close to one. We considered two different values for the lower $p_{T,j}/E_\gamma$ limits required for this ratio, depending on the experimental setup (with or without EMCal). We defined empirically the selection windows shown in Fig. 7.9, which depend on the energy of the reconstructed jet.

The jet reconstruction algorithm failed for low p_T jets because the ratio $p_{T,j}/E_\gamma$ suffers from large fluctuations as shown in Fig. 7.10. Therefore, we excluded jets with p_T values lower than 10 GeV/c from our investigation.

7.4 Jet selection efficiency and contamination

The jet selection efficiency was defined as the ratio of the number of identified γ-tagged jets to the number of prompt photons found in PHOS. This efficiency is shown in Fig. 7.11 for both pp and Pb-Pb collisions. The efficiency for the configuration with EMCal was about 30 %. For the configuration without EMCal we obtained a higher efficiency (40-50 %) due to the wider selection range (which is accompanied by a lower identification

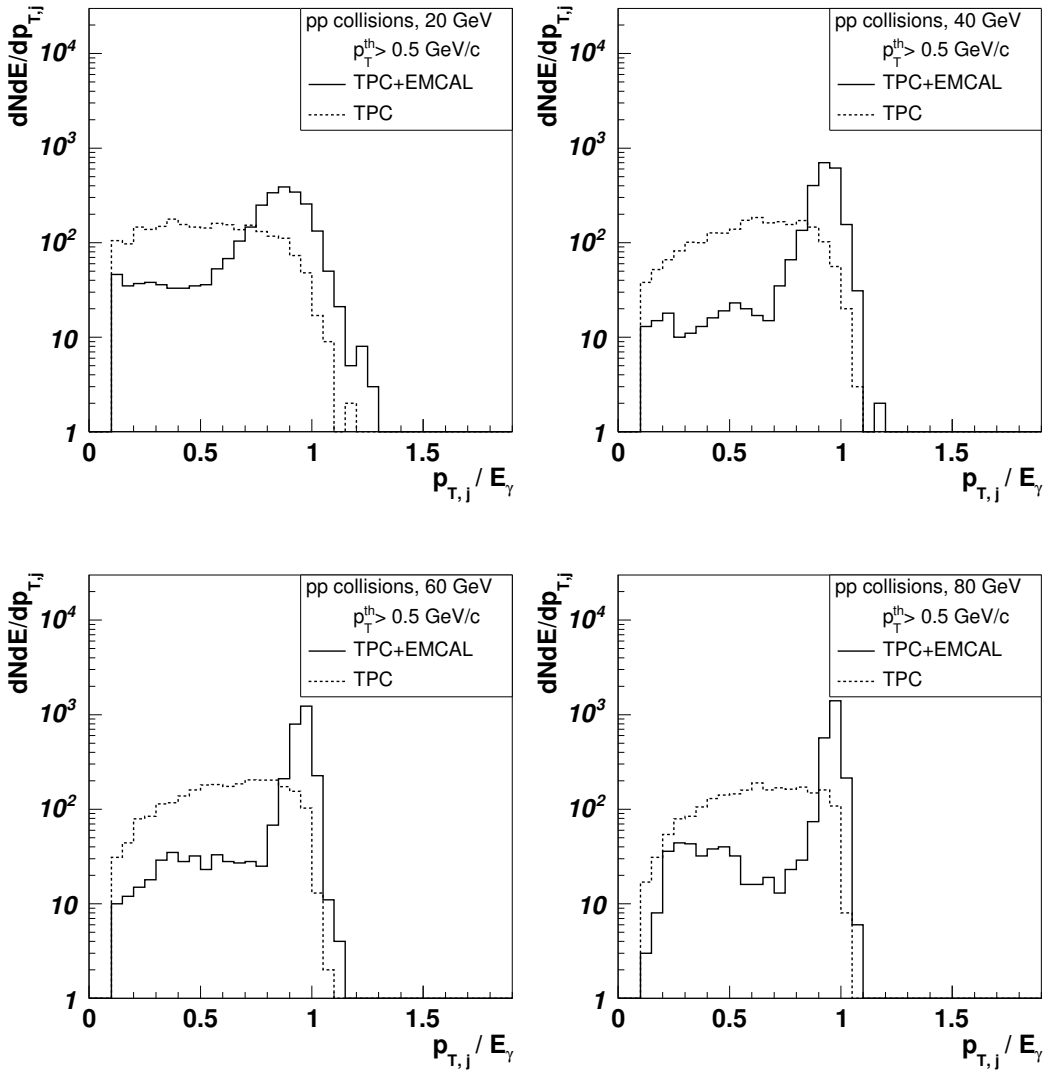

Figure 7.6: Jet distribution as a function of the ratio $p_{T,j}/E_\gamma$ for γ-jet events simulations in the case of pp collisions. A jet cone of $R = 0.3$ and a jet particle threshold of $p_T > 0.5$ GeV/c were assumed. Results for the setups without EMCal (dashed line) and with EMCal (solid line) are given.

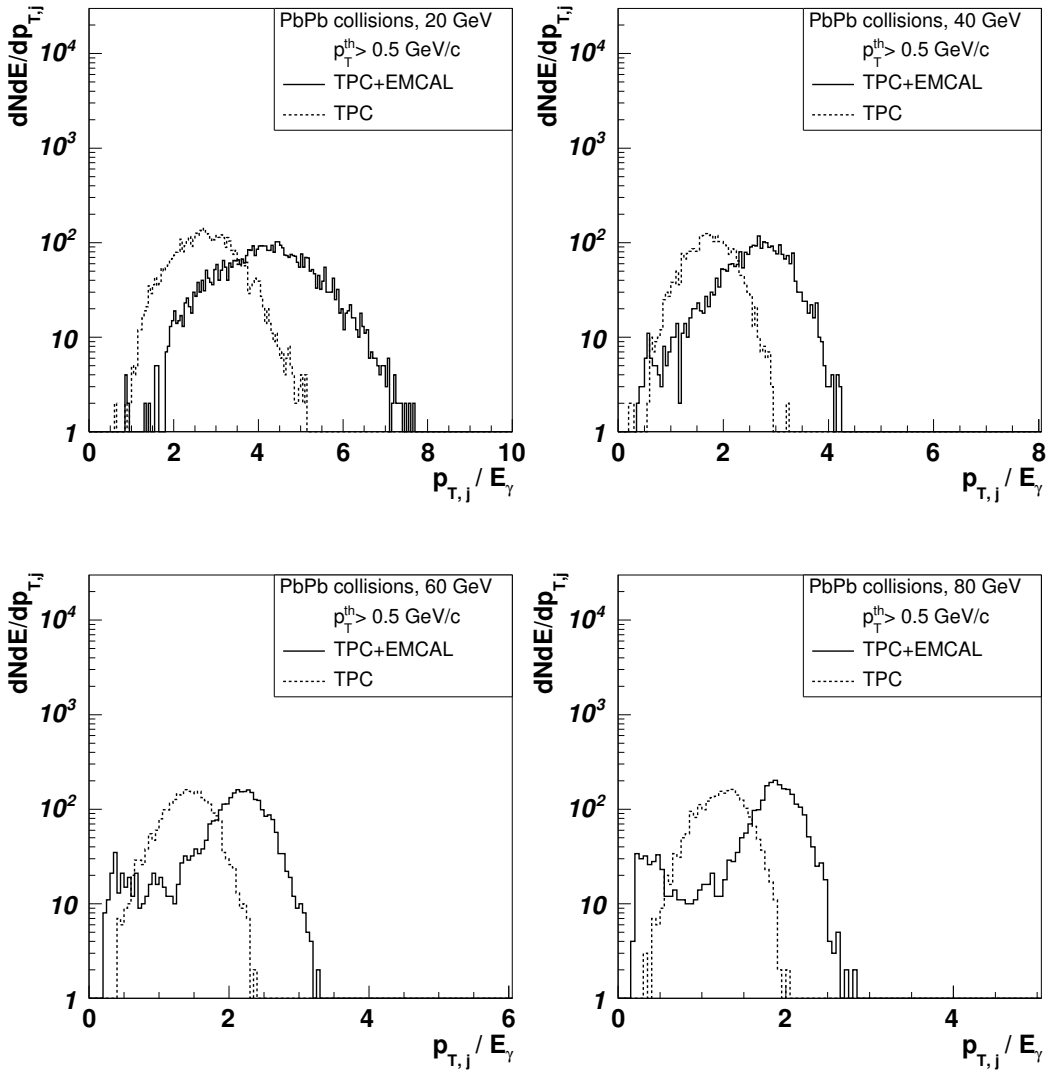

Figure 7.7: Jet distribution as a function of the ratio $p_{T,j}/E_\gamma$ for γ-jet events simulations in the case of Pb-Pb collisions. A jet cone of $R = 0.3$ and a jet particle threshold of $p_T > 0.5$ GeV/c were assumed. Results for the setups without EMCal (dashed line) and with EMCal (solid line) are given.

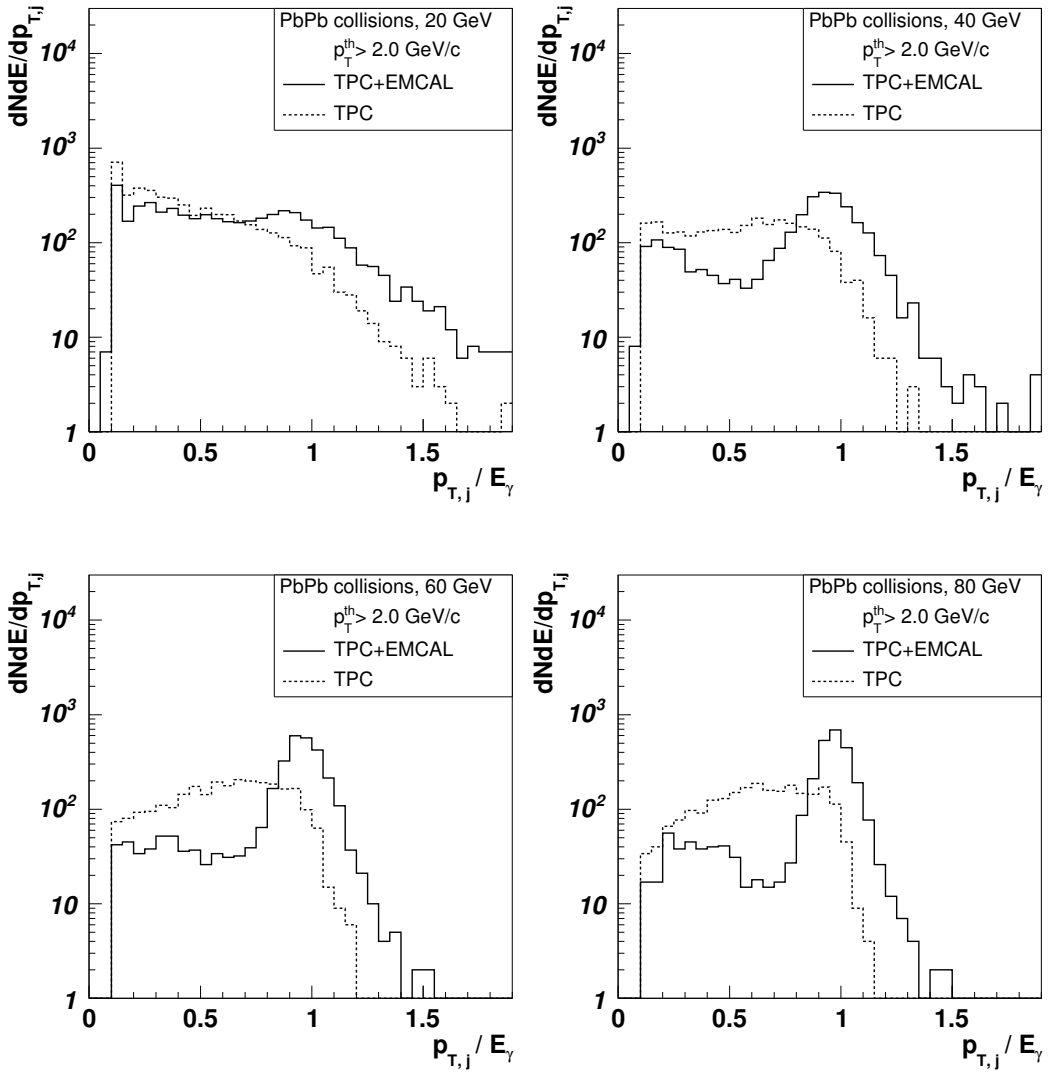

Figure 7.8: Jet distribution as a function of the ratio $p_{T,j}/E_\gamma$ for γ-jet events simulations in the case of Pb-Pb collisions. A jet cone of $R = 0.3$ and a jet particle threshold of $p_T > 2$ GeV/c were assumed. Results for the setups without EMCal (dashed line) and with EMCal (solid line) are given.

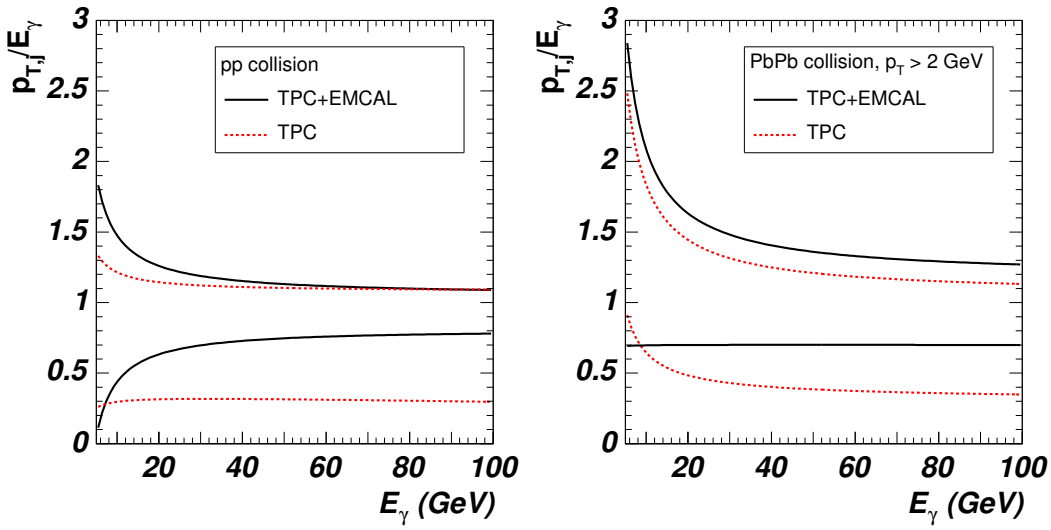

Figure 7.9: Maximum (upper line) and minimum values (lower line) of the $p_{T,j}/E_\gamma$ ratio used to select photon-jet events in the configurations with EMCal (solid line) and without EMCal (dashed line) for pp (left figure) and Pb-Pb collisions (right figure).

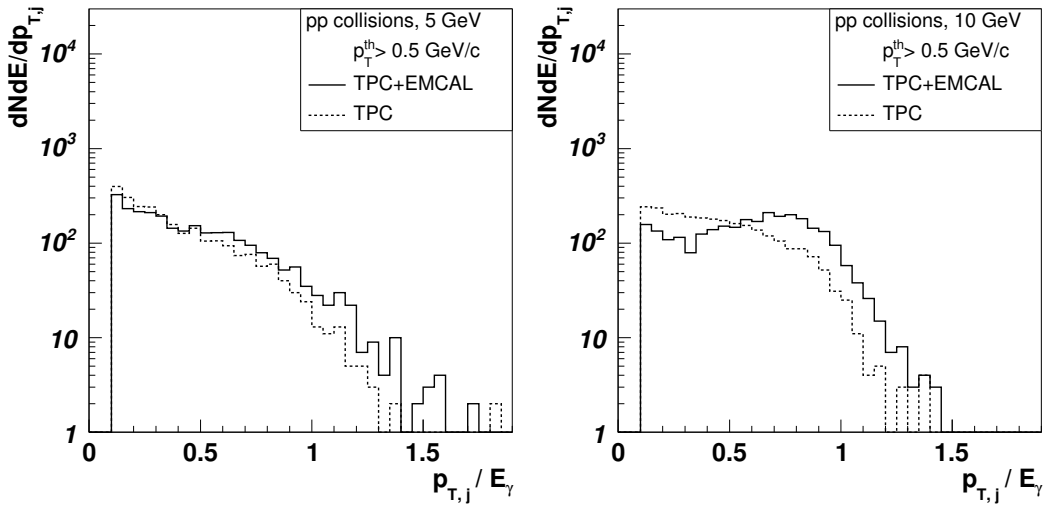

Figure 7.10: Simulated jet distribution as a function of the ratio $p_{T,j}/E_\gamma$ for 5 GeV (left) and 10 GeV (right) jets for pp collisions. A jet cone of $R = 0.3$ and a jet particle threshold of $p_T > 0.5$ GeV/c were assumed. Results for the setups without EMCal (dashed line) and with EMCal (solid line) are given.

quality). A second reason for the lower efficiency in the configuration with EMCal is that we requested that the jet entered completely in EMCal which has a smaller acceptance in azimuth than the central tracking system.

We also applied the γ-jet algorithm to jet-jet events in order to estimate the contamination level. Jets reaching PHOS may contain decay photons which, when misidentified as prompt photons, provide a seed for the algorithm. By comparing the expected rate of prompt photons and γ-like particles detected in PHOS and originating in γ-jet and jet-jet events, shown in Fig. 6.1, we deduced that the contribution of γ-like particles is comparable and often larger than the contribution of prompt photons. By the application of γ-tagging algorithm to jet-jet events we rejected a substantial fraction of misidentified prompt photons. When no prompt photon identification was performed in PHOS, only about 10 % of the events were accepted in the setup with EMCal but this value raised to 40-50 % in the absence of EMCal for both *pp* and Pb-Pb collisions as shown in Fig. 7.11.

We also studied the purity $\mathcal{P}$ and the contamination $\mathcal{C}$ of the γ-jet selected events. We define the purity as the fraction of γ-jet events over the total number of identified events and the contamination as the fraction of jet-jet events accepted as γ-jet events over the total number of identified events, i.e. $\mathcal{C} = 1 - \mathcal{P}$. In a first step, we applied the γ-tagging algorithm to any high-p_T neutral signal detected in PHOS. In the case of the TPC+EMCal configuration, the application of the γ-tagging algorithm leaded to purities of about 80 % and 60 % in the case of *pp* and Pb-Pb collisions, respectively as observed in Fig. 7.12. Without EMCal, the achieved purity was only between 20-40 %. In a second step, we switched on the prompt photon identification (SSA and ICM) in PHOS, which produced an enhancement of the purity, as shown in Fig. 7.13. In the case of *pp* collisions the purity was larger than 90 % for the configuration without EMCal and approached 100 % for the configuration with EMCal. As expected, in the case of Pb-Pb collisions and for the configuration with EMCal, the purity was barely 90 % for low E_γ but at 40 GeV it was near to 100 %; without EMCal the purity stayed around 80 % in all the energy range.

7.5 Fragmentation functions

A satisfactory method of studying quantitatively the interaction of jets with the medium is to investigate how the produced hadrons are distributed in phase space [Sal04], i.e. to measure the jet fragmentation function. The experimental fragmentation function is defined as the distribution of charged hadrons within jets as a function of the variable z, defined for hard processes with a γ-jet pair in the final state as $z = p_T/E_\gamma$. Simulations of jet fragmentation functions to be measured in a standard year of LHC running for both *pp* and Pb-Pb collisions, performed for identified γ-jet events in the energy range from 20 to 100 GeV by integrating all events with prompt photon energy larger than 20 GeV/c, are

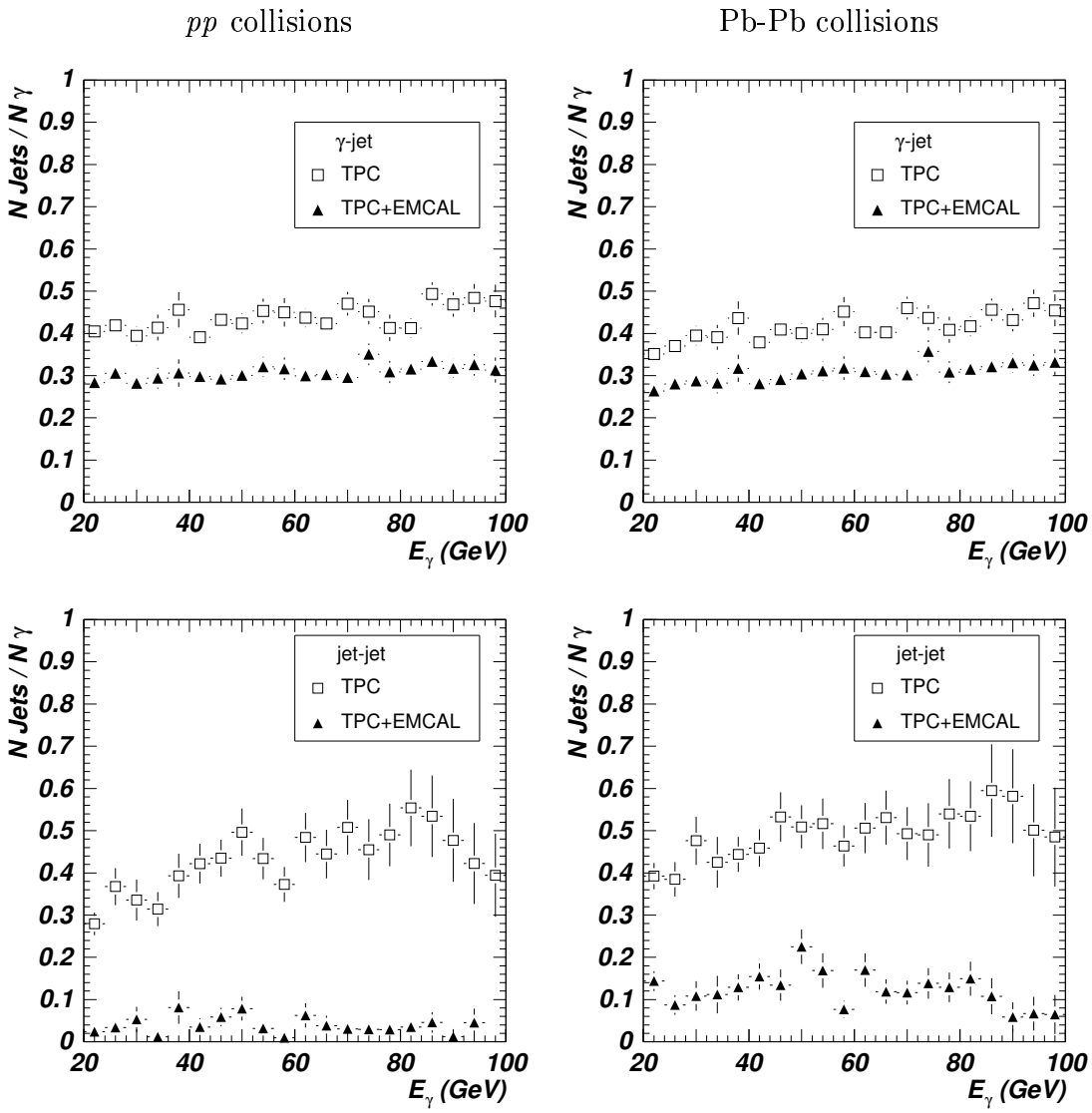

Figure 7.11: Upper frames: Jet selection efficiency. Lower frames: Number of accepted jet-jet events divided by the number of γ-like particles detected in PHOS (not identified), for *pp* (left) and Pb-Pb (right) collisions. Results for the setups without EMCal (□) and with EMCal (▲).

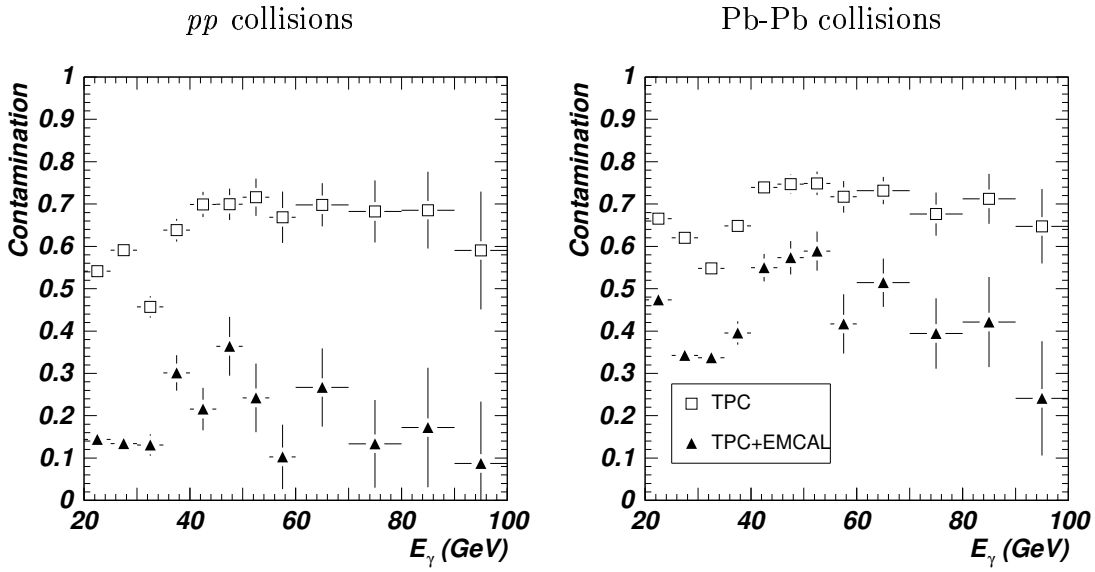

Figure 7.12: γ-tagging contamination without prompt photon identification in PHOS, i.e. a high-p_T neutral signal triggers the jet finding algorithm. Left (right) frame corresponds to pp (Pb-Pb) collisions. Results shown for the setups without EMCal (□) and with EMCal (▲).

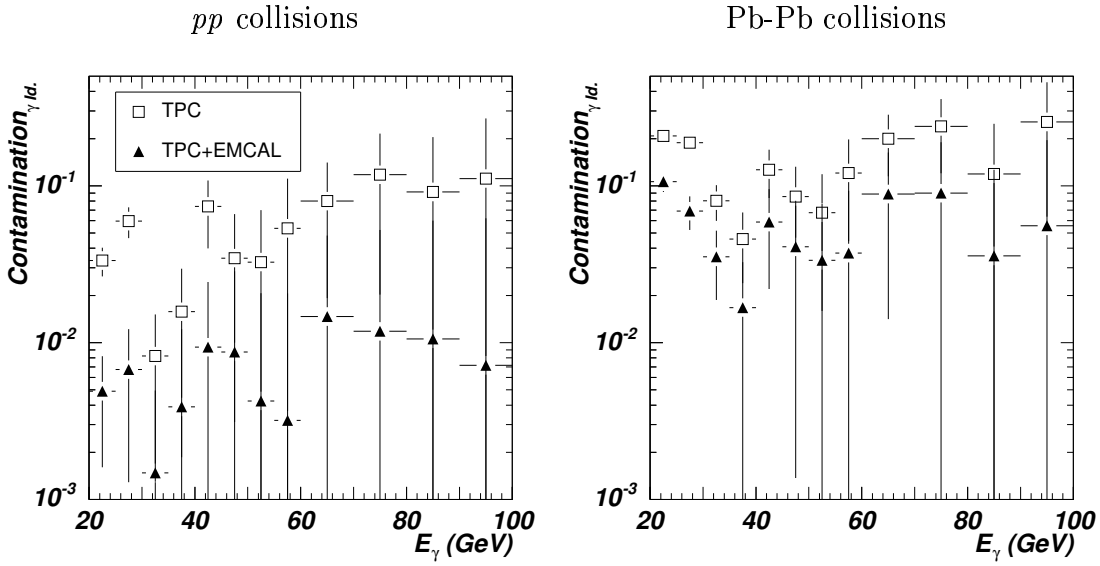

Figure 7.13: γ-tagging contamination with prompt photon identification in PHOS (SSA+ICM). Left (right) frame correspond to pp (Pb-Pb) collisions. Results shown for the setups without EMCal (□) and with EMCal (▲).

displayed in Fig. 7.14; the fragmentation functions obtained for jet-jet events misidentified as γ-jet events are also displayed. The following conclusions are drawn:

- In the case of *pp* collisions, the contamination due to misidentified jet-jet events dominates the true γ-jet contribution in the absence of EMCal if no prompt photon identification is performed in PHOS. In the setup with EMCal, the contamination is suppressed, leading to a signal to background ratio of about four. If prompt photons in PHOS are identified by medium purity SSA and ICMS, the contamination of misidentified jet-jet events is dramatically reduced, leading to a signal to background ratio of about 20 in the configuration without EMCal and near to 100 % background rejection for the setup with EMCal. The reduction of background only produces a reduction of 10 % of the γ-jet statistics.

- Concerning Pb-Pb collisions, the fragmentation function has very large values at low z due to low-p_T charged hadrons coming from the HIC underlying event. This contribution can be eliminated by subtracting a pseudo-fragmentation function calculated outside the cone of the leading particle. This subtraction is not performed event-by-event but for the final distributions. We constructed the pseudo-fragmentation function with particles inside a cone centered at (ϕ_γ, $\eta_{leading}$) which is a region where there is no contribution from the jet in γ-jet events and only particles from the HIJING event are found. Prompt photon identification by medium purity SSA and ICM is required to reduce the contamination of wrongly identified jet-jet events to an acceptable level. The final signal to background ratio obtained is about four in the case without EMCal and rises to about ten with EMCal. Prompt photon identification reduces the statistics of γ-jet events to about 60 %.

The measured fragmentation functions, calculated as the sum of the identified γ-jet events and jet-jet background events scaled by the cross section, are shown in Fig. 7.15. The statistical errors were calculated from the statistics predicted for a standard LHC running year. The systematic errors reflect the amount of contamination. We considered also the case of jet-jet events quenched by a factor 5 as observed at RHIC. Without quenching, the systematic errors were similar to the statistical errors in the range $0.1 < z < 0.5$, whether EMCal is present or not. The statistical errors outside this z range were too large. With EMCal, the systematic errors were reduced by a factor larger than 5 in *pp* collisions and about 2 in Pb-Pb collisions as compared with the setup without EMCal. When quenching was considered, the systematic errors were reduced by an additional factor 5 and they were always smaller than the statistical errors with or without EMCal.

To evaluate the sensitivity of photon-tagged jet fragmentation functions to nuclear medium modifications, we calculated the nuclear modification factor R_{FF} which is defined as the ratio of the fragmentation function measured in AA collisions to the fragmentation

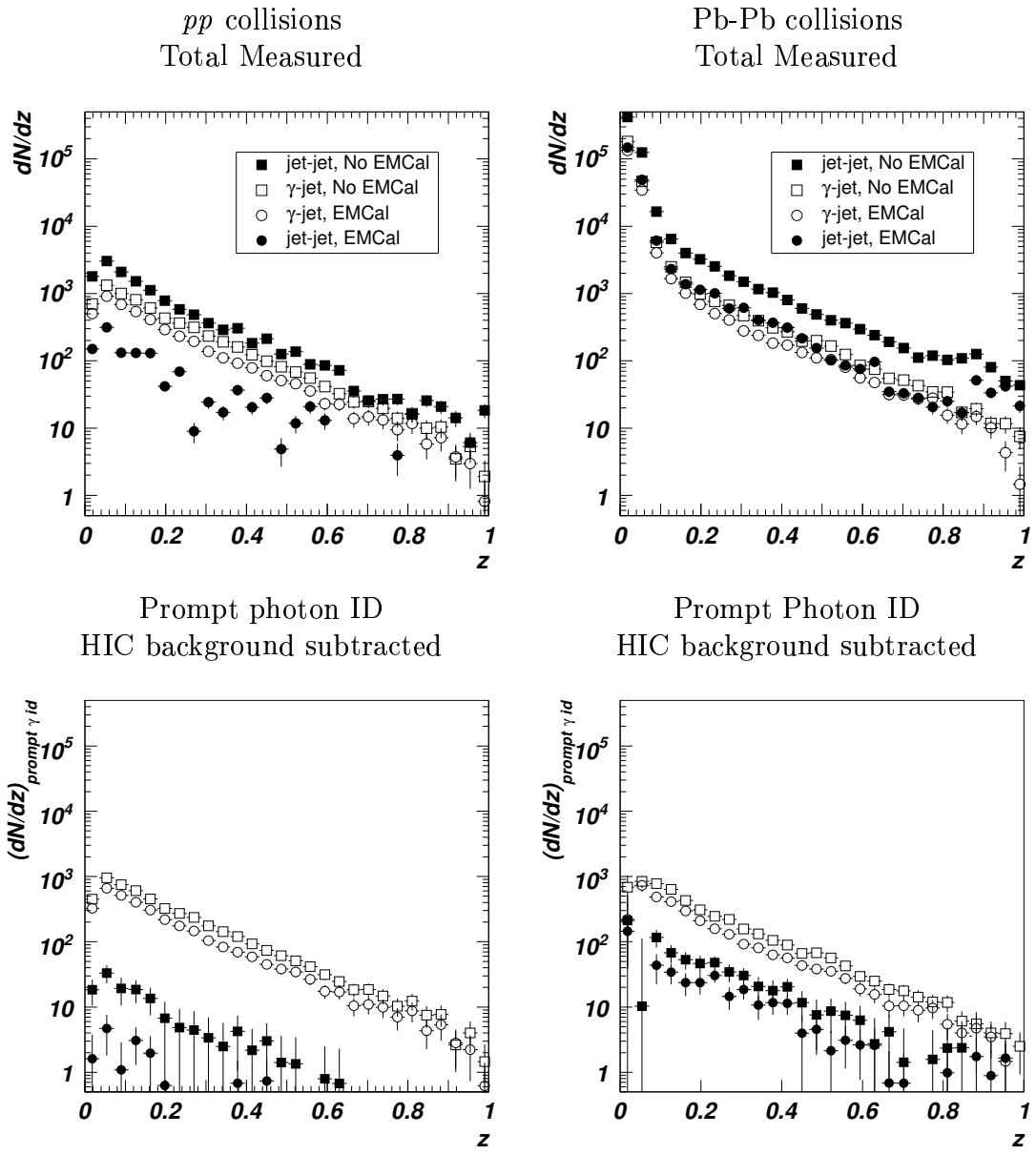

Figure 7.14: Fragmentation function for γ-jet and jet-jet events with energy larger than 20 GeV for *pp* (left) and Pb-Pb (right) collisions. The upper figures were calculated with neither prompt photon identification in PHOS nor HIC background subtraction. The lower figures show the fragmentation function for prompt photons identified in PHOS by medium purity SSA and ICM (*pp* collisions) or ICMS (Pb-Pb collisions), and for HIC background subtracted.

function measured in *pp* collisions scaled to the number of binary *NN* collisions, both fragmentation functions calculated for the same beam luminosity and running time. This factor should be equal to one in the absence of nuclear effects. We indeed obtained a value close to one over the entire z range as shown in Fig. 7.16 because no medium modification effect was included in our simulations. The statistical and systematic errors indicate that in the range $0.1 < z < 0.5$ variations of the R_{FF} of the order of 5 % could be measured for both setups. When a quenching factor of 5 for hadrons produced in jet-jet events was included, the systematic error was under 5 % for both setups. However, the measurement of the nuclear modification factor with an accuracy better than 5 % is limited by the whole statistics expected.

We may still consider another measurement approach in which EMCal is in charge of the prompt photon detection and jets are only detected by the central tracking system[2]. In this setup, assuming similar prompt photon identification features of PHOS and EMCal, the prompt photon detection is enhanced by a factor seven and consequently the statistical errors are reduced by a factor 2.6. In this case, modifications in the fragmentation function in a wider z range could be measured which is a crucial issue because nuclear medium modifications are expected to increase with z.

7.6 Conclusions

We developed an algorithm to identify γ-jet events generated in *pp* and Pb-Pb collisions at LHC energies in ALICE. γ-jet events were identified by selecting a prompt photon in PHOS and searching for a leading particle in the opposite direction inside the ALICE central tracking system. Setups with and without EMCal were considered. Jets were reconstructed by an algorithm in which the leading particle was used as a seed; the reconstructed jet was taken as correlated to the photon if a number of conditions were fulfilled. The efficiency of identifying γ-jet events was mainly limited by the acceptances of the central tracking system and EMCal. For jets of energy larger than 20 GeV, this efficiency was found to be between 40 % to 50 % without EMCal and about 30 % with EMCal due to the smaller EMCal acceptance. As jet-jet cross sections are larger than γ-jet cross sections, jet-jet events produce a considerable background due to photons from π^o decay misidentified in PHOS as prompt photons. If EMCal is included, jet-jet background is satisfactorily rejected and the contamination is reduced to a negligible level if shower shape and isolation cut analyses are employed. We obtain from our simulations that fragmentation functions can be accurately measured in order to obtain the nuclear modification factor R_{FF}. We conclude that nuclear medium modifications can be measured if they produce variations of R_{FF} larger than 5 % in the region $0.1 < z < 0.5$.

[2] It is not well advise to use PHOS as a detector of jet neutral particles due to its reduced acceptance.

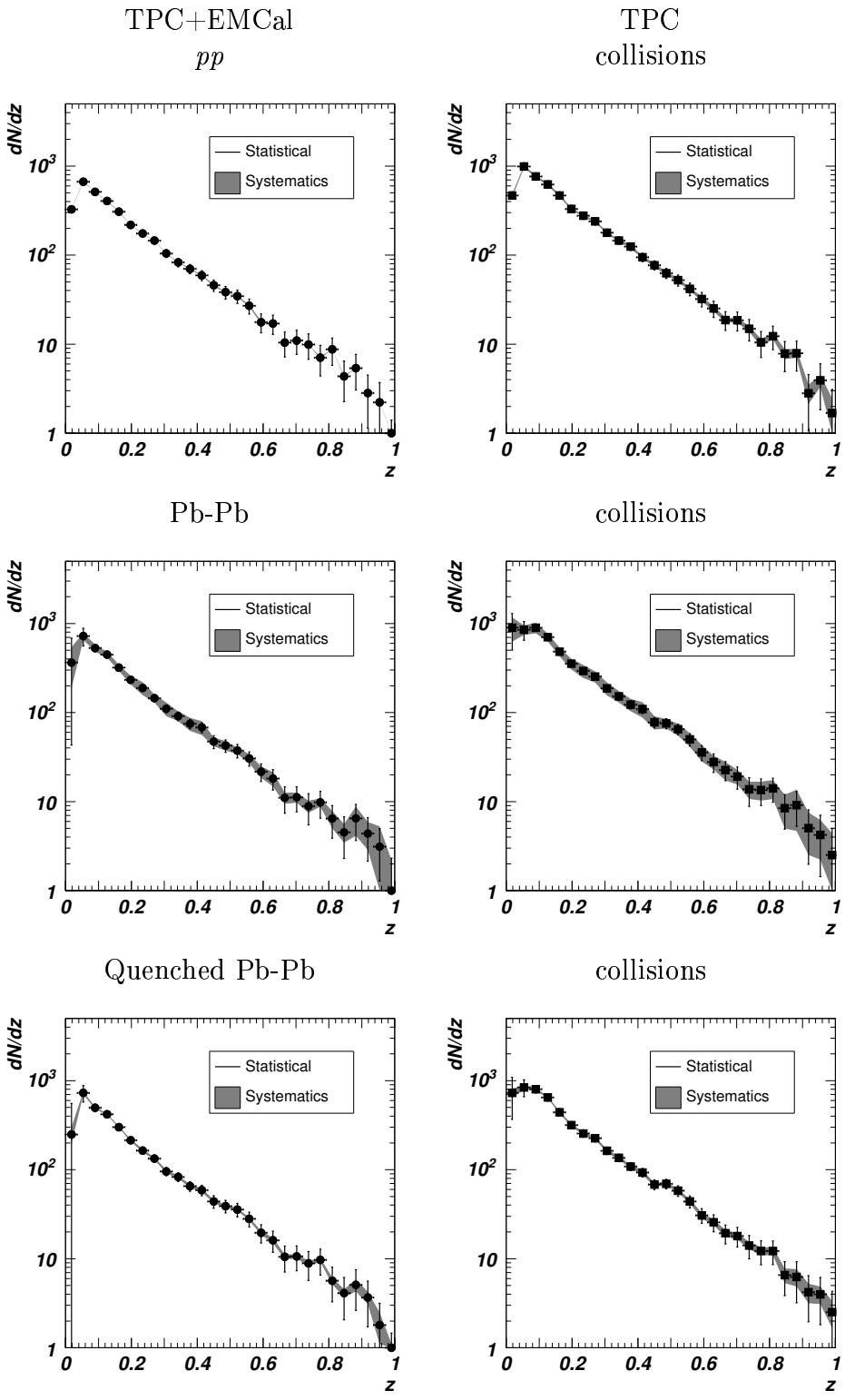

Figure 7.15: Fragmentation function of γ-tagged jets (γ-jet+jet-jet events after prompt photon identification) with energy larger than 20 GeV for a whole ALICE year, detected in the central tracking system and EMCal (left frames) and in the central tracking system alone (right frames), for *pp* (upper frames), Pb-Pb (central row frames) collisions and quenched Pb-Pb collisions (lower frames). The shaded regions represent the systematic error due to jet-jet contamination.

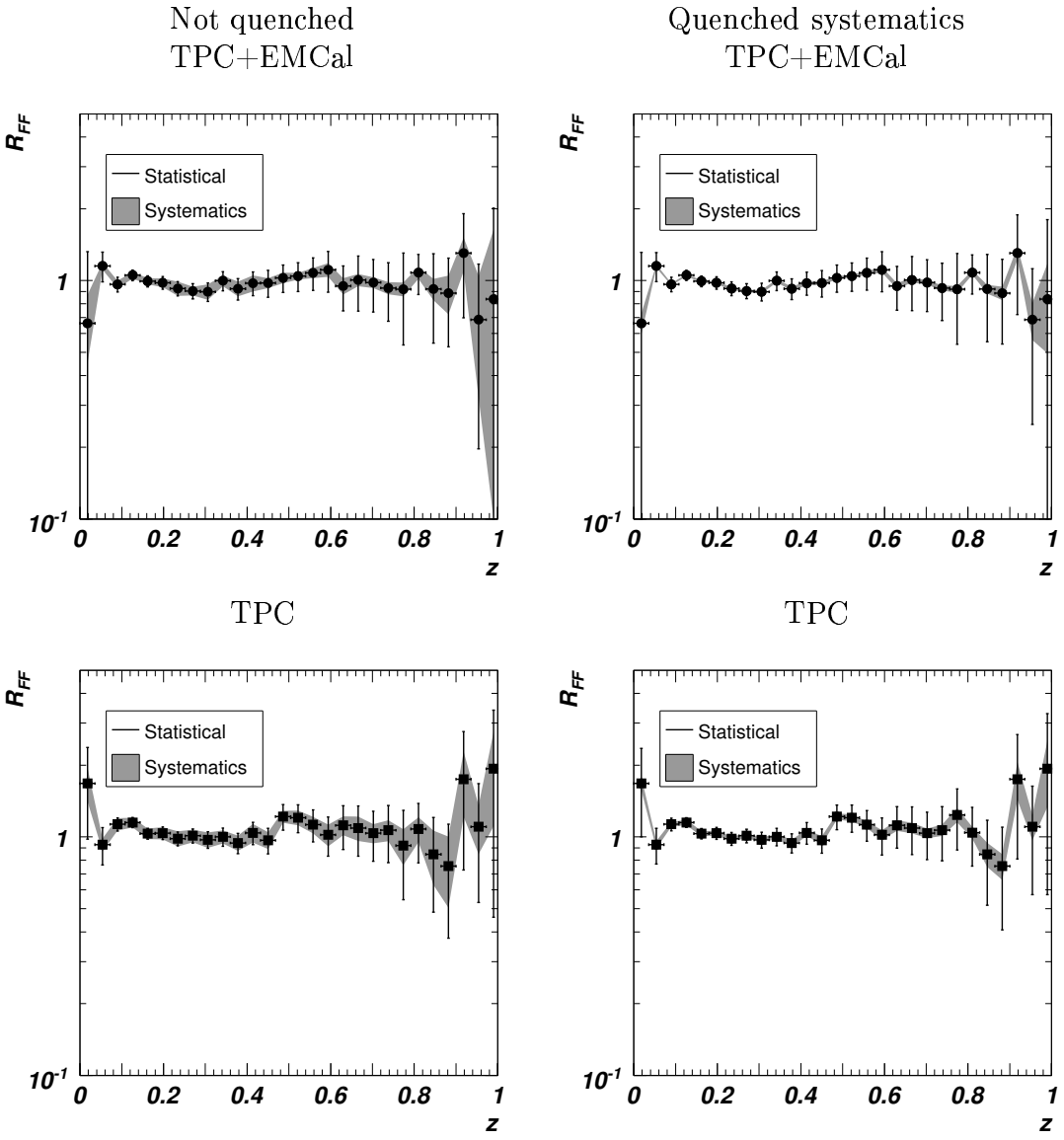

Figure 7.16: Ratio of the fragmentation functions of γ-tagged jets with energy larger than 20 GeV for Pb-Pb collisions scaled by Eq. (6.1) to *pp* collisions detected in the central tracking system and EMCal (upper figures) or in the central tracking system alone (lower figures). The shaded region represents the systematic error due to the contamination from jet-jet events. In left figures no quenching is assumed and in right ones the background is quenched.

Conclusions

The aim of this thesis is to study the performance of the PHOS detector and to develop tools to identify photons and hard processes associated to photons in the ALICE experiment at the LHC accelerator. The ALICE experiment is mainly devoted to the study of the Quark-Gluon Plasma formed in heavy-ion collisions at ultra-relativistic energies (Pb-Pb collisions at $\sqrt{s} = 5.5A$ TeV). Among the signals conveying information on the properties of this medium, photons are particularly useful. Since they are produced in all stages of the heavy-ion collision and they do not interact strongly, they carry undistorted information of the nuclear medium which is not perturbed by their emission. The following topics are studied in different chapters: PHOS performance, particle identification, prompt photon identification and identification of γ-jet events. The conclusions obtained are:

PHOS performance The PHOton Spectrometer consists of modules of $PbWO_4$ crystals that constitute the Electromagnetic Calorimeter, associated to a Charged Particle Veto, and has been designed to measure and identify with high accuracy photons, electrons, and neutral mesons. The following conclusions about its performance are obtained:

1. We performed measurements with a PHOS prototype in test experiments. The results obtained were used to tune the parameters of the algorithms developed to simulate the response of PHOS and to perform the reconstruction of the signals collected by PHOS. Simulations and test data confirm that PHOS can measure photons with a high energy resolution, ranging from 5 % at 0.5 GeV to 1 % at 120 GeV. Simulations indicate, in addition, that a position resolution from 3-4 mm at 1 GeV to 0.7-2.5 mm at 50 GeV can be achieved, depending on the incidence angle of photons on PHOS.

2. A heavy-ion environment simulated by the HIJING event generator worsens the energy resolution by about 2 % for photon energies below 10 GeV, and by less than 1 % for higher photon energies.

3. The effect of the ALICE material environment was studied considering two detector configurations in ALICE: configurations with and without holes in the detectors Time-Of-Flight and Transition Radiation Detector in front of the PHOS acceptance. In the configuration with holes, at most 10 % of photons are lost due to absorption or conversion in the material of Time Projection Chamber and Inner Tracking System detectors (the

ALICE central tracking system), and of the ALICE frame, but the lost increases to 30 % when Time-Of-Flight and Transition Radiation Detector have no holes.

Particle identification Particle identification with PHOS relies on three identification criteria: time of flight measurement; charged particle track matching between the Charged Particle Veto and the Electromagnetic Calorimeter; and shower shape analysis. In this thesis I conclude that:

4. If the time of flight, Charged Particle Veto and Principal Component Analysis of shower shape are combined, photons, electrons and hadrons are discriminated with good accuracy in the energy range from 0.5 to 120 GeV. The method has been tested with both single photons, and photons embedded in a heavy-ion environment simulated with the HIJING event generator. The contamination of wrongly identified photons is small, ranging from about 3 % to 1 % depending on the requested level of identification purity and on the particle environment.

5. Neutral pions can be identified through an invariant-mass analysis in the energy range between 0 and 40 GeV, and by an event-by-event shower shape analysis for energies from 40 GeV to 120 GeV at which the two decay photons are detected as a single cluster in PHOS. In the latter energy range, the misidentification probability of neutral mesons as photons is a few percent for energies below 70 GeV but increases up to about 5-15 % at 120 GeV.

6. High-energy photons converted in the material in front of PHOS can be recovered with the help of the tracking information collected by the Time Projection Chamber. Photons converted in the material between the Time Projection Chamber and PHOS in e^-e^+ pairs are identified as a hit in the Charged Particle Veto that has no corresponding charged track in the Time Projection Chamber. By an invariant mass analysis, the energy of parent photon ($M_{e^-e^+} = 0$) is obtained. This method is only useful in the configuration without holes for which the photon detection efficiency of the configuration with holes is almost recovered.

Prompt Photon identification Prompt photons are produced in Compton and annihilation processes at the parton level in *pp* and Pb-Pb collisions. The main background are photons produced in events with two jets in the final state. The event generator PYTHIA was used to generate both prompt photons and the background. I obtained the following results:

7. The prompt photon production rate expected in one ALICE running year is sufficiently high to measure prompt photons with energies up to about 100 GeV with PHOS.

8. As the predicted background (π^0 photon decay, single and overlapped clusters, and bremsstrahlung) exceeds by a factor two the prompt photon signal for prompt photon energies larger than 20 GeV, the application of the photon identification methods men-

tioned in the point 4 above, is not sufficient to reduce the contamination to an acceptable level. I developed therefore an additional identification method, the Isolation Cut Method. This method is based on the fact that prompt photons are produced isolated whereas the background, mainly produced by π^0 mesons belonging to jets, is therefore accompanied by other particles. I developed an isolation criteria based on the particle multiplicity inside a cone of size R around the direction of prompt photon candidates, and on the momentum of the particles inside this cone. I obtained the following conclusions:

- In the case of *pp* collisions, prompt photons are best identified by the condition that the total sum of the transverse momentum of all the particles inside a cone of size $R = 0.2$ is smaller than 0.7 GeV/c. The resulting prompt photon identification efficiency approaches 100 % and the misidentification probability is less than 5 %.

- In the case of Pb-Pb collisions, prompt photons are identified by requiring that there is no particle inside a cone of size $R = 0.2$ with transverse momentum larger than 2 GeV/c. The resulting prompt photon identification efficiency is about 50 % and the misidentification probability about 7 %.

9. I applied the Isolation Cut Methods to PYTHIA simulated data to construct the prompt photon spectrum expected to be measured during one year of data taking. The cross section corrected for the identification probabilities and with both statistical and systematic errors was calculated. Systematic errors due to the identification method are negligible and only those due to the background are significant, about a 20 % in the photon energy range $20 < E_\gamma < 100$ GeV. The statistical errors are dominant for photon energies larger than 60 GeV.

Identification of γ-jet events A prompt photon is associated with a recoiling jet which is sensitive to the nuclear medium produced in the heavy-ion collision. I studied these events with the following conclusions:

10. I developed an algorithm to identify γ-jet events based on the identification of the prompt photon in PHOS and the measurement of the recoiling jet particles in the central tracking system and (if available) in an ElectroMagnetic CALorimeter placed opposite to PHOS. This algorithm was tested with signal (γ-jet) and background (jet-jet) events of Pb-Pb and *pp* collisions. I conclude that for jets with energies larger than 20 GeV, the probability of identifying γ-jet events is limited by the acceptance of the central tracking system and the ElectroMagnetic CALorimeter to 30 % - 50 %, depending on the detector configuration used for the jet reconstruction.

11. Since the cross section of jet-jet production is much larger than the cross section of γ-jet production, there is a huge background due to π^o decay photons. I showed that

the background of prompt photon identification can be reduced to a negligible level by the γ-jet identification algorithm together with shower shape and isolation cut analyses.

12. The parton fragmentation function, which is affected by the parton energy loss in the nuclear medium, was calculated for the simulated γ-jet events, for both pp and Pb-Pb collisions. A nuclear modification factor R_{FF} close to one was obtained, as expected for simulated data that do not contain any nuclear medium modification. From these simulations I obtained that, independently of the detector configuration employed, variations of the nuclear modification factor larger than 5 % in the range $0.1 < z < 0.5$ could be measured.

In summary, direct photon production is a promising signature to study nuclear matter under extreme conditions. I have shown in the present thesis that the PHOS detector possesses the very adequate capabilities to carry out such studies in the ALICE experiment. The algorithms developed for photon detection with PHOS have been tuned to obtain particle identifications with high purity and efficiency and are important tools for the collaboration when the experiment is operational. Of prime importance, I report in this thesis the first hints of how to measure the properties of high-p_T processes through jet analysis. By combining PHOS with other ALICE detectors, effects due to a hot and dense nuclear medium could be probed with a good sensitivity.

Conclusiones

El objetivo de esta tesis es el estudio del rendimiento del detector PHOS y el desarrollo de herramientas para la identificación de fotones y procesos duros en el experimento ALICE que se realizará en el acelerador LHC. El experimento ALICE está dedicado principalmente al estudio del Plasma de Gluones y Quarks producido en colisiones de iones pesados a energías ultrarrelativistas (colisiones de Pb-Pb a $\sqrt{s} = 5.5A$ TeV). Entre los observables experimentales que proporcionan información de este medio, los fotones son particularmente útiles, dado que son producidos en todas las fases de la colisión y no interaccionan fuertemente con la materia nuclear, por lo que los fotones en el momento de su detección son portadores de información no distorsionada del medio nuclear que los produjo. Se estudian los siguientes temas en los diferentes capítulos: rendimiento del detector PHOS, identificación de partículas, identificación de fotones rápidos e identificación de sucesos γ-jet. Se han obtenido las siguientes conclusiones:

Rendimiento de PHOS El espectrómetro de fotones PHOS consiste en módulos de cristales de $PbWO_4$, asociados a un detector veto de partículas cargadas. PHOS fue diseñado para medir e identificar con gran precisión fotones, electrones, y mesones neutros. Las siguientes conclusiones acerca de su rendimiento han sido obtenidas:

1. Hemos realizamos medidas con un prototipo de PHOS en test experimentales. Los resultados obtenidos se han utilizado para afinar los parámetros de los algoritmos desarrollados para simular la respuesta del detector y para realizar la reconstrucción de las señales recogidas por PHOS. Tanto las simulaciones como los datos experimentales confirman que PHOS es capaz de medir fotones con una alta resolución en energía, que varía del 5 % para fotones de 0.5 GeV al 1 % para fotones de 120 GeV. Además, las simulaciones indican que se puede obtener una resolución de la posición de alrededor de 3-4 mm para fotones de 1 GeV y de 0.7-2.5 mm para fotones de 50 GeV, dependiendo del ángulo de incidencia de los fotones en PHOS.

2. Un entorno de partículas producido por colisiones de iones pesados, simulado por el generador de sucesos HIJING, empeora la resolución en energía como mucho en un 2 % para fotones de energía por debajo de 10 GeV, y menos de un 1 % para fotones de energías mayores.

3. El efecto del material de ALICE entre el punto de interacción y PHOS se estudió

considerando dos posibles configuraciones de los detectores: configuraciones con y sin agujeros en frente de PHOS en los detectores de Tiempo De Vuelo y de Radiación de Transición. En la configuración con agujeros al menos un 10 % de los fotones se pierde debido a absorciones y conversiones en el material de los detectores Cámara de Proyección Temporal y Sistema de Seguimiento Interno (detectores que conforman el sistema central de muestreo en ALICE), y el armazón de ALICE, pero la pérdida se incrementa al 30 % cuando los detectores Tiempo De Vuelo y de Radiación de Transición no tienen agujeros.

Identificación de partículas La identificación de partículas con PHOS se apoya en tres criterios de identificación: medida del tiempo de vuelo; identificación de partículas cargadas por medio de la proximidad de los impactos de la partícula en el Veto de Partículas cargadas y el Calorímetro Electromagnético de PHOS; análisis de la forma de la cascada. En esta tesis concluyo que:

4. Si se combinan la medida del tiempo de vuelo, la identificación de partículas cargadas por el veto y el análisis de la forma de la cascada mediante el Análisis de los Componentes Principales, somos capaces de diferenciar entre fotones, electrones y hadrones con una buena precisión para energías entre 0.5 y 120 GeV. El método ha sido probado con simulaciones de fotones simples y fotones en un entorno de partículas producido en colisiones de iones pesados, simulado con el generador de sucesos HIJING. La contaminación por partículas identificadas incorrectamente como fotones es pequeña, variando del 3 % al 1 % dependiendo del grado de pureza y eficiencia requerido en la identificación, así como del entorno de partículas considerado.

5. Los piones neutros pueden ser identificados mediante análisis de masa invariante para energías comprendidas entre 0 y 40 GeV, o bien suceso a suceso mediante análisis de la forma de la cascada en el dominio de energía entre 40 y 120 GeV, en el cual los dos fotones de la desintegración del mesón son detectados como una sola partícula en PHOS. En este último dominio de energía, el porcentaje de mesones neutros como fotones es menor del 5 % para energías de los π^0 por debajo 70 GeV, pero aumenta hasta el 5-15 % para π^0 de 120 GeV, dependiendo del método de identificación empleado.

6. Los fotones de alta energía convertidos en el material delante de PHOS, pueden ser recuperados con la ayuda de la información proporcionada por la Cámara de Proyección Temporal. Los fotones que se convierten en el material entre la Cámara de Proyección Temporal y PHOS, produciendo pares e^-e^+, son identificados si la detección de una partícula cargada en el Veto de Partículas Cargadas no se corresponde con su detección en la Cámara de Proyección Temporal. Mediante el análisis de la masa invariante ($M_{e^-e^+} = 0$), la energía del fotón original puede ser obtenida. Este método es sólo útil en la configuración sin agujeros, y permite obtener casi la misma eficiencia de detección que en la configuración con agujeros.

Identificación de fotones rápidos Los fotones rápidos se producen en procesos Compton y de aniquilación a nivel de partones, en colisiones *pp* y Pb-Pb. El mayor fondo de contaminación es debido a fotones producidos en sucesos con dos jets en el estado final. He utilizado el generador de sucesos PYTHIA para generar tanto fotones rápidos como el fondo. Obtuve los siguientes resultados:

7. La tasa de producción de fotones rápidos en un año de funcionamiento de ALICE muestra que se puede medir con PHOS fotones rápidos de hasta 100 GeV.

8. Como el fondo que se predice (fotones producidos en la desintegración del π^0 y bremsstrahlung) excederá un factor dos la señal de fotones rápidos con energías mayores de 20 GeV, los métodos de identificación de fotones desarrollados anteriormente no son suficientes para reducir la contaminación a un nivel aceptable. Se consideró por lo tanto un método de identificación adicional, el Método por Corte de Aislamiento. Este método se basa en el hecho que los fotones rápidos son producidos aislados mientras que el fondo es principalmente producido por mesones π^0 pertenecientes al jet, y por lo tanto acompañados por otras partículas. He desarrollado un criterio de aislamiento basado en la multiplicidad de partículas dentro de un cono de radio R alrededor de la dirección de una partícula candidata a fotón rápido, y en el momento de las partículas dentro del cono. Se obtuvieron los siguientes parámetros óptimos para la identificación:

- En el caso de colisiones *pp*, los fotones rápidos son mejor identificados si la suma del momento transverso de las partículas dentro de un cono de radio $R = 0.2$ es más pequeña que 0.7 GeV/c. La eficiencia de detección de fotones rápidos resultante es cercana al 100 % y la probabilidad de identificación de fondo como fotones rápidos es menor que el 5 %.

- En el caso de colisiones Pb-Pb, los fotones rápidos son identificados si no hay partículas dentro de un cono de radio $R = 0.2$ con momento transverso superior a 2 GeV/c. La eficiencia de identificación de fotones rápidos resultante es del 50 % y la probabilidad de identificación del fondo como fotones rápidos es del 7 %.

9. Apliqué ambos métodos de identificación a simulaciones de PYTHIA con el fin de construir el espectro de fotones rápidos que se espera medir en un año de funcionamiento del experimento ALICE. He calculado la sección eficaz de producción, y corregida por las eficiencias de identificación, y he estimado los errores sistemáticos y estadísticos. He obtenido que los errores sistemáticos debidos a los métodos de identificación son despreciables, y sólo los errores debidos al fondo son considerables, alrededor del 20 % para fotones de energías comprendidas en la región $20 < E_\gamma < 100$ GeV. Los errores estadísticos son dominantes para fotones de energías superiores a 60 GeV.

Identificación de sucesos γ-jet Los fotones rápidos están asociados con un jet en la dirección opuesta, el cual es sensible al medio nuclear formado en la colisión de iones pesados. He estudiado estos sucesos, llegando a las siguientes conclusiones:

10. He desarrollado un algoritmo de identificación de procesos γ-jet basado en la identificación de un fotón rápido en PHOS y en la medida de las partículas del jet en dirección opuesta por el sistema central de muestreo y (si está disponible) por el calorímetro electromagnético EMCal que será colocado opuesto a PHOS. Este algoritmo fue afinado y probado con sucesos señal (γ-jet) y fondo (jet-jet) de colisiones Pb-Pb y *pp*. Concluyo que la probabilidad de identificar un suceso γ-jet viene limitada por el tamaño del sistema de muestreo central y del calorímetro electromagnético, variando de un 30 % a un 50 %, dependiendo de la configuración de detectores utilizada para la reconstrucción de jets.

11. Dado que la sección eficaz de producción de procesos jet-jet es mucho mayor que la sección eficaz de sucesos γ-jet, hay un gran fondo debido a los fotones de desintegración de los mesones π^o. El fondo debido a la identificación de los fotones rápidos puede ser reducido a un nivel despreciable utilizando el algoritmo de identificación de sucesos γ-jet conjuntamente con los análisis de la forma de la cascada y del Método del Corte por Aislamiento.

12. La función de fragmentación de los partones, que contiene información sobre la pérdida de energía del partón en el medio nuclear, se calculó para los sucesos γ-jet generados tanto en colisiones *pp* como en Pb-Pb. Se obtuvo un factor de modificación nuclear $R_{FF} \simeq 1$, como se esperaba, dado que los sucesos simulados no incluyen ninguna modificación debida al medio nuclear. Con estas simulaciones obtuve que, independientemente de la configuración de detectores utilizada, variaciones del factor de modificación nuclear mayores que el 5 % en la región $0.1 < z < 0.5$ podrían ser medidas.

En resumen, la producción de fotones directos es una señal prometedora para estudiar la materia nuclear en condiciones extremas. He demostrado en la presente tesis que el detector PHOS posee capacidades muy adecuadas para realizar estos estudios en el experimento ALICE. Los algoritmos desarrollados para la detección de fotones en PHOS han sido afinados para obtener una identificación de partículas de gran pureza y eficiencia, y serán herramientas importantes para la colaboración cuando el experimento esté operativo. Es de destacar en este trabajo el estudio de la medida de las propiedades de procesos de alto momento transverso mediante el análisis de los jets. Si se combina PHOS con los otros detectores de ALICE, los efectos debidos al medio nuclear caliente y denso pueden ser probados con una buena sensibilidad.

Conclusions

Les objectifs de cette thèse sont l'étude des performances du détecteur PHOS et le développement des outils nécessaires pour l'identification de particules et la caractérisation des processus durs associés aux photons, dans le cadre de l'expérience ALICE en cours d'installation auprès du collisioneur LHC au CERN. L'expérience ALICE est dédiée principalement à l'étude du Plasma de Gluons et de Quarks produit dans des collisions d'ions lourds à des énergies ultra-relativistes (collisions Pb-Pb à $\sqrt{s} = 5.5A$ TeV). Parmi les signatures qui apportent des informations cruciales sur les propriétés du milieu nucléaire fortement perturbé, les photons sont particulièrement intéressants. En effet, ils sont produits au cours de toutes les étapes de la collision d'ions lourds et n'interagissent pas fortement avec le milieu nucléaire. Par conséquent les photons apportent des information non perturbées sur le milieu au sein duquel ils sont émis, jusqu'au moment où ils sont détectés. Les suivants sujets ont été étudiés aux différents chapitres: performance de PHOS, identification de particules, identification de photons prompts et identification d'événements γ-jet. Les conclusions obtenues sont:

Performances de PHOS Le spectromètre de photons, PHOS, est constitué de modules de cristaux de $PbWO_4$, chaque module couplé à un détecteur Veto de Particules Chargées. PHOS a été conçu pour mesurer et identifier, avec une grande précision, photons, électrons et mésons neutres. Les suivants conclusions à propos de la performance de PHOS ont été obtenues:

1. Nous avons mesurées des données à l'aide d'un prototype de PHOS pendant des test expérimentaux sous faisceau. Les résultats obtenus ont été employés pour ajuster les paramètres des algorithmes développés pour simuler le fonctionnement de PHOS et pour reconstruire les signaux collectés par PHOS. Les simulations et les données confirment que PHOS pourra mesurer avec une grande résolution en énergie qui varie de 5 % pour des énergies de photons de 0.5 GeV à 1 % pour des énergies des photons de 120 GeV. Les résultats des simulations indiquent, en plus, que la résolution en position qui pourrait être obtenue, est d'environ 3-4 mm pour des photons d'énergie de 1 GeV, et de 0.7-2.5 mm pour des photons d'énergie de 50 GeV, à différents angles d'incidence des photons sur PHOS.

2. L'environnement de particules créé par les collisions d'ions lourds, simulé par le

générateur d'événements HIJING, dégrade la résolution en énergie d'environ 2 % pour énergies de photons inférieures à 10 GeV, et de moins de 1 % pour des énergies de photons plus élevées.

3. L'effet des matériaux d'ALICE situés entre le point d'interaction et PHOS a été étudié. On a considéré deux configuration des détecteurs: configurations avec et sans des ouvertures pratiquées dans les détecteurs de Temps de Vol et de Radiation de Transition vis-à-vis de PHOS. Avec la configuration avec ouvertures, je trouve qu'environ 10 % des photons seront absorbés ou convertis dans les détecteurs Chambre de Projection Temporaire et le Système de Trajectographie Interne, ainsi que dans la structure mécanique portante d'ALICE. Mais cette perte augmente jusqu'à 30 % quand les détecteurs de Temps de Vol et de Radiation de Transition restent dans leur intégralité.

Identification de particules L'identification de particules avec PHOS repose sur trois méthodes : la mesure du temps de vol; l'identification des particules chargées grâce au lien entre l'impact au Veto de Particules Chargés et le Calorimètre Électromagnétique de PHOS; l'analyse de la forme de la gerbe électromagnétique. Dans cette thèse je conclue que:

4. Si nous combinons le temps de vol, le Veto de Particules Chargées et l'analyse de la forme de la gerbe avec l'Analyse des Composants Principales, les photons, électrons et hadrons sont discriminés avec une bonne précision dans le domaine d'énergie de particules s'étendant de 0.5 à 120 GeV. La méthode a été testée avec d'une part, un ensemble uniquement composé de photons et, d'autre part, une population de photons mélangés à un environnement de particules créées par des collision d'ions lourds, qui a été simulé par le générateur d'événements HIJING. Une des principales conclusions que j'obtiens, est que la contamination due à des photons mal identifiés est faible, et qu'elle varie d'environ 3 % à 1 % en fonction du niveau de pureté et de l'efficacité d'identification et en fonction de l'environnement de particules.

5. Les mésons π^0 peuvent être identifiés soit par l'application de méthodes statistiques avec analyse de la masse invariante pour des énergies de mésons entre 0 et 40 GeV, soit par recours à des analyses, événement par événement, prenant en compte la forme de la gerbe électromagnétique pour des mésons d'énergies entre 40 et 120 GeV, énergies pour lesquelles les deux photons de décroissance sont détectés comme une seule particule par PHOS. Dans cette dernière méthode, la mauvaise identification des mésons neutres comme photons est négligeable pour des énergies inférieures à 70 GeV mais cette perte d'efficacité s'accroît jusqu'à 5-15 % à 120 GeV en fonction de la méthode d'identification employé.

6. Les photons de haute énergie convertis dans les matériaux présents entre le point d'interaction et PHOS peuvent être récupérés en tirant profit d'informations disponibles grâce à la Chambre de Trajectographie Temporaire. Les photons convertis dans les matériaux situés entre la Chambre de Trajectographie Temporaire et PHOS en paires e^-e^+ sont

identifiés grâce à la présence d'un impact dans le Veto de Particules Chargées et son absence dans la Chambre de Trajectographie Temporaire. Par considération de la masse invariante ($M_{e^-e^+} = 0$), l'énergie du photon original peut être calculée. Cette méthode est seulement applicable dans le cas de la configuration d'ALICE sans ouvertures supplémentaires et dans ce cas on obtient une efficience de détection de photons qui s'approche à celle du cas avec ouvertures supplémentaires.

Identification des photons prompts Les photons prompts sont produits lors de collisions de partons, par, d'une part, processus Compton et, d'autre part, annihilation dans des collisions *pp* et Pb-Pb. La principal source de contamination sont les photons produits dans des événements avec deux jets à l'état final. Nous avons employé le générateur d'événements PYTHIA pour simuler les photons prompts et les événements de fond contaminant. J'ai obtenu les suivants résultats:

7. Le taux de production de photons prompts attendue pendant une année de fonctionnement de l'expérience ALICE montre que des photons prompts avec des énergies jusqu'à environ 100 GeV peuvent être mesurées avec PHOS.

8. Étant donnée que le fond prédit (photons de la décroissance du π^0 et radiation de freinage "bremsstrahlung") dépassera d'un facteur deux le signal dû aux photons prompts d'énergies plus larges que 20 GeV, les méthodes d'identification de photons développés ici, et juste résumées ci-dessus, n'est donc pas suffisante pour réduire le contamination à un niveau acceptable. Pour remédier à ce handicap, j'ai considéré une méthode d'identification additionnelle, la Méthode par Coupure d'Isolement. Cette méthode est basée sur le fait que les photons prompts sont produits isolés tandis que le fond est principalement dû à des mésons π^0 qui appartiennent à des jets qui sont, donc accompagnés par d'autres particules. Par conséquent, j'ai développé un critère d'isolement basé sur la considération de la multiplicité de particules dans le cône de taille R autour la direction d'un possible photon prompt, et sur une sélection appliquée à l'impulsion de ces particules présentes dans le cône. Cette approche m'a permis d'obtenir les paramètres idéaux suivants :

- Dans le cas des collisions *pp*, les photons prompts sont mieux identifiés si la somme de l'impulsion transversale de toutes les particules dans un cône de taille $R = 0.2$ est inférieure à 0.7 GeV/c. L'efficacité d'identification des photons prompts, dans ce cas, atteint environ 100 % et la perte d'efficacité due à une identification erronée ne dépasse pas 5 %.

- Dans le cas des collisions Pb-Pb, les photons prompts sont identifiés comme tels en l'absence de particules dans le cône de taille $R = 0.2$ possédant une impulsion transversale supérieure à 2 GeV/c. Dans le cas de telles collisions, l'efficacité

d'identification des photons prompts est environ égale à 50 % et la perte d'efficacité due à une identification erronée s'établit à 7 %.

9. J'ai appliqué les deux méthodes d'identification aux résultats des simulations PYTHIA et j'ai déterminé le spectre attendu de photons prompts, pendant une année de prise de données par l'expérience ALICE. La section efficace a été calculée, en tenant compte des efficacités d'identification et les erreurs systématiques et statistiques ont, également, été estimées. Les erreurs systématiques dues aux méthodes d'identification sont négligeables et seulement celles dues à la contribution du bruit de fond sont significatives, environ 20 % dans le domaine en énergie des photons de $20 < E_\gamma < 100$ GeV. Les erreurs statistiques dominent pour les énergies des photons supérieures à 60 GeV.

Identification d'événements γ-jet Les photons prompts sont couplés à un jet qui recule, lequel est sensible au milieu nucléaire produit dans des collisions d'ions lourds. J'ai étudié ces événements avec les conclusions suivants:

10. Pour isoler de tels événements, j'ai développé une méthode qui permet d'identifier ceux-ci, basée sur l'identification des photons prompts par PHOS et par la mesure des propriétés des particules du jet par le système central de trajectographie et, s'il est installé, par un CALorimètre ÉlectroMagnétique placé à la direction opposé à PHOS. Cet algorithme a été testé avec des évènements de type "signal" (γ-jet) et de type "bruit de fond" (jet-jet) produits en collisions Pb-Pb et *pp*. Grâce à l'emploi de cette approche, j'en ai conclu que la probabilité d'identifier des événements γ-jet, limitée par l'acceptance du système central de trajectographie et du CALorimètre ÉlectroMagnétique, atteint des valeurs comprises entre 30 % et 50 %, suivant la configuration de détecteurs employée pour la reconstruction des jets.

11. Étant donnée que la valeur de la section efficace de production des événements jet-jet est plus élevée que celle des événements γ-jet, il existe un bruit de fond important dû à la décroissance des mésons π^o. Néanmoins, j'ai été capable de montrer que la contribution du bruit de fond aux spectres des photons prompts peut être réduite à un niveau négligeable par l'algorithme d'identification d'événements γ-jet s'il est utilisé, conjointement, avec les analyses d'isolement et de forme de gerbe.

12. La fonction de fragmentation des partons, laquelle est modifié par la perte d'énergie des partons dans le milieu nucléaire, a été calculé pour les événements γ-jet simulés, pour collisions *pp* et Pb-Pb. Un facteur de modification nucléaire $R_{FF} \simeq 1$ a été obtenu, comme s'attend des données simulées qui ne contiennent pas des modifications induites par le milieu. Par contre, nos simulations permettent d'apprécier qu'indépendamment de la configuration de détecteurs employée, des variations du facteur de modification nucléaire supérieures à 5 % dans la région $0.1 < z < 0.5$ pourraient être mesurées.

En résumé, la production de photons directs est une signature prometteuse pour l'étude de la matière nucléaire dans des conditionnes extrêmes. J'ai montré dans cette thèse que le détecteur PHOS possède des capacités très adéquates pour réaliser de telles études pour l'expérience ALICE. Les algorithmes de détection de photons avec PHOS développés ont été ajustés afin d'obtenir identification de particules avec une grand pureté et efficacité, et sont des outils très importants pour la collaboration quand l'expérience soit opérationnel. Très important, je montre dans cette thèse les premières idées de comment mesurer les propriétés des processus à haut p_T par médiation de l'analyse des jets. Si nous combinons PHOS et autres détecteurs d'ALICE, les effets dues au milieu nucléaire dense et chaud pourraient être prouvés avec une bonne sensibilité.

Appendix A

Commonly used abbreviations

- AGS: Alternate Gradient Synchrotron
- APD: Avalanch Photo-Diode
- ATLAS: A Toroidal LHC ApparatuS
- ANN: Artificial Neural Network
- ALICE: A Large Ion Collider Experiment
- BNL: Brookhaven National Laboratory
- CERN: European Center for high energy physics
- CPV: Charged Particle Veto
- CMS: Compact Muon Spectrometer
- EMC: ElectroMagnetic Calorimeter
- EMCal: ElectroMagnetic Calorimeter
- FMD: Forward Multiplicity Detector
- HERWIG: Hadron Emission Reactions With Interfering Gluons
- HMPID: High Momentum Particles Identification Detector
- HIC: Heavy-Ion Collision
- HIJING: Heavy-Ion Jet INteraction Generator
- ICM: Isolation Cut Method
- ICMS: Isolation Cut Method with Sum threshold
- IP: Interaction Point

- ITS: Inner tracking system
- QCD: Quantum ChromoDynamics
- QED: Quantum ElectroDynamics
- QGP: Quark-Gluon Plasma
- LEP: Large Electron and Positron collider
- LHC: Large Hadron Collider
- LHCb: LHC beauty experiment
- MIP: Minimum Ionizing Particle
- MRPC: Multi-gap Resistive-Plate Chamber
- MWPC: Multi-Wire Particle Chamber
- NLO: Next to Leading Order
- PCA: Principal Components Analysis
- PHENIX: Pioneering High Energy Nuclear Interaction eXperiment at RHIC
- PHOS: PHOton Spectrometer
- PID: Particle Identification
- PMD: Photon Multiplicity Detector
- pQCD: perturbative QCD
- *pp*: proton-proton
- PS: Proton Synchrotron
- RHIC: Relativistic Heavy Ion Collider
- SPS: Super Proton Synchrotron
- SSA: Shower Shape Analysis
- TEC: Time Expansion Chamber
- TOF: Time of flight
- TPC: Time Projection Chamber
- TRD: Transition Radiation Detector
- ZDC: Zero Degree Calorimeter

Appendix B

Kinematics

In this Appendix, I review some of the most common kinematic variables in HIC. For more details see [Eid04].

Lorentz transformation

The energy E and 3-momentum $\mathbf{p}$ of a particle of mass m form a 4-vector $p = (E, \mathbf{p})$, being $p^2 = E^2 - |\mathbf{p}|^2 = m^2$. The velocity of the particle is $\beta = \mathbf{p}/E$. The energy and momentum $p' = (E', \mathbf{p}')$ viewed from a frame moving with velocity β_f are given by

$$\begin{pmatrix} E' \\ p'_{||} \end{pmatrix} = \begin{pmatrix} \gamma_f & -\gamma_f\beta_f \\ -\gamma_f\beta_f & \gamma_f \end{pmatrix} \begin{pmatrix} E \\ p_{||} \end{pmatrix}, \; p'_T = p_T, \tag{B.1}$$

where $\gamma_f = 1/\sqrt{1-\beta_f^2}$ is the Lorentz factor and $p_{T(||)}$ is the component of $\mathbf{p}$ transverse (longitudinal) to β_f. Other 4-vectors, such as the space-time coordinates transforms in the same way. The scalar product of two 4-momenta $p_1 p_2 = E_1 E_2 - \mathbf{p}_1\mathbf{p}_2$ is invariant (independent of the frame).

Lorentz contraction An observer moving with respect to an object will observe it to be contracted along the direction of motion by the factor

$$l' = l\sqrt{1-\beta^2}. \tag{B.2}$$

Consequently, two colliding heavy-ions at ultra-relativistic energies see one to each other as pancakes in their direction of motion.

Kinematic variables

Transverse momentum In HIC the beam direction is usually the z-axis. The momentum components p_x and p_y are unchanged by a Lorentz transformation (boost) along

the z-axis, so the transverse momentum defined as

$$p_T = \sqrt{p_x^2 + p_y^2}, \tag{B.3}$$

is boost invariant.

Rapidity The most commonly used longitudinal variable is the rapidity y defined as

$$y = \frac{1}{2} \ln \left(\frac{E + p_z}{E - p_z} \right), \tag{B.4}$$

which is additive under Lorentz transformations along z-axis. This means that the difference in rapidity dy and the rapidity density distribution dy/dN are invariant under Lorentz transformations along the z-axis.

Pseudorapidity If the mass and momentum of the particle are unknown, it is convenient to use the pseudorapidity,

$$\eta = -\ln \left[\tan \left(\frac{\theta}{2} \right) \right] = \frac{1}{2} \ln \left(\frac{|\mathbf{p}| + p_z}{|\mathbf{p}| - p_z} \right), \tag{B.5}$$

where θ is the polar angle between the particle momentum and the beam axis. If $|\mathbf{p}| \gg m$, then $\eta \sim y$.

Invariant mass Given 2 particles with $(E_1, \mathbf{p}_1)$ and $(E_2, \mathbf{p_2})$, the invariant mass is defined as

$$M_{12} = \sqrt{(E_1 + E_2)^2 - (\mathbf{p}_1 + \mathbf{p}_2)^2}. \tag{B.6}$$

The invariant mass of 2 photons produced by the decay of a neutral meson is

$$M_{\gamma_1\gamma_2} = \sqrt{2E_1E_2\,(1 - \cos\theta_{12})}, \tag{B.7}$$

where θ_{12} is the relative angle between the photons in the laboratory frame being

$$\cos\theta_{12} = \frac{\gamma_\pi^2\beta_\pi^2 - \gamma_\pi^2\alpha^2 - 1}{\gamma_\pi^2(1 - \alpha^2)}, \tag{B.8}$$

where α is the decay asymmetry defined as

$$\alpha = \frac{|E_1 - E_2|}{E_1 + E_2}. \tag{B.9}$$

Appendix C

PYTHIA cross sections

We have generated PYTHIA γ-jet [Eq. (3.2)] and jet-jet [Eq. (3.3)] events for pp collisions at $\sqrt{s_{NN}} = 5.5$ TeV with the default PYTHIA parametrization in AliRoot [ALI]. These events have been generated for a restricted acceptance:

- γ-jet events: pseudorapidity in the final event center-of-mass system $|\eta_\gamma| < 0.2$; azimuthal aperture of the photon $200^\circ < \phi_\gamma < 340^\circ$
- jet-jet events: rapidity in the subprocess center-of-mass system $|y_{parton}| < 0.2$ and pseudorapidity in the final event center-of-mass system $|\eta_{jet}| < 0.15$; no restriction in the azimuthal aperture.

PYTHIA calculates the cross sections for these processes at the different momentum bins generated. These values and the total number of generated events are shown in Tab. C.1.

$< p_T >$(GeV/c)	σ(mb)	N events
	γ-jet	
20-40	$1.16 \cdot 10^{-6}$	17,000
40-60	$1.14 \cdot 10^{-7}$	14,500
60-80	$2.53 \cdot 10^{-8}$	12,000
80-100	$8.31 \cdot 10^{-9}$	9,500
	jet-jet	
30-40	$2.13 \cdot 10^{-4}$	178,500
40-50	$6.68 \cdot 10^{-5}$	161,500
50-60	$2.62 \cdot 10^{-5}$	141,000
60-70	$1.19 \cdot 10^{-5}$	145,500
70-80	$5.98 \cdot 10^{-6}$	151,500
80-90	$3.29 \cdot 10^{-6}$	171,500
90-100	$1.89 \cdot 10^{-6}$	154,000
100-150	$2.97 \cdot 10^{-6}$	152,500
150-200	$4.76 \cdot 10^{-7}$	86,500
200-250	$1.20 \cdot 10^{-7}$	93,000
250-300	$3.75 \cdot 10^{-8}$	136,000

Table C.1: Cross sections and number of γ-jet and jet-jet events generated with the PYTHIA event generator.

Bibliography

[Abr97] M. C. Abreu *et al.*, Phys. Lett. **B410** (1997) 337–343.

[Abr99] M. C. Abreu *et al.*, Phys. Lett. **B450** (1999) 456–466.

[Abr00] M. C. Abreu *et al.*, Phys. Lett. **B477** (2000) 28–36.

[Acc03] A. Accardi *et al.*, hep-ph/0310274 (2003). Writeup of the working group "Jet Physics" for the CERN Yellow Report on "Hard Probes in Heavy Ion Collisions at the LHC: Jet Physic".

[Adc04] K. Adcox *et al.*, Nucl. Phys. **A** (2004). To be published, nucl-ex/0410003.

[Adl05] S. S. Adler *et al.*, nucl-ex/0503003 (2005).

[Aga98] G. Agakichiev *et al.*, Phys. Lett. **B422** (1998) 405–412.

[Agg98] M. Aggarwal *et al.*, Phys. Rev. Lett. **81** (1998) 4087–4091.

[Agg00a] M. Aggarwal *et al.*, Phys. Rev. Lett. **84** (2000) 578–579.

[Agg00b] M. Aggarwal *et al.*, Phys. Rev. Lett. **85** (2000) 3595–3599.

[Alb95] T. Alber *et al.*, Phys. Rev. Lett. **75** (1995) 3814–3817.

[Alb96] R. Albrecht *et al.*, Phys. Rev. Lett. **76** (1996) 3506–3509.

[ALI] *AliRoot: ALICE offline project*, URL `http://aliceinfo.cern.ch/Offline/`.

[ALI95] ALICE Collaboration, CERN/LHCC/95-71 (1995).

[ALI98] ALICE Collaboration, ALICE TDR **1** (1998).

[ALI99a] ALICE Collaboration, ALICE TDR **4** (1999).

[ALI99b] ALICE Collaboration, ALICE TDR **5** (1999).

[ALI99c] ALICE Collaboration, ALICE TDR **2** (1999).

[ALI99d] ALICE Collaboration, ALICE TDR **6** (1999).

[ALI99e] ALICE Collaboration, ALICE TDR **3** (1999).

[ALI00a] ALICE Collaboration, ALICE TDR **8** (2000).

[ALI00b] ALICE Collaboration, ALICE TDR **7** (2000).

[ALI01] ALICE Collaboration, ALICE TDR **9** (2001).

[ALI04] ALICE Collaboration, J. Phys. G: Nucl. Part. Phys. **30** (2004) 1517–1763.

[Amb98] G. Ambrosini *et al.*, Phys. Lett. **B417** (1998) 202–210.

[Amb99] G. Ambrosini *et al.*, New J. Phys. **1** (1999) 22.1–22.23.

[And99] E. Andersen *et al.*, Phys. Lett. **B449** (1999) 401–406.

[Ant99a] F. Antinori *et al.*, Nucl. Phys. **A661** (1999) 130c–139c.

[Ant99b] F. Antinori *et al.*, Nucl. Phys. **A661** (1999) 481c–484c.

[Aph02] L. Aphecetche *et al.*, ALICE Note **ALICE-INT-2002-02** (2002).

[Aph03] L. Aphecetche *et al.*, Nucl. Intr. Method. Phys. Res. **A499** (2003) 521–536.

[App98] H. Appelshäuser *et al.*, Eur. Phys. J. **C2** (1998) 661–670.

[Arl03] F. Arleo *et al.*, hep-ph/0311131 (2003). Writeup of the working group "Photon Physics" for the CERN Yellow Report on "Hard Probes in Heavy Ion Collisions at the LHC".

[Arl04] F. Arleo, P. Aurenche, Z. Belghobsi and J.-P. Guillet, JHEP **11** (2004) 009.

[Arm02] N. Armesto, A. Capella, E. Ferreiro and A. Kaidalov, Nucl. Phys. A **698** (2002) 583–586.

[Ase02] A. Aseev, M. Bogolyubsky, V. Viktorov *et al.*, Preprint IHEP 2002-3, Protvino (2002).

[Bea97] H. I. Bearden *et al.*, Phys. Rev. Lett. **78** (1997) 2080–2083.

[Bea99] H. I. Bearden *et al.*, Phys. Lett. **B471** (1999) 6–12.

[Bek95] H. Beker *et al.*, Phys. Rev. Lett. **74** (1995) 3340–3343.

[Bha90] P. Bhat, L. Lönnblad, K. Meir and K. Sugano, Proceedings of the 1990 DPF Summer, Study in High Energy Physics, Ed. E.L. Berger (1990) 168.

[Bit81] S. Bityukov, S. Sadovsky, V. Semenov and V. Smirnova, Preprint IHEP 81-45, Serpukhov (1981).

[Bjo83] J. D. Bjorken, Phys. Rev. **D27** (1983) 140–151.

[Bli00] A. Blick, M. Bogolyubsky, A. D. Mauro *et al.*, ALICE Note **ALICE-INT-2000-021** (2000).

[BNL] *BNL*, URL `http://www.bnl.gov/`.

[Bog02] M. Bogolyubsky *et al.*, Tech. Exp. Tech. **45** (2002) 327–340.

[Bog04] M. Bogolyubsky, Y. Kharlov and S. Sadovsky, ALICE Note **ALICE-INT-2003-037** (2004).

[Bru79] R. Brun, M. Hansroul and J. Kubler, CERN preprint DD/EE/79-5 (1979).

[Cam01] X. Camard *et al.*, ALICE Note **ALICE-INT-2001-27v01** (2001).

[Cas04] J. Castillo, J. Phys. G: Nucl. Part. Phys. **30** (2004) S1207–S1211.

[CER] *CERN*, URL `http://www.cern.ch/`.

[CMS97] CMS Collaboration, CMS TDR **4** (1997), URL `http://cmsdoc.cern.ch/cms/TDR/ECAL/ecal.html`.

[Cor04] T. M. Cormier, Eur. Phys. J. **C34** (2004) s333–s345.

[Dai03] A. Dainese, *Ph.D. Thesis: Charm production an in-medium QCD energy loss in nucleus-nucleus collisions with ALICE. A performance study* (2003). nucl-ex/0311004.

[Del01] H. Delagrange *et al.*, ALICE Note **ALICE-INT-2001-01** (2001).

[Eid04] S. Eidelman *et al.*, Phys. Lett. **B592** (2004) 1.

[Esk95] K. J. Eskola, R. Vogt and X. N. Wang, Int. J. Mod. Phys. **A10** (1995) 3087–3090.

[Esk00] K. J. Eskola, K. Kajantie, P. Ruuskanen and K. Tuominen, Nucl. Phys. **B570** (2000) 379–389.

[Esk01] K. J. Eskola, K. Kajantie, P. Ruuskanen and K. Tuominen, Nucl. Phys. **A696** (2001) 715–728.

[Esk03] K. J. Eskola *et al.*, hep-ex/0110348 (2003). Contribution to CERN Yellow Report on Hard Probes in Heavy Ion Collisions at the LHC.

[Fan02] K. Fanebust *et al.*, J. Phys. **G28** (2002) 1607–1614.

[Fas01] A. Fassò, A. Ferrari, J. Ranft and P. Sala, *FLUKA: Status and Prospective for Hadronic Applications* (Springer-Verlag Berlin, 2001). 955-960.

[Fri04] R. J. Fries and B. Müller, Eur. Phys. J. **C34** (2004) S279–S285.

[GEAa] *GEANT3*, URL `http://wwwasd.web.cern.ch/wwwasd/geant/`.

[GEAb] *GEANT4*, URL `http://wwwasd.web.cern.ch/wwwasd/geant4/geant4.html`.

[Gla70] R. Glauber and G. Matthias, Nucl. Phys. **B21** (1970) 135–157.

[Gyu94] M. Gyulassy and X.-N. Wang, Comput. Phys. Commun. **83** (1994) 307–331.

[Han01] S. Hands, Contemp. Phys. **42** (2001) 209–225.

[Her98] M. J. Herrero, *The standard model* (1998). hep-ph/9812242. Lectures presented at the NATO ASI 98 School, Techniques and Concepts of High Energy Physics; St. Croix, Virgin Islands, USA, June 18-29.

[Jac05] P. Jacobs and X.-N. Wang, Prog. Part. Nucl. Phys. **54** (2005) 443–534.

[Kad02] K. Kadija *et al.*, J. Phys. **G28** (2002) 1675–1682.

[Kli96] R. Klingenberg *et al.*, Nucl. Phys. **A610** (1996) 306c–316c.

[Kow02] M. Kowalski, *Presentation at the TPC meeting* (2002). ALICE-PR-2002-131.

[Len99a] B. Lenkeit *et al.*, Nucl. Phys. **A654** (1999) 627c–630c.

[Len99b] B. Lenkeit *et al.*, Nucl. Phys. **A661** (1999) 23c–32c.

[LHC] *LHC*, URL `http://lhc-new-homepage.web.cern.ch`.

[MÖ1] B. Müller, nucl-th/0404015 (2001). Contribution to RBRC Scientific Articles Proceedings Series "New Discoveries at RHIC".

[Mag97] T. Maggipinto *et al.*, Phys. Lett. **B409** (1997) 517–522.

[Mat86] T. Matsui and H. Satz, Phys. Lett. **B178** (1986) 416–422.

[Min94] N. Minaev, Preprint IHEP 94-142, Protvino (1994).

[Mol03] A. Molinari, L. Riccati, W. Alberico and M. Morando (eds.), *Proceedings of the international school of physics Enrico Fermi: From Nuclei and their constituents to stars, course CLIII* (IOS Press, 2003).

[Nov00] S. F. Novaes, *Standard model: An introduction* (2000). hep-ph/0001283. Published in "Particle and Fields", Proceedings of the X J. A. Swieca Summer School (World Scientific, Singapore.

[Pei02] T. Peitzmann and H. Thoma, Phys. Report **364** (2002) 175–246.

[Pet90] C. Peterson, L. Lönnblad and T. Rögnvaldsson, Phys. Rev. Lett **65** (1990) 1321–1324.

[Pet91] C. Peterson, L. Lönnblad and T. Rögnvaldsson, Nucl. Phys. **B349** (1991) 675–702.

[Pet94] C. Peterson, L. Lönnblad and T. Rögnvaldsson, Comp. Phys. Comm **81** (1994) 185–291.

[Rei00] E. Reid and H. Heath, CMS Note **2000/063** (2000).

[RHI] *RHIC*, URL `http://www.bnl.gov/rhic`.

[Rit04] H. G. Ritter and X.-N. Wang (eds.), *Proceedings of the 17th International Conference of Ultra-Relativistic Nucleus-Nucleus Collisions*, vol. 30 (IoP, 2004).

[Roo] *Root*, URL `http://root.cern.ch/`.

[Sal04] C. A. Salgado and U. A. Wiedemann, Phys. Rev. Lett. **93** (2004) 042301.

[Sca90] I. Scabai, F. Czako and Z. Fodor, *Quark and gluon jet separation using neural networks*, Tech. Rep. 477, ITP Budapest (1990).

[Sik99] F. Siklér *et al.*, Nucl. Phys. **A661** (1999) 45c–54c.

[Sjo01a] T. Sjostrand, L. Lönnblad and S. Mrenna, hep-ph/0108264 (2001). PYTHIA 6.2: Physics and manual.

[Sjo01b] T. Sjostrand *et al.*, Comput. Phys. Commun. **135** (2001) 238–259.

[Sus02] T. Susa, Nucl. Phys. A **698** (2002) 491–494.

[Wib98] T. Wibig and D. Sobezynska, J. Phys. G: Nucl. Part. Phys. **24** (1998) 2037–2047.

[Wie04] U. A. Wiedemann, J. Phys. G: Nucl. Part. Phys. **30** (2004) S649–S657.

[Yin04] Z. Yin, *Ph.D. Thesis: High p_T physics in heavy ion collisions at $\sqrt{s_{NN}} = 200$ GeV* (2004).